JYU DISSERTATIONS 236

Miika Leppänen

Infection under the Ion Beam

Focused Ion Beams and Antibacterial Properties of Biomaterials

UNIVERSITY OF JYVÄSKYLÄ
FACULTY OF MATHEMATICS
AND SCIENCE

JYU DISSERTATIONS 236

Miika Leppänen

Infection under the Ion Beam

Focused Ion Beams and Antibacterial Properties of Biomaterials

Esitetään Jyväskylän yliopiston matemaattis-luonnontieteellisen tiedekunnan suostumuksella
julkisesti tarkastettavaksi
kesäkuun 17. päivänä 2020 kello 12.

Academic dissertation to be publicly discussed, by permission of
the Faculty of Mathematics and Science of the University of Jyväskylä,
on June 17, 2020 at 12 o'clock noon.

JYVÄSKYLÄN YLIOPISTO
UNIVERSITY OF JYVÄSKYLÄ

JYVÄSKYLÄ 2020

Editors
Timo Sajavaara
Department of Physics, University of Jyväskylä
Päivi Vuorio
Open Science Centre, University of Jyväskylä

Permanent link to this publication: http://urn.fi/URN:ISBN:978-951-39-8187-7

ISBN 978-951-39-8187-7 (PDF)
URN:ISBN:978-951-39-8187-7
ISSN 2489-9003

ABSTRACT

Leppänen, Miika
Infection under the ion beam - Focused ion beams and antibacterial properties of biomaterials

Jyväskylä: University of Jyväskylä, 2020, 58 p.
(JYU Dissertations
ISSN 2489-9003; 236)
ISBN 978-951-39-8187-7 (PDF)

In this thesis, Helium Ion Microscopy (HIM) imaging and milling on organic and antibacterial materials will be discussed. In addition, I will discuss the antibacterial properties of surface-immobilized bacteriophages. HIM is a recently developed imaging method, which is especially suitable for biological samples because they can be imaged without a metal coating. Because of the state-of-the-art ion source, the microscope has also a higher imaging resolution compared to the scanning electron microscope (SEM). The suitability of HIM imaging for the bacteria-phage interactions is discussed in addition to the more delicate nanocellulose samples. High beam damage on the cellulose was found which has not been reported previously with HIM. Indeed an ion beam can have a milling property, which is demonstrated here with bacteria, bacteria-dragonfly interactions and encapsulated bacteriophages to obtain volumetric information. The antibacterial effectivity of immobilized bacteriophages was analyzed quantitatively with HIM-imaging and biological measures. It was found that detaching phages from the material are likely the major contributor to the infectivity of the phage-biomaterial.

Keywords: helium ion microscopy, focused ion beam milling, nanocellulose, phage therapy, phage-biomaterial, bacteriophage immobilization

Author's address

Miika Leppänen
Department of Physics
University of Jyvaskyla
Finland
miika.j.leppanen@gmail.com
miika.j.leppanen@jyu.fi

Supervisors

Professor Ilari Maasilta
Department of Physics
University of Jyvaskyla
Finland

Associate professor Lotta-Riina Sundberg
Department of Biological and Environmental Science
University of Jyvaskyla
Finland

Reviewers

Dr. Matthias Schmidt
Helmholtz Centre for Environmental Research - UFZ
Leipzig
Germany

Dr. Teemu Ihalainen
Faculty of Medicine and Health Technology
Tampere University
Finland

Opponent

Dr. Gregor Hlawacek
Helmholtz-Zentrum Dresden-Rossendorf
Germany

PREFACE

The work reviewed in this thesis has been carried out during the years 2015-2020 at the Nanoscience Center, Department of Physics and Department of Biological and Environmental Science at the University of Jyvaskyla.

I would like to thank my supervisors Ilari Maasilta and Lotta-Riina Sundberg for the opportunity to work in their groups and for making everything possible. Thanks to all the co-authors for the smooth cooperation. Thanks to Gabriel Almeida, Annika Ketola, Danish Malik and Chaturanga Bandara for their inspiring projects, which made this thesis to that special form. Special thanks to Elina Laanto and Petri Papponen for the introduction to the phage- and laboratory work and Kai Arstila for all the time with the microscope. Thanks to the Visa Ruokolainen and Kosti Tapio for the help in the laboratory. Thanks to the technical personnel, Kimmo Kinnunen, Tarmo Suppula and Alli Liukkonen for their kind help. Thanks to the follow-up group members Janne Ihalainen and Jussi Toppari. Thanks to all co-workers within NSC for those important discussions in the lab or the aisle. Warmest thanks to all supporting departmental staff, both in Physics and Biology. My dear wife Hanna, caring parents, special family members and all the great friends who have involved along the journey.
Financial support from the Jane and Aatos Erkko Foundation.

Pomarkku 23.5.2020
Miika Leppänen

LIST OF PUBLICATIONS

The main results of this thesis have been reported in the following articles:

A.I Leppänen, M., Maasilta, I. J., & Sundberg, L. (2019). Antibacterial efficiency of surface-immobilized Flavobacterium-infecting bacteriophage. *ACS Applied Bio Materials, 2*(11), 4720-4727

A.II Leppänen, M., Sundberg, L., Laanto, E., de Freitas Almeida, Gabriel Magno, Papponen, P., & Maasilta, I. J. (2017). Imaging bacterial colonies and Phage–Bacterium interaction at sub-nanometer resolution using helium-ion microscopy. *Advanced Biosystems, 1(8),* 1700070

A.III Ketola, A., Leppänen, M., Turpeinen, T., Papponen, P., Strand, A., Sundberg, A., Arstila, K., & Retulainen, E. (2019). Cellulose nanofibrils prepared by gentle drying methods reveal the limits of helium ion microscopy imaging. *RSC Advances, 9*(27), 15668-15677.

A.IV Vinner, G. K., Rezaie-Yazdi, Z., Leppanen, M., Stapley, A. G. F., Leaper, M. C. & Malik, D. J. (2019). Microencapsulation of Salmonella-Specific Bacteriophage Felix O1 Using Spray-Drying in a pH-Responsive Formulation and Direct Compression Tableting of Powders into a Solid Oral Dosage Form. *Pharmaceuticals 12 (1),* 43.

A.V Vinner, G. K., Richards, K., Leppanen, M., Sagona, A. P., & Malik D. J. (2019). Microencapsulation of enteric bacteriophages in a pH responsive solid oral dosage formulation using a scalable membrane emulsification process. *Pharmaceutics, 11*(9), 475.

A.VI Bandara, C., Ballerin, G., Leppänen, M., Tesfamichael, T., Ostrikov K., Whitchurch, C. (2020). Resolving Bio-Nano Interactions of *E.Coli* Bacteria-Dragonfly Wing Interface with Helium Ion and 3D-Structured Illumination Microscopy to Understand Bacterial Death on Nanotopography. ACS Biomater. Sci. Eng (forthcoming)

A.VII Almeida, G. M., Leppanen, M., Maasilta, I. J. & Sundberg, L. R. (2018). Bacteriophage imaging: past, present and future. *Research in microbiology 169 (9)*, 488-494.

Author's contribution

In **A.I** author planned and performed the experiments and the analysis and wrote the first draft.

In **A.II** author planned and performed the experiment and the analysis and wrote the first draft.

In **A.III** author participated in the planning of the study, performed the experimental part regarding the ion microscopy, and participated in the analysis and writing.

In **A.IV** author planned and performed the experiments regarding the ion microscopy and participated in the writing process.

In **A.V** author planned and performed the experiments regarding the ion microscopy and participated in the writing process.

In **A.VI** author planned and performed the experiments regarding the ion microscopy and participated in the writing process.

In **A.VII** author participated in the writing process.

CONTENTS

1 INTRODUCTION

Nanoscience and nanotechnology are activities happening on the scale of nanometers. Interest in the small nanometer-sized phenomena has increased recently in different scientific disciplines. For example, chemists have found that a large surface-area-to-volume ratio of nanoparticles enables reactions not happening on the macroscopic scale. Physicists have found that electronics in the nanoscale have exciting quantum effects, which for example, can be used to build a quantum computer. Finally, life is naturally happening in the nanoscale. That is because all the biological interactions of proteins and nucleic acids, which make us live, happen at the nanoscale.

To be able to understand or control things, the ability to see is important. For the human senses, it is impossible to see things smaller than hundreds of micrometers and therefore, microscopes are needed. This tool improves the resolving power of the eye and has been used already for hundreds of years. Philosopher Seneca has written circa A.D. 63 "Letters, however small and dim are comparatively large and distinct when seen through a glass globe filled with water" (Singer, 1914). Here the refraction of the light created the magnified image of the letters.

First microscopes had quite modest magnifications, but as technology has developed, more advanced instruments and methods have been introduced. One significant step during the modern times was the invention of the electron microscope in the 1930s'. This instrument made a leap from the microscale to the nanoscales. Indeed, it is fascinating that the first sub-micron particles imaged were viruses, whose nature was unknown before Ruska's discoveries (von Borries, Ruska, & Ruska, 1938). Ion microscopy is a very recent advancement in the field of microscopy and I will discuss its benefits on the biological materials within this thesis.

Antimicrobial-resistant (AMR) bacteria cause every year thousands of deaths and suffering globally. In 2016, a UK government-commissioned review estimated that in 2050 AMR could cause 10 million deaths globally in a year, surpassing cancer (The Review on Antimicrobial Resistance Chaired by Jim O'Neill, 2014). This has received attention also from the UN General Assembly in 2016

(The PLOS Medicine Editors, 2016). To meet the challenge reduced and restricted use of current antimicrobials is needed. In this transition, alternative antimicrobials are also needed. This alternative antimicrobial could be for example bacteriophages or antimicrobial surfaces (Abedon, Kuhl, Blasdel, & Kutter, 2011; Rigo et al., 2018). This option will be discussed in this thesis.

2 BACKGROUND: MICROSCOPY IN THE NANOSCALE

Microscopy in the nanoscale can be divided into the two main classes by the operating principle, *touching* or *seeing*. The two classes are scanning probe microscopy (SPM) and wave-matter microscopy respectively (FIGURE 1). Atomic force microscopy (AFM) is a well-known member of the SPM family. In this method, the nanometer-scale forces between the probe and the sample are used to map out the topographical shapes of the sample. The benefits of the method are the very high vertical resolution and the low interaction energies. The ultimate limit for the SPM resolution is the interaction area by the nanometer-sized scanning tip head.

Wave-matter microscopes, on the other hand, utilize interaction of the electromagnetic radiation with the sample to study its structure. The best-known instrument of this class is the optical light microscope, which uses photons of visible wavelengths to create a magnified image from the object. Like a glass globe filled with water.

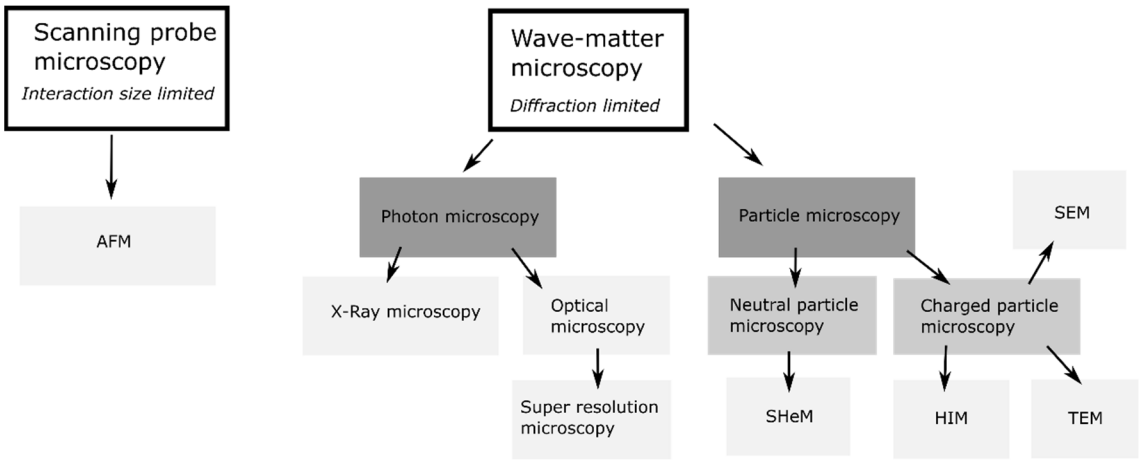

FIGURE 1 Nanoscale microscopy classified by operating principle.

When smaller and smaller structures are studied with the optical microscope, the image will be fuzzy even with the best objectives. That is because the diffraction of light will distort the image. This limitation was found already in 1873 and it is called the Abbe diffraction limit

$$d = \frac{\lambda}{2NA}, \tag{1}$$

where d is the smallest resolvable distance between the objects with a wavelength λ and NA is the numerical aperture of the lens, which describes the optical system and has a maximum value of approximately two. This resolution restriction has been circumvented in several super-resolution methods based on for example a near field properties of the light or use of fluorophores. It is clear from equation 1 that the nanometer-scale imaging, without special methods, requires shorter wavelengths. In the case of photons, this will mean x-ray or shorter wavelengths (FIGURE 2). These short-wavelength photons are already used within the x-ray diffraction methods, where the structures of the materials are resolved at atomic resolution. With these methods, parallel probes are used to form a diffracted image from periodic structures like crystals. Therefore, these methods are not usually classified as microscopy. True x-ray microscopy methods like X-ray tomography have several magnitudes lower resolution compared to x-ray diffraction. The underlying reason is that the photons with short wavelengths are challenging to handle optically e.g. to focus.

Because of the challenges to control the short wavelength photons, particles with mass have been adopted for nanoscale microscopy. Charged particles are especially convenient because they can be controlled with electromagnetic fields. The wavelength for the particles depends on the mass and the speed of the particle according to the de Broglie equation

$$\lambda = \frac{h}{mv} \tag{2}$$

From the equation, it is found that electrons accelerated with a couple of hundreds of volts have short enough wavelengths for nanoscale imaging (FIGURE 2). This property has been utilized already for a long time as the first images of viruses were obtained with a transmission electron microscope (TEM) (FIGURE 1). In practice, electrons are accelerated with an electric field and focused with electromagnetic lenses to the sample. Interactions of the particle beam with the sample are detected and a micrograph is formed. The measured observables depend on the instrument, and could be atomic density (TEM) or secondary electron emission like in Scanning electron microscope (SEM). With the high voltage (or energy) TEMs, even the atoms are possible to resolve (Erni, Rossell, Kisielowski, & Dahmen, 2009). However, with high energies, the damage caused to the material can be significant especially with soft biological samples. To overcome this, special methods like single-particle cryo-EM has been developed where averaging over multiple similar particles is done. With this method,

atomic resolution imaging on identical biological particles like proteins is made possible.

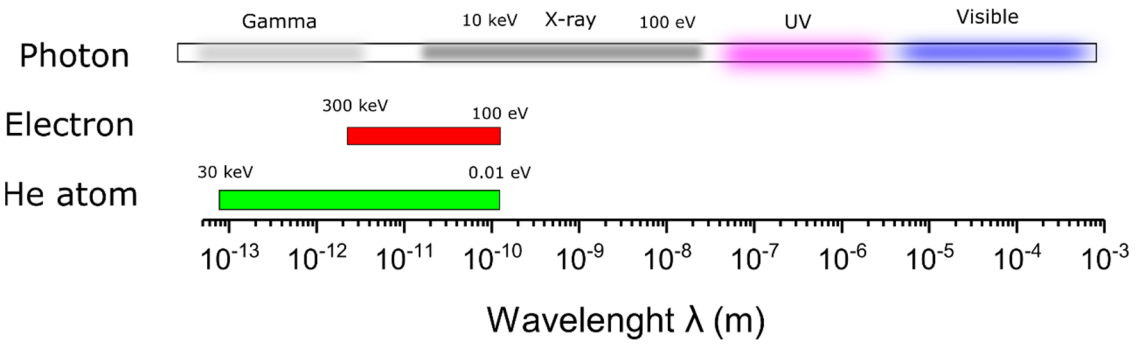

FIGURE 2 Wavelengths and energies for photons and particles. For particles, equal wavelengths are reached with much smaller energies compared to photons.

The transition from photons to electrons with similar energies shortens the wavelength and increases the resolving power of the probe over 100 fold. Heavier particles, like He atoms, have even shorter wavelengths with equal energies or conversely, equal wavelengths can be achieved with much lower energies (FIGURE 2). The reduction is even bigger when moving from electrons to ions than from photons to electrons. Therefore, atoms or ions are an appealing choice for microscopy. Ions are the first bet because they can be controlled with electrostatic lenses. Ion microscopy will be discussed in the next section.

Many wave-matter microscopy methods have also the possibility for 3D imaging. Photons penetrate liquids and this has been used for example in confocal microscopy. Shorter wavelength photons penetrate also solid materials and this has used with x-ray tomography. Particles with mass, like electrons or ions, do not travel long distances in solid materials and volumetric methods are limited to thin samples. This can be overcome with serial sectioning methods, where a knife or an ion beam has been used to create a stack of thin sections to be imaged.

For biological imaging, liquid environment is required if interactions need to be visualized when they happen. Scanning probe microscopy or photon microscopy are clear choices because they do not require a vacuum environment. With these methods, even living things can be studied. Particle microscopes, on the other hand, require a vacuum, and biological samples should be prepared properly. Commonly used preparation methods are chemical fixing, resin embedding or cryo-freezing, where the biological state is “frozen” before the imaging. Understanding the requirements for the sample preparation prior to the specific method is central for acquiring reliable results.

Because of the high complexity of the most advanced microscopes, the commercial potential of the technology is driving its development. For example, the semiconductor industry has been driving the development of Focused Ion Beam (FIB) methods. A recent example of commercialization is the Helium ion

microscopy (HIM) method, which is realized as a product currently by a single company.

At the moment, the boundaries between microscopy and spectroscopy are falling. Confocal microscopy with fluorescent labels can be understood as fluorescence spectroscopy with spatial information, or FIB-SIMS (Secondary ion mass spectrometry) imaging as mass spectrometry with spatial information. Understanding the physical basis of the used methods is important for one to be able to draw reliable conclusions of the results.

2.1 Ion microscopy

Ion microscopy approaches belong to the family of charged particle microscopies, which includes, for example, scanning electron microscopy (SEM) and transmission electron microscopy (TEM) (FIGURE 1). In scanning ion microscopy, the basic principle is quite similar compared to SEM, but instead of electrons, ions are used as the charged particles. In the scanning method, the ion or electron beam is focused on a small nanometer-sized spot on the sample in which interaction with the material is measured. A common interaction to measure is the secondary electron emission, which gives information about the topographical shapes of the sample. That is due to more secondary electrons are emitted from the edges than from flat surfaces (
FIGURE 3). When secondary electron emission is measured point by point over the sample, the rasterized data form the final image. The image formed in
FIGURE 3 is two dimensional but the height information is not quantitative. That is why regular 2D scanning microscope images have a 3D sensation and are sometimes called pseudo-3D or 2.5D.

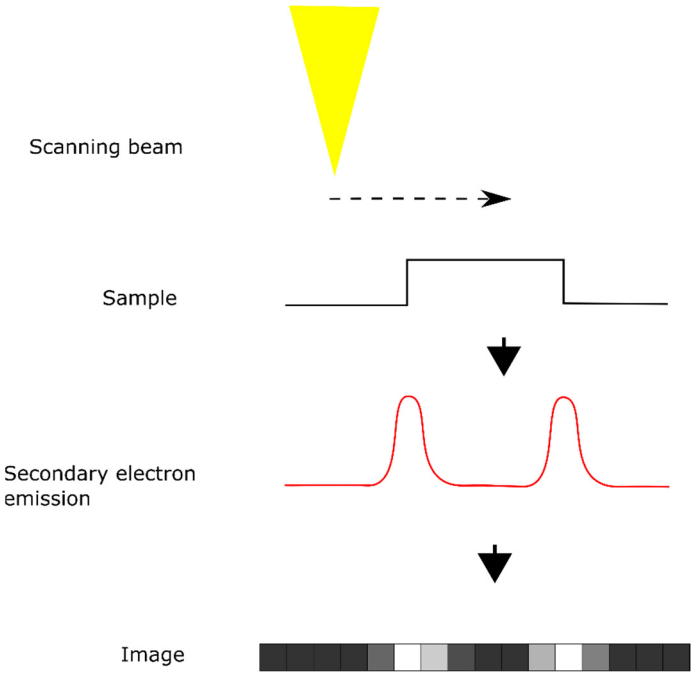

FIGURE 3 Image formation in the scanning beam microscope by the secondary electron emission. When the scanning beam is moved over a square-shaped sample, more secondary electron emission is generated from the edges, which forms the topographical image.

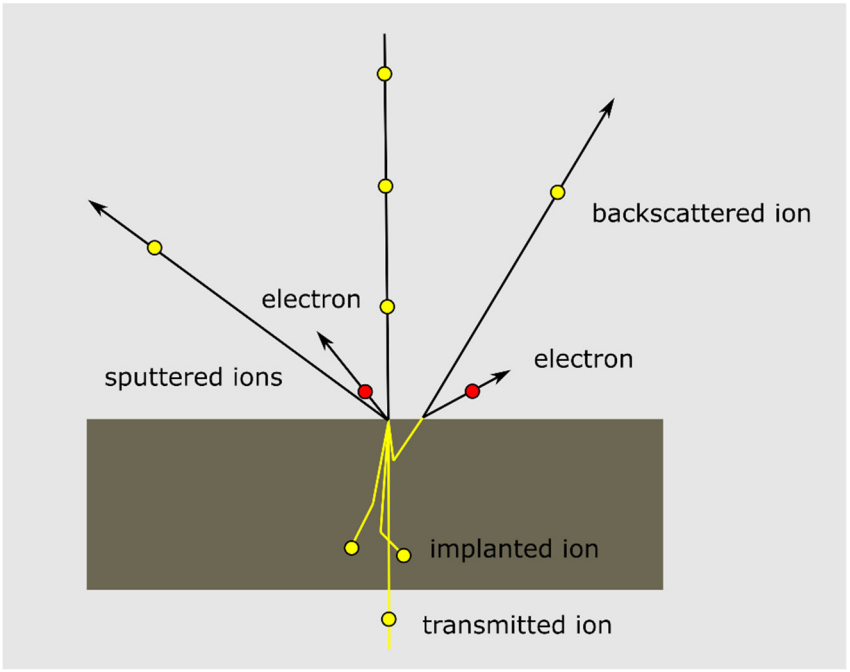

FIGURE 4 Ion beam interactions with matter. The distribution of different generated particle species will vary depending on the mass and the energy of the ion.

Accelerated ions have varying interactions with the material (FIGURE 4). Briefly, high-speed ions lose their energy in collisions until they end up being implanted,

transmitted or backscattered. Collisions can lead to sputtering of the target material from the sample surface or displacements in the crystal lattice. The mass and the energy of the accelerated ion will affect the distribution of the different species. Other interactions include secondary electron emission that can be used for the topographical image formation as in the SEM.

Sputtering properties of the ions are used in the Focused ion beam (FIB) milling method and secondary-ion mass spectrometry (SIMS) (FIGURE 4).

Traditionally, milling applications of the ion beam have been dominating over imaging. Common applications include TEM lamella preparation and photomask repairs in the semiconductor industry. More recently this technology has been adopted to biological imaging as TEM lamella preparation and slice and image methods with FIB-SEM (Narayan & Subramaniam, 2015).

Commercial FIB systems usually have a liquid metal ion sources (LMIS) in which the field emission from the liquid metal tip is used to rip the ions to produce the ion beam (FIGURE 5a). A commonly used metal is gallium, but in practice, other elements could be used as well. The field emission is based on the phenomenon where the electric field between the anode and cathode has a maximum at the sharp point of the tip and electron emission or ionization is happening at this localized area (FIGURE 5a). Tungsten is a widely used tip material because of its high work function.

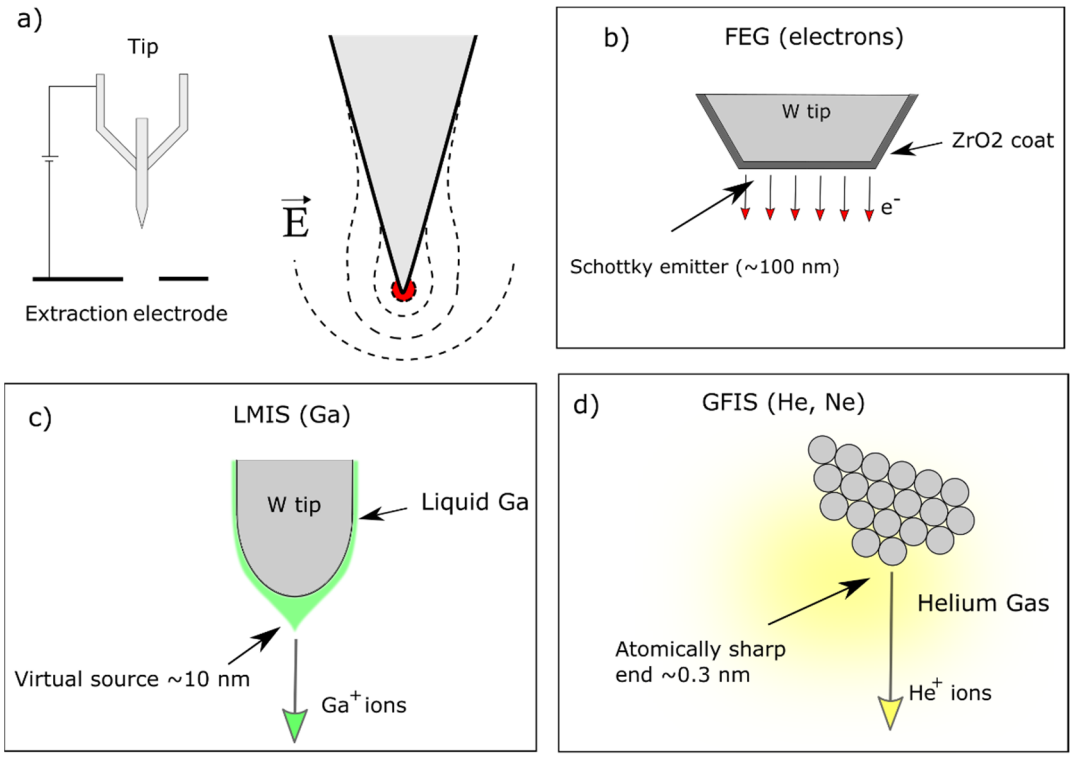

FIGURE 5 Field emission sources a) Electric field has a maximum in the small red spot around the tip b) Field emission sources using electrons c) Gallium liquid metal d) Helium and neon gas

The quality of the ion source has been the limiting factor for the development of ion microscopy for imaging purposes. The realized probe sizes with the commonly used LMIS sources are tens of nanometers, which limits the achievable imaging resolution. The probe size is mostly determined by the brightness (or brilliance) of the source defined as

$$\beta = \frac{4\,I}{(\pi\, d\, \alpha)^2} \tag{3}$$

Here I is a current from the source with diameter d and semi-convergence angle α in steradian (FIGURE 6). From the equation, it is clear that a small diameter source with the high current is preferred to obtain small probe sizes.

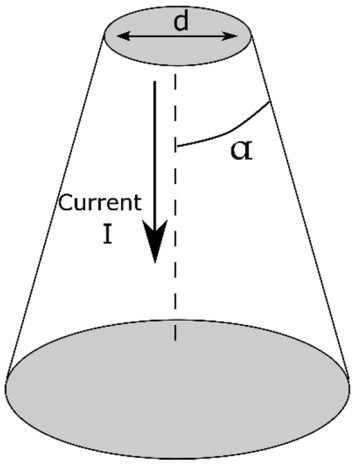

FIGURE 6 Source brightness schematics for equation 3.

The brightness for the state-of-the-art field electron emission gun (FEG) (FIGURE 5b) could be as high as 10^8 A/cm^{2}str whereas for the LMIS it is about 5×10^6 A/cm^2 str (Orloff, 2001). Therefore, the achieved spot sizes are much lower for the LMIS. The recently developed Gas Field Ion Source (GFIS) uses gaseous He or Ne as the ion source. This source utilizes the same field emission principle as the other state-of-the-art charged particle microscopes but with an atomically sharp tip end (FIGURE 5d). The brightness of the GFIS source can be as high as 10^9 A/cm^{2}str (Joy, 2013). In the next chapter, I will discuss the principles of HIM-instrument which uses this GFIS source. Interestingly, the GFIS source is also used in the recent extreme ultraviolet lithography (EUV) mask repair instrument by Hitachi (Yasaka Anto, Aramaki Fumio, Kozakai Tomokazu, & Matsuda Osamu, 2016).

2.2 Helium ion microscope (HIM)

Scanning helium ion microscope (HIM) is the only commercially available ion microscope with GFIS source (Hill, Notte, & Scipioni, 2012; Hlawacek, Veligura, van Gastel, & Poelsema, 2014; Ward, Notte, & Economou, 2006). It has been stated that major benefits of HIM over SEM in imaging are the increased lateral resolution by the smaller probe size, the smaller excitation volume by ions compared to electrons, and the possibility to image dielectric samples uncoated (Hill et al., 2012). A smaller probe size is possible because of the high brightness of the source, as discussed in the previous chapter. Low energy spread of the accelerated ions is also helping to achieve the small probe size because it reduces aberrations in the electrostatic lenses (Hlawacek & Gölzhäuser, 2016). Another contribution to the small spot size is the reduced diffraction of the ions in the aperture compared to the electrons with similar energies. That is due to the shorter wavelength of the ions compared to the electrons as discussed earlier.

The electro-optical system of the HIM is quite similar compared to the SEM. The notable differences are the electrostatic lenses and the source demagnification. Electrostatic lenses are needed because electromagnetic forces are not strong enough for ions. The source demagnification is not used in practice with HIM because the source size is already small enough and the total emitted current is low. With a typical electron FEG, 20x or higher source demagnification is used to reduce the 20-100 nm diameter source to a nanometer-sized spot (Hlawacek & Gölzhäuser, 2016). At the same time, the probe current is reduced accordingly. The disadvantage of the lack of source demagnification in the HIM is the visible source vibrations (Hlawacek & Gölzhäuser, 2016). With no demagnification, source vibrations are transferred directly to the ion beam spot.

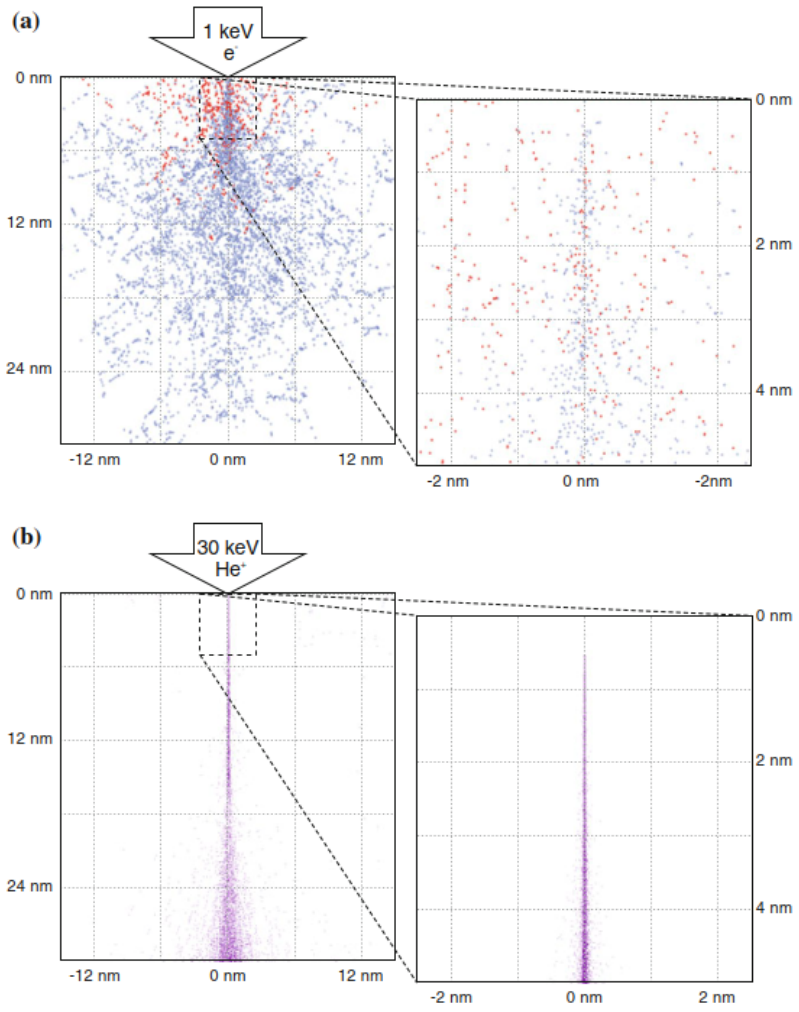

FIGURE 7 Monte-Carlo simulation of scattering events for a 1 keV SEM electron beam, and a 30 keV HIM helium ion beam in silicon. Reproduced from (Hlawacek & Gölzhäuser, 2016) Figure adapted with permission from (Hlawacek & Gölzhäuser, 2016) © Springer International Publishing Switzerland 2016

The major benefit of helium ions over electrons for the imaging applications is the smaller excitation volume where the secondary electrons are excited (FIGURE 7). That is because the He ion with its higher mass will penetrate much deeper in the material compared to an accelerated electron and at the same time produce enough secondary electrons at the surface. This surface sensitivity of the ions has been discussed also in the literature (Hlawacek & Gölzhäuser, 2016). The high energy electron beam (20 keV) will have a somewhat similar penetration profile as the 30 keV ions in FIGURE 7b. However, in that case, the number of secondary electrons produced from the surface is much lower compared to the 1 kV electrons or 30 keV ions.

Another major benefit of the HIM is the possibility to image non-conductive samples uncoated, with the flood gun charge compensation (Joens et al., 2013; Leppänen et al., 2017). When low energy electrons are flooded to the area to be imaged they compensate positive charge by the ion beam. One more benefit of

the HIM compared to the SEM is the increased depth of focus because of the small convergence angle of the beam.

2.3 Biological HIM imaging

Because of the charge compensation, the HIM has an especially interesting application for biological samples. So far, biological imaging with HIM has included, for example, human colon cancer cells (Bazou, Behan, Reid, Boland, & Zhang, 2011), rabbit cartilage collagen networks (Vanden Berg-Foels, Scipioni, Huynh, & Wen, 2012) and rat kidney cells (Rice et al., 2013). Bazou et al. (2011) compared HIM and SEM methods on coated and uncoated cell samples and concluded that uncoated samples reveal finer surface structures of the cells. However, charging effects of the SEM restricted the imaging resolution on the uncoated samples whereas the HIM was found to be a better choice when the fine surface structures were the interest. Similar conclusions have been drawn in several studies where nonconductive samples have been studied. Joens et al. (2013) compared HIM and low voltage FE-SEM methods on uncoated biological samples and concluded that HIM outperformed the FE-SEM at high magnification because of the higher resolution and lower charging effects (Joens et al., 2013). Despite several studies on biological HIM-imaging, viruses had not been imaged at all before work described in this thesis, and bacteria had been included only in the single study (Joens et al., 2013). Because of that, the possibilities of HIM-microscopy for virus and bacterial imaging are still mostly unexplored.

2.3.1 Cellulose

Cellulose-based materials are another interesting biological application for the HIM. Cellulose nanofibrils (CNF) are structural parts of the plant cell wall, which are formed from the cellulose molecule chains. Smallest fibril bundles for the wood cellulose are about 3.5 nm in diameter and are called elementary fibrils. These elementary fibril form thicker micro- or macrofibril bundles and together with lignin and hemicellulose, they form the actual plant cell wall or fiber (FIGURE 8). (Nishiyama, 2009) CNFs has many exciting properties like its large specific surface area and the affinity to film formation (Lavoine, Desloges, Dufresne, & Bras, 2012). Nanocellulose based materials have already promising applications for example in biodegradable plastics.

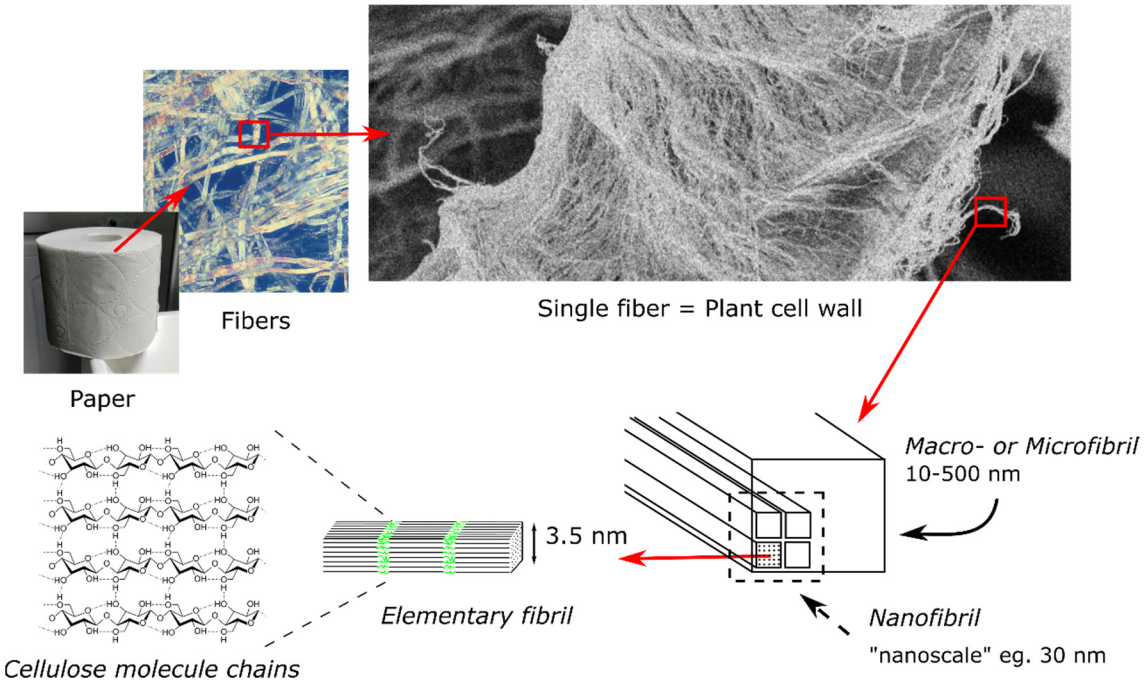

FIGURE 8 Cellulose fiber structure down to the molecular scale. Fibril bundles form the structural part of the plant cell wall.
"Cellulose strand.svg" by Laghi.l retrieved from https://commons.wikimedia.org/wiki/File:Cellulose_strand.svg, used under CC BY-SA 3.0.

Among the microscopy methods, SEM is widely used to characterize CNF materials (Kangas et al., 2014). CNF as an insulating material requires a conductive coating with SEM, which might introduce artifacts and reduce the resolving power. Therefore, HIM-microscopy is an interesting choice over SEM. Also, HIM will have a higher ultimate resolution. Cellulose-based materials have been previously imaged with HIM, but usually with low to intermediate magnifications (Li, Liu, Jiang, & Thundat, 2016; Torvinen et al., 2017; Virtanen, Janka, & Tuukkanen, 2018). There has been only one study published with high magnification (Postek et al., 2010) before the study presented in this thesis (**A.III**) and therefore, full the capabilities of HIM are still unknown for cellulosic material.

2.3.2 Beam damage on biological samples

Even if quite low He ion doses have been found to modify materials, beam damage during imaging on biological samples has not been reported. In the literature, dislocations in silicon and copper lattices are found after He^+ dose 4 x 10^{15} ions/cm^2 (Livengood, Tan, Greenzweig, Notte, & McVey, 2009). Ten times lower dose of 4 x 10^{14} ions/cm^2 was enough to cause significant damage to the graphene lattice when studied with Raman spectroscopy. At the same time, it was found that about 10^{17} ions/cm^2 was required to obtain a sub-nanometer imaging resolution on that sample (Fox et al., 2013). Given the above results, it is quite clear that damage during high-resolution imaging will always be present. However,

no reports about visible damage during imaging of biological samples have been published so far.

2.4 HIM milling

Sputtering properties of the Ga ion beams have been utilized for milling and cutting of materials as discussed previously. The newly developed HIM instrument can do this same, but with much smaller spot sizes. This has already been demonstrated by several examples like when 10 nm gaps were fabricated on the graphene with He ions (Lemme et al., 2009). The sputter yield of the focused ion beam is highly dependent on the mass of the ion, thus the relative yield per ion is 100 times lower with He compared to Ga. With Ne, the yield is only 2-3 times lower, therefore Ne has been commonly used for milling with HIM (Hlawacek & Gölzhäuser, 2016). Another benefit of Ne compared to Ga is low contamination, which is especially important during the integrated circuit analysis (Tan et al., 2011).

The traditional Ga FIBs have been used also for biological samples as discussed. However, with HIM-FIB not a lot of biological milling has been done. The only published study before my study (**A.II**) was by Joens et al. (2013) where a nematode (*pristionchus pacificus*) head was cut (Joens et al., 2013) and later by Said et al. (2019) where *Bdellovibro bacteriovorus* was milled (Said, Chatzinotas, & Schmidt, 2019). In contrast to a traditional microtome blade, FIBs can be also used to cut non-embedded biological samples. The reason is that the embedding is needed to support the soft sample during the mechanical cutting with the blade. However, this property of the FIBs has not been utilized a lot. One reason might be that embedding serves also as the charge compensation for both the FIB and the SEM. HIM has the possibility of charge compensation which is why non-embedded samples are especially interesting. Also, the high resolution and the relatively low sputter rate will favor the small-scale cutting actions with HIM compared to the epon block cuts with Ga FIBs. Therefore, the milling of biological non-embedded samples with HIM is an interesting area of study, with results shown in later sections.

3 BACKGROUND: ALTERNATIVE ANTIBACTERIALS

Alternative antibacterials are needed to reduce the usage of the traditional broad-spectrum antibacterials. The very first widely used antibiotic on humans was penicillin produced by the *Penicillium* mold which has been used since the 1940s. Antibacterials used today can also be semi- or fully synthetic but they are still commonly called antibiotics. These chemical antibacterial have been very efficient against all kinds of bacterial infections over the past decades, however, the usage has led to serious problems with the antimicrobial resistance (AMR). To overcome this problem new antibacterials have been developed over the years, and the new ones have worked well until the bacteria have developed the resistance again. Unfortunately, from the 1970s the discovery rate of novel drugs has declined (Aminov, 2010). This has led to serious problems in the 2000s when even last line antibacterial like carbapenems are found to be inefficient against several bacterial strains (Codjoe & Donkor, 2017).

Alternative antibacterials could help the AMR problem at least two ways; first by treating the AMR infections directly or second by reducing the total antibacterial usage (Aminov, 2010). When the total antibiotic usage is reduced, the increase in resistant bacteria will not develop, and less last-line antibiotics are needed which means that their effectiveness can be retained. Alternative antimicrobials include for example bacteriophages, lysins, antibodies, probiotics and different antimicrobial peptides (Ghosh, Sarkar, Issa, & Haldar, 2019) I will focus on the bacteriophages in the next chapter.

3.1 Bacteriophages

Bacteriophages (phages) are viruses that use bacteria as their hosts and can have a lytic life cycle for the production of the progeny. Therefore, phages are found everywhere bacteria are found. It has been estimated that phages are the most numerous organisms on the planet surpassing the bacterial numbers tenfold (Wommack & Colwell, 2000). Bacteriophages come in many shapes and sizes but

most commonly their capsid diameters are some tens of nanometers. Phages have a protein capsid with DNA or RNA inside, which is injected to the host during the infection. Probably one of the most well-known phages is the T4 infecting *Escherichia coli*, which belongs to the family of *Myoviriade* (FIGURE 9). Myoviruses have a head, a contractile tail and tailfibers, which are used to recognize the host.

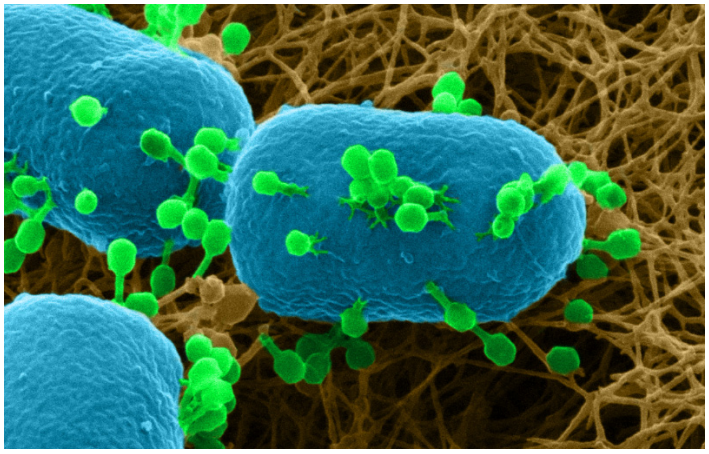

FIGURE 9 Bacteriophage T4 (green) infecting its host *Escherichia coli* (blue) on the agar plate. Manually colored HIM image.

The initial discovery of the viruses and phages is an interesting piece of scientific history. Back in the 1890s in Russia Dimitri Ivanovsky found that the tobacco mosaic disease was caused by the filterable "contagium vivum fluidum", contagious living fluid. Later 1910s Twort and d'Herelle found independently that also bacteria can be affected by this invisible agent. The form of the agent was under the debate until D'Herelle plaque assay experiments 1917 proved for the particulate nature. The final confirmation was received in the 1930s with a moment ago developed electron microscopy method (Lustig & Levine, 1992). Even if the character of the particles was unknown for 40 years it did not stop the utilization of phages, as we will see later.

3.1.1 Bacteriophage imaging

Traditionally viruses including bacteriophages, have been imaged with electron microscopes, with TEM or SEM. TEM with negative staining has been the standard method for the characterization of the phage morphology and it has offered a great insight into the phage world (Ackermann, 2007). Lately, the single-particle Cryo-EM method has started to be used for detailed structural characterization of the viruses. With this method, even the full atomic structure of the virus proteins are possible to resolve (Sun et al., 2015). In this method, averaging over multiple particles is done during the process and therefore it is not well suited to study phage-bacterium interactions. These interactions can be studied with TEM-tomography methods like cryo-TEM tomography or with serial thin-section TEM. However, the resolution of these methods is lower compare to a

single-particle approach (Guerrero-Ferreira & Wright, 2013; Narayan & Subramaniam, 2015) With TEM methods, the physical size of the samples are small and sample preparations are complicated. Scanning microscopy methods like SEM can be used to image these interactions in more relevant environments, but with even lower resolution. With HIM a higher resolution than with SEM can be obtained, and for the uncoated samples as discussed earlier.

3.1.2 Phage therapy

Phages can be used to control the growth and infectivity of the host bacteria. This method is called phage therapy. First therapy trials were made in France in 1919, and the method quickly spread all over the world. Phage therapy lived its golden age in the 1930s with several successful examples (Almeida, Gabriel Magno de Freitas & Sundberg, 2020; Summers, 2012). After the discovery of the antibiotic drugs, phage therapy disappeared silently to the margins. Still, in some regions of the former Soviet Union phage therapy has continued to these days (Myelnikov, 2018). Over the last decades, it has been noticed that the usage of antibiotics will lead to serious side effects such as the increase of drug-resistant infections as discussed earlier. Because of that, phage therapy is experiencing its renaissance (Roach & Debarbieux, 2017). Regulations regarding the therapy use in humans are limiting the growth, though the first clinical trials have been done already also in the EU (Jault et al., 2019).

Compared to other antimicrobials, phages are highly host specific which can be a benefit or a challenge for the treatment. One benefit is that the possible side effects are reduced, because the bacteria populations are not altered. Challenges are that bacteria causing the infection must be known and the evolution of bacteria requires up-to-date phage drugs. For different kinds of infections, different approaches for phage therapy are required, because phages need to be introduced to close contact with the bacteria. For example, infections on the skin can be treated quite straightforwardly with topical application of the phages. On the other hand, infections in the respiratory tract or intestines might need more sophisticated approaches (Abedon et al., 2011; Vandenheuvel et al., 2013).

3.1.2.1 Phage encapsulation

Bacterial infections in the intestines are particularly challenging to treat with phage therapy because the oral administration of phages will lead to their inactivation by gastric acids (Smith, Huggins, & Shaw, 1987). Encapsulation of the phages to a pH-responsive protective capsule could overcome this problem (Ma, Y. et al., 2008; Malik et al., 2017). When the capsule material is stable in the low pH of the stomach but dissolves in the neutral pH, it can be used to evade the body's protection system (FIGURE 10). For the phage encapsulation, several methods exist such as spray-drying, freeze-drying, extrusion dripping, liposomes and polymerization techniques (Malik et al., 2017).

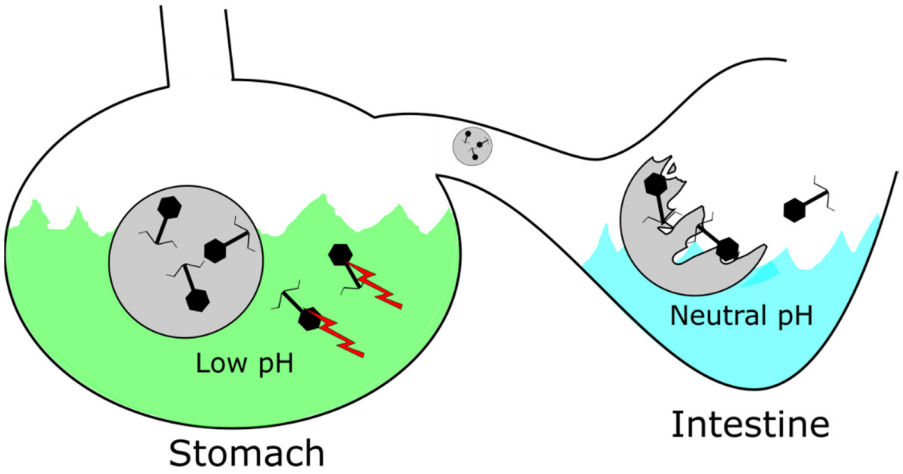

FIGURE 10 Encapsulated and free phage in the digestive system. The capsule is resistant to acidic conditions but will dissolve in the neutral pH leading to the release of phages.

Microscopy is one part of the process determining the functionality of the encapsulation method. It can be used for example to determine the outer and inner structure of the capsules and the efficiency of the encapsulation. To study the inner structures, capsules must be opened, or a penetrative imaging method must be used. For relatively small capsules, penetrative methods like light or transmission electron microscopy could be used. Fluorescence microscopy methods with nucleic acid labeling have been commonly used to determine if the phages are found inside of particles (Colom et al., 2015). With this method, no information about the structure of the capsule can be obtained. Fluorescence microscopy combined with Cryo-TEM offered detailed information about the phages and their positioning inside of the capsules (Colom et al., 2015). This method is well suited to relatively small particles (~1 µm) because the electrons do not travel long distances in the solids. The commonly used method for bigger particles is TEM from thin sections (Ma, Y. et al., 2008; Ma, Y. et al., 2012).

FIB-based methods like FIB-SEM have not been used to study phage capsules. The probable reason is that high-resolution SEM imaging of the non-conductive polymers of the capsule is challenging without a charge compensation. HIM, on the other hand, might be very well suited for this kind of work because it has the milling capability, the resolution and the charge compensation required.

3.1.2.2 Phage immobilization

In some cases, the immobilization of phages on the surface could be a suitable way to introduce an antibacterial effect. For example, the immobilized phages might provide a prolonged antibacterial effect for the environment to be protected, or the phages could prevent the growth of the bacteria locally. It has been already shown that immobilized phages can reduce the growth of the bacteria in

packed food (Anany, Chen, Pelton, & Griffiths, 2011; Lone et al., 2016) or in the health care equipment's (Curtin & Donlan, 2006; Nogueira et al., 2017). In these studies, the material with attached phages showed antibacterial activity by reducing the growth of the host bacteria. However, the magnitude of the antibacterial effect was not measured and the role of the immobilized or detached phages was unclear. In some cases, high numbers of detached phages produce the antibacterial effect measured (Liana, Marquis, Gunawan, Justin Gooding, & Amal, 2018). On the other hand, some studies have suggested that covalent immobilization of phages increases the antibacterial activity (Tawil, Sacher, Mandeville, & Meunier, 2013) but some studies have found an opposite effect (Wang, Sauvageau, & Elias, 2016). Because of these contradictory results, guidelines for designing antibacterial surfaces with phages are unclear.

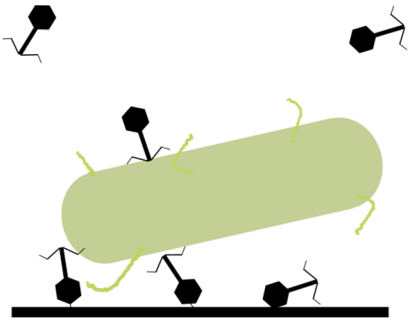

FIGURE 11 Immobilized and free phages infecting. The role of immobilized or detached phages for the infectivity is controversial in the literature.

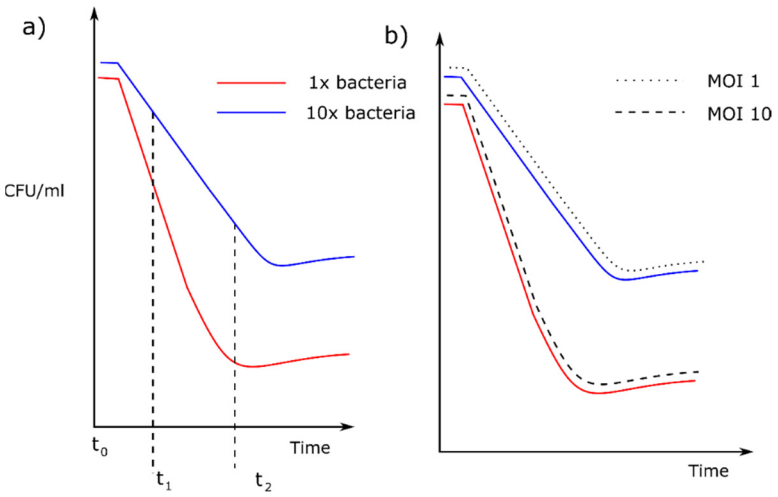

FIGURE 12 Common ways to measure the infectivity of the phage biomaterials. a) CFU reduction by the material with different initial numbers of bacteria measured at different time points. b) Equivalent MOI with different initial numbers of bacteria. Red line: CFU reduction by the material. Dashed line: CFU reduction by the MOI 10. Blue line: CFU reduction by the material when the bacteria number is tenfold. Dotted line: CFU reduction by MOI 1.

In addition, the measurement of the antibacterial effect has some ambiguity. The infectivity of immobilized phages has commonly been measured as the reductions in the bacterial CFU (colony forming unit)/ml compared to the reference without phage (Liana et al., 2018; Tawil et al., 2013). This approach is simple to implement but has problems for interpretation. These problems are demonstrated in FIGURE 12a. Depending on the conditions, like initial bacteria concentration and the time difference between the measurement steps (from t_0 to t_1 or t_2) different values for reduction are obtained. It means that results are comparable between studies only if the conditions and the time of the measurement are fixed.

A recent study by Wang et al. (2016) presented improved metrics for the infectivity where the time dependence of the measurement was eliminated (Wang et al., 2016). They determined the antibacterial effect of the material by comparing it to the effect by a known ratio (MOI=multiplicity of the infection) of phage and bacteria. With this "equivalent MOI" metric, the time-dependent error was removed (FIGURE 12b). However, this metric is still troublesome as it depends on the conditions like bacteria numbers. For example, if an equivalent MOI 10 is measured for the phage-biomaterial and thereafter the number of bacteria is increased tenfold, the measured equivalent MOI will be 1 (FIGURE 12b). For this reason, the metric needs improvement. The surface area of the antibacterial material should be also taken into account in the metric. To solve these challenges, a study on the infectivity of immobilized phages was made, with an introduction of an improved metrics for the infectivity.

3.2 Antibacterial surfaces

Antibacterial surfaces are one of the important tools on the fight against antibiotic-resistant bacteria. The reason is that bacteria are likely to colonize and form biofilms on almost any surface and cause problems for example in hospitals and in the food industry. In the food industry, the high density of livestock worsens the situation and bacterial outbreaks can cause major economic losses and environmental problems (Hollis & Ahmed, 2013). The long shelf-life of the food products is the desired attribute in the food industry and antibacterial packaging plays a major role there. In the hospital environment, challenging surfaces are the interfaces between the tissues and the medical devices like implants and catheters, because from there the bacteria can have a direct route to the body (Madkour & Tew, 2008).

A surface is antibacterial if bacteria are not able to live on it or colonize it. In the literature, engineered antibacterial surfaces have been divided into chemical and physical antibacterial surfaces. Chemical antibacterial surfaces have either a more active coating that kills the bacteria, or a less active "antifouling" coating which prevents the biofilm formation. Typical chemical coatings are polymers mixed with an active compound which can be for example silver, hydrox-

yapatite or antibiotics. Chemical coatings are commonly used in medical applications like implants or catheters (Hasan, Crawford, & Ivanova, 2013; Madkour & Tew, 2008)

Physical antibacterial surfaces have repeating micro- or nanoscale patterns that kill the bacteria or alter their attachment on it. The clear benefit of the physical surfaces compared to the chemical ones is the long lifetime and no need for the chemical antimicrobials. Physical surfaces are less studied and used compared to the chemical ones, partly because their properties are not well known. It has been found quite recently that micrometer-scale patterns can alter the attachment of bacteria by contact area maximization (Hsu, Fang, Borca-Tasciuc, Worobo, & Moraru, 2013). In addition to that, several other mechanisms have been suggested for the micrometer-scale patterns, such as hydrodynamic effects (Cheng, Feng, & Moraru, 2019; Chung et al., 2007). For nanoscale patterns, the suggested mechanisms are for example surface wettability, air entrapment and cell membrane deformation (Cheng et al., 2019).

3.2.1 Natural nanotextured antibacterial surfaces

Insect wings have been found to have interesting antibacterial properties caused by nanoscale physical structures. The nanopillar structuring on the cicada wing has been found to rupture the cell wall of bacteria and cause lysis (Ivanova et al., 2012). This property has also been successfully mimicked on synthetic surfaces (Ivanova et al., 2013).

One study with the dragonfly wing suggested that nanopillars do not pierce the membrane, but the membrane damage occurs upon the movement of the bacteria on pillars by the EPS (extracellular polymeric substance) mediated adhesion forces between the bacteria and the pillars (Bandara et al., 2017). However, the mechanisms for the action are still under discussion (Bandara et al., 2017; Linklater, Juodkazis, Rubanov, & Ivanova, 2017). Recently it has been found that the adhesion forces by the EPS can be strong enough to kill the surface attached bacteria without the piercing action on the synthetic surface (Linklater et al., 2018).

To prove this action on the dragonfly wing, more studies are required. In a previous study, advanced microscopy technics like cross-sectional TEM and FIB-SEM were used when resolving the problem (Bandara et al., 2017). TEM imaging was done for serially sectioned resin-embedded samples. The FIB-SEM sample was not resin embedded but was coated with platinum to reduce charging effects. It was possible that the resin embedding or the metal coating caused artifacts to the sample, and thus, a method without embedding or coating could offer some additional information. HIM can mill and image non-conductive samples without coating because of the charge compensation. Also, imaging resolution with HIM is higher compared to FIB-SEM. Because of that, later we describe how HIM was used to mill and image the bacteria interactions on the dragonfly wing.

4 AIMS OF THE THESIS

A. Study the antibacterial properties of the surface-immobilized bacteriophages (I).

B. Examine the HIM method for phage-bacteria interactions (II) and for the phage-biomaterial characterization (I).

C. Study the high-resolution HIM imaging for cellulosic materials (III).

D. Survey the beam damage during the HIM imaging (III).

E. Explore the in situ milling and imaging of the microbiological samples with HIM.
    I. Bacteria (II)
    II. Encapsulated bacteriophages (IV, V)
    III. Dragonfly wing-bacteria interactions (VI)

5 HIM MICROSCOPY

5.1 Source vibrations

The HIM (Zeiss, Peabody) has a low source demagnification because of its physically small source and low current as discussed earlier. This might cause issues during imaging or milling, because mechanical vibrations from the ion source can be easily transferred to the ion beam spot. This topic has been discussed but not fully demonstrated in the literature, therefore I will do that. The size of the ion beam spot on the sample surface is adjusted by the combination of the beam limiting aperture and the condenser lens voltage (FIGURE 13). The increased “spot size” value in the software (Zen) moves the crossover position of the ion beam up by increasing the condenser lens voltage (FIGURE 13) (FIGURE 14). This reduces the beam current through the aperture and forms a smaller, demagnified image of the source onto the sample.

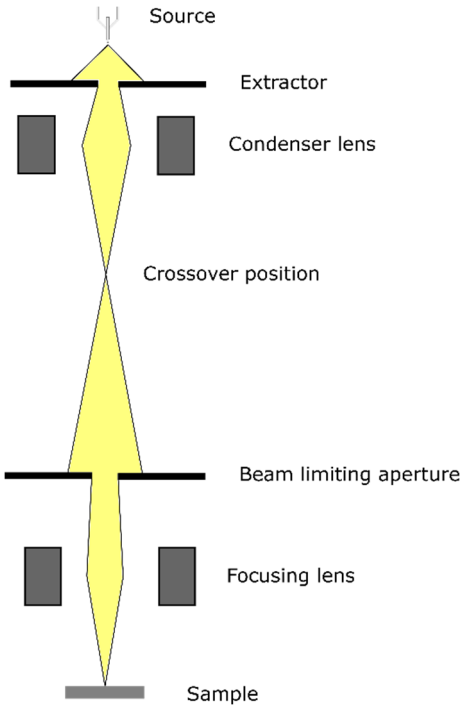

FIGURE 13 Ion optical system of the HIM. The condenser lens and beam limiting aperture are used in together to reduce the beam current and form a demagnified image of the source to the sample.

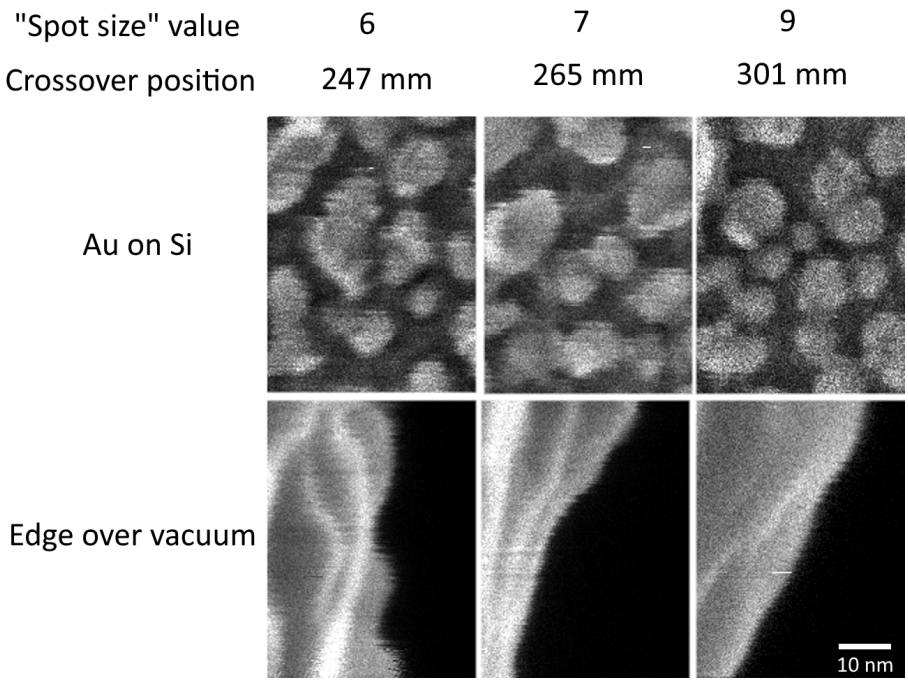

FIGURE 14 Artifacts by source vibrations in the HIM with different spot size values. The effect of the vibrations on the image was reduced by moving the crossover position up and by increasing the demagnification. Crossover position was acquired from Zen software and is millimeters from the bottom of the focusing lens. All images have the same parameters except the beam current was reduced.

In theory, the effect of the source vibrations should be reduced by an increased "spot size" value because of the increased source demagnification. This is demonstrated in FIGURE 14. The horizontal stripes in this high magnification images are due to the acoustic noise in a cleanroom environment. When the spot size value is increased, moving the crossover position up and increasing the source demagnification, the striping effect is reduced. The downside of this tuning was the reduced current, as seen with spot size 9, where the image is grainy because of the low signal to noise ratio. Similar parameters were used for all the images except the beam current was reduced.

From the above results, it is clear that a demagnification increased even more would further reduce the artifacts caused by the vibrations. However, an increased demagnification will lower the ion current on the sample as seen already. Low current can be compensated by increasing the "dwell time" of the beam on the specific spot on the sample but this increases the time required for imaging and milling. Also, artifacts caused by drifting in mechanical and electrical systems increases as the dwell time is longer. The stability of the GFIS source is currently setting the limit to its maximum current. Therefore, careful restriction of vibrations to the instrument is important to limit the problem to a negligible level. In the future, the development of the source stability towards higher currents is important.

5.2 Phage –bacteria interactions

A brief history of phage imaging was discussed in the review article **A.VII.** First TEM images from phages have been published in the 1930s as discussed and later the TEM became a widely used method for structural characterization of the phages. For the phage-bacteria interactions, the wide variety of imaging methods exists as discussed earlier, all of those being electron beam based. In the research article **A.II,** the novel helium ion microscope was used for the first time to image phage-bacteria interactions on a bacterial culture plate.

5.2.1 Phage-bacteria sample preparation for HIM

A bacterial plate with E.Coli and T4 phage plaques was selected for imaging. Pieces about 5 mm × 5 mm in size were cut from the bacterial plates and attached to 10 mm glass coverslips with epoxy glue. Pieces were let to adhere 20 min before adding fixative containing 2% glutaraldehyde in a 0.1 m sodium cacodylate (NaCac) buffer (pH 7.4) in which samples were incubated for 5 h. After primary fixation, samples were washed twice with a 0.1 m NaCac buffer and and fixated a second time with 1% OsO4 in 0.1 m NaCac for 30 min. After fixations, samples were washed three times with 0.1 m NaCac. Next, samples were dehydrated in ethanol (99.5%) with a step series (50%, 70%, 95%, 99.5%, 99.5%). Ethanol was removed with a Bal-Tec CPD 030 critical point dryer. Dried samples were set to metal stubs with the carbon tape before HIM-imaging.

5.2.2 Results for phage-bacteria interaction

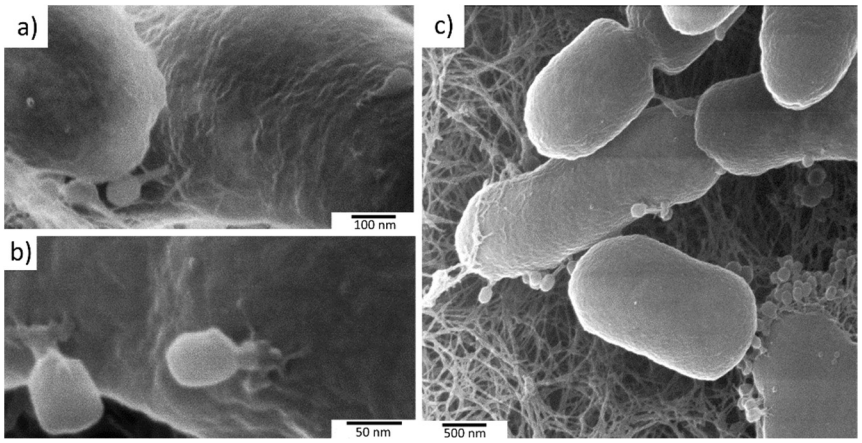

FIGURE 15 Different stages of the T4 phage infection on the *E. coli* imaged with HIM. a) Attached phage on the surface of bacteria b) Attached phages with contracted tails indicating genome injection. c) Lysed bacteria cell with bursting progeny. Reproduced from **A.II** © 2017 WILEY - VCH Verlag GmbH & Co. KGaA, Weinheim

This study shows that the HIM method could be used to image phages and the phage-bacteria interaction in a way like no other scanning microscopy methods can. One example of that is the possibility to see the different stages of the phage infection (FIGURE 15). The initial attachment of the phage is seen in FIGURE 15a. In FIGURE 15b, the contracted tails of the phages indicate the genome injection. An outburst of the phage progeny is seen in the lower right corner of FIGURE 15c. Because of the scanning principle of the HIM-method, the wide areas on the bacteria plate could be explored to find out the different stages of the spreading infection. This kind of imaging is not possible to do with the TEM methods. This study was the first demonstration of the HIM-method for this kind of uncoated microbial sample, to show what are its capabilities.

5.2.3 Bacteriophage –biomaterial

Application of HIM for the bacteriophage-biomaterial characterization was explored in the research article **A.I.** The objective was to count the number of attached phages on different surfaces. A scanning microscope method is required for virus-biomaterial characterization because transmission-methods like TEM does not work with the thick samples. From the scanning microscopy methods SEM, HIM or AFM could be equally used but the AFM was discarded because of its low speed. Here, HIM was chosen over SEM because of the charge compensation.

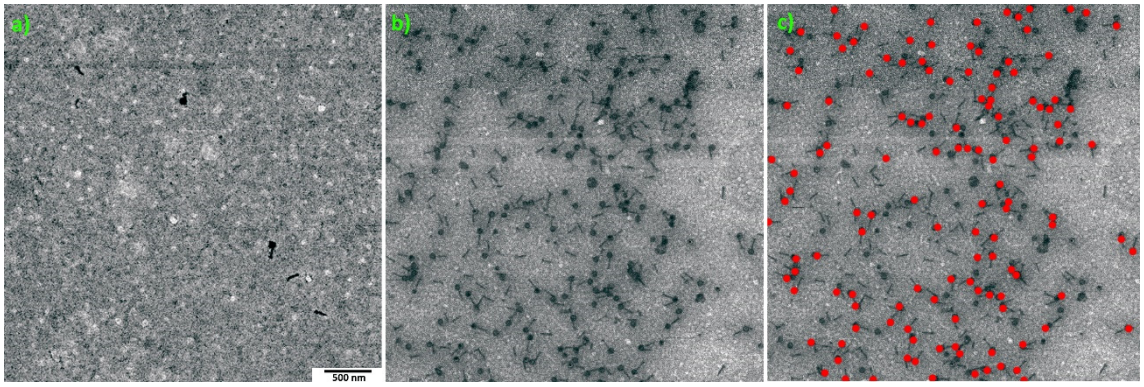

FIGURE 16 An example of the phage-biomaterial characterization done in the article **A.I.** with HIM. Carboxyl coated gold surface a) without a carbodiimide crosslinker b) with the carbodiimide crosslinker. c) Counted up phage particles from b marked out.

Areas to be imaged were selected systematically from the samples and the number of intact phage particles was counted **(**FIGURE 16**)**. On well-conducting samples, SEM might be a better choice over HIM because it is faster to use in practice and the resolution required for counting particles is not too high. Later, data was used to determine the efficiency of phage immobilization.

5.3 Beam damage by Ion beams

Several interactions of an ion beam with a material are irreversible. The sputtered ions leave empty vacancies, secondary electrons modify the electrical properties and implanted ions modify the lattice structure. Damage for example on graphene has been found with relatively low ion doses as discussed. However, the damage of biological material during He imaging has not been reported in the literature. Because of that, it was studied on cellulose samples.

5.3.1 Nanocellulose imaging with the HIM

High-resolution HIM-imaging of cellulose-based materials was studied and reported in article **A.III**. The material used was a cellulose nanofibril gel which is formed from the nanometer-sized cellulose fibrils (CNF). Because of its nanoscale structures, it will reveal the capabilities of the HIM method. CNFs used forms a gel when it is diluted to 1 % w/w mixture with water. To remove the water from the gel, two different methods were used, freeze-drying and critical point drying (CPD).

To evaluate the success of each drying process Brunauer–Emmett–Teller (BET) analysis was used to determine the specific surface area of the dried product. Here, CPD performed better to preserve the wet structure of the CNF. This was seen also seen already with the naked eye as CPD drying produced a transparent aerogel structure (FIGURE 17a). This was confirmed with HIM imaging

which revealed that CPD dried CNFs have a more uniform structure compared to the freeze-dried.

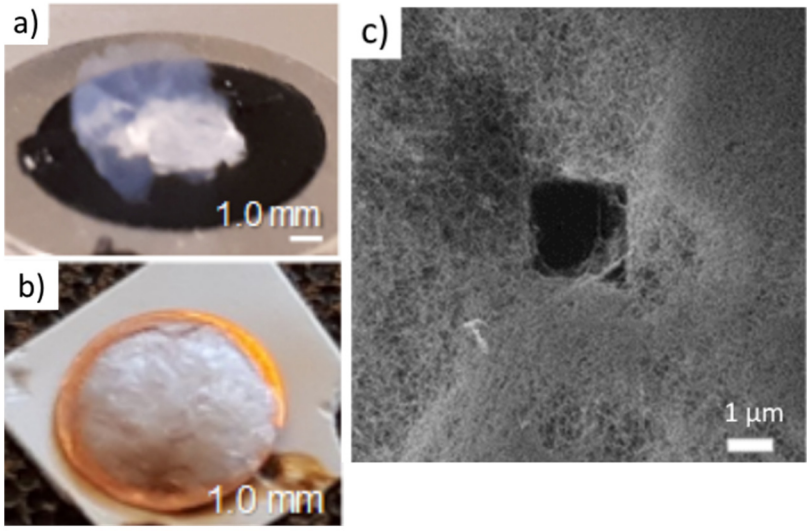

FIGURE 17 CNF dried with the different methods: a) CPD b) Freeze-drying. c) Hole in the CPD dried CNF sample produced by the ion beam. Reproduced from A.III licensed under CC BY 3.0.

During the high-resolution imaging, instant damage to the material was detected. After zooming out of the high-resolution imaging area, a clear hole was visible in the CNF network (FIGURE 17c). This was a sign of the high destructivity of the ion beam towards the CNF.

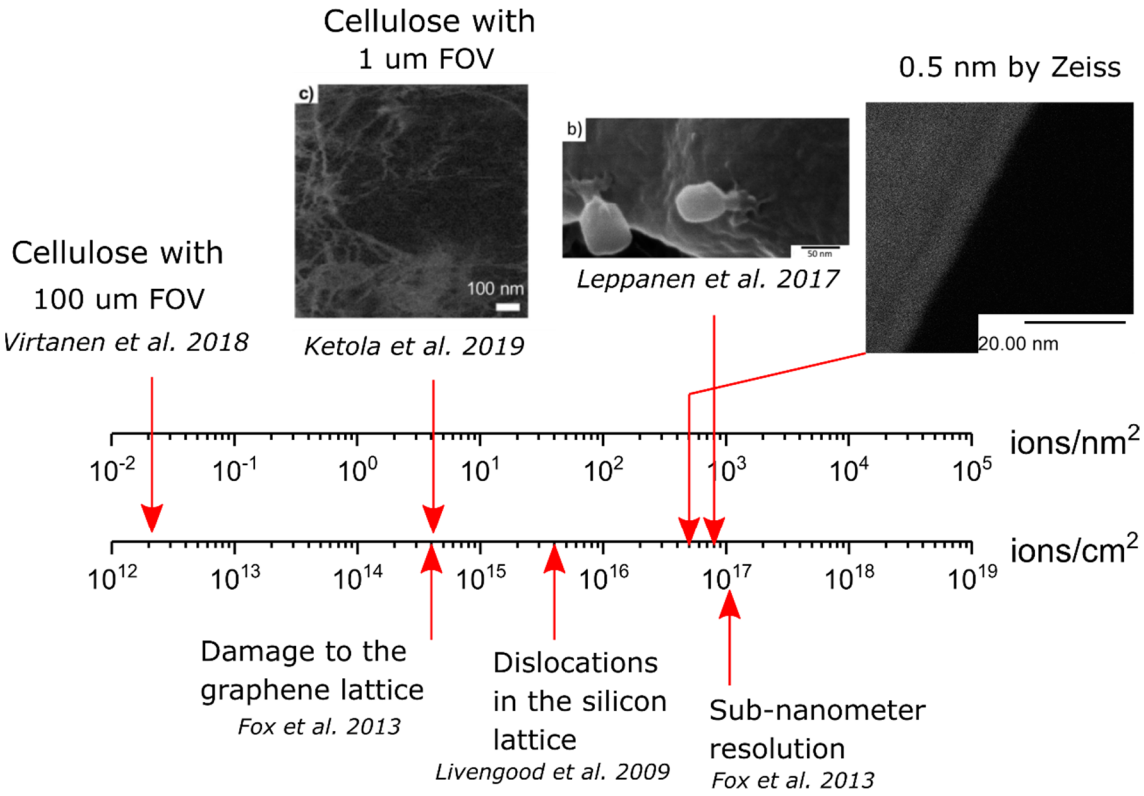

FIGURE 18 Ion doses and damage reported during HIM imaging. Reproduced from A.III licensed under CC BY 3.0 and from A.II © 2017 WILEY - VCH Verlag GmbH & Co. KGaA, Weinheim.

To study the damage more closely, different ion doses for the imaging were used. Areal doses can be calculated with the equation

$$Areal\ dose = \frac{I * t}{q * A}, \tag{4}$$

where I is the ion current reported by the instrument, t is the pixel dwell time, A is the pixel area and q is the elementary charge. It was found that with 4 x 10^{13} ions/cm^2 the damage was not visible, but with a ten times higher dose 4 x 10^{14} ions/cm^2 the fibril structure was collapsed. To have an idea about the magnitudes, 4 x 10^{14} ions/cm^2 corresponds to four ions/nm^2 (FIGURE 18). For comparison, Virtanen et al. (2018) studied freeze-dried nanocellulose aerogels with HIM and they did not report any damage. The obvious reason was the several magnitudes lower dose, due to several magnitudes lower magnification (FIGURE 18). Dose during imaging has usually not been reported with HIM. In article **A.II,** a He dose 8.4 × 10^{16} ions/cm^2 was used to image the bacteriophages, and no clear damage was observed. This was close to the dose used in the 0.5 nm resolution evaluation during the installation of the instrument (FIGURE 18).

Among the other charged particle microscopes, damage during the TEM imaging is widely discussed. Organic materials are found to be challenging and different averaging methods like single-particle reconstructions have been adopted. Cellulose as an organic and polymeric material has been especially challenging for the TEM. Even if the crystalline structure of the algal elementary fibrils have been resolved with electron microscopy methods, it has not been done for the wood cellulose (Ogawa & Putaux, 2019). A common way to describe the damage in TEM is to define the critical dose where the intensity of the diffraction spots is halved. This has been found to be about 60 electrons/nm^2 for wood cellulose (Ogawa & Putaux, 2019). Interestingly this dose is about 10 times higher than the dose which causes the collapse of the fibril structure with He ions. The probable mechanism for damage with the HIM is the ionization of the cellulose by the ion collisions, which destroys the hydrogen bonding between and covalent bonding within the molecular chains. Besides, damage by ion collisions, which increase the temperature, might be significant because the thermal conductivity of the CNF aerogel structure is low.

6 HIM ION MILLING OF BIOLOGICAL SAMPLES

FIB-SEMs have been commonly used for the volumetric imaging of resin embedded biological samples. Here I will present results from a different kind of FIB-approach where the He or Ne ions are used to cut small cross-sections to non-embedded or coated samples. After cutting, the same instrument was used to image the cross-section with He ions.

6.1 Phage-bacteria interactions

He and Ne milling of bacteria was also demonstrated for the first time in article **A.II.** It was found that He ions could be used to cut the agar substrate and the phage-infected bacteria (FIGURE 19a). The phage infecting the bacteria had a hollow head after cutting which could be expected. The cut cross-sectional surface of the bacterium, on the other hand, did not show a lot of contrast, which means that the surface was completely flat. It is not clear if this is expected, as these kinds of experiments are rarely done. With the FIB-SEM, the contrast from the cross-section is elemental contrast from the backscattered electrons. HIM, on the other hand, does not have high elemental contrast, because the image is formed by the secondary electrons. Recently Said et al. (2019) studied the *Bdellovibrio*-bacteria interaction with HIM (Said et al., 2019). Ne milling of the bdelloplast revealed that the bacteria have a somewhat porous internal structure. They speculated that the higher beam current and the longer dwell time used in our experiments (**A.II)** have resulted in the local melting of the material, causing the smooth cross-section. That is a possible explanation.

Temperature increase ΔT by the ion beam could be estimated with a simple 1D heat transfer model as Wolff et al. (2018) has demonstrated (equation 5). They estimated the heating effect by Ga ions in collagen samples and found that the local temperature could be as high as 2000 K for a 3 nA current. They found also a correlation with experimental results and concluded that a current reduction reduced the damage caused by heating (Wolff et al., 2018).

$$\Delta T = \frac{E*I}{C*A} * \frac{R}{k} \quad (5)$$

In eq. (5), E is the energy of the ion beam, I is the ion current, C the elementary charge, A the beam interaction area, R the projected range of the ions in the material and k is the thermal conductivity. When this calculation is done for a 10 pA Ne beam on the same model surface (k=0.29 W/mK), the temperature rise is 69 K. The projected range R was obtained from SRIM simulation and was 47 nm. The radius of the interaction area was estimated to be 15 nm. This low increase in temperature compared to Ga is mostly because of the 100 times lower current. In these calculations it was assumed that all the energy was transferred from the ions to the material, so this is the upper limit. However, this model is for a single scan point and not for the bulk of the sample. If the sample has a low thermal conductivity, the wider bulk temperature could rise even if the single scan points have enough time to release most of the heat. Also, the thermal conductivity might be lower on our sample compared to the model surface used.

6.2 Encapsulated phages

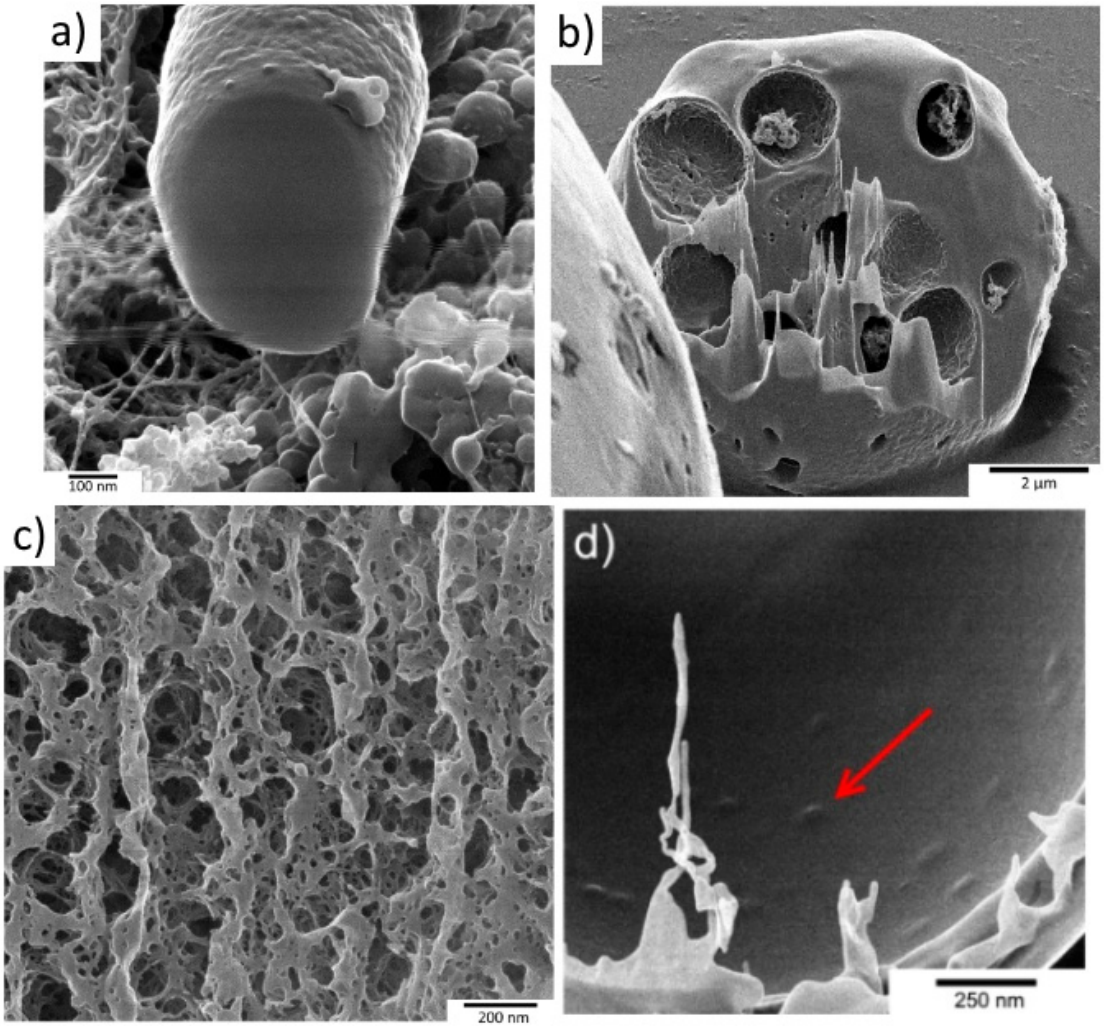

FIGURE 19 HIM-milled and imaged bacteriophage samples a) Bacteria with infecting phage, reproduced from A.II with permission. b) The freeze-dried microsphere has an internal structure with micrometer-sized chambers. c) CPD dried microspheres have a matrix-like nanometer-sized internal structure. d) Spray-dried microsphere with the arrow pointing to the embedded phage particle. b), c) and d) reproduced from A.IV and A.V under CC BY 4.0. a) reproduced from A.II © 2017 WILEY - VCH Verlag GmbH & Co. KGaA, Weinheim .

Ne beam was used to cut in half polymer microspheres encapsulating phages in articles **A.IV** and **A.V.** In **A.IV** the microparticles were prepared with spray-drying from a mixture of pH-responsive polymer, trehalose, and bacteriophages. An end product was powder formed from about 10 µm sized solid spheres. Spheres were found to be hollow when cut in half and imaged with HIM. No intact phages were visible, but phage sized bumps were found on the inside sur-

face of the microspheres, which were not visible in the phage-free reference samples (FIGURE 19d). We interpret that these bumps are most likely remnants of phages.

In study **A.V** a similar cutting and imaging method was used for microspheres prepared with the membrane emulsification method. In the method, an aqueous mix of phage and the pH-responsive polymer was pumped through a perforated membrane to an oil phase to form W/O emulsion. Emulsion droplets in the oil were crosslinked with an acid to form solid microspheres which were transferred to an aqueous solvent to form a hydrogel. Before the examination, the microparticle hydrogel was dried.

As a comparison, both freeze-drying and critical point drying (CPD) were used. The freeze-drying resulted in particles with smooth surfaces whereas the critical point dried particles had a more porous surface. Particles were cut half with the Ne^+ beam and imaged with He^+. The freeze-dried particles were found to include separate micrometer-sized hollow chambers (FIGURE 19b). In contrast, the CPD dried particles were found to have a matrix-like inside structure with much smaller holes in the size scale of tens of nanometers (FIGURE 19c). The conclusion is that the CPD dried particles resemble better the native wet structure of the particles. The phages were not visible in the matrix (FIGURE 19c). Most probably, they are embedded inside of the polymer structure.

6.3 Dragonfly wing - bacteria interaction

The imaging of interactions of bacteria with a dragonfly wing has limitations with more standard imaging methods, as discussed earlier. Because of that, HIM milling and imaging were used to study this interaction in article **A.VI**.

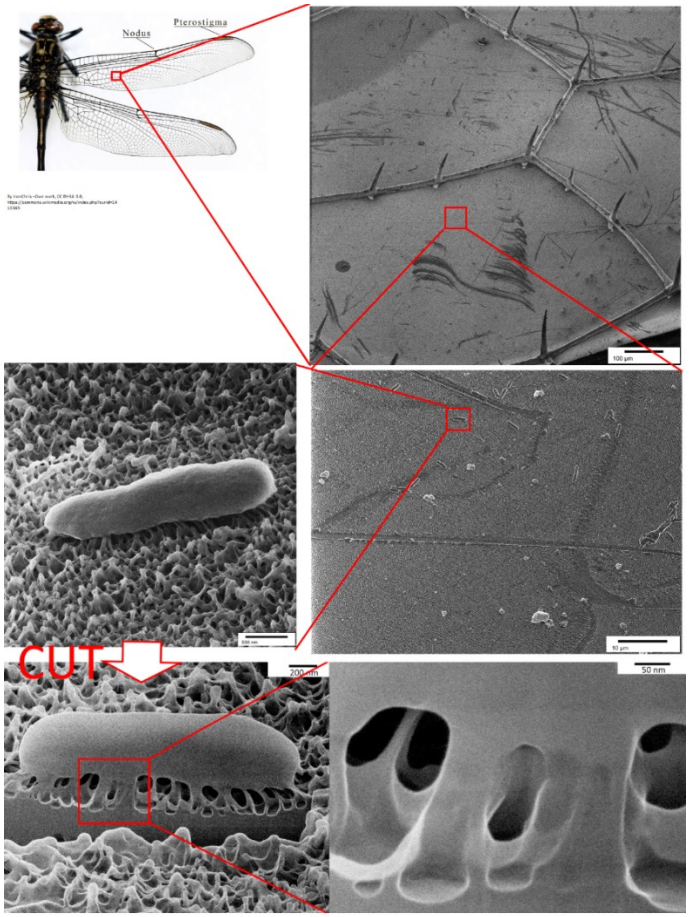

FIGURE 20 Cut bacteria on the dragonfly wing. The contrast between the nanopillar and the bacteria is found but the bacterial membrane is not visible.

From the results, it was clear that the resolution with HIM was higher than in the previous FIB-SEM experiments on similar samples(Bandara et al., 2017), and it was more comparable to the TEM results. The goal of the study was to see the interactions of the bacterial EPS, the membrane, the cytoplasmic content, and the nanopillars. It would have been desirable to distinguish these components in the images from the cross-section. The HIM-images have some contrast between nanopillar and the material protruding from the bacteria, but it is not clear if this is for example EPS or cytoplasmic fluid (FIGURE 20 lower right). The contrast in the cut surfaces has been found to be low with the HIM milling and imaging experiments. The probable reason is that even though the HIM has great topographical contrast, the mass contrast is low. Mass contrast could be produced with additional equipment like for example the secondary ion mass spectrometry (SIMS). The HIM with time-of-flight SIMS detector can do the compositional analysis of materials with under 10 nm resolution (Klingner, Heller, Hlawacek, Facsko, & von Borany, 2019).

Sato et al. (2018) found a good contrast with HIM when epon embedded tissue sections were imaged. They proposed that the contrast was the result of the charging phenomena, which alters the local secondary electron emission

(Sato, Sato, & Ogawa, 2018). Because of that observation, HIM milling and imaging approach of biological samples should be studied on the embedded samples, as well.

7 IMMOBILIZED PHAGES

Previous studies of the infectivity of the immobilized phages were discussed in section 3.1.2.2, with some inconsistencies existing between them. Besides, the measurement of the antibacterial effect and metric needs to be improved. Therefore, an experiment with systematic measures for the infectivity of the immobilized phage was performed in research article **A.I**.

7.1 Effectivity of immobilized phages

The number of attached, detached and infective phage particles on different model surfaces was studied in research article **A.I**. Phage used in the study was the tailed flavobacteria infecting phage FL-1. The number of attached phages was analyzed with HIM (FIGURE 22). The highest number of phages was found from the surface with a covalent carbodiimide crosslinker and the second highest from the aminosilane treated silicon. The number of detached phages was analyzed by titering the washing buffer and was found to be highest on the aminosilane treated silicon.

The metric how to measure the antibacterial effect and the infectivity of immobilized phages needed improvement. Therefore, we presented a novel measure "Effective infectivity" (PFU/area). This measure represents the number of infective phages per surface area, which was determined with the help of a free phage reference. In practice, it was done by comparing the antibacterial effect of the biomaterial to the antibacterial effect by the known number of phages. The measure is an improvement over the "equivalent MOI" measure (FIGURE 21b), used in the previous study (Wang et al., 2016) because it does not require a knowledge of the bacteria numbers. For example, if the measured effective infectivity for the phage-biomaterial is 10 PFU and it is then measured with ten times larger number of bacteria it will still be 10 PFU (FIGURE 21c). It is important to keep in mind that the free phage reference should be measured for a similar system and in the best case simultaneously.

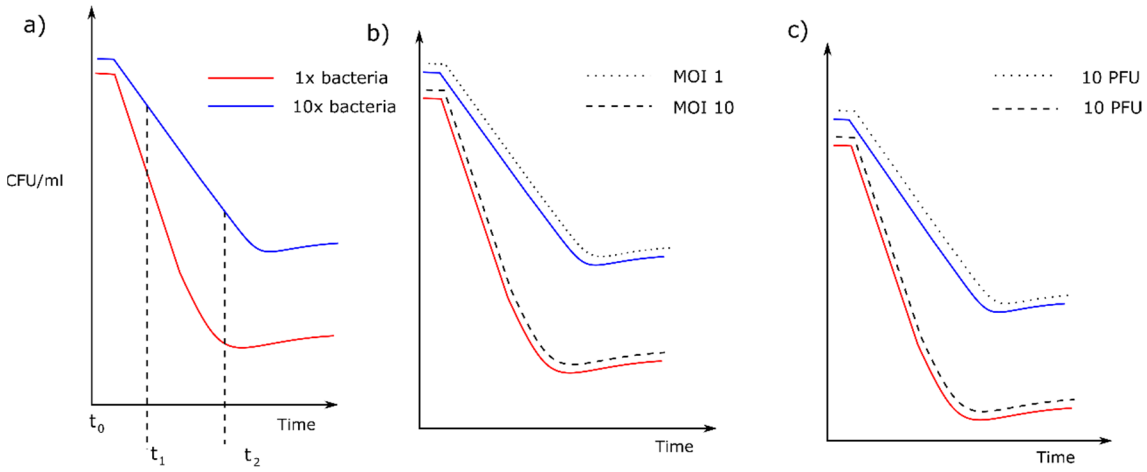

FIGURE 21 Different ways to measure the antibacterial effect by the phage-biomaterial. a) CFU reduction by the material with different initial numbers of bacteria measured at different timepoints. b) Equivalent MOI. Red line: CFU reduction by the material. Dashed line: CFU reduction by the MOI 10. Blue line: CFU reduction by the material when the bacteria number is tenfold. Dotted line: CFU reduction by the MOI 1 c) Effective infectivity Red line: CFU reduction by the material. Dashed line: CFU reduction by 10 PFU. Blue line: CFU reduction by the material when the bacteria number is tenfold. Dotted line: CFU reduction by 10 PFU.

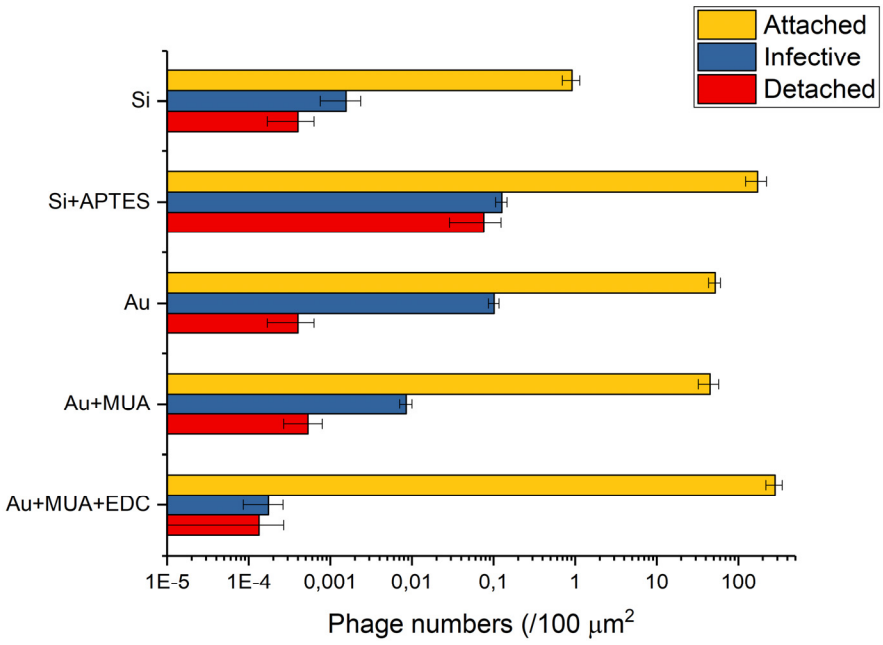

FIGURE 22 Attached, detached and infective phage numbers for the phage-biomaterials studied. From top to bottom: silicon, amine coated silicon, gold, carboxyl coated gold, carboxyl coated gold with carbodiimide crosslinker

The highest effective infectivity was found on phages loaded onto the aminosilane coated silicon (FIGURE 22). Experiments, where the biomaterial was moved from one incubation well to another suggested that the infectivity was mainly produced by the detached phages. Interestingly, on a plain gold surface, a low number of detached phages resulted in the relatively high infectivity, which suggests that phages could retain infectivity while being attached to the gold surface. The surface where covalent crosslinker was used has the lowest infectivity, even if it has the highest number of attached phages. This agrees with the literature were low infectivity of covalently bound phages is found (Wang et al., 2016). When antibacterial activity by the immobilized phages is compared to the free phage, comparison between the studies becomes more convenient. The material which releases infective particles to the surroundings might be relevant for practical applications. The orientation of the bound phages is crucial for infectivity, but it could not be resolved with the microscopy methods used.

7.2 The orientation of bound phages by microscopy methods

The expected orientation of the surface attached phage has been found to greatly affect its activity. For example, Richter et al. (2017) showed that the bacterial capture by the bound phages was greatly increased when they were oriented by the electric field (Richter et al., 2017). The straightforward explanation offered is that the tail up oriented phages can infect more easily compared to the side-lying orientation. However, so far no one has been able to show the orientation of the bound phage by microscopic methods. This challenge has been widely discussed in the review article by Hosseindoust et el. 2014 (Hosseinidoust, Olsson, & Tufenkji, 2014). In one study, SEM images showed oriented phages but the results were not very clear (Tolba, Minikh, Brovko, Evoy, & Griffiths, 2010). It could be questioned if the dried samples could ever represent the true orientation of the phages in the liquid. Of the possible microscopy methods, SPM could offer the resolution and the environmental capabilities required for unperturbed imaging (FIGURE 24). The benefit of SPM methods is that the experiments can be performed in liquid because no vacuum is required. Another choice might be the Cryo-TEM method with rapid freezing.

I studied the immobilized phages with the AFM PeakForce tapping (FIGURE 23). During these experiments, not a single tail-up oriented phage was found. It is possible that most of the phages have the side-lying orientation or that the scanning causes the phages to change their orientation.

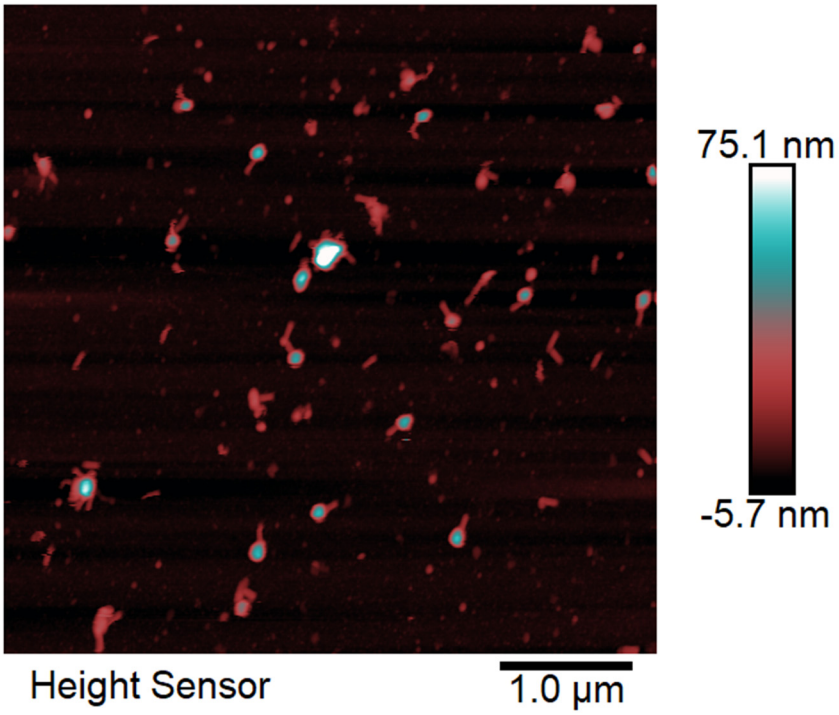

FIGURE 23 Liquid AFM-imaging of immobilized FL-1 phages with PeakForce tapping.

Among the parallel probe methods, there are more choices to study phage orientation as discussed by Hosseindoust et el. For example, x-ray-based or optical methods might give information about average phage orientation. However, most probably these methods still need to be validated with a "real" imaging method.

CONCLUSIONS AND FUTURE PERSPECTIVES

HIM enables imaging of bacteria and bacteria-bacteriophage interactions in a way that has not been seen before. The benefit of the HIM method compared to the transmission-based methods like TEM is that the samples do not need to be thin. HIM microscopy could be performed also as part of correlative imaging to link it to the functional information.

In situ milling and imaging with the HIM is an alternative for the biological samples compared to the other volumetric imaging methods. With the method, the cross-section can be cut precisely to the desired area and after that imaged with high resolution. However, secondary electron contrast on the cross-sections seems to be low and additional contrast mechanisms are needed. Charging contrast is an interesting phenomenon to be studied more in detail in the future. Compositional contrast by secondary ion mass spectrometry is also possible to obtain relatively easily. Possible artifacts during the HIM-milling are the redeposition of the milled material and the heat-induced damage (melting). The bulk heating effect during the milling should be estimated or measured in the future.

The damage caused by the ions for the material during HIM-imaging can be significant and should be always considered. Potential causes of damage are ionization damage by ion neutralization or secondary electron emission and kinetic energy-based damage by sputtering or heating. Fortunately, damage during the imaging is quite easy to detect with temporal imaging.

Imaging of the cellulose nanofibrils is an interesting example of the limits of the current microscopy methods. The limiting factor for high-resolution imaging is the energy of the probe, which can destroy the material before enough signal is generated. Because nanofibrils are disordered material, parallel methods like single-particle Cryo-EM or X-ray diffraction are not suitable methods for it.

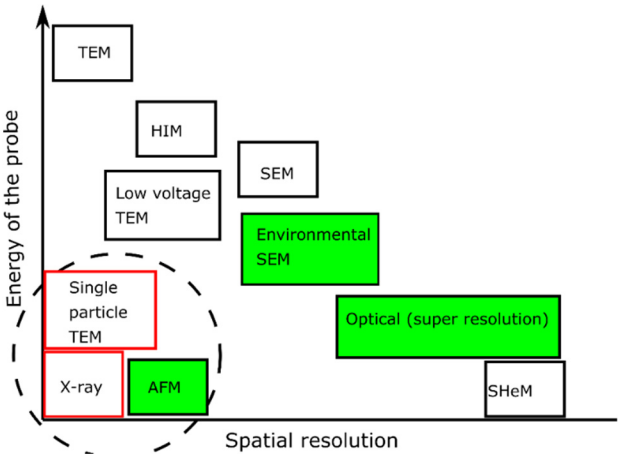

FIGURE 24 Imaging methods with resolution and the probe energy. Red boxes denote the parallel probes and green the methods with live imaging.

Truly non-invasive imaging needs probe energies lower than the bond dissociation energies, which are a few eV. Of the currently available high-resolution imaging methods, this is only possible with AFM (FIGURE 24). In the case of the particle microscopes, these low energies are thermal energies. This has been already studied with Scanning Helium Microscope (SHeM), which uses the scattering of the neutral helium atoms from the material to form the image of the sample. This far the highest lateral resolution achieved is not good, just under a micrometer, but is theoretically limited only by the wavelength of the particles (under nm for 0.01 eV). In practice, the focusing optics (atomic mirrors) and the atom source are limiting factors this far (Koch et al., 2008).

Effective infectivity is a good measure for the phage-based antibacterial surfaces. Infectivity of the studied phage-biomaterials originates from the detached phages, meaning that this type of phage reservoir approach might be good for practical applications. On some materials such as Au, it seems that the attached phages can have high infectivity also. Finding the orientation of the phage on the phage-biomaterial is another example of the limits of the current imaging methods. There, nanometer resolution imaging is challenging in this application because of the required liquid environment. The resolution of light-based methods is not high enough, and the particle-based methods require vacuum. Cryo-EM with rapid freezing could be a plausible method, but it is limited to transparent samples. In practice, SPM methods are the best suited for this application right now (FIGURE 24).

The role of electron microscopes in determining the nature of viruses is a fascinating story. As well as how the focused ion beams from the semiconductor industry were introduced in the biological imaging. Or how the nature's antibacterials can be used to help suffering people. Stories have the power to influence, as do images.

REFERENCES

Abedon, S. T., Kuhl, S. J., Blasdel, B. G., & Kutter, E. M. (2011). Phage treatment of human infections. *Bacteriophage, 1*(2), 66-85. doi:10.4161/bact.1.2.15845

Ackermann, H. -. (2007). 5500 phages examined in the electron microscope. *Archives of Virology, 152*(2), 227-243. doi:10.1007/s00705-006-0849-1

Almeida, Gabriel Magno de Freitas, & Sundberg, L. (2020). The forgotten tale of brazilian phage therapy. *The Lancet Infectious Diseases,* doi:10.1016/S1473-3099(20)30060-8

Aminov, R. I. (2010). A brief history of the antibiotic era: Lessons learned and challenges for the future. *Frontiers in Microbiology, 1*, 134. doi:10.3389/fmicb.2010.00134

Anany, H., Chen, W., Pelton, R., & Griffiths, M. W. (2011). Biocontrol of listeria monocytogenes and escherichia coli O157:H7 in meat by using phages immobilized on modified cellulose membranes; PMC3187159. *Appl.Environ.Microbiol., 77*(18), 6379-6387. doi:10.1128/AEM.05493-11

Bandara, C. D., Singh, S., Afara, I. O., Wolff, A., Tesfamichael, T., Ostrikov, K., & Oloyede, A. (2017). Bactericidal effects of natural nanotopography of dragonfly wing on escherichia coli. *ACS Applied Materials & Interfaces, 9*(8), 6746-6760. doi:10.1021/acsami.6b13666

Bazou, D., Behan, G., Reid, C., Boland, J. J., & Zhang, H. Z. (2011). Imaging of human colon cancer cells using he-ion scanning microscopy. *J.Microsc., 242*(3), 290-294. doi:10.1111/j.1365-2818.2010.03467.x

Cheng, Y., Feng, G., & Moraru, C. I. (2019). Micro- and nanotopography sensitive bacterial attachment mechanisms: A review. *Frontiers in Microbiology, 10*, 191. doi:10.3389/fmicb.2019.00191

Chung, K. K., Schumacher, J. F., Sampson, E. M., Burne, R. A., Antonelli, P. J., & Brennan, A. B. (2007). Impact of engineered surface microtopography on biofilm formation of staphylococcus aureus. *Biointerphases, 2*(2), 89-94. doi:10.1116/1.2751405

Codjoe, F. S., & Donkor, E. S. (2017). Carbapenem resistance: A review. *Medical Sciences (Basel, Switzerland), 6*(1), 1. doi:10.3390/medsci6010001

Colom, J., Cano-Sarabia, M., Otero, J., Cortés, P., Maspoch, D., & Llagostera, M. (2015). Liposome-encapsulated bacteriophages for enhanced oral phage therapy against salmonella spp. *Applied and Environmental Microbiology, 81*(14), 4841. doi:10.1128/AEM.00812-15

Curtin, J. J., & Donlan, R. M. (2006). Using bacteriophages to reduce formation of catheter-associated biofilms by staphylococcus epidermidis. *Antimicrob.Agents Chemother., 50*(4), 1268-1275.

Erni, R., Rossell, M. D., Kisielowski, C., & Dahmen, U. (2009). Atomic-resolution imaging with a sub-50-pm electron probe. *Physical Review Letters, 102*(9), 096101. doi:10.1103/PhysRevLett.102.096101

Fox, D., Zhou, Y. B., O'Neill, A., Kumar, S., Wang, J. J., Coleman, J. N., . . . Zhang, H. Z. (2013). Helium ion microscopy of graphene: Beam damage, image quality and edge contrast. *Nanotechnology, 24*(33), 335702-

4484/24/33/335702. Epub 2013 Jul 24. doi:10.1088/0957-4484/24/33/335702

Ghosh, C., Sarkar, P., Issa, R., & Haldar, J. (2019). Alternatives to conventional antibiotics in the era of antimicrobial resistance. *Trends in Microbiology; Special Issue: Antimicrobial Resistance and Novel Therapeutics, 27*(4), 323-338. doi:10.1016/j.tim.2018.12.010

Guerrero-Ferreira, R., & Wright, E. R. (2013). Cryo-electron tomography of bacterial viruses. *Virology, 435*(1), 179-186. doi:10.1016/j.virol.2012.08.022

Hasan, J., Crawford, R. J., & Ivanova, E. P. (2013). Antibacterial surfaces: The quest for a new generation of biomaterials. *Trends in Biotechnology, 31*(5), 295-304. doi:10.1016/j.tibtech.2013.01.017

Hill, R., Notte, J. A., & Scipioni, L. (2012). Chapter 2 - scanning helium ion microscopy. In Peter W. Hawkes (Ed.), *Advances in imaging and electron physics* (pp. 65-148) Elsevier. doi:10.1016/B978-0-12-394396-5.00002-6

Hlawacek, G., & Gölzhäuser, A. (2016). In Hlawacek G., Gölzhäuser A. (Eds.), *Helium ion microscopy* Springer International Publishing.

Hlawacek, G., Veligura, V., van Gastel, R., & Poelsema, B. (2014). Helium ion microscopy. *J.Vac.Sci.Technol.B Nanotechnol.Microelectron., 32*(2), 020801. doi:10.1116/1.4863676

Hollis, A., & Ahmed, Z. (2013). Preserving antibiotics, rationally. *N Engl J Med, 369*(26), 2474-2476. doi:10.1056/NEJMp1311479

Hosseinidoust, Z., Olsson, A. L. J., & Tufenkji, N. (2014). Going viral: Designing bioactive surfaces with bacteriophage. *Colloids Surf.B Biointerfaces, 124*, 2-16.

Hsu, L. C., Fang, J., Borca-Tasciuc, D., Worobo, R. W., & Moraru, C. I. (2013). Effect of micro- and nanoscale topography on the adhesion of bacterial cells to solid surfaces. *Applied and Environmental Microbiology, 79*(8), 2703. doi:10.1128/AEM.03436-12

Ivanova, E. P., Hasan, J., Webb, H. K., Truong, V. K., Watson, G. S., Watson, J. A., . . . Crawford, R. J. (2012). Natural bactericidal surfaces: Mechanical rupture of pseudomonas aeruginosa cells by cicada wings. *Small, 8*(16), 2489-2494. doi:10.1002/smll.201200528

Ivanova, E. P., Hasan, J., Webb, H. K., Gervinskas, G., Juodkazis, S., Truong, V. K., . . . Crawford, R. J. (2013). Bactericidal activity of black silicon. *Nature Communications, 4*(1), 2838. doi:10.1038/ncomms3838

Jault, P., Leclerc, T., Jennes, S., Pirnay, J. P., Que, Y. A., Resch, G., . . . Gabard, J. (2019). Efficacy and tolerability of a cocktail of bacteriophages to treat burn wounds infected by pseudomonas aeruginosa (PhagoBurn): A randomised, controlled, double-blind phase 1/2 trial. *The Lancet.Infectious Diseases, 19*(1), 35-45. doi:S1473-3099(18)30482-1

Joens, M. S., Huynh, C., Kasuboski, J. M., Ferranti, D., Sigal, Y. J., Zeitvogel, F., . . . Fitzpatrick, J. A. J. (2013). Helium ion microscopy (HIM) for the imaging of biological samples at sub-nanometer resolution. *Sci.Rep., 3*, 3514. doi:10.1038/srep03514

Joy, D. C. (2013). *Helium ion microscopy: Principles and applications*. New York: Springer-Verlag.

Kangas, H., Lahtinen, P., Sneck, A., Hell 駭, E., Saariaho, A., & Laitinen, O. (2014). Characterization of fibrillated celluloses. A short review and evaluation of characteristics with a combination of methods. *Nordic Pulp and Paper Research Journal, 29*(1), 129-143. doi:10.3183/NPPRJ-2014-29-01-p129-143

Klingner, N., Heller, R., Hlawacek, G., Facsko, S., & von Borany, J. (2019). Time-of-flight secondary ion mass spectrometry in the helium ion microscope. *Ultramicroscopy, 198*, 10-17. doi:10.1016/j.ultramic.2018.12.014

Koch, M., Rehbein, S., Schmahl, G., Reisinger, T., Bracco, G., Ernst, W. E., & Holst, B. (2008). Imaging with neutral atoms—a new matter-wave microscope. *Journal of Microscopy, 229*(1), 1-5. doi:10.1111/j.1365-2818.2007.01874.x

Lavoine, N., Desloges, I., Dufresne, A., & Bras, J. (2012). Microfibrillated cellulose - its barrier properties and applications in cellulosic materials: A review. *Carbohydrate Polymers, 90*(2), 735-764. doi:10.1016/j.carbpol.2012.05.026

Lemme, M. C., Bell, D. C., Williams, J. R., Stern, L. A., Baugher, B. W. H., Jarillo-Herrero, P., & Marcus, C. M. (2009). Etching of graphene devices with a helium ion beam. *ACS Nano, 3*(9), 2674-2676. doi:10.1021/nn900744z

Leppänen, M., Sundberg, L., Laanto, E., de Freitas Almeida, Gabriel Magno, Papponen, P., & Maasilta, I. J. (2017). Imaging bacterial colonies and Phage–Bacterium interaction at sub-nanometer resolution using helium-ion microscopy. *Advanced Biosystems, 1*(8), 1700070. doi:10.1002/adbi.201700070

Li, Z., Liu, J., Jiang, K., & Thundat, T. (2016). *Carbonized nanocellulose sustainably boosts the performance of activated carbon in ionic liquid supercapacitors* doi:10.1016/j.nanoen.2016.04.036

Liana, A. E., Marquis, C. P., Gunawan, C., Justin Gooding, J., & Amal, R. (2018). Antimicrobial activity of T4 bacteriophage conjugated indium tin oxide surfaces. *J.Colloid Interface Sci., 514*, 227-233.

Linklater, D. P., De Volder, M., Baulin, V. A., Werner, M., Jessl, S., Golozar, M., . . . Ivanova, E. P. (2018). High aspect ratio nanostructures kill bacteria via storage and release of mechanical energy. *ACS Nano, 12*(7), 6657-6667. doi:10.1021/acsnano.8b01665

Linklater, D. P., Juodkazis, S., Rubanov, S., & Ivanova, E. P. (2017). Comment on "Bactericidal effects of natural nanotopography of dragonfly wing on escherichia coli". *ACS Applied Materials & Interfaces, 9*(35), 29387-29393. doi:10.1021/acsami.7b05707

Livengood, R., Tan, S., Greenzweig, Y., Notte, J., & McVey, S. (2009). Subsurface damage from helium ions as a function of dose, beam energy, and dose rate. *Journal of Vacuum Science & Technology B: Microelectronics and Nanometer Structures Processing, Measurement, and Phenomena, 27*(6), 3244-3249. doi:10.1116/1.3237101

Lone, A., Anany, H., Hakeem, M., Aguis, L., Avdjian, A., Bouget, M., . . . Griffiths, M. W. (2016). Development of prototypes of bioactive packaging materials based on immobilized bacteriophages for control of growth of bacterial pathogens in foods. *Int.J.Food Microbiol., 217*, 49-58.

Lustig, A., & Levine, A. J. (1992). One hundred years of virology. *Journal of Virology, 66*(8), 4629-4631.

Ma, Y., Pacan, J. C., Wang, Q., Xu, Y., Huang, X., Korenevsky, A., & Sabour, P. M. (2008). Microencapsulation of bacteriophage felix O1 into chitosan-alginate microspheres for oral delivery. *Applied and Environmental Microbiology, 74*(15), 4799-4805. doi:10.1128/AEM.00246-08

Ma, Y., Pacan, J. C., Wang, Q., Sabour, P. M., Huang, X., & Xu, Y. (2012). Enhanced alginate microspheres as means of oral delivery of bacteriophage for reducing staphylococcus aureus intestinal carriage. *Food Hydrocolloids; 10th International Hydrocolloids Conference, 26*(2), 434-440. doi:10.1016/j.foodhyd.2010.11.017

Madkour, A. E., & Tew, G. N. (2008). Towards self-sterilizing medical devices: Controlling infection. *Polymer International, 57*(1), 6-10. doi:10.1002/pi.2399

Malik, D. J., Sokolov, I. J., Vinner, G. K., Mancuso, F., Cinquerrui, S., Vladisavljevic, G. T., . . . Kirpichnikova, A. (2017). Formulation, stabilisation and encapsulation of bacteriophage for phage therapy. *Adv.Colloid Interface Sci., 249*, 100-133.

Myelnikov, D. (2018). An alternative cure: The adoption and survival of bacteriophage therapy in the USSR, 1922-1955. *Journal of the History of Medicine and Allied Sciences, 73*(4), 385-411. doi:10.1093/jhmas/jry024

Narayan, K., & Subramaniam, S. (2015). Focused ion beams in biology. *Nat Meth, 12*(11), 1021-1031.

Nishiyama, Y. (2009). Structure and properties of the cellulose microfibril. *Journal of Wood Science, 55*(4), 241-249. doi:10.1007/s10086-009-1029-1

Nogueira, F., Karumidze, N., Kusradze, I., Goderdzishvili, M., Teixeira, P., & Gouveia, I. C. (2017). Immobilization of bacteriophage in wound-dressing nanostructure. *Nanomedicine, 13*(8), 2475-2484.

Ogawa, Y., & Putaux, J. (2019). Transmission electron microscopy of cellulose. part 2: Technical and practical aspects. *Cellulose, 26*(1), 17-34. doi:10.1007/s10570-018-2075-x

Orloff, J. (2001). Focused ion beam characterization techniques. In K. H. J. Buschow, R. W. Cahn, M. C. Flemings, B. Ilschner, E. J. Kramer, S. Mahajan & P. Veyssière (Eds.), *Encyclopedia of materials: Science and technology* (pp. 3226-3231). Oxford: Elsevier.

Postek, M. T., Vladár, A., Dagata, J., Farkas, N., Ming, B., Wagner, R., . . . Beecher, J. (2010). Development of the metrology and imaging of cellulose nanocrystals. *Measurement Science and Technology, 22*(2), 024005. doi:10.1088/0957-0233/22/2/024005

Rice, W. L., Van Hoek, A.,N., Păunescu, T.,G., Huynh, C., Goetze, B., Singh, B., . . . Brown, D. (2013). High resolution helium ion scanning microscopy of the rat kidney. *PLoS ONE, 8*(3), e57051. doi:10.1371/journal.pone.0057051

Richter, L., Bielec, K., Le 'sniewski, A., \Lo\'s Marcin, Paczesny, J., & Ho lyst, R. (2017). Dense layer of bacteriophages ordered in alternating electric field and immobilized by surface chemical modification as sensing element for bacteria detection. *ACS Appl.Mater.Interfaces, 9*(23), 19622-19629.

Rigo, S., Cai, C., Gunkel-Grabole, G., Maurizi, L., Zhang, X., Xu, J., & Palivan, C. G. (2018). Nanoscience-based strategies to engineer antimicrobial surfaces. *Advanced Science, 5*(5), 1700892. doi:10.1002/advs.201700892

Roach, D. R., & Debarbieux, L. (2017). Phage therapy: Awakening a sleeping giant. *Emerging Topics in Life Sciences, 1*(1), 93-103. doi:10.1042/ETLS20170002

Said, N., Chatzinotas, A., & Schmidt, M. (2019). Have an ion on it: The life-cycle of bdellovibrio bacteriovorus viewed by helium-ion microscopy. *Advanced Biosystems, 3*(1), 1800250. doi:10.1002/adbi.201800250

Sato, C., Sato, M., & Ogawa, S. (2018). Imaging of immunogold labeling in cells and tissues by helium ion microscopy. *International Journal of Molecular Medicine, 42*(1), 309-321. doi:10.3892/ijmm.2018.3604

Singer, C. (1914). Notes on the early history of microscopy. *Proceedings of the Royal Society of Medicine, 7*, 247-279.

Smith, H. W., Huggins, M. B., & Shaw, K. M. (1987). Factors influencing the survival and multiplication of bacteriophages in calves and in their environment. *Journal of General Microbiology, 133*(5), 1127-1135. doi:10.1099/00221287-133-5-1127

Summers, W. C. (2012). The strange history of phage therapy. *Bacteriophage, 2*(2), 130-133. doi:10.4161/bact.20757

Sun, L., Zhang, X., Gao, S., Rao, P. A., Padilla-Sanchez, V., Chen, Z., . . . Rossmann, M. G. (2015). Cryo-EM structure of the bacteriophage T4 portal protein assembly at near-atomic resolution. *Nature Communications, 6*, 7548. doi:10.1038/ncomms8548

Tan, S., Livengood, R., Hack, P., Hallstein, R., Shima, D., Notte, J., & McVey, S. (2011). Nanomachining with a focused neon beam: A preliminary investigation for semiconductor circuit editing and failure analysis. *Journal of Vacuum Science & Technology B, 29*(6), 06F604. doi:10.1116/1.3660797

Tawil, N., Sacher, E., Mandeville, R., & Meunier, M. (2013). Strategies for the immobilization of bacteriophages on gold surfaces monitored by surface plasmon resonance and surface morphology. *J.Phys.Chem.C, 117*(13), 6686-6691. doi:10.1021/jp400565m

The PLOS Medicine Editors. (2016). Antimicrobial resistance: Is the world UNprepared? *PLOS Medicine, 13*(9), e1002130. doi:10.1371/journal.pmed.1002130

The Review on Antimicrobial Resistance Chaired by Jim O'Neill. (2014). *Antimicrobial resistance: Tackling a crisis for the health and wealth of nations.*

Tolba, M., Minikh, O., Brovko, L. Y., Evoy, S., & Griffiths, M. W. (2010). Oriented immobilization of bacteriophages for biosensor applications; PMC2805203. *Appl.Environ.Microbiol., 76*(2), 528-535. doi:10.1128/AEM.02294-09

Torvinen, K., Pettersson, F., Lahtinen, P., Arstila, K., Kumar, V., Österbacka, R., . . . Saarinen, J. J. (2017). Nanoporous kaolin—cellulose nanofibril composites for printed electronics. *Flexible and Printed Electronics, 2*(2), 024004. doi:10.1088/2058-8585/aa6d97

Vanden Berg-Foels, W. S., Scipioni, L., Huynh, C., & Wen, X. (2012). Helium ion microscopy for high-resolution visualization of the articular cartilage

collagen network. *Journal of Microscopy, 246*(2), 168-176. doi:10.1111/j.1365-2818.2012.03606.x

Vandenheuvel, D., Singh, A., Vandersteegen, K., Klumpp, J., Lavigne, R., & Van den Mooter, G. (2013). Feasibility of spray drying bacteriophages into respirable powders to combat pulmonary bacterial infections. *European Journal of Pharmaceutics and Biopharmaceutics, 84*(3), 578-582. doi:10.1016/j.ejpb.2012.12.022

Virtanen, J., Janka, M., & Tuukkanen, S. (2018). (2018). Fabrication and characterization of nanocellulose aerogel structures. Paper presented at the *Embec & Nbc 2017,* 1029-1032.

von Borries, B., Ruska, E., & Ruska, H. (1938). Bakterien und virus in ubermikroskopischer aufnahme. *Klin.Wochenschr., 17*(27), 921-925.

Wang, C., Sauvageau, D., & Elias, A. (2016). Immobilization of active bacteriophages on polyhydroxyalkanoate surfaces. *ACS Appl.Mater.Interfaces, 8*(2), 1128-1138.

Ward, B. W., Notte, J. A., & Economou, N. P. (2006). Helium ion microscope: A new tool for nanoscale microscopy and metrology. *Journal of Vacuum Science & Technology B, 24*(6), 2871-2874. doi:10.1116/1.2357967

Wolff, A., Klingner, N., ThompsonN, W., Zhou, Y., Lin, J., Peng, Y. Y., . . . Xiao, Y. (2018). Modelling of focused ion beam induced increases in sample temperature: A case study of heat damage in biological samples. *Journal of Microscopy, 272*(1), 47-59. doi:10.1111/jmi.12731

Wommack, K. E., & Colwell, R. R. (2000). Virioplankton: Viruses in aquatic ecosystems; PMC98987. *Microbiol.Mol.Biol.Rev., 64*(1), 69-114.

Yasaka Anto, Aramaki Fumio, Kozakai Tomokazu, & Matsuda Osamu. (2016). Nanoscale imaging, material removal and deposition for fabrication of cutting-edge semiconductor Devices ―Ion-beam-based photomask defect repair technology―. *Hitachi Review, 65*(7), 233-237.

ORIGINAL PAPERS

I

ANTIBACTERIAL EFFICIENCY OF SURFACE-IMMOBILIZED FLAVOBACTERIUM-INFECTING BACTERIOPHAGE

by

Leppänen, M., Maasilta, I. J., & Sundberg, L. 2019.

ACS Applied Bio Materials, 2(11), 4720-4727

ACS APPLIED BIO MATERIALS Cite This: ACS Appl. Bio Mater. XXXX, XXX, XXX−XXX

Article

www.acsabm.org

Antibacterial Efficiency of Surface-Immobilized *Flavobacterium*-Infecting Bacteriophage

Miika Leppänen,[†,‡] Ilari J. Maasilta,[†] and Lotta-Riina Sundberg*[,‡]

[†]Nanoscience Center, Department of Physics, [‡]Nanoscience Center, Department of Biological and Environmental Science, University of Jyvaskyla, P.O. Box 35, FI-40014 Jyväskylä, Finland

Supporting Information

ABSTRACT: Control of bacterial diseases by bacteriophages (phages) is gaining more interest due to increasing antibiotic resistance. This has led to technologies to attach phages on surfaces to form a biomaterial that can functionally display phages that interact with bacteria, to carry out successful infection cycles. Such a material could be applied in many environments where the target pathogens are expected. Although this approach has been applied successfully in a few studies already, the basis of the antibacterial effect by the immobilized phages is unclear, and the interpretation of the results depends on the study. Here, we studied the phage attachment density, their detachment rate, and infectivity on five different surfaces: silicon, amine-treated silicon, gold, carboxylate-treated gold, and cross-linker-activated carboxylate-treated gold. The density of attached phages varied between the different surfaces and was the highest on the cross-linker-activated carboxylate-treated gold. To understand whether the antibacterial effect is caused by the attached or the detached phages, the strength of the immobilization was analyzed by performing 3−12 washing steps. The detachment rates differed between the materials, with the amine-treated silicon surface generating the highest release of phages and maintaining the highest infectivity, even after extensive washing. However, covalent cross-linking seemed to interfere with the infectivity. Our results suggest that the detachment of the phages from the surface is a possible mechanism for the antibacterial effect. Furthermore, we introduce a measure of the infectivity by comparing the bacterial growth reductions produced by the phage-treated materials to the effect caused by a known number of free phages, resulting in a unit "effective PFU/surface area", a comparable standard between different studies.

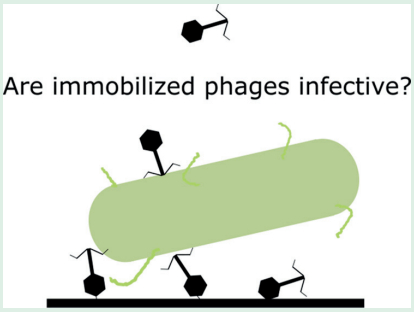

KEYWORDS: *phage therapy, surface adsorbed bacteriophages, antibacterial surfaces, aquaculture, virus material, biomaterial*

1. INTRODUCTION

Bacteriophages are viruses that parasitize bacteria to produce progeny, and due to this property, they can be used to control the growth and infectivity of the host. Although this approach, phage therapy, has been known already for a century, interest is increasing due to rising antibiotic resistance.[1] Because of their host-specific infectivity, phages can be used as specialized killers toward pathogenic bacteria in contrast to antibiotics, which generally have a wide impact on microorganisms.

Aquaculture, i.e., fish farming, is a growing food production industry because of the collapse of many natural fisheries.[2] Fish are grown in high densities, which increases the possibility of disease outbreaks that can cause high mortalities.[3] Usually, the treatment of these diseases requires the use of antibiotics, which has been shown to lead to an increase in antibiotic resistance among environmental bacteria.[4,5] Columnaris disease caused by the *Flavobacterium columnare* is a bacterial disease in freshwater fish resulting in devastating epidemics at fish farms around the world.[6] It has been shown that phage therapy can be used to prevent columnaris disease in the laboratory environment by direct addition of phages in the water.[7] However, in a typical fish farm environment (net pens and flow-through systems), the water volumes can be extremely high, diluting or removing the added phages via the water flow. Therefore, the immobilization of phages on a surface to provide a long-lasting antibacterial effect could be an optimal solution. But the question remains: Are surface attached phages any good? Furthermore, is the antibacterial effect caused by the attached or the detached phages? This information is central to understand the antibacterial effect of surface-immobilized phages.

Although an antimicrobial effect of immobilized phages has been demonstrated already in studies regarding food packaging[8,9] and health care equipment,[10,11] there is very little consistency regarding the mechanisms of antibacterial effect of surface-immobilized phages. In these previous studies, neither the number of detached nor attached phages were reported, leaving the mechanism of phage infection unclear. Covalent cross-linking of phages to a surface has been found to increase the density and activity of phages in biosensor applica-

Received: March 21, 2019
Accepted: October 8, 2019
Published: October 8, 2019

DOI: 10.1021/acsabm.9b00242
ACS Appl. Bio Mater. XXXX, XXX, XXX−XXX

tions[12−15] and has also been utilized in antibacterial studies.[16−18] However, the mechanisms behind the results remain unclear. Covalently immobilized phages were found to cause the lysis of the bacteria on the surface,[16] and to have a higher antibacterial effect compared to physisorbed phages.[18] In contrast, Liana et al. found that the infectivity of the chemically modified and T4-phage-treated indium tin oxide surfaces was produced by the detached phages.[19] Also, Wang et al. detected a higher infectivity on a plasma-treated surface without a covalent cross-linker than with it.[17]

To clarify the mechanisms involved with antimicrobial effects of immobilized phages, we studied the phage attachment density, the detachment rate, and the infectivity of surface-immobilized *Flavobacterium*-infecting bacteriophages on five different surfaces: silicon, amine-treated silicon, gold, carboxylate-treated gold, and cross-linker-activated carboxylate-treated gold. These specific surfaces were selected because they have been used in the previous immobilization studies and are known to result in different surface densities of phages.[20,21] To understand whether the antibacterial effect of these surfaces is caused by the attached or the detached phages, the strength of the immobilization was also analyzed by 3−12 washing steps. The amine-treated silicon surface generated a high release of phages and maintained the highest infectivity, even after extensive washing, suggesting that detached phages are important. On the other hand, covalent cross-linking seemed to interfere with the phage infectivity. Furthermore, by using a combination of microbiological and imaging methods, we define a standard for reporting the antibacterial efficiency of phage-based biomaterials.

2. MATERIALS AND METHODS

2.1. Phage Production. Phage FL-1 is originally isolated from a fish farm in Finland,[22] and it infects *Flavobacterium sp.* It was obtained from the +4 °C stock, and its amplification was done using the standard double-layer agar method with a phage−bacteria ratio producing semiconfluent Shieh-agar[23] plates. After overnight incubation, 5 mL of Shieh was added per plate, and plates were shaken overnight at +4 °C to elute the phages. The lysate was filtered with a 0.45 μm filter to remove the bacteria. The filtered lysate was then purified using an ÄKTAprime plus chromatography system with a quaternary-amine-activated ion-exchange column QA-1 by BIA Separations (Figures S1 and S2). The remaining salt was removed by a two-step buffer replacement with a cellulose dialysis tube in a 50 mM sodium phosphate buffer. Eventually, a pure phage solution with 8×10^{10} PFUs/mL was obtained (PFU = plaque forming unit).

2.2. Substrates. The five selected substrate surfaces for this study were untreated crystalline silicon with a thin native oxide surface, amine-treated crystalline silicon (with native oxide), untreated gold, carboxylate-treated gold, and carboxylate-treated gold with a covalent cross-linker. Precut (5 mm × 5 mm) crystalline silicon substrates were purchased from Ted Pella, USA. (3-Aminopropyl)triethoxysilane (APTES) was used as the amine compound treating Si. The surface was prepared by first treating silicon substrates for 1 min with 100 W O_2 plasma in a reactive ion etcher (Oxford Plasmalab 80 Plus) to obtain hydroxyl groups to the silicon surface. A 1:2 mixture of APTES/EtOH (99.5%) was then added for 20 min at 50 °C, washed with 99.5% EtOH and DI (deionized) water, and baked at 108 °C for 50 min. The gold surface was prepared on a silicon substrate with the JEOL JFC-1100 sputter coater using about 1 kV energy, 10 mA current, and 1 h processing time. The carboxylate treatment for the gold consisted of an MUA (11-Mercaptoundecanoic acid) coating, done by submerging Au-coated Si substrates to 10 mM MUA for 24 h, followed by washings with 99.5% EtOH and twice with sterile DI water. Additional cross-linker activation of the MUA-treated gold was done by preparing a 0.1 M EDC (1-ethyl-3-(3-(dimethylamino)-propyl)carbodiimide hydrochloride) and 0.4 M NHS (*N*-Hydroxysuccinimide) mixture to DI water, incubating the substrate in it at room temperature (RT) for 40 min and dip washing it twice with DI water.

2.3. Phage Immobilization, Detachment, and Titration. All of the immobilization experiments were conducted in a 50 mM phosphate buffer at pH 7.2. FL-1 bacteriophage solutions (200 μL) with 1.5×10^8 PFUs were pipetted on the substrates individually and left to adhere overnight at +4 °C under 90 rpm shaking. Next, the materials were washed six times in 1 mL of 20 mM phosphate buffer (pH 7.2) by dipping to remove most of the unbound phages. After these baseline washes, phages were detached from the sample surfaces by first placing the samples into the well of a 24-well plate with 1 mL of phosphate buffer and shaking at 400 rpm for a set period of time. The buffer was then replaced, and the shaking was repeated 3, 6, 10, or 12 times. The first detachment was done for 90 min and the following detachments for 20−30 min. In addition, some samples were washed four extra times by dipping after the last detachment treatment (12 + 4 samples). This extra wash was used to minimize the number of phages transferred from the detachment buffer. Fresh buffers were used for every sample at every step during the detachments. The number of detached phages was analyzed by titering. Plates were prepared by mixing 100 μL of overnight grown *Flavobacterium sp.* and 2 mL of Shieh with 0.7% low melt agarose tempered to 40 °C and poured over the Petri dish. After the agarose was solidified, a 10 μL droplet of raw or diluted detachment buffer was pipetted over it and incubated 48 h, after which the plaques were counted. Three individual replicates were done for all samples, and the standard error of the mean (SEM) was calculated.

Activation of phage carboxyl groups with the EDC cross-linker was studied by adding 1 mg of EDC and 1 mg of NHS to 1 mL of 2×10^9 PFUs/mL FL-1 phage solution, resulting in 5 mM EDC and 9 mM NHS. The solution was incubated for 15 min at RT, and a dilution series was plated with the double layer agar method. A diluted cross-linker experiment was performed with 50 μM EDC and 90 μM NHS.

2.4. Helium Ion Microscopy (HIM) and Transmission Electron Microscopy (TEM). Samples were prepared for TEM using negative staining with 2% Phosphotungstic acid (PTA). Five microliters of purified FL-1 phage stock was pipetted on a Formvar-carbon-coated TEM-grid and let to adhere there for 2 min, 5 μL of staining was added, and after 2 min, the excess was dried off. Imaging was done with a JEOL JEM-1400 HC Transmission Electron Microscope. Substrates with immobilized phages were prepared for HIM imaging by removing the excess buffer with a corner of a paper, and then air-drying them in ambient conditions. Samples were imaged with Zeiss Orion Nanofab using helium as the imaging gas. An acceleration voltage of 30 kV and an aperture size of 10 μm were used, resulting in an ion current of 0.5 pA.

2.5. Infectivity Measurements. Infectivity of the surfaces with immobilized phages was measured on a 24-well plate (Sarstedt, TC-plate 24 well, Standard, F). The substrate was placed in 1 mL of Shieh medium, and 50 μL of fresh overnight grown *Flavobacterium sp.* culture (2.5×10^6 CFU) was added. The culture was mixed for 15 s at 400 rpm and then incubated at RT without shaking for 48 h. Before the addition of the bacteria, some substrates were shaken at 400 rpm for 5 s, incubated for 5 min and moved to a second well (containing the Shieh medium), to study the effect of detached phages on bacterial growth. To compare the effect of immobilized phages to the one caused by free phages, infections with free phages with multiplicities of infection (MOI) between 1 and 0.0001 were performed by adding 10 μL of FL-1 serial dilutions to some wells. The optical density of the culture at the wavelength 590 nm was measured with a Multiskan microplate photometer after 18, 27, and 48 h, after the latent period of the phage, known to be 1−2 h (Figure S3). A duplicate measurement was made at every time point, and the average value was calculated. Three individual replicates were done for all the infectivity samples. The statistical significance of the results was analyzed with the Student's two-sample *t* test.

DOI: 10.1021/acsabm.9b00242
ACS Appl. Bio Mater. XXXX, XXX, XXX−XXX

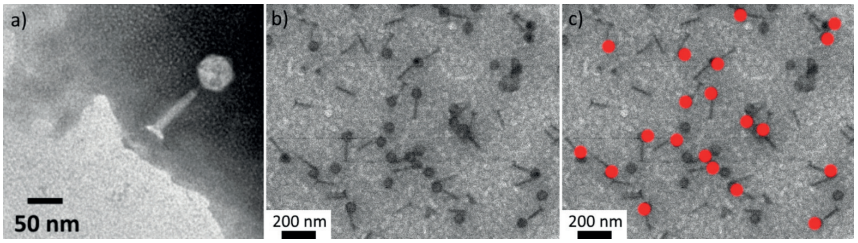

Figure 1. Phage FL-1 samples were imaged with TEM and HIM. (a) TEM image of phage FL-1 (b) 12 + 4 detached Au+MUA+EDC sample imaged with HIM. (c) Panel b with red dots marking the counted (intact) phage particles.

3. RESULTS AND DISCUSSION

Purified FL-1 phage was imaged with TEM (Figure 1a). It is a myophage with an icosahedral head (diameter 55 nm) and approximately 100 nm long tail.

3.1. Attached Phages. The number of attached phages for different surface treatments was analyzed by imaging the samples with HIM (Figure 1b). Four systematically selected areas (100 μm^2) per sample were imaged, and only phage particles with an intact head and tail were counted (Figure 1c). More information is found in Supplementary Table S1. Three individual replicates were done per treatment.

As expected, the density of the attached phages varied between the surfaces (Figure 2). For each surface, no

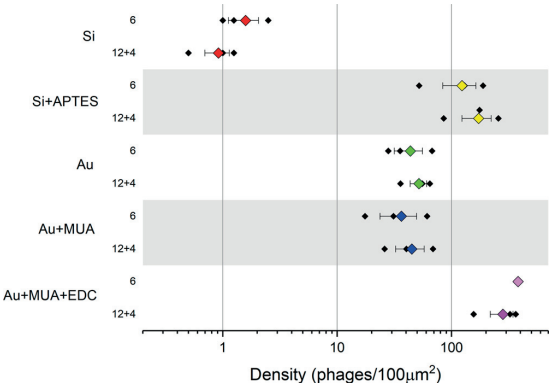

Figure 2. Average density of attached phages on the different surfaces calculated from the HIM images. The numbers after the name of the material are the number of detachment steps (6 or 12 + 4). Each replicate is shown by small black diamonds; the colored symbols + error bars show the mean ± SEM (n = 3). For the Au+MUA+EDC 6 sample, only one image area was used.

significant differences were found between 6 and 12 + 4 detachment treatments ($p > 0.05$). After the full set of 12 + 4 detachment steps, silicon had clearly the lowest phage density. The silicon surface is covered with a native oxide, giving it the chemical properties of silicon oxide.[24] Silicon oxide surface is negatively charged in pH 7,[25] polar[24] and weakly polarizable, which means that neither electrostatic (as phages typically have an effective negative charge at pH 7),[26] van der Waals (vdW), nor hydrophobic forces are likely responsible for the phage adsorption.

The density of phages on the APTES-treated silicon surface was about 100-fold compared to the untreated silicon after a full set of detachment treatments. This can be explained by the positive charge of the APTES-surface at pH 7.2 due to the protonated amine groups. Phage FL-1 has an effective negative charge at this pH, as demonstrated during the purification of the phage stock when phages were bound to the amine-treated surfaces of the monolithic column at pH 7.2.

The average phage density on the gold surface was about 50 phages/100 μm^2, even though gold has been shown to have a slightly negative charge at pH 7.[27] The binding may have, however, been caused by high polarizability, which results in strong vdW and hydrophobic interactions.[28] Indeed, a previous study[21] on adsorption of nontailed phages to SiO_2, gold, carboxyl, methyl, and amine-treated surfaces in different pH and ionic concentrations found that for some phages, adsorption to the gold surface was almost as high as to the amine-treated surface at pH 7. When the unfavorable electrostatic effect was shielded by increasing the ionic strength from 0.01 to 0.1 M, adsorption increased even more. High adsorption of tailed phages on gold is reported in the literature with densities of 0.7,[29] 0.49[30] and 10.12 phages/μm^2,[31] with the first two of those comparable to our observation of 50 phages/100 μm^2.

The phage density on MUA-treated gold surface was comparable to gold and APTES-coated silicon. A previous study found fewer attached phages on the APTES-treated ITO-surface compared to the carboxylate-treated one,[20] suggesting planar surfaces have distinct adsorption dynamics compared to particulate surfaces, for which amine treatment resulted in strong adsorption.[32,33] This suggestion was not confirmed by our study. Although the phage density on the APTES is higher than on MUA in our measurements, the difference is not significant ($p = 0.07$).

The highest density of all the five surfaces was found on the Au+MUA surface treated with EDC. Compared to untreated MUA, the density was significantly higher ($p < 0.05$), which was the result of covalent immobilization by the carbodiimide chemistry.

In the literature, covalent cross-linking has been done either by activating the phage itself[12,34] or by activating the surface.[17] In our study, the EDC cross-linker was used to activate the carboxylates on the MUA surface prior to the reaction with the amines on the phage (Figure 3a). Because the APTES surface had a higher number of attached phages than the MUA surface, we were also interested in activating the carboxylate groups on the phage (Figure 3b). Preliminary experiments suggested that the infectivity of the surface was lost when using this approach. Therefore, we tested the infectivity of the phage after an EDC activation with the double layer method. Treatment of phages with 5 mM EDC and 9 mM NHS (concentration commonly used in the literature) reduced the infectivity (PFUs) of the phage solution from (1.2 ± 0.2) ×

DOI: 10.1021/acsabm.9b00242
ACS Appl. Bio Mater. XXXX, XXX, XXX−XXX

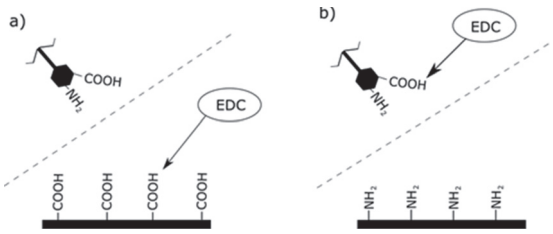

Figure 3. Different strategies for the covalent immobilization with the EDC (a) Activation of the carboxylates on the MUA surface with EDC. (b) Activation of the carboxylates on the phage proteins with EDC.

10^9 PFUs/mL to $(1 \pm 0.6) \times 10^3$ PFUs/mL. When EDC was diluted 100-fold (50 μM EDC, 90 μM NHS), phage infectivity was reduced to $(4 \pm 2) \times 10^8$ PFUs/mL. Therefore, activation of phages with the cross-linker was not pursued further. Some previous studies have discussed the possible harmful effects of phage activation with EDC,[16,34] but direct evidence of the loss of infectivity was not shown before. We note that EDC activation of phages is not location-specific, which could prevent the phage from binding the host, or could cross-link the phages with each other, compromising the infectivity.

To give an indication of the efficiency of phage attachment on different surfaces, we calculated the ratio of the total number of attached phages, calculated by multiplying the average phage density from HIM images with the total substrate area, to the number of PFUs in the purified phage stock used for the immobilization. For the Au+EDC+MUA surface, the percentage is high, over 40%, but for silicon about 0.1% (Figure 4a). It must be noted, however, that PFU of the initial stock was determined by plaque assay in which only the number of infective phages are counted. Imaging, on the other hand, sees all intact phage particles, but their infectivity cannot be concluded. Thus, the estimate of phage attachment is actually an upper limit.

3.2. Detached Phages. To study the release of phages from the surfaces, we titered the detachment buffers. After the first three rounds of detachment washes, the highest number of phages were released to the detachment buffer from the Si +APTES surface. For silicon, Au and Au+MUA, the number of detached phages decreased with the increase in the number of performed detachment steps. For the Si + APTES sample, the change was not significant ($p > 0.05$). After a full set of 12 detachment steps, APTES still has the highest release. However, the number of attached phages did not really seem to change on APTES, along with the increase in the number of detachment steps (Figure 2). This apparent contradiction may be explained by the high number of phages still attached to the APTES sample after 12 + 4 detachments compared to the number of detached phages, being only ~0.1% of the attached (Figure 4b).

Next, we estimated the strength of the phage binding on different surfaces by studying the detached-attached ratios (Figure 4b). The ratio was lowest for the Au+MUA+EDC (4×10^{-7}), suggesting strong binding. Indeed, EDC covalently cross-links the surface carboxylates and the phage amines. For gold and gold+MUA, the result of relatively strong binding was not entirely expected, as hydrophobic and vdW interactions are usually considered weaker interactions compared to the electrostatic (as in APTES). In the literature, a higher detachment ratio of 0.007% for gold with a tailed phage has been reported;[29] however, fewer washing steps (5 vs 18) were made.

Previous studies of the release of the surface-immobilized phages are rare. Vonasek et al.[35] found that amine-treated cellulose releases a significant number of phages in the aqueous environment. Liana et al.[19] studied the infectivity of immobilized phages on COOH-, NH_2-, and CH_3-functionalized, and untreated ITO surfaces. All the studied surfaces had a similar number of detaching phages (10^6 PFUs/mL), and they concluded that these phages produced the antibacterial effect measured. Our results suggest that the number of released phages varies between different surface treatments, and also with the number of detachment steps done.

3.3. Effective Infectivity. Infectivity of the immobilized phage was studied by measuring the optical density of the host bacteria when exposed to the phage-treated material.

An example of results for the antibacterial effect of phage-immobilized surfaces is presented in Figure 5a. First of all, the phage-treated surfaces were able to significantly reduce the growth of the bacteria compared to the reference (no added

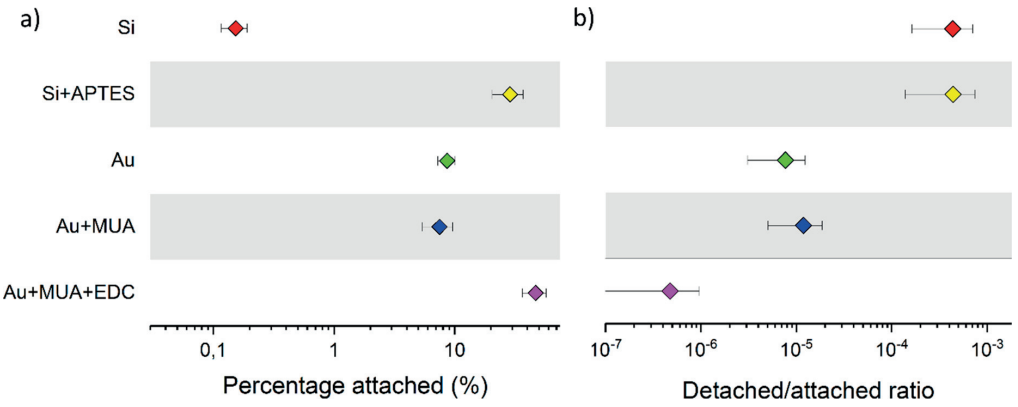

Figure 4. Phage attachment and detachment. (a) Percentage of attached phages of the initial phage stock (1.5×10^8 PFU). (b) The number of detached phages from detachment step 12 divided by the attached phages after 12 + 4 rounds. Errors were calculated by adding the relative uncertainties in quadrature. Mean ± SEM ($n = 3$).

DOI: 10.1021/acsabm.9b00242
ACS Appl. Bio Mater. XXXX, XXX, XXX−XXX

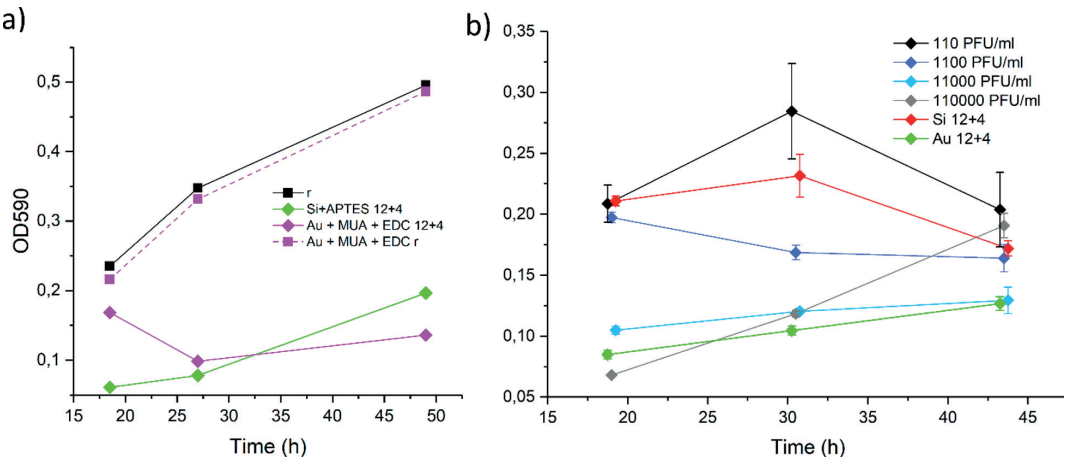

Figure 5. Effect of phage-treated surfaces and free phage on *Flavobacterium sp.* growth curves. (a) Bacterial growth is reduced by the phage-treated surfaces (Si+APTES, Au+MUA+EDC) but not with the phage-free surface (dashed line) or when no phage or surface is added (r, black line). (b) Bacterial growth is reduced by both the phage-treated surfaces and added phage. Phage concentration 110 000 PFUs/mL equals MOI 0.04 (with bacterial concentration of 2.5×10^6 CFU/mL). Mean ± SEM (n = 3).

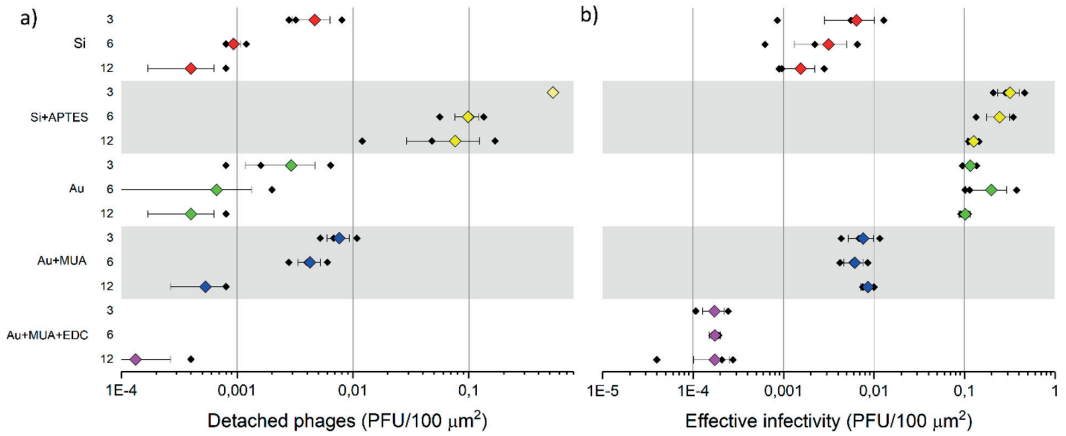

Figure 6. Phage detachment and effective infectivity of different surfaces with immobilized phage. Samples were dip-washed 6 times before detachments. The number after the name of the material indicates the number of detachment steps after dip washing. (a) The number of infective phages in the detachment buffer per sample surface area. (b) Average values of effective infectivity (defined in the text) of the phage-treated materials per surface area. All 12-detachment step samples were washed an additional four times before infectivity tests. Colored symbols: mean ± SEM (n = 3). Black symbols: individual replicates.

phage), as expected. For the Si+APTES 12 + 4 sample, the bacterial growth reduction occurred already at the first time point (19 h), or even before, demonstrating high antibacterial efficiency. For the Au+MUA+EDC surface, the maximum in the growth reduction occurred at 27 h. In a longer time scale, the turbidity of the culture increased again even with the phage-treated surfaces, as a result of the growth of phage-resistant bacteria.[36]

Often, the efficiency of the phage-treated surfaces has been studied by comparing the growth of phage-exposed bacteria to the growth of untreated bacteria to calculate the reduction in the (logarithmic) colony-forming unit (CFU). Another measure is the equivalent multiplicity of infection for the materials, which makes comparisons between different materials easier. There, the growth reduction caused by the immobilized phage is compared to different (known) MOIs of the free phage, and efficiency is presented as equivalent MOI.[17] However, here, we have developed the approach further and present infectivity as "effective infectivity" (PFU) per surface area. The benefit of this approach, compared to the equivalent MOI,[17] is that information on bacterial numbers is not required. In this study, effective infectivity is computed by linear interpolation between the closest measured free phage reference treatment optical densities OD_1 and OD_2 corresponding to PFUs P_1 and P_2, giving an Effective PFU for a measured optical density OD_{sample} of a phage-treated material:

$$\text{effective PFU} = P_1 + \frac{P_1 - P_2}{OD_2 - OD_1} \times (OD_1 - OD_{sample}) \quad (1)$$

Figure 5b demonstrates the experiments where the optical density of the Si and Au 12 + 4 surfaces is compared to the

DOI: 10.1021/acsabm.9b00242
ACS Appl. Bio Mater. XXXX, XXX, XXX−XXX

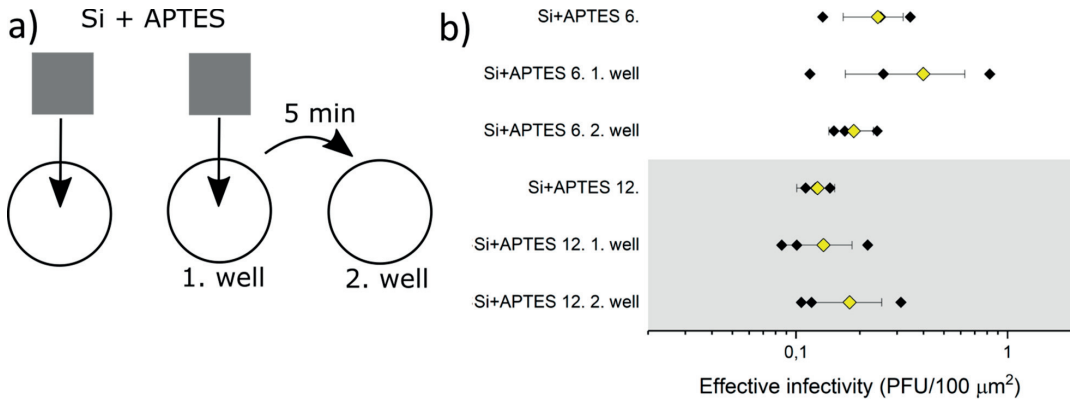

Figure 7. A well-change experiment was used to resolve the effect of the detached phages. (a) The sample substrate was transferred to another sample well after 5 min incubation. (b) The effect of the well change on the effective infectivity for the 6 and 12 times detached Si + APTES sample. Colored symbols: mean ± SEM (n = 3). Black symbols: individual replicates.

optical densities produced by known numbers of free phages. For example, for the silicon sample, the optical density of the sample falls between the values of 110 and 1100 PFUs/mL of added free phage at second and third time points, so those are the data points used in the interpolation. The first time point was left out from the calculation because it does not fall between any free phage data points. Similar calculations were conducted for every sample, interpolating the efficiency separately for all time points, which thus produced several measurement points for mean effective infectivity over time. Three individual replicates were done for all of the samples, and the standard error of the mean (SEM) was calculated. The fractional error of the free phage titer was 23% (phage stock titer (6.2 ± 1.4) × 10^9 PFUs/mL), and it was added in quadrature. When using this approach for other phage−bacterium systems, it should be noted that the bacterial growth dynamics with phage differ between strains and species, and the Flavobacterium strain used here responds relatively slowly compared to, e.g., *E. coli*, which may require shorter incubation times. In addition, it is important to have a free phage reference infection in the same conditions (simultaneously), to rule out the effects of culture conditions and, e.g., the growth phase of the bacteria. The accuracy of the effective PFU can be increased by using more free phage references, for example, 100, 200, 500, and 1000 PFUs/mL instead of 100 and 1000 PFUs/mL.

When comparing the infectivity and the number of detached phages, common trends but also differences can be found (Figure 6). APTES with a high number of detached phages had high infectivity, but gold with a low number of detached phages also had high infectivity. APTES infectivity shows a trend of decrease with the detachment steps (3−12), but the change was not statistically significant (p > 0.05). After all of the 12 + 4 detachment steps, APTES had the highest infectivity, 26% higher than gold (P < 0.05) and 160-fold compared to untreated silicon. The MUA-treated gold surface had about ten times lower infectivity than untreated gold. EDC-treated MUA has the lowest infectivity, about ten times lower than silicon.

Previously, Liana et al.[19] reported that all surfaces (carboxyl, amine, neutral) produced an equal antibacterial effect by the released phages. According to our results, the infectivity and the number of released phages vary between the surface treatments. Tawil et al.[18] found that covalent immobilization with MUA+EDC resulted in 10-fold growth reduction compared to plain gold. Their result is contradictory to our results which show over 100-fold infectivity of the plain Au compared to the MUA+EDC-treated case.

According to our results, the number of washes or detachment treatments does not have a significant effect on the infectivity of the surfaces. However, the number of detached phages varies between the detachment treatments. Long-lasting infectivity is a desirable feature of the material for prolonged use in an aquatic environment. Within this study, the Si+APTES or gold surface is most suitable from that point of view.

While the actual antibacterial effect is caused by the phage replication, one of the main questions in using surfaces with immobilized phages is whether the initial effect is caused on the surface by the attached phages or in the solution by the detached phages. To separate the effects, we performed an experiment, where a Si + APTES surface was transferred from one well to another before the addition of bacteria. The sample was placed in 1 mL of Shieh medium, shaken 400 rpm 5 s, incubated 5 min, and moved to another well (Figure 7a). We expect that if the antibacterial effect is caused by the detaching phages, we should see bacterial growth reduction in both of the wells. On the other hand, if the effect is caused by the attached phages, the antibacterial effect should be seen only in the second well, where the surface is present. We observed that infections occurred similarly in both wells (Figure 7b), suggesting that the antibacterial effect is mainly caused by detached phages for this surface.

As a final conclusion, the numbers of attached, detached, and effectively infecting phages of all five materials are presented in Figure 8, after the full set of detachment and washing steps. Silicon and gold had an equal number of detaching phages, but the number of attached and effective PFUs was a 100-fold on gold vs silicon. This suggests that phages were attaching on the gold surface in such a way that they retained their infectivity. In the literature, when T4 phages were immobilized on the gold surface by physisorption, the attachment and the lysis of the bacteria on the surface were detected,[37,38] proving that infection on the surface is possible. However, it is worth to keep in mind that in real-life scenarios like in aquaculture it is possible that infectivity is reduced by

DOI: 10.1021/acsabm.9b00242
ACS Appl. Bio Mater. XXXX, XXX, XXX−XXX

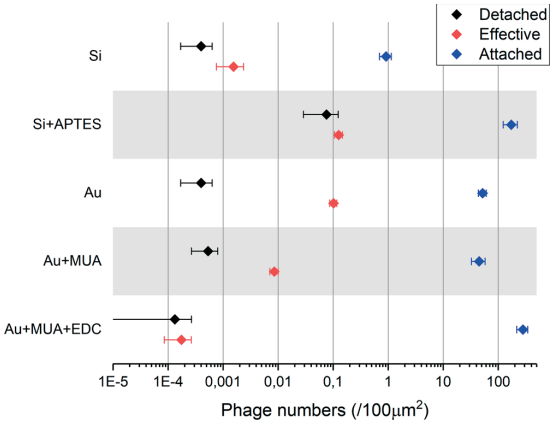

Figure 8. All three PFUs (attached, detached, effective infecting) for the 12 or 12 + 4 detached substrates. Mean ± SEM (n = 3).

the presence of substances such as other organic material on the surface.

In contrast, APTES-treated silicon had the highest infectivity and also the highest number of detaching phages. Additionally, it was confirmed by the well-change experiment that detaching phages produced the effect. The EDC cross-linked surface had the highest number of attached phages, but the infectivity was lowest. The high number of attached phages did not result in high infectivity. It is possible that the infectivity was lost upon the chemical interaction with the EDC-treated surface, or by the imperfect orientation of the phage. Unfortunately, it was not possible to resolve the orientation of the immobilized phages with the imaging methods used. In the literature, inequality between the infectivity and the number of covalently bound phages has been found before, with a suggestion that some phages are inactive or misoriented.[17]

CONCLUSIONS

We studied the attachment density, detachment rate, and infectivity of *Flavobacterium*-infecting FL-1 bacteriophage on different surfaces: silicon, amine-treated silicon, gold, carboxylate-treated gold, and cross-linker-activated carboxylate-treated gold. It was found that detached phages could produce a significant antibacterial effect, especially on the amine-treated silicon. Therefore, when studying phage immobilization, one must be careful with what is causing the measured effect. Covalent cross-linking between the phages and surface, on the other hand, produced the highest numbers of attached phages but seemed to interfere with infectivity. Therefore, we suggest that the controlled release of antibacterial phage, i.e., the phage reservoir approach, might be preferable for practical applications. In the future, the development of imaging methods capable of resolving the orientation of the immobilized phage could make a tremendous contribution to this field. We also introduced a novel, standardizable, way to quantify the antibacterial effects of surfaces, by comparing the antibacterial effect of the material surface to the effect caused by a known number of free phages. This effective PFU/surface area will make results from different studies comparable.

ASSOCIATED CONTENT

Supporting Information

The Supporting Information is available free of charge on the ACS Publications website at DOI: 10.1021/acsabm.9b00242.

Purification data, data for density, and growth curves (PDF)

AUTHOR INFORMATION

Corresponding Author

*E-mail: lotta-riina.sundberg@jyu.fi.

ORCID

Ilari J. Maasilta: 0000-0001-8566-1569

Lotta-Riina Sundberg: 0000-0003-3510-4398

Author Contributions

The experiments were conceived by all authors and performed by M.L. The manuscript was written through the contributions of all authors. All authors have given approval to the final version of the manuscript.

Notes

The authors declare no competing financial interest.

ACKNOWLEDGMENTS

The authors would like to thank Dr. Elina Laanto for providing the bacterial and phage isolate used in this study. L.-R.S. acknowledges funding from the Academy of Finland (266879 and 314939) and from the Jane and Aatos Erkko Foundation.

REFERENCES

(1) Roach, D. R.; Debarbieux, L. Phage Therapy: Awakening a Sleeping Giant. *Emerg. Top. Life Sci.* **2017**, *1* (1), 93−103.

(2) Costa-Pierce, B. A. Sustainable Ecological Aquaculture Systems: The Need for a New Social Contract for Aquaculture Development. *Mar. Technol. Soc. J.* **2010**, *44* (3), 88−112.

(3) Bustos, P.; Young, N. D.; Rozas, M. A.; Bohle, H. M.; Nowak, B. F. Amoebic Gill Disease (AGD) in Atlantic Salmon (Salmo Salar) Farmed in Chile. *Aquaculture* **2011**, *310*, 281−288.

(4) Burridge, L.; Weis, J. S.; Cabello, F.; Pizarro, J.; Bostick, K. Chemical Use in Salmon Aquaculture: A Review of Current Practices and Possible Environmental Effects. *Aquaculture* **2010**, *306* (1), 7−23.

(5) Tamminen, M.; Karkman, A.; Lõhmus, A.; Muziasari, W. I.; Takasu, H.; Wada, S.; Suzuki, S.; Virta, M. Tetracycline Resistance Genes Persist at Aquaculture Farms in the Absence of Selection Pressure. *Environ. Sci. Technol.* **2011**, *45* (2), 386−391.

(6) Declercq, A. M.; Haesebrouck, F.; Van den Broeck, W.; Bossier, P.; Decostere, A. Columnaris Disease in Fish: A Review with Emphasis on Bacterium-Host Interactions. *Vet. Res.* **2013**, *44*, 27.

(7) Laanto, E.; Bamford, J. K. H.; Ravantti, J. J.; Sundberg, L.-R. The Use of Phage FCL-2 as an Alternative to Chemotherapy against Columnaris Disease in Aquaculture. *Front. Microbiol.* **2015**, *6*, 829.

(8) Lone, A.; Anany, H.; Hakeem, M.; Aguis, L.; Avdjian, A.-C.; Bouget, M.; Atashi, A.; Brovko, L.; Rochefort, D.; Griffiths, M. W. Development of Prototypes of Bioactive Packaging Materials Based on Immobilized Bacteriophages for Control of Growth of Bacterial Pathogens in Foods. *Int. J. Food Microbiol.* **2016**, *217*, 49−58.

(9) Anany, H.; Chen, W.; Pelton, R.; Griffiths, M. W. Biocontrol of Listeria Monocytogenes and Escherichia Coli O157:H7 in Meat by Using Phages Immobilized on Modified Cellulose Membranes. *Appl. Environ. Microbiol.* **2011**, *77* (18), 6379−6387.

(10) Curtin, J. J.; Donlan, R. M. Using Bacteriophages to Reduce Formation of Catheter-Associated Biofilms by Staphylococcus Epidermidis. *Antimicrob. Agents Chemother.* **2006**, *50* (4), 1268−1275.

(11) Nogueira, F.; Karumidze, N.; Kusradze, I.; Goderdzishvili, M.; Teixeira, P.; Gouveia, I. C. Immobilization of Bacteriophage in

Wound-Dressing Nanostructure. *Nanomedicine* **2017**, *13* (8), 2475−2484.
(12) Handa, H.; Gurczynski, S.; Jackson, M. P.; Auner, G.; Mao, G. Recognition of Salmonella Typhimurium by Immobilized Phage P22 Monolayers. *Surf. Sci.* **2008**, *602* (7), 1392−1400.
(13) Shabani, A.; Zourob, M.; Allain, B.; Marquette, C. A.; Lawrence, M. F.; Mandeville, R. Bacteriophage-Modified Microarrays for the Direct Impedimetric Detection of Bacteria. *Anal. Chem.* **2008**, *80* (24), 9475−9482.
(14) Shabani, A.; Marquette, C. A.; Mandeville, R.; Lawrence, M. F. Magnetically-Assisted Impedimetric Detection of Bacteria Using Phage-Modified Carbon Microarrays. *Talanta* **2013**, *116*, 1047−1053.
(15) Naidoo, R.; Singh, A.; Arya, S. K.; Beadle, B.; Glass, N.; Tanha, J.; Szymanski, C. M.; Evoy, S. Surface-Immobilization of Chromatographically Purified Bacteriophages for the Optimized Capture of Bacteria. *Bacteriophage* **2012**, *2* (1), 15−24.
(16) Hosseinidoust, Z.; Van de Ven, T. G. M.; Tufenkji, N. Bacterial Capture Efficiency and Antimicrobial Activity of Phage-Functionalized Model Surfaces. *Langmuir* **2011**, *27* (9), 5472−5480.
(17) Wang, C.; Sauvageau, D.; Elias, A. Immobilization of Active Bacteriophages on Polyhydroxyalkanoate Surfaces. *ACS Appl. Mater. Interfaces* **2016**, *8* (2), 1128−1138.
(18) Tawil, N.; Sacher, E.; Mandeville, R.; Meunier, M. Strategies for the Immobilization of Bacteriophages on Gold Surfaces Monitored by Surface Plasmon Resonance and Surface Morphology. *J. Phys. Chem. C* **2013**, *117* (13), 6686−6691.
(19) Liana, A. E.; Marquis, C. P.; Gunawan, C.; Justin Gooding, J.; Amal, R. Antimicrobial Activity of T4 Bacteriophage Conjugated Indium Tin Oxide Surfaces. *J. Colloid Interface Sci.* **2018**, *514*, 227−233.
(20) Liana, A. E.; Chia, E. W.; Marquis, C. P.; Gunawan, C.; Gooding, J. J.; Amal, R. Adsorption of T4 Bacteriophages on Planar Indium Tin Oxide Surface via Controlled Surface Tailoring. *J. Colloid Interface Sci.* **2016**, *468*, 192−199.
(21) Armanious, A.; Aeppli, M.; Jacak, R.; Refardt, D.; Sigstam, T.; Kohn, T.; Sander, M. Viruses at Solid-Water Interfaces: A Systematic Assessment of Interactions Driving Adsorption. *Environ. Sci. Technol.* **2016**, *50*, 732.
(22) Laanto, E.; Sundberg, L.-R.; Bamford, J. K. H. Phage Specificity of the Freshwater Fish Pathogen Flavobacterium Columnare. *Appl. Environ. Microbiol.* **2011**, *77* (21), 7868−7872.
(23) Shieh, H. S. Studies on the Nutrition of a Fish Pathogen, Flexibacter Columnaris. *Microbios Letters* **1980**, *13* (51/52), 129−133.
(24) Morita, M.; Ohmi, T.; Hasegawa, E.; Kawakami, M.; Ohwada, M. Growth of Native Oxide on a Silicon Surface. *J. Appl. Phys.* **1990**, *68* (3), 1272−1281.
(25) Parks, G. A. The Isoelectric Points of Solid Oxides, Solid Hydroxides, and Aqueous Hydroxo Complex Systems. *Chem. Rev.* **1965**, *65* (2), 177−198.
(26) Michen, B.; Graule, T. Isoelectric Points of Viruses. *J. Appl. Microbiol.* **2010**, *109* (2), 388−397.
(27) Giesbers, M.; Kleijn, J. M.; Cohen Stuart, M. A. The Electrical Double Layer on Gold Probed by Electrokinetic and Surface Force Measurements. *J. Colloid Interface Sci.* **2002**, *248* (1), 88−95.
(28) Abdelsalam, M. E.; Bartlett, P. N.; Kelf, T.; Baumberg, J. Wetting of Regularly Structured Gold Surfaces. *Langmuir* **2005**, *21* (5), 1753−1757.
(29) Guntupalli, R.; Sorokulova, I.; Olsen, E.; Globa, L.; Pustovyy, O.; Moore, T.; Chin, B.; Barbaree, J.; Vodyanoy, V. Detection and Identification of Methicillin Resistant and Sensitive Strains of Staphylococcus Aureus Using Tandem Measurements. *J. Microbiol. Methods* **2012**, *90* (3), 182−191.
(30) Singh, A.; Glass, N.; Tolba, M.; Brovko, L.; Griffiths, M.; Evoy, S. Immobilization of Bacteriophages on Gold Surfaces for the Specific Capture of Pathogens. *Biosens. Bioelectron.* **2009**, *24* (12), 3645−3651.
(31) Singh, A.; Arya, S. K.; Glass, N.; Hanifi-Moghaddam, P.; Naidoo, R.; Szymanski, C. M.; Tanha, J.; Evoy, S. Bacteriophage Tailspike Proteins as Molecular Probes for Sensitive and Selective Bacterial Detection. *Biosens. Bioelectron.* **2010**, *26* (1), 131−138.
(32) Cademartiri, R.; Anany, H.; Gross, I.; Bhayani, R.; Griffiths, M.; Brook, M. A. Immobilization of Bacteriophages on Modified Silica Particles. *Biomaterials* **2010**, *31* (7), 1904−1910.
(33) Zerda, K. S.; Gerba, C. P.; Hou, K. C.; Goyal, S. M. Adsorption of Viruses to Charge-Modified Silica. *Appl. Environ. Microbiol.* **1985**, *49* (1), 91−95.
(34) Bone, S.; Alum, A.; Markovski, J.; Hristovski, K.; Bar-Zeev, E.; Kaufman, Y.; Abbaszadegan, M.; Perreault, F. Physisorption and Chemisorption of T4 Bacteriophages on Amino Functionalized Silica Particles. *J. Colloid Interface Sci.* **2018**, *532*, 68−76.
(35) Vonasek, E.; Lu, P.; Hsieh, Y.-L.; Nitin, N. Bacteriophages Immobilized on Electrospun Cellulose Microfibers by Non-Specific Adsorption, Protein-ligand Binding, and Electrostatic Interactions. *Cellulose* **2017**, *24* (10), 4581−4589.
(36) Luria, S. E.; Delbrück, M. Mutations of Bacteria from Virus Sensitivity to Virus Resistance. *Genetics* **1943**, *28* (6), 491−511.
(37) Mejri, M. B.; Baccar, H.; Baldrich, E.; Del Campo, F. J.; Helali, S.; Ktari, T.; Simonian, A.; Aouni, M.; Abdelghani, A. Impedance Biosensing Using Phages for Bacteria Detection: Generation of Dual Signals as the Clue for in-Chip Assay Confirmation. *Biosens. Bioelectron.* **2010**, *26* (4), 1261−1267.
(38) Balasubramanian, S.; Sorokulova, I. B.; Vodyanoy, V. J.; Simonian, A. L. Lytic Phage as a Specific and Selective Probe for Detection of Staphylococcus aureus—A Surface Plasmon Resonance Spectroscopic Study. *Biosens. Bioelectron.* **2007**, *22* (6), 948−955.

DOI: 10.1021/acsabm.9b00242
ACS Appl. Bio Mater. XXXX, XXX, XXX−XXX

II

IMAGING BACTERIAL COLONIES AND PHAGE–BACTERIUM INTERACTION AT SUB-NANOMETER RESOLUTION USING HELIUM-ION MICROSCOPY

by

Leppänen, M., Sundberg, L., Laanto, E., de Freitas Almeida, Gabriel Magno, Papponen, P., & Maasilta, I. J. 2017.

Advanced Biosystems, 1(8), 1700070

Imaging Bacterial Colonies and Phage-bacterium Interaction at Sub-nanometer Resolution Using Helium Ion Microscopy

*Miika Leppänen, Lotta-Riina Sundberg, Elina Laanto, Gabriel Magno de Freitas Almeida, Petri Papponen and Ilari J. Maasilta**

M. Leppänen, Prof. I. J. Maasilta
Nanoscience Center, Department of Physics, University of Jyvaskyla, P. O. Box 35, FI-40014 Jyväskylä, Finland
E-mail: ilari.j.maasilta@jyu.fi

M. Leppänen, Dr. L.-R. Sundberg, Dr. E. Laanto, Dr. G.M.F. Almeida, P. Papponen
Nanoscience Center, Center of Excellence in Biological Interactions, Department of Biological and Environmental Science, University of Jyvaskyla, FI-40014 Jyväskylä, Finland

Imaging of microbial interactions has so far been based on well-established electron microscopy methods. Here we present a new way to study bacterial colonies and interactions between bacteria and their viruses, bacteriophages (phages), in-situ on agar plates using helium ion microscopy (HIM). In biological imaging, HIM has advantages over traditional scanning electron microscopy with its sub-nanometer resolution, increased surface sensitivity, and the possibility to image non-conductive samples. Furthermore, by controlling the He beam dose or by using heavier Ne ions, the HIM instrument provides the possibility to mill out material in the samples, allowing for sub-surface imaging and in-situ sectioning. Here, we present the first HIM-images of bacterial colonies and phage-bacterium interactions at different stages of the infection as they occur on an agar culture. We also demonstrate the feasibility of neon and helium milling to reveal the sub-surface structures of bacterial colonies on agar substrate, and in some cases also structure inside individual bacteria after cross-sectioning. We conclude that helium ion microscopy offers great opportunities to advance the studies of microbial imaging, in particular in the area of interaction of viruses with cells.

1. Introduction

Helium ion microscope (HIM) is a recently developed scanning microscopy tool, which utilizes a positively charged He+ or Ne+ ion beam for imaging and nanopatterning.[1-3] It resembles scanning electron microscopy (SEM) in the sense that the raster scanned beam excites secondary electrons from the surface region of the specimen, and these electrons, whose emission is sensitive to surface topography, form the image. Compared to the best modern SEMs, the probe size can be up to five times smaller down to a diameter ~0.3 nm, and the probe-sample surface interaction volume is also much reduced due to the much heavier mass of the ions.[2] Both of these factors result in a higher imaging resolution, ultimately limited by the probe size. In addition, the depth of focus is about five times larger, as well.[2] Even more importantly for biological imaging, a conductive coating isn't required at all in HIM so that fragile sub-nanometer structures in a native state can be imaged with HIM without masking or artefacts due to the coating.[4]

So far, nanoscale features have been imaged with HIM mostly in mammalian cells, such as human colon cancer cells,[5] human liver cells,[6] rabbit cartilage collagen networks,[7] HeLa cells,[4] rat kidney,[8] rat and mouse epidermis,[9] and human neural stem cells, neurons and mouse neurons.[10] Many of these studies have shown that uncoated samples reveal more ultrastructures than coated samples. Outside of the mammalia, HIM has been used to image scales of lepidoptera (butterfly) wings[11] and cuticle structures in Drosophila.[12] The study by Joens *et al*[4] included also examples of imaging of a plant (*Arabidopsis thaliana*), a nematode (*Pristionchus pacificus*), and nitrate reducing *Acidovorax sp*. bacteria. Apart from that lone study, HIM microscopy of microbes has not been pursued before this work, where our aim was to explore the nanoscale imaging capacity of HIM for microbiological samples; for bacteria and their viruses.

Bacteriophages (phages), the viruses infecting bacteria, can cause lethal infections in their bacterial hosts, thus participating in global biogeochemical processes that involve bacteria.[13, 14] Phage infection occurs when a phage binds to specific structures on the surface of its host bacterium (outer membrane proteins, lipopolysaccharides, pili or flagella etc.) and injects its genome. In tailed phages[15], the binding in the host is mediated by the tail fibers of the phage. After binding, the phage injects its genome inside the bacterial cell in a syringe-like manner, which results in conformational changes and shortening of the phage tail in phages of the family *Myoviridae*.[16] During the lytic cycle, new phage particles are then produced inside the infected cell, and eventually released into the surroundings upon eruption and death of the host.

While these general steps in the life cycle of the phage are relatively well known, the imaging of bacterial cells and their phages has remained challenging and has been restricted by the resolution limits and complexity of commonly used microscopy techniques. Scanning electron microscopy (SEM) has provided details on bacterial surface structures and phage-bacterium interactions[17], but it requires that the sample is coated with a metal (e.g. gold, platinum), which typically leads to the loss of resolution and artefacts in the smallest scale ultrastructures. Transmission electron microscopy (TEM) methods are currently the most widely used methods to study bacteria-phage interaction at high resolution. There, requirements for the sample preparation limit the feasibility of TEM for studying interaction in natural microbial communities. Recently, atomic force microscopy (AFM) has also been applied to image phage-bacterium interactions.[18,19]

In addition to imaging, by increasing the He dose or by changing to the heavier Ne ions, HIM can also be used to modify the sample by “milling” off material from a wanted area. Most milling applications have so far been in materials science applications[2, 3] with very little

biological work. The only example of HIM milling of a biological sample we are aware of is that of Joens *et al.*,[4] where a membranous sheath of the mouth of a nematode was cut out using Ne to reveal structures inside it. On the other hand, ion beam milling in combination with biological cellular imaging is already widely used using the more mature FIB-SEM dual beam instruments, where a Ga ion beam is used for milling to expose new cross-sectional surfaces to be imaged by a standard SEM column.[20] Compared to HIM, this technique suffers from an order of magnitude lower milling resolution due to the larger sample-beam interaction volume, in addition to the degraded SEM imaging capabilities and sensitivities to charging artefacts. Moreover, delicate biological samples are typically encased in a protective resin for FIB-SEM 3D-imaging.

In this work, we present the first HIM images of bacteria-phage interactions at various stages of the infection, at sub-nm imaging resolution. We also investigate the possibilities to mill and image microbial samples with HIM, without any protective resins or coatings, made possible because of the more gentle nature of the HIM milling. Subsurface *E. coli* microcolonies inside an agar plate were imaged after milling a view-through hole. In addition, individual bacterial cross-sections were performed.

2. Results and discussion

2.1. HIM imaging of phage-bacterium interaction

The sample containing viral plaques formed by the phage T4 on the *E. coli* bacterial lawn on agar was first investigated with an optical microscope to map out areas for HIM-studies, with one ~700 μm diameter plaque shown in **Figure 1** both optically (Figure 1a) and with the HIM (Figure 1b). The diffuse plaque borders seen in the optical image are also visible in the HIM image as changing morphology (Figure 1b). To visualize various stages of the T4 infection,

we explored different regions of the plaque. These regions represent different temporal phases of the infection, because the center of the plaque is the origin of the infection, from which the phage multiplication spreads out radially.

Close ups of region 1 are shown in **Figure 2**, first in an area ~17 μm x 17 μm (Figure 2a), with a further zoom-in of a 2.6 μm x 2.6 μm region (Figure 2b). This kind of zooming into the nanoscale is quite easy with the HIM during an imaging session, facilitating the searching of most interesting regions from a large area samples. From Figure 2a we see that the central region of the plaque is almost free from bacteria, as the infection has already killed most of the bacteria and spread out. In the higher, nanoscale resolution image, Figure 2b, some phages can be seen lying on the agar surface.

By proceeding outwards along the direction of the spread of the infection to region 2 in Figure 1b, which is closer to the edge of the plaque, we find active infections, as shown in more detail in **Figure 3**. Figure 3a shows a ~ 13 μm x 13 μm image of several micron-scale *E. coli* bacteria, with all of them having phages attached on their surfaces. No bacteria have managed to avoid the infection. The zoomed-in image of Figure 3b (area 1.5 μm x 1.5 μm) shows three infected bacteria with multiple phages on each of them. With this magnification, the tailed morphology of the phage is clearly visible. Even more notably, we can compare within this same image the tails of phages that either are or are not attached to the bacteria. The length of the tail of the non-attached phages can be as long as ~100 nm, whereas some of the phages connected to the bacterial cell wall show much more contracted tails, indicating genome injection in progress.

Finally, at the edge of the plaque there are numerous bacterial cells, as they are in a stationary growth phase as a colony (**Figure 4**). Phage infection is much rarer, however, some ongoing

infections are still visible. There is also an exceptionally long *E. coli* cell shown in Figure 4, which are only recently described.[21]

To further highlight the abilities of HIM imaging of bacteriophages and their interactions with bacterial cells, we discuss additional details observed from the images. As already pointed out, different stages of infection were seen at different locations. An example of a high resolution image of a T4 phage anchored on the cell surface at an early stage is shown in **Figure 5**a. In this image, as in others, the icosahedral shape of the head capsid of the phage is clearly visible. In the active infection stage shown in high resolution in Figure 5b, the tails of the phages are clearly contracted down to lengths ~ 25 nm. Additional details can also be seen. For example, the image shows a widening of the end of the tail due to the baseplate structure, and even the tail fibers attached on the bacterial cell surface are visible, with fiber diameters in the range of a few nm. In Figure 5c, on the other hand, we likely see an example of the last stage of the infection, where new phage particles have burst out from a bacterium.

In all the images discussed above, the dried agar gel matrix structure in the background could be imaged with fiber widths down to the nanometer scale. In its important to point out that the smallest scale fragile structures such as the thinnest agar fibers and the thinnest phage tail fibers could not be resolved anymore if a thin gold metal coating was used on the samples (as is typically necessary with SEM). In addition, we sometimes observed broken agar fibers in the gold coated samples (not shown), whereas in the non-coated, directly HIM imaged samples broken fibers were never seen.

2.2. HIM-imaging of interactions between bacterial cells

As an additional example of the power of biological HIM imaging, we also show examples of visualizing interactions between bacterial cells of another bacterial species, the fish pathogen *Flavobacterium columnare*, on an agar plate culture. Images of a *F. columnare* B185 colony growing on an agar plate are shown in **Figure 6**. In addition to the bacterial cells, a lot of extracellular material such as round vesicles and nanoscale fibers between bacteria are found in the colony. Figure 6a also demonstrates the high depth of view available in a helium ion microscope, as the image is sharp everywhere even though the sample stage was tilted 45º (top and bottom of the image at different distances from the objective). In this particular case the depth of view was thus over 16 µm. In the higher resolution image, Figure 6b, we focused on the edge of the colony, where the interaction between the bacterial cells and the agar substrate network can clearly be seen. Extracellular, straight, thin fibers of nanometer scale are seen to emanate from the bacterial cell bodies, which the bacteria seem to utilize to attach to the underlying agar surface. Similar fibers also connect from bacteria to other bacteria, better seen in Figure 6a. In addition, small nanoscale membrane vesicles[22] are visible in several bacteria. Again, a metal coating of the samples can be very detrimental, possibly destructive to these smallest structures.

2.3. Helium milling

By increasing the He ion current, the He ions can start milling out softer materials. This possibility was tested on agar substrate samples, by drawing shapes with the pattern generator of our HIM setup. Initial tests using a current of 3 pA led to massive rupturing and cracks hundreds of micrometers long on the agar substrate, possibly because of local charge buildup issues. This problem was remedied by performing the milling with the floodgun on in the linescan mode. With a milling current 3 pA and a 3 minute exposure time, a square shaped

hole of size 100 nm x 100 nm was formed in the agar (**Figure 7**a) without any rupturing problems.

Helium milling was done also on the *E. coli* bacterial culture containing the T4 phage, with the idea of making a cross-sectional cut of a bacterial cell. During the milling, a current of 10 pA and a dwell time of 10 µs were used, with the flood gun on. In this case, the sample stage was tilted by 45 degrees, and the milling was performed layer-by-layer by moving a reduced-raster line scan view to the desired position. This way, monitoring of the milling process in real time is possible, and charge compensation prevents unwanted disruptions. The total milling time in this test was about 5 minutes. After milling the sample, the stage was rotated by 180º and the sectioned surface was imaged. An example of a cross-sectioned bacterium with a half-cut phage particle on it is shown in Figure 7b. The cross-sectional surface of the bacterium is smooth with no internal details. On can also see modified ("melted") phage particles in the right-bottom corner where the beam has hit.

Helium milling was done also to a *Flavobacterium sp.* B183 lying on a silicon substrate. Single lines were drawn by the pattern generator cross-sectionally over the bacterial body, the exposure was done with a dose 2 nC/µm^2, a current 1.272 pA and a total exposure time of 55 s. Flood gun use was not necessary because the charging effect is much weaker on a silicon substrate. After the exposure, sharp and narrow cut-out sections are found (**Figure 8**a). To remove the separated "head" section of the cell seen in Figure 8a, a pattern was drawn over it with a dose 3 nC/ µm^2 and the same current 1.272 pA, resulting in total exposure time of 186 s. After this second exposure, the "head" part disappeared, and interestingly, some inner structural details of the bacterium became visible on the remaining cut out surface (Figure 8b). Note also how the Si substrate under the area of milling is protruding. This bubble formation

is a common result seen with HIM on silicon substrates[2], and results from helium having been trapped inside the silicon lattice.

2.4. Neon milling

Neon milling was tried on the sample containing *E.coli* and T4-phage on an agar substrate. With the heavier Ne ions, milling is faster and thus larger areas can be milled, with a trade-off of decreased resolution. A slot with a size 13x5 micrometers was milled with a 35 pA Ne beam in 45 minutes from a 45º angle. It was imaged from a 90º angle (looking straight down) with Ne as the imaging ion, as well, see **Figure 9**a. Bacterial colony is clearly seen to grow inside of the agar matrix. In this figure, the black regions represent areas, from where no secondary electrons can reach the detector because of shading. For that reason, the slot was imaged also by tilting the sample 45 degrees and by rotating by 90 degrees, see Figure 9b, providing a better view of the trench. With the help of the milling, we can therefore conclude that we can image portions of the colony under the agar surface, as well.

3. Conclusion

We have demonstrated that helium ion microscopy is a powerful tool to study bacterial colonies and bacteria-phage interactions on a natural agar growth substrate. This is the first time that such a high resolution imaging of an infecting virus attached to the host cell is imaged, at different stages of the infection, as it happens on an agar plate. The main advantages of HIM imaging over the related standard scanning electron microscopy technique are the higher depth of view, the lack of the need of metal coating and improved resolution. In addition, by increasing the current or by switching from He to Ne ions, samples can be milled in situ to expose sub-surface features, or milling can be used for cross-sectioning single cells

or even single virus particles. More understanding is still required on how to best perform the cross-sectional milling, as we saw in this work that sometimes image contrast on the cross sectional surface was lost. Tentative reasons for this could be redeposition of the milled out material or modification due to heating. What is promising about HIM milling is that the milling can be done in a point-and-shoot mode, at sub-nanometer resolution, without the typical and restricting resin embedding techniques often used with focused gallium ion beam milling (FIB) of biological samples in FIB- instruments.[20]

Naturally, it is possible also to compare HIM to other advanced biological imaging techniques. Higher resolution can be achieved with transmission electron microscopy (TEM), and it has been a standard method for the characterization of novel bacteriophage species for a long time.[23] With the addition of advanced image reconstruction techniques for sets of particles, cryo-electron microscopy methods can used to resolve virus structures down to below 4 Å.[24,25] However, because of the transmission principle, the required thin sectioning cause limitations in many cases, and the focus is typically in single cell and virus level imaging. HIM, in contrast, does not require any sectioning and can be applied directly to complex specimens of bacterial colonies without any image reconstruction methods. Another possibility is to use atomic force microscopy (AFM), which has been applied for imaging of viruses and virus-cell interactions,[18,19,26] but not nearly to the extent of electron microscopy. It can image samples in air or even in a wet environment and provides quantitative height information, but has a limited dynamic range perpendicular to the scanning direction, is not straightforward to implement for soft biological samples, and suffers often from tip contamination. HIM seems to offer a higher resolution, has a much higher depth of view and can image bacterial samples on irregular, non-flat substrates. Compared to TEM and AFM and cryo-EM, HIM is a more straightforward technique to use, providing information at various length scales, on whole colonies of microbes and interactions between the microbes

and the substrate, and interactions between the microbes and their viruses, all together in one image, down to sub-nm resolution.

4. Experimental Section

Bacterial cultures

To study the phage-bacterium interaction we used *Escherichia coli* (DSM613) and its phage T4 (DSM4505) obtained from DSMZ GmbH (Braunschweig, Germany), *Flavobacterium columnare* B185,[27] and *Flavobacterium sp.* B183.[28] The bacteria and the phages were cultured either in a lysogeny broth (LB) medium (*E. coli*) or in a Shieh-medium (*Flavobacterium*). Phage infecting cultures were prepared by first making double agar plates containing *E. coli* (300 microliters of a 4h turbid *E. coli* culture added to 3ml of soft LB agar, mixing, and then pouring on top of a LB agar plate). After that, 10 microliter drops of a dilution series of our T4 stock were added to plates, which were incubated overnight at room temperature until clear plaques on the bacterial lawns could be seen. A plate with individual plaques was selected for imaging. In addition, a silicon chip containing bacteria B183 was prepared by incubating the chip in a liquid culture overnight at room temperature, containing only bacteria.

Sample preparation

Pieces of approximately 5 mm x 5 mm size were cut from the agar plates, glued to glass coverslips with epoxy and left to adhere for 20 minutes. Next, the samples were incubated for 5h in a fixative containing 2 % glutaraldehyde in a 0.1 M sodium cacodylate (NaCac) buffer (pH 7.4). The samples were then washed with a 0.1 M NaCac buffer and incubated with 1% OsO_4 in 0.1 M NaCac for 30 min, after which the washing with 0.1 M NaCac was repeated.

After fixation, the samples were dehydrated in absolute ethanol (99.5%) with a step series (50%, 70%, 95%, 99.5%, 99.5%). The final drying from ethanol was done with a Bal-Tec CPD 030 critical point dryer. The dried samples were attached to metal stubs with the carbon tape for HIM-imaging. A silicon chip containing the *flavobacterium* B183 was prepared in a similar manner, expect that the CPD drying protocol was replaced by a hexamethyldisilazane (HMDS) drying. In that case, after the ethanol series, ethanol was replaced by HMDS via an intermediate 50/50 ethanol-HDMS mixture. The final HDMS solution was let to evaporate overnight.

HIM imaging and milling

Samples ware first investigated with optical microscope (Olympus BX51M) to find out interesting spots for HIM-studies. The helium ion microscope used was the Zeiss Orion Nanofab at the University of Jyväskylä Nanoscience Center cleanroom. For imaging, acceleration voltage of 30 kV and an aperture 10 µm was used. The spot size was varied between 5 and 6 to obtain an ion current in the range 0.3-0.7 pA. As all samples studied were non-conductive, the flood gun charge compensation was used, together with line averaging with 16 or 32 lines and a 0.5 or 1 µs dwell time.

Milling with helium was done by changing the spot size to 2 or 3, to increase the current to 3-9 pA, with milling patterns produced by the ELPHY Multibeam pattern generator (Raith GmbH, Dortmund, Germany) of our HIM setup. In addition, high current neon milling was performed with a 70 µm aperture and spot size 2 to obtain current of 30-40 pA. Neon imaging was performed with a 20 µm aperture and a spot size 7, with current 0.3-0.7 pA.

Acknowledgements

This work was supported by the Finnish Centre of Excellence Program of the Academy of Finland; the CoE in Biological Interactions 2012-2017 (#252411), by Academy of Finland grant #266879, and by Jane and Aatos Erkko Foundation, and by the Academy of Finland FIRI2014 infrastructure programme. We acknowledge technical guidance by K. Arstila.

References

[1] B. W. Ward, J. A. Notte, N. P. Economou, *Journal of Vacuum Science & Technology B.* **2006**, 24, 2871.

[2] R. Hill, J.A. Notte, L. Scipioni in *Chapter 2 - Scanning Helium Ion Microscopy*, Vol. 170 (Ed.: Peter W. Hawkes), Elsevier, **2012**, pp. 65-148.

[3] G. Hlawacek, V. Veligura, R. van Gastel, B. Poelsema, *J.Vac.Sci.Technol.B Nanotechnol.Microelectron.* **2014**, 32, 020801.

[4] M. S. Joens, C. Huynh, J. M. Kasuboski, D. Ferranti, Y. J. Sigal, F. Zeitvogel, M. Obst, C. J. Burkhardt, K. P. Curran, S. H. Chalasani, L. A. Stern, B. Goetze, J. A. J. Fitzpatrick, *Sci.Rep.* **2013**, 3, 3514.

[5] D. Bazou, G. Behan, C. Reid, J. J. Boland, H. Z. Zhang, *J. Microsc.* **2011**, 242, 290.

[6] X. Chen, C. N. B. Udalagama, C. Chen, A. A. Bettiol, D. S. Pickard, T. Venkatesan, F. Watt, *Biophys. J.* **2011**, 101, 1788.

[7] W.S. Vanden Berg-Foels, L. Scipioni, C. Huynh, X. Wen, *J. Microsc.* **2012**, 246, 168.

[8] W. L. Rice, A. Van Hoek N., T. Paunescu G., C. Huynh, B. Goetze, B. Singh, L. Scipioni, L. A. Stern, D. Brown, *PLoS One.* **2013**, 8, e57051.

[9] T. Paunescu G., W. W. C. Shum, C. Huynh, L. Lechner, B. Goetze, D. Brown, S. Breton, *Mol. Hum. Reprod.* **2014**, 20, 929.

[10] M. Schurmann, N. Frese, A. Beyer, P. Heimann, D. Widera, V. Mönkemöller, T. Huser, B. Kaltschmidt, C. Kaltschmidt, A. Gölzhäuser, *Small.* **2015**, 11, 5781.

[11] S. A. Boden, A. Asadollahbaik, H. N. Rutt, D. M. Bagnall, *Scanning.* **2012**, 34, 107.

[12] A. Boseman, K. Nowlin, S. Ashraf, J. Yang, D. Lajeunesse, *Micron.* **2013**, 51, 26.

[13] R. W. Hendrix, *Theor. Popul. Biol.* **2002**, 61, 471.

[14] C. A. Suttle, *Nat.Rev.Microbiol.* **2007**, 5, 801.

[15] H. -. Ackermann, *Res. Microbiol.* **2003**, 154, 245.

[16] P. G. Leiman, M. M. Shneider, *Adv. Exp. Med. Biol.* **2012**, 726, 93.

[17] G. Wendelschafer-Crabb, S. L. Erlandsen, D. H. Walker, *J. Virol.* **1975**, 15, 1498.

[18] E. V. Dubrovin, A. V. Popova, S. V. Kraevskiy, S. G. Ignatov, T. E. Ignatyuk, I. V. Yaminsky, N. V. Volozhantsev, *PLoS One.* **2012**, 7, e47348.

[19] E. V. Dubrovin, A. G. Voloshin, S. V. Kraevsky, T. E. Ignatyuk, S. S. Abramchuk, I. V. Yaminsky, S. G. Ignatov, *Langmuir.* **2008**, 24, 13068.

[20] K. Narayan, S. Subramaniam, *Nat Meth.* **2015**, 12, 1021.

[21] Z. W. El-Hajj, E. B. Newman, *J. Bacteriol.* **2015**, 197, 1507.

[22] E. Laanto, R. K. Penttinen, J. K. H. Bamford, L. Sundberg, *BMC Microbiol.* **2014**, 14, 170.

[23] H. W. Ackermann, *Adv. Virus Res.* **2012**, 82, 1.

[24] N. M. Taylor, N. S. Prokhorov, R. C. Guerrero-Ferreira, M. M. Shneider, C. Browning, K. N. Goldie, H. Stahlberg, P. G. Leiman, *Nature.* **2016**, 533, 346.

[25] K. K. Lee, L. Gui, *PLoS Pathog.* **2016**, 12, e1005625.

[26] Y. G. Kuznetsov, A. McPherson, *Microbiol. Mol. Biol. Rev.* **2011**, 75, 268.

[27] E. Laanto, J. K. H. Bamford, J. J. Ravantti, L. Sundberg, *Front.Microbiol.* **2015**, 6, 829.

[28] E. Laanto, L. R. Sundberg, J. K. Bamford, *Appl. Environ. Microbiol.* **2011**, 77, 7868.

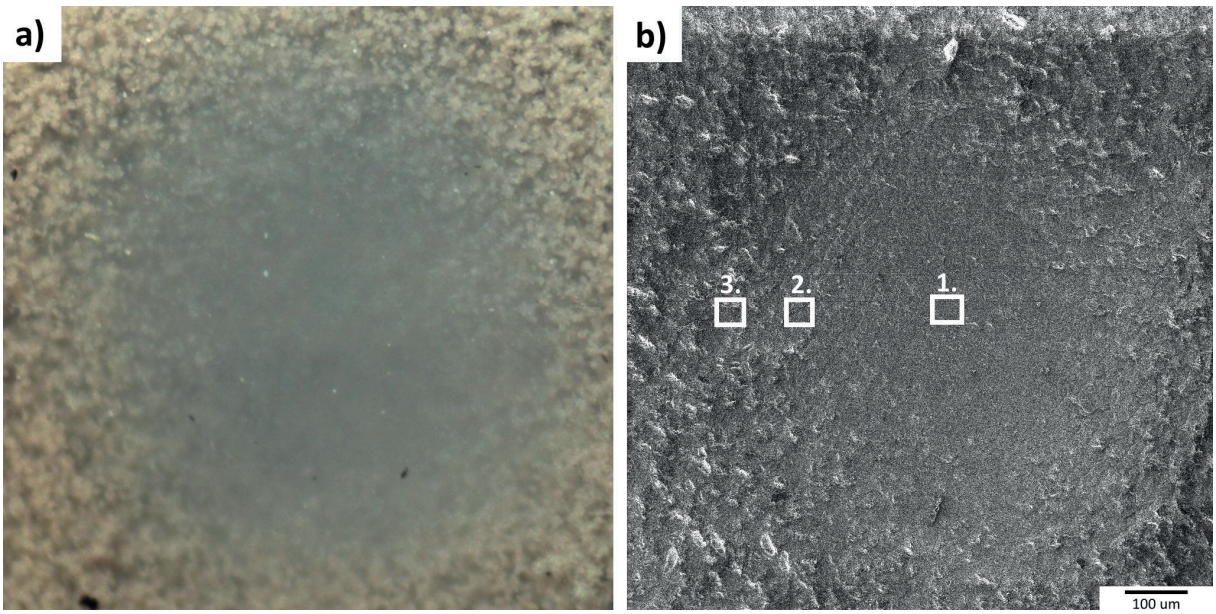

Figure 1. Images of a plaque formed by T4-infection in an *E. coli* lawn on an agar plate. The same plaque is shown here imaged with a) an optical microscope and b) with HIM. The areas investigated further in finer detail with HIM are shown with numbered squares.

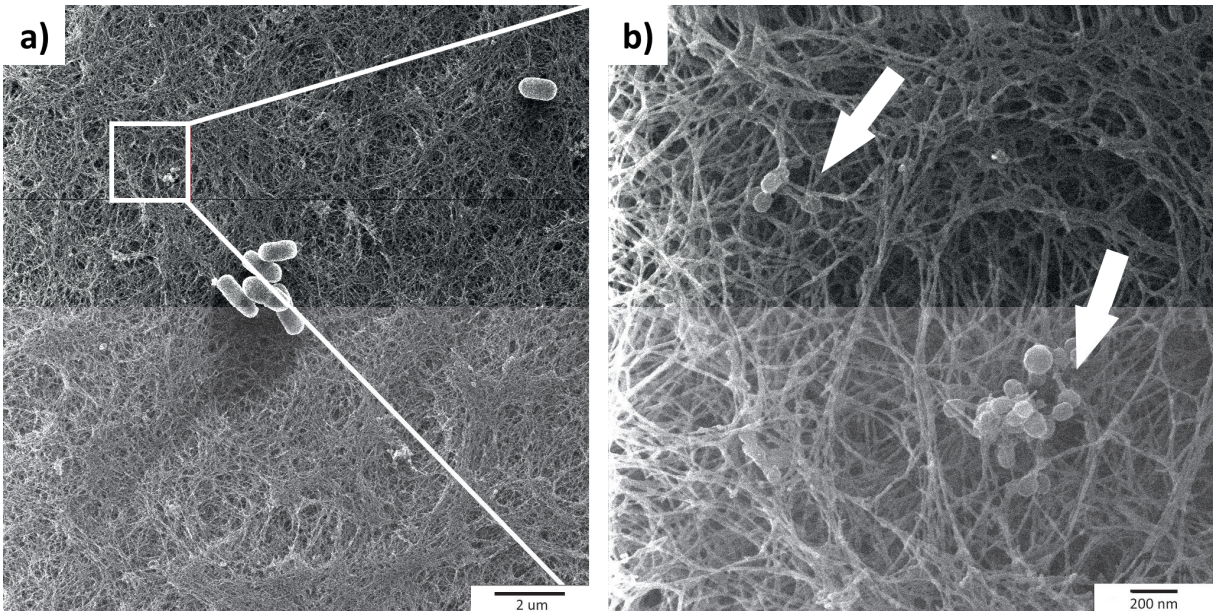

Figure 2. a) HIM image of area 1 in Figure 1b from the center of the plaque. Only few individual *E. coli* cells are visible. b) With a higher magnification T4 phages (arrows) can also be seen on the thin fibrous agar surface.

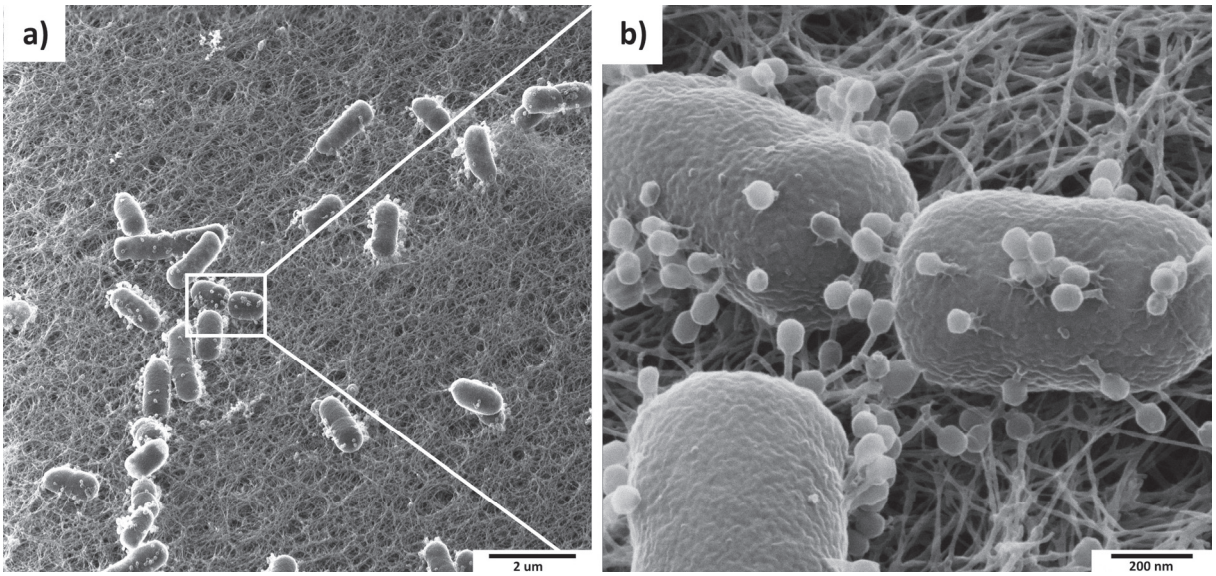

Figure 3. a) HIM image of area 2 in Figure 1b closer the edge of the plaque showing more bacterial cells with ongoing phage infections. b) Higher magnification of allows visualization of individual T4-phages attached onto the bacterial cell surface, some with contracted tails indicating genome injection. Free phages next to bacterial cells are also found.

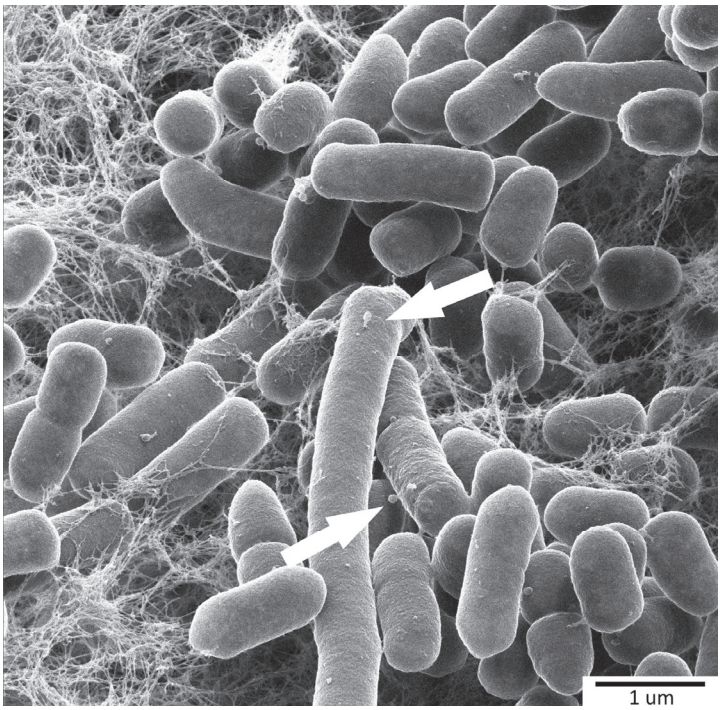

Figure 4. HIM image of area 3 in Figure 1b at the edge the plaque. The bacterial cells form microcolonies and few infecting phages are found (arrows).

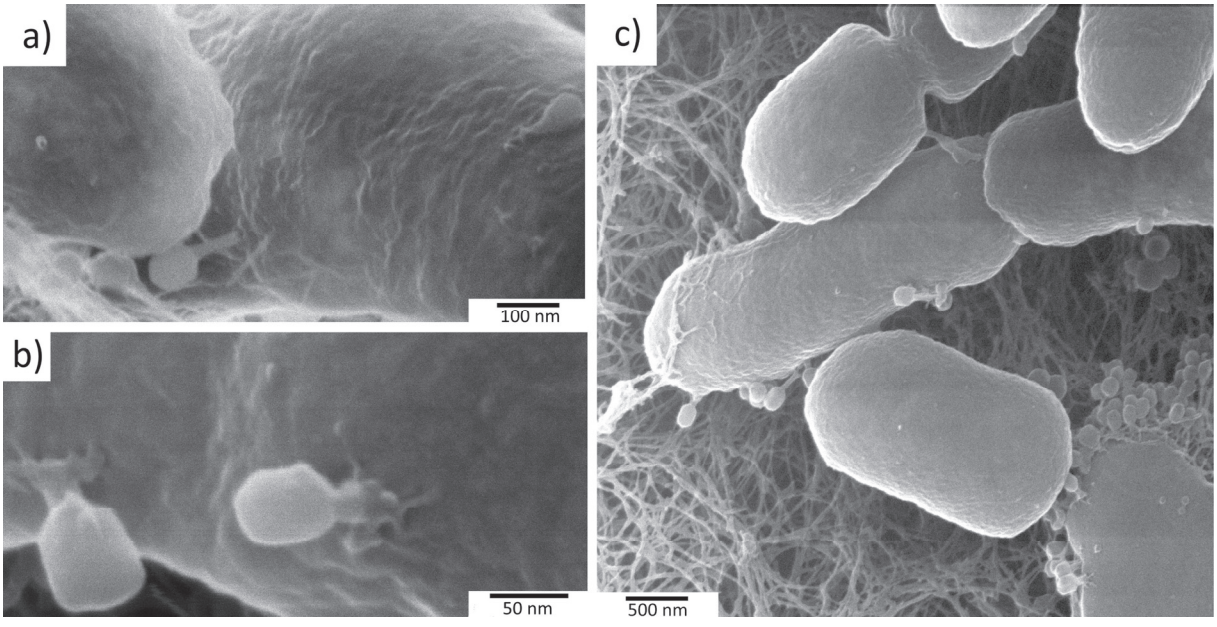

Figure 5. Visualization of the life cycle of a phage using HIM. a) A high resolution image of an early stage of the phage infection: T4 phage is attached on the surface of an *E. coli* bacterium. b) Several phages with contracted tails and spread out tail fibers indicating an active infection and genome injection. c) Lower right hand corner: Lysis of a bacterial cell and bursting out of a large number of new phage particles.

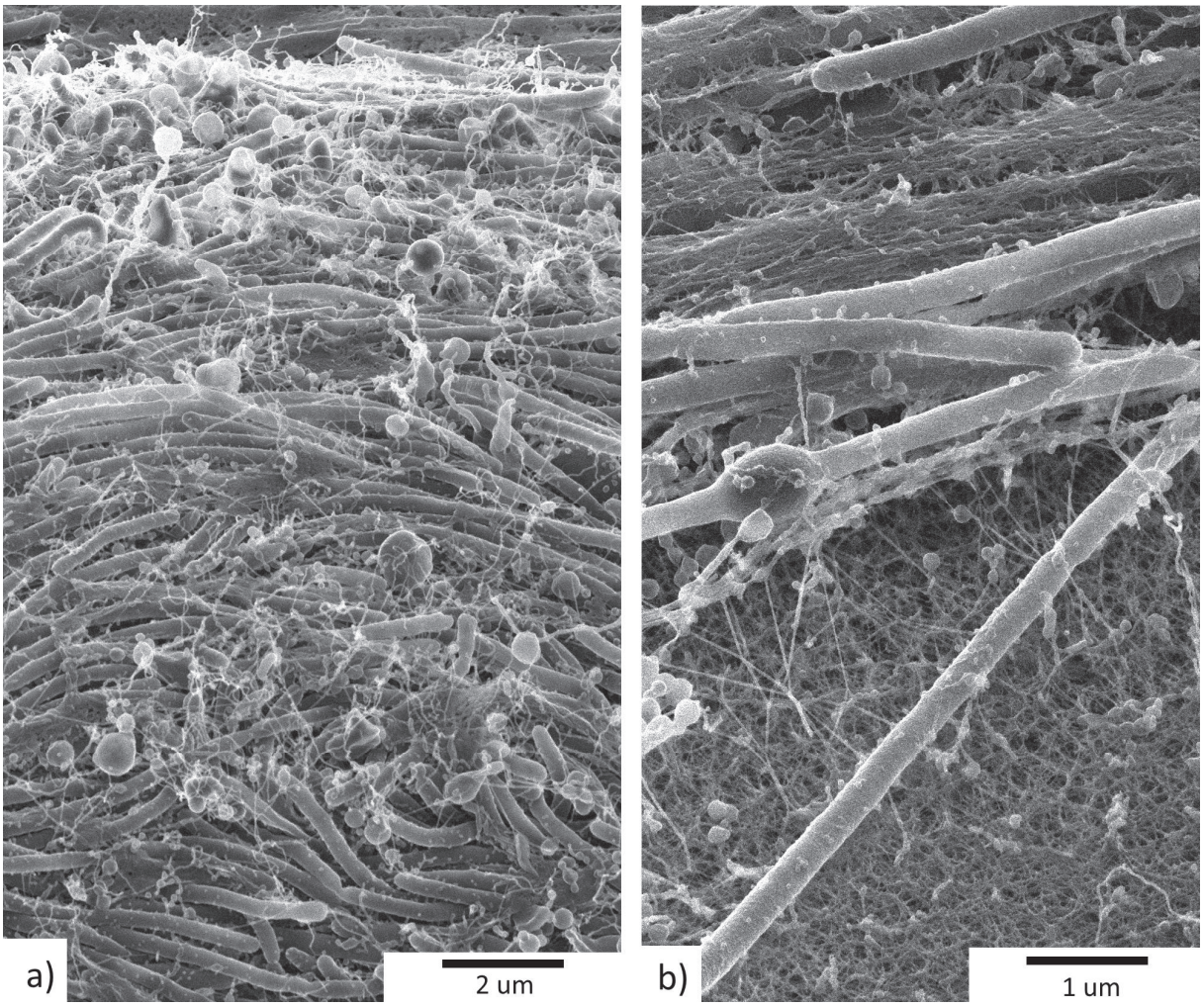

Figure 6. a) An image form a *Flavobacterium columnare* (B185) colony. A lot of extracellular vesicles and fibers are seen. b) A higher resolution image of an area where the contact between the colony and the agar substrate medium can be seen. Note the straight fibers connecting the cells to the substrate.

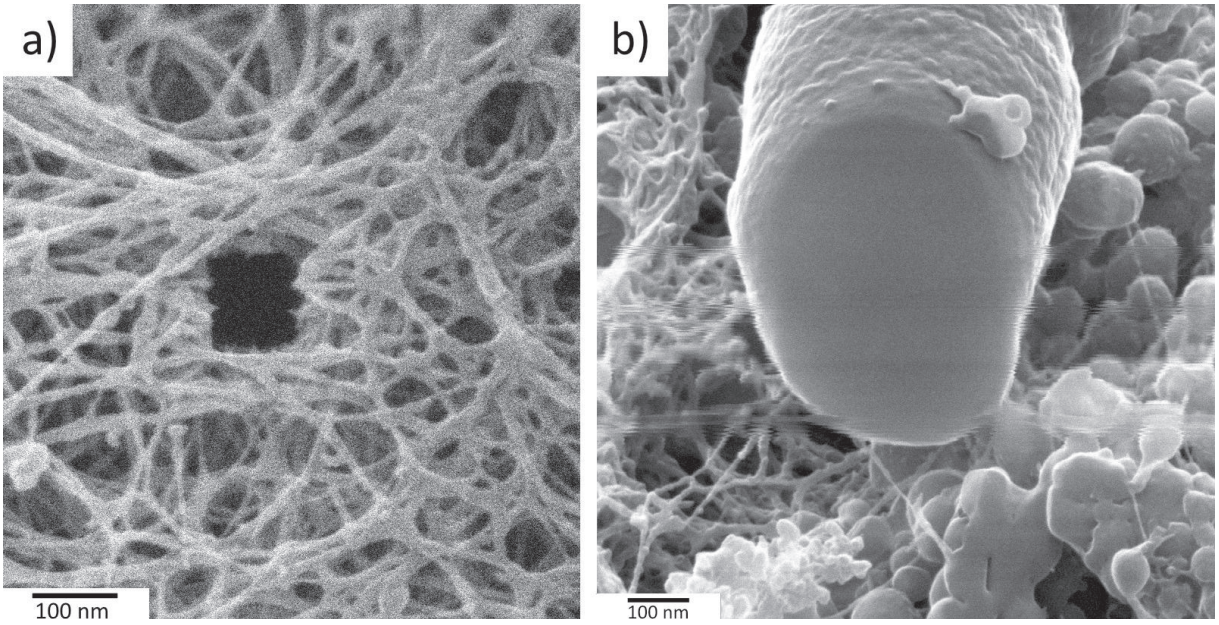

Figure 7. a) 100 x 100 nm area milled to the agar substrate with the flood gun on. b) He-milled bacteria showing up cut-off surface and a half-away cut phage particle on top of it. Milling was done from the 45º angle and imaging after 180º rotation.

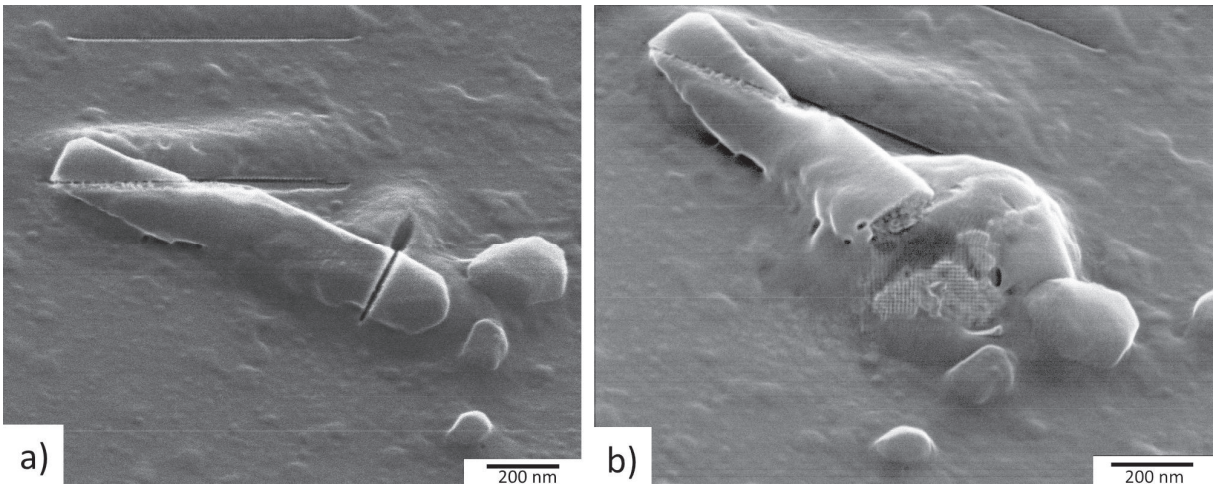

Figure 8. a) *Flavobacterium sp.* 183 after exposing line structures over its body. b) The same bacterium after the removal of the cut out "head" portion, revealing some inner structural details of the cell.

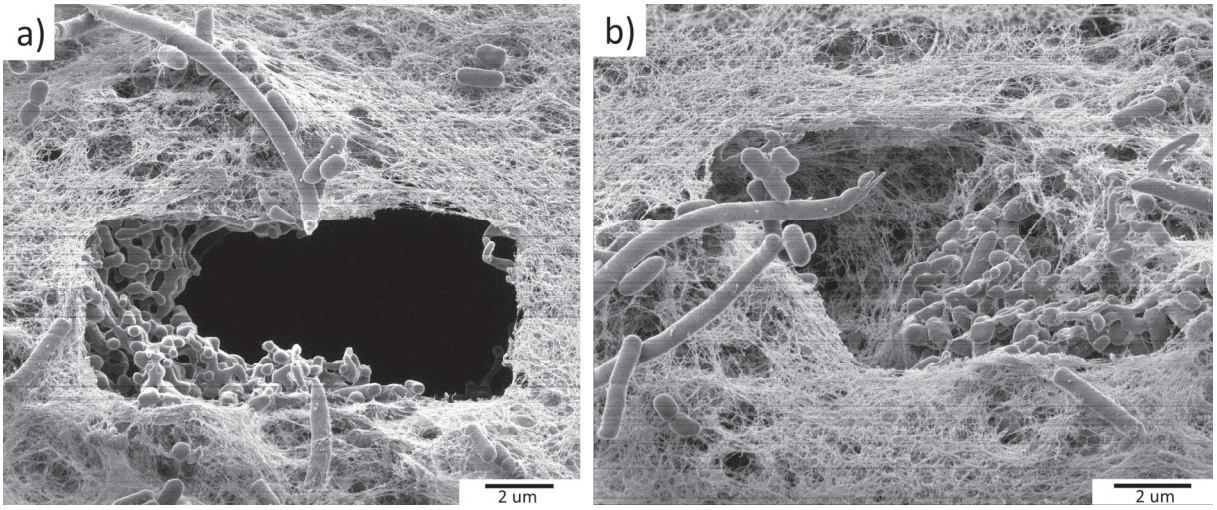

Figure 9. a) Slot milled to the agar substrate from an 45º angle with neon and imaged from 90 degree angle. b) The same milled area imaged with a 45º tilt and a 90º rotation.

III

CELLULOSE NANOFIBRILS PREPARED BY GENTLE DRYING METHODS REVEAL THE LIMITS OF HELIUM ION MICROSCOPY IMAGING

by

Ketola, A., Leppänen, M., Turpeinen, T., Papponen, P., Strand, A., Sundberg, A., Arstila, K., & Retulainen, E. 2019.

RSC Advances, 9(27), 15668-15677

RSC Advances

PAPER

View Article Online
View Journal | View Issue

Cite this: *RSC Adv.*, 2019, **9**, 15668

Cellulose nanofibrils prepared by gentle drying methods reveal the limits of helium ion microscopy imaging

Annika E. Ketola,[a] Miika Leppänen,[b] Tuomas Turpeinen,[a] Petri Papponen,[b] Anders Strand,[c] Anna Sundberg,[c] Kai Arstila[b] and Elias Retulainen *[a]

TEMPO-oxidized cellulose nanofibrils (TCNFs) have unique properties, which can be utilised in many application fields from printed electronics to packaging. Visual characterisation of TCNFs has been commonly performed using Scanning Electron Microscopy (SEM). However, a novel imaging technique, Helium Ion Microscopy (HIM), offers benefits over SEM, including higher resolution and the possibility of imaging non-conductive samples uncoated. HIM has not been widely utilized so far, and in this study the capability of HIM for imaging of TCNFs was evaluated. Freeze drying and critical point drying (CPD) techniques were applied to preserve the open fibril structure of the gel-like TCNFs. Both drying methods worked well, but CPD performed better resulting in the specific surface area of 386 m^2 g^{-1} when compared to 172 m^2 g^{-1} and 42 m^2 g^{-1} of freeze dried samples frozen in propane and nitrogen, respectively. HIM imaging of TCNFs was successful but high magnification imaging was challenging because the ion beam tended to degrade the TCNFs. The effect of the imaging parameters on the degradation was studied and an ion dose as low as 0.9 ion per nm^2 was required to prevent the damage. This study points out the differences between the gentle drying methods of TCNFs and demonstrates beam damage during imaging like none previously reported with HIM. The results can be utilized in future studies of cellulose or other biological materials as there is a growing interest for both the HIM technique and bio-based materials.

Received 26th February 2019
Accepted 13th May 2019

DOI: 10.1039/c9ra01447k

rsc.li/rsc-advances

1 Introduction

Cellulose nanofibrils (CNFs) have been under intensive investigation due to their unique properties, such as high tensile strength, large specific surface area, rheology and tendency for film formation.[1] CNFs can be prepared from natural cellulose wood fibres by mechanical and chemical treatments,[2] which makes them a biodegradable and renewable material. Various different application fields exist for CNFs ranging from paper, composites and food additives to bio-film material for printed electronics or packaging, biomedical applications and aerogels.[3–8] Thus, proper characterisation of CNFs is important for quality control and safety assessment.[9] The nanoscale size, the branched fibril structure and the high water content make the characterisation of CNFs challenging and demand sophisticated techniques. Scanning electron microscopy (SEM) is often used for characterisation of the morphology of CNFs and fibril dimensions in the mm to nm scale.[9–13] Transmission electron microscopy (TEM) is the most powerful imaging technique and can be utilized for detailed nanoscale evaluation of single fibril dimensions of CNFs.[9,14–17] SEM usually requires a conductive coating before imaging and the TEM method is limited to thin samples like single fibrils, and because of that, the new imaging method scanning helium ion microscopy (HIM) has aroused interest during recent years.

In the HIM method, a focused helium ion beam releases secondary electrons (SE) from the sample surface and creates an image in a similar way to SEM.[18–20] Because of the HIM single atom source, the probe is smaller compared to SEM, which together with the smaller excited surface volume makes higher imaging resolution possible.[18,21] Another advantage is that non-conductive samples do not need coating because the charging can be compensated for with an electron flood gun. HIM is widely utilized as a nanofabrication tool because helium ion beams can modify surfaces in the nanoscale by ion sputtering or implantation;[22–24] however, it is reported that in imaging applications the beam damage for organic samples is negligible.[20,25,26]

Thus far the HIM-imaging method has been used for cellulose-based materials usually with low to intermediate resolutions. Li *et al.* (2016)[27] used HIM for successful imaging of

[a]*VTT Technical Research Centre of Finland Ltd, P. O. Box 1603, FI-40101 Jyväskylä, Finland. E-mail: elias.retulainen@vtt.fi*
[b]*University of Jyväskylä, Nanoscience Centre, Department of Physics and Department of Biological and Environmental Science, FI-40014 Jyväskylä, Finland*
[c]*Åbo Akademi University, Johan Gadolin Process Chemistry Centre, Porthansgatan 3, FI-20500 Åbo/Turku, Finland*

paper-like composites of activated carbon and mechanically fibrillated CNFs whereas Torvinen *et al.* (2017)[4] studied kaolin—CNF composites of different CNF-types. Virtanen *et al.* (2018)[28] studied mechanically fibrillated CNF-aerogels, and HIM had a good depth of view for the freeze-dried CNF-aerogel when compared to SEM. The only study with high-resolution imaging of cellulose-based materials is by Postek *et al.* (2011)[21] where cellulose nanocrystals on mica were imaged. Because of that, the high-resolution imaging capabilities of HIM for cellulosic materials are still unclear.

Vacuum based imaging methods require dry samples and in order to obtain images that represent the nanocellulose structure in the wet-state, a gentle drying procedure is necessary. Improper drying will result in the collapse of the pores and coalescence of fibrils.[29] This can be prevented, for example, by using cryofixing, in which the sample is rapidly frozen in a cryoliquid, followed by drying of the frozen sample under a vacuum, where the ice sublimates into a gas without collapsing the structure. Liquid nitrogen (LN_2) is commonly used for freezing of various samples but is known to be affected by the Leidenfrost-effect where the boiling liquid forms an insulating gas layer between the sample and the coolant. This delays the freezing process, giving time for unwanted structural changes caused by ice crystal formation. With liquid propane (LPGS), used near its freezing point, this effect is reduced.[15] Another method for the preservation of the wet structure of the material is the critical point drying (CPD), where the collapse of the sample structure is prevented by passing the liquid–gas interphase in the drying by replacing the solvent with the supercritical fluid which is then turned into gas.[30]

Gentle drying of CNFs from water using cryofixing or CPD results an aerogel-like materials with large surface area.[11,31,32] Porous aerogels are often used as an insulators or adsorbents, but unlike brittle silica or carbon, native CNF-aerogels have been shown to possess mechanical toughness, flexibility and softness.[11,33–35] CNF-aerogel studies have involved CNFs of different types, drying techniques and applications, including conductive enzymatic-CNF aerogels dried with cryo-LPGS,[33] insulating and transparent TEMPO-oxidized liquid crystalline CNF aerogels dried with CPD,[34] magnetic bacterial-CNF aerogels dried with freeze drying,[35] soft enzymatic-CNF and TCNF aerogels dried with CPD[11] and hydrophobic mechanically fibrillated CNF aerogels dried with freeze drying.[31] The effect of drying techniques on CNFs structure[31,36] and properties[37,38] has been demonstrated showing unambiguously how the CPD drying is able to preserve the open fibril structure of CNFs better than freeze drying. TCNF aerogels have been also shown to have higher specific surface area (SSA)[39] than bacterial-CNF when dried with the same technique.[11] A high SSA indicates that the original open fibril structure has been well preserved during and SSA as high as 480 $m^2\ g^{-1}$ has been reported for TEMPO-oxidized CNFs after CPD.[40] Also freeze drying can achieve relatively high (100–300 $m^2\ g^{-1}$) SSA values for CNFs depending on the applied procedure.[10–12,32,41]

The objective of this study was to find the optimal preparation methods for wet TEMPO-oxidized CNFs (TCNFs) in order to preserve its fine fibril structure and evaluate the suitability of HIM for imaging the porous CNF-material with high resolution. TCNFs were selected for the work over other CNF-types as they have well-characterized fine and homogeneous structure, large specific surface area and high charge;[14] thus, they can be considered to be the most delicate structures to reveal the convenience of the methods. Also, TCNFs alone have not been imaged with HIM and the effect of different drying techniques on TCNF aerogel structures has not been evaluated before.

TCNFs were dried with four different drying procedures including cryofixing with LN_2 or LPGS followed by freeze drying and solvent exchange followed by CPD including two different solvent exchange procedures. The first CPD procedure involved sample fixation with glutaraldehyde (GA) and osmium tetroxide (OsO_4) and dehydration with ethanol (EtOH) before CPD. The second procedure involved only dehydration using EtOH and acetone (AE) prior to CPD. Nitrogen (N_2)-sorption and BET-analysis were used to determine the SSA of the TCNFs samples in order to quantify the differences between the drying methods. The results are expected to give useful information for the future studies of delicate bio-based structures with HIM.

2 Experimental

2.1. Materials

2.1.1. Chemicals. Propane (class 2, UN 1965: 95% propane and 5% butane) and liquefied nitrogen (LN_2) was purchased from AGA Gas Ab, Lidingö, Sweden. Acetone (AE, ≥99.9%) was obtained from Sigma-Aldrich, Darmstadt, Germany. Sodium cacodylate (NaCac, R1104, Agar Scientific, Stansted, UK) was acquired as a powder and a 0.4 M buffer stock-solution was prepared using ultrapure-water. Glutaraldehyde (GA, 25%-solution for electron microscopy) was obtained from Merck (Darmstadt, Germany) and used as a 2%-solution in 0.1 M NaCac-buffer solution (pH 7.4). Osmium tetroxide (OsO_4, Electron Microscopy Sciences, Hatfield, USA) was a 4%-solution, which was diluted to a 2%-stock solution with ultrapure-water. Ethanol (EtOH, absolute AA, Etax) was obtained from Altia Oyj, Rajamäki, Finland.

2.1.2. TEMPO-oxidized CNFs. TCNFs were prepared from never-dried birch kraft pulp by TEMPO-mediated oxidation and fluidization. TEMPO-mediated oxidation was performed according to a previously described procedure,[2,14] in which fibres were first suspended in a water solution of TEMPO and sodium bromide. Then, NaClO solution was added to the suspension (5 mmol to 15 mmol per gram of fibres) and the pH was adjusted to 10 at room temperature with NaOH. The reaction was considered complete when the pH remained stable. After oxidation, the fibres were washed thoroughly with deionized water followed by treatment with a microfluidizer M7115-30 (2 passes). The carboxylic content of TCNFs, determined by conductometric titration, was approximately 1.0 mmol g^{-1} of dry CNFs. Detailed characterisation of these particular TCNFs can be found elsewhere.[42]

2.2. Methods

2.2.1. Gentle drying of TCNFs using cryofixing. The TCNFs were cryofixed in LN_2 (cryo-LN_2) and in LPGS (cryo-LPGS). LPGS was prepared by liquefying propane gas using LN_2 and cooled until its freezing temperature (−189 °C) was nearly reached. A drop of TCNF-gel (1.08% [w/w]) was placed on a TEM grid (300 mesh) and immediately plunged in LN_2 (approximately −196 °C) or in LPGS. The cryofixed samples were placed on a LN_2 cooled metal plate and dried in a freeze drier at −50 °C under vacuum (Christ LOC-1m) over night. The dried samples were kept in a desiccator until HIM imaging or BET-analysis was carried out.

2.2.2. Gentle drying of TCNFs using solvent exchange and critical point drying (CPD). Two different methods for solvent exchange prior to CPD of TCNFs were used. Solvent exchange with GA, OsO_4 and EtOH was performed by first attaching a drop of TCNF-gel (1.08% [w/w]) to a glass coverslip with epoxy-based glue. Samples were placed in a 24-microtiter plate containing a fixative (2% GA in a 0.1 M NaCac buffer, pH 7.4) and incubated for 4 h. The samples were then washed with 0.1 M NaCac buffer twice and incubated with 1% OsO_4 in 0.1 M NaCac for 30 min, after which the washing with 0.1 M NaCac was repeated three times. After fixation with GA and OsO_4, the samples were dehydrated to EtOH by using a series of steps with increasing EtOH concentration: 50, 70, 90, 95 and 2 × 99.5%. The dwell time in each step was 30 min, and the final step took place overnight.

Solvent exchange with EtOH and AE was done first by dehydrating drops of TCNF-gel in an EtOH stepwise, as explained earlier. After the last step in 99.5% EtOH the sample was placed in AE overnight. CPD (Leica CPD 300, University of Jyväskylä, Finland) was the last step from EtOH or AE to the ambient conditions. The CPD programme included 16 exchange cycles of CO_2 at medium speed (speed value 5) without stirring. Slow speed was used for gas filling, heating, and venting steps. The dried samples were attached to metal stubs using carbon tape and kept in a desiccator until HIM-imaging.

2.2.3. Helium ion microscopy (HIM). HIM (Zeiss Orion Nanofab, University of Jyväskylä Nanoscience Centre, Finland) was used for imaging the dried TCNFs. Acceleration voltage of 30 to 35 kV with aperture 10 μm was used resulting to an ion current of 0.1–0.3 pA. Image size 1024 × 1024 pixels, line averaging between 4 to 16 lines, dwell time 0.5 or 1.0 μs and working distance approximately 9 mm were used as the imaging parameters. All samples were studied without metal coating, and the electron flood gun with 750 eV energy was used to neutralize the sample charging. Fibril dimensions were estimated from HIM images by using ImageJ software (ImageJ freeware, USA). The scale bar of the images was used to turn the software pixels into nanometers and the fibrils width were collected from different spots of the image so that rough estimation of different fibril widths could be done.

2.2.4. N_2-sorption. The SSA of the TCNFs was determined using the Brunauer–Emmett–Teller (BET) method.[39] Approximately 70 mg of dried TCNFs was prepared for the analysis. TCNFs were dried using the procedures described before (Sections 2.2.1 and 2.2.2) with small modifications. In cryofixing, the sample volume was increased to approximately 0.2–0.3 g so that the structure was still able to freeze rapidly during the plunge-freezing in LN2 or in LPGS. In solvent exchange, the sample volume was increased to approximately 0.4 g (a large drop), incubation time in GA-solution was for overnight and in OsO_4 for 60 min. The dwell time in EtOH series was 60 min (the final step took place overnight) and after the last step in 99.5% EtOH the samples were placed in AE over two nights. Prolonged incubation times were conducted to ensure proper replacement of water in the structure. Samples were kept in a desiccator until N_2-sorption measurement.

The dried TCNFs was weighed in sample flasks and degassed in a vacuum at 110 °C for 30 min. After that the temperature was raised to 125 °C for 4 h. Finally, the temperature was increased to 150 °C for 15 min. The samples were then placed in a N_2-sorption device (Micromeritics 3Flex Version 4.04, VTT Espoo) and the adsorption data was collected at −196 °C by adjusting the relative nitrogen pressure from 0 to 0.99 and back. The Barrett–Joyner–Halenda (BJH) theory was used to calculate the average equivalent pore size of the TCNFs based on the N_2-sorption isotherms.[43] The model is based on an assumption of spherically shaped pores, which is not the case in a fibril network system. Thus, the obtained values were mainly used as relative guidelines when comparing the samples. The average equivalent fibril diameter (d) was also estimated from the SSA values using eqn (1). The density of cellulose was assumed to be 1600 kg m^{-3} (ref. 44 and 45) and fibrils were assumed to be infinitely long rods with a cylindrical cross section.

$$d = \frac{4}{\rho_c \times \mathrm{BET}} \quad (1)$$

d = fibril diameter, ρ_c = cellulose density and BET = BET specific surface area.

3 Results and discussion

3.1. HIM-imaging of TCNF-gel

Both cryofixation and CPD preserved well the shape of the TCNFs. The samples could be handled without being fractured and not any clear shrinkage of the samples were observed. Cryofixed samples were white in colour and resembled dry polystyrene foam in appearance (Fig. 1a and b). CPD dried samples were light blue, transparent and resembled fine-structured cottonwool (Fig. 1c and d). Blue colour could be a result of the Rayleigh scattering in the material with small length scales, previously observed also with TEMPO-oxidized liquid crystalline CNF-aerogels dried by using CPD[34] and silica-based aerogels.[46]

Low magnification HIM images of dried TCNFs with a field of view (FoV) of 400 and 100 μm presents dense and wavy surfaces (Fig. 2a–k). Waviness was most probably caused by sample handling and liquid fluctuations during the drying. In order to see the differences between the actual fibril structures, a closer investigation with higher magnification (FoV 10 μm) was needed. High magnification HIM images (Fig. 1c, f, i and l)

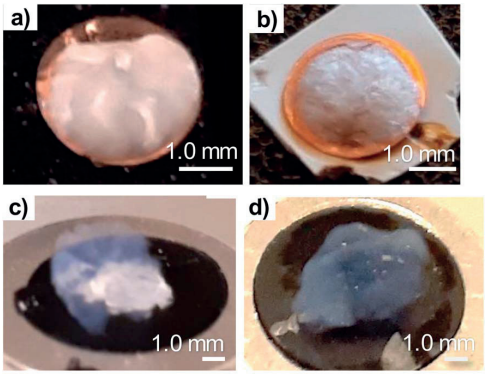

Fig. 1 Dried TCNFs attached on black carbon tape ready for HIM imaging. (a) cryo-LN2, (b) cryo-LPGS (white epoxy glue shows underneath the slightly transparent sample), (c) CPD (EtOH, AE) (d) CPD (GA, OsO_4, EtOH).

show that TCNF-surfaces consisted of a very fine fibrillar material. The CPD-dried samples resembled each other also at higher magnification. Rough estimation of fibril dimensions from the HIM images showed approximately 20 nm-wide fibrils, or fibril bundles, in all samples. Accurate statistical analysis of fibril dimensions and distributions was not possible as the sample degraded during imaging or pictures were too noisy (Fig. 3). TCNFs are found to consist of single fibrils of 3–4 nm in width[14] but fibrils of those dimensions could not be distinguished here. There were also much thicker 100 nm wide fibril bundles in the cryofixed samples. Similar structural differences between freeze dried and CPD dried commercial-CNF[36] and enzymatic-CNF[15] have been observed before with SEM.

The formation of clear TCNF-films was more severe in cryo-LN_2 samples than cryo-LPGS samples. The heterogeneous structure and the film formation indicated that there was ice crystal formation during cryofixing of the sample that pushed the fine material to the edges of the ice crystals.[10,16,40,47] The CPD-dried samples showed a more homogenous microstructure. In addition to the small size, TCNFs have high negative charge and high specific surface area,[14] meaning that they bind a lot of water in their structure. Removal of the water in such a way that the fine fibril structure remains open is challenging and was not fully achieved with the used cryofix-methods.

Detection of single fibrils turned out to be challenging because of the sample degradation during the imaging. Especially, the CPD-dried TCNFs were sensitive at higher magnifications. Imaging, as in Fig. 2c, f, i and l, was conducted by first using the 2 μm FoV to focus a beam and align the flood gun and then the actual image was taken with 10 μm FoV. Because of the focusing step, a clear hole was formed to the center of the image as can be seen in Fig. 2i and l. Smaller FoV had a higher ion dose per area and to confirm that the effect was dose based, the imaging was done to the fresh areas with

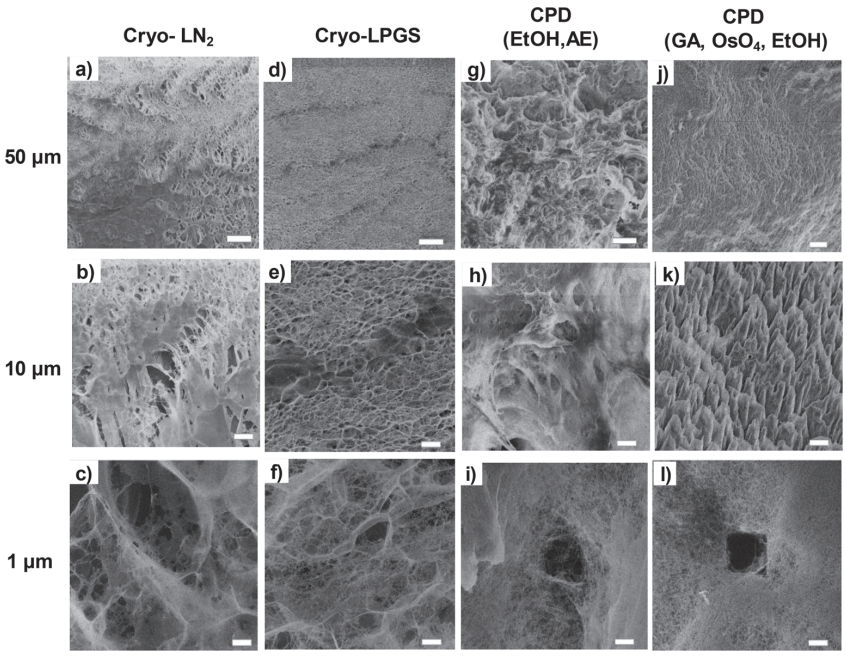

Fig. 2 HIM-images of dried TCNFs with different magnifications. (a), (b), (c) cryo-LN_2, (d), (e), (f) cryo-LPGS, (g), (h), (i) CPD (EtOH, AE) and (j), (k), (l) CPD (GA, OsO_4, EtOH). Top row FoV 400 μm, middle row FoV 100 μm and bottom row FoV 10 μm. Fig. 1i and l show clearly the holes caused by the ion beam.

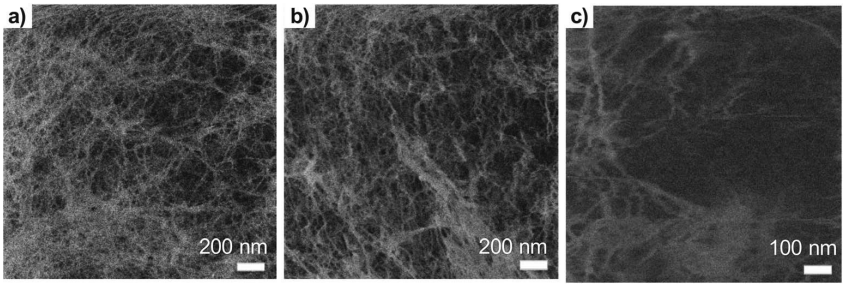

Fig. 3 The effect of the ion dose to the beam damage on the TCNFs (a) ion dose 4×10^{13} ions per cm^2 (b) 9×10^{13} ions per cm^2 (c) 4×10^{14} ions per cm^2 (eqn (2)).

different doses by adjusting the amount of averaging. The total ion dose was calculated with eqn (2):

$$D = \frac{I \times t}{e \times A} \quad (2)$$

D = areal dose, I = ion current, t = pixel dwell time and A = pixel area.

With dose of 4.9×10^{13} ions per cm^2 some fibrillar network could be resolved, but the noise level was quite high, which caused the graininess of the image (Fig. 3a). When the dose was doubled (Fig. 3b), some deformations of the fibril structure was detected already. Interestingly, this dose was under the theoretical limit of the sub-nanometer imaging because there were 0.9 ions per nm^2. When tenfold dose was used (Fig. 3c) the structure of the fibril network was collapsed leaving some individual fibrils drift over the imaging area.

Degradation of the bio-based materials during the HIM-imaging has not been described in the literature previously. For example, Joens *et al.* (2013)[26] demonstrated how biological organisms can be imaged with high magnifications without damage and in the study by the Leppänen *et al.* (2017)[22] the dose 1.1×10^{16} ions per cm^2 was used to image the dried agar gel network of 10 nm fibrils with no clear damage. Comparison of the ion doses among the literature is challenging because usually not all the imaging parameters are listed. Fox *et al.* (2013)[48] studied a graphene flakes with HIM and Raman spectroscopy and found that dose of 10^{17} ions per cm^2 was required for proper edge contrast to obtain sub-nanometer resolution and 5×10^{14} ions per cm^2 already caused significant damage to graphene lattice. Livengood *et al.* (2009)[49] studied the defect formation in the silicon and copper by HIM and found that with over 5×10^{15} ions per cm^2, subsurface lattice dislocations are found from the TEM cross-sections. These materials are quite different compared to the polymeric CNFs and the direct comparison is not possible.

CNFs consist of cellulose chain bundles with alternating amorphous and crystalline regions having intermolecular hydrogen bonding between the chains on the crystalline part.[50,51] The amorphous regions of the network can be considered the weakest points of the structure. Most probably, the ionization of the cellulose by the ion beam, especially in the amorphous regions collapses the structure. Actually, single ion can cause several ionizations because it is known that secondary electron yield of helium ranges from 3 to 10 depending on the material[18] Crystalline CNCs, in which the amorphous regions are no longer present, have been imaged with HIM without similar degradation.[21,28] However, the quality and magnification of the images and sample preparation methods cannot be directly compared to this work.

Cellulose-based materials have been found to be a highly sensitive also to the electron beams and the imaging of the single cellulose nanofibril or cellulose nanocrystal is challenging with TEM.[52] More specifically, a critical dose where the diffraction from the crystalline part of nanocellulose has been halved as the sign of destruction has been found to be about 6×10^{15} electrons per cm^2. This is about 10-times more than the helium ion dose causing the collapse of the fibrillar network in our experiment.

An interesting application of the beam damage is demonstrated in Fig. 4, which shows the time series over the sample area with 0.3 pA ion current with total imaging time of couple of minutes. The overall structure in the first figure was quite plain with no individual fibrils observed. When the same area was imaged multiple times, a hole started to form in the right-upper corner as a loosely bound film-like fibril layer on top of the sample milled away revealing the underlying fibril network. This, so-called "unwrapping" property of the ion beam could be generally utilized to detect different materials based on the milling rate. The image area shifts a little bit upward and right during the imaging, which was also a common finding. The fibril network underneath was most likely collapsing and resulted in an overall change of shape. In principle, helium ions can penetrate tens of μm deep with this acceleration voltage, which means that also the structure underneath the surface can be damaged.

Traditionally OsO_4 has been used to reduce sample charging during imaging with SEM.[53,54] In the current study the fixation with glutaraldehyde and OsO_4 (Fig. 1l) did not protect the TCNFs against degradation. Atomic layer deposition or chemical vapour deposition of titanium oxide[16,31] or sputtering of a Pt or Au/Pd layer on the sample surface could provide a protective layer for fibrils and enable imaging with high magnifications; however, metal sputtering can distort

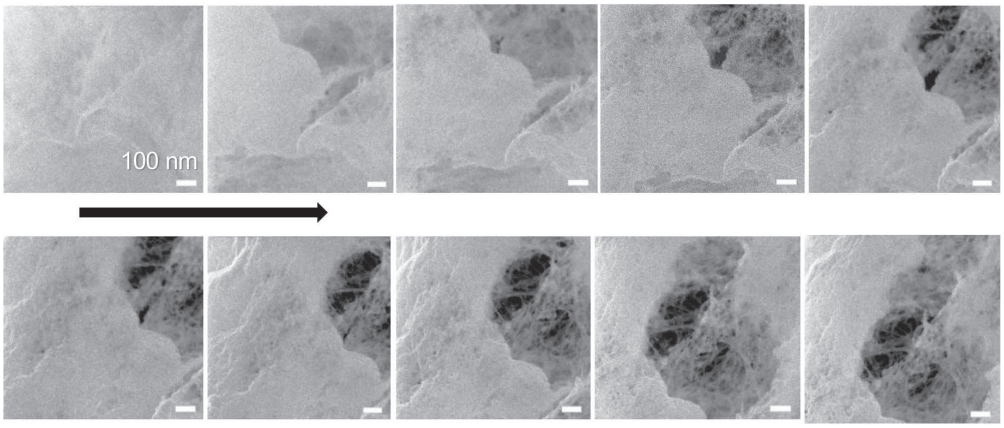

Fig. 4 Time series of the same area of TCNFs dried with CPD (GA, OsO_4, EtOH) showing the effect of beam damage (or ion milling) on the sample surface within seconds when using the 0.3 pA ion current. Total imaging time 80 seconds (8 s per image). Imaged using a 16-line average with FoV 1 μm. Scale bar is 100 nm for all the images.

the fibril dimensions[26,55,56] and possibly damage the finer fibril structure.

3.2. Specific surface area (SSA) of TCNFs

Quantitative evaluation of the differences between the gentle drying methods of TCNFs was done by using BET-analysis, which determines the specific surface area (SSA) of a material that is accessible to nitrogen. In the case of TCNFs, the higher the SSA, the more open the structure and the less coalescence of fibrils has taken place during drying. All of the samples had a type IV N_2-sorption isotherm curves with a type H3 hysteresis loop (Fig. 5), which means monolayer-multilayer adsorption of nitrogen on mesoporous structure with pore widths between 2–50 nm.[57,58] This hysteresis type typically indicates that the structure was formed of aggregates of platy particles with slit-shaped pores (Fig. 6).[11,32,57–60] This slit-shape possibly makes pores prone to collapse during drying, as surfaces want to minimize their energies by binding to each other and the closer they are, the stronger are the surface energies leading to collapse.[61] Samples dried with cryo-LN_2 did not show any hysteresis loop in the N_2-sorption isotherms. When the adsorbed quantities were plotted as relative values (Fig. 5b; the adsorbed quantity divided by the highest detected adsorption), a small hysteresis loop could be detected. There

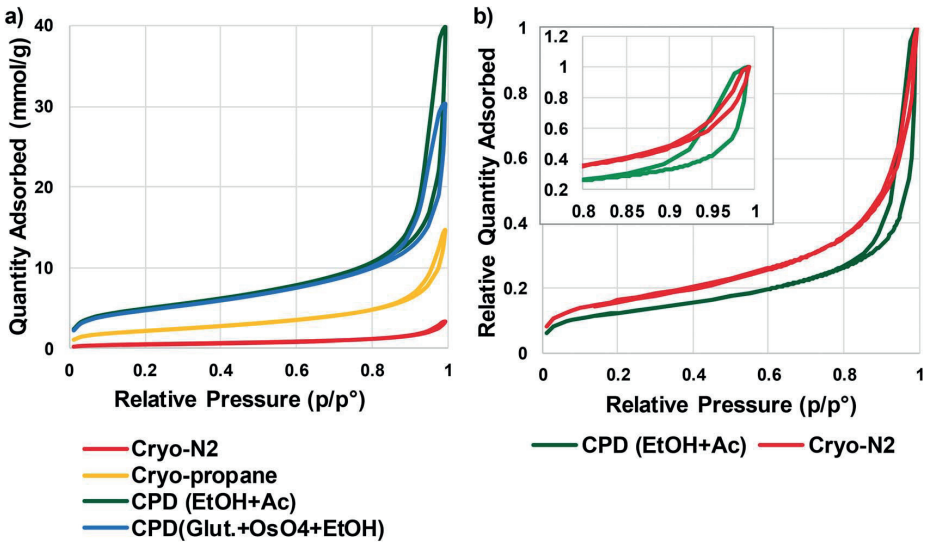

Fig. 5 (a) N_2-sorption isotherms of TCNFs dried with gentle drying methods (b) relative N_2-sorption isotherms of cryo-N_2 and CPD (EtOH, Ac) dried TCNFs.

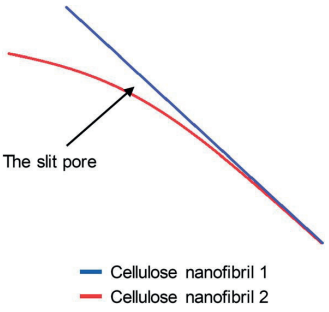

Fig. 6 A sketch of possible configuration of a slit-shaped pore between two cellulose nanofibrils.

was a steep increase in the isotherms after the relative pressure of 0.82, and because capillary condensation in mesopores occurs at the higher pressure values, the result indicates that most of the pores were larger in size. This was also seen in the pore size distribution (Fig. 7.) of the samples where most of the pores were in the mesopore and micropore range (15–100 nm). Over 50 nm pores or pores under 2 nm cannot be detected accurately by BET, and for this reason, it is probably not the most suitable method for fibrillated materials like TCNFs, but the results were still useful for comparing differences between the samples in the current study.

Table 1 shows the mean values of SSA, equivalent pore size, pore volume, and fibril diameter values. The Barrett–Joyner–Halenda (BJH) method was used to calculate the pore size distributions of the samples. The CPD-dried samples adsorbed more nitrogen than cryofixed samples and had higher SSA, equivalent pore size and pore volume. CPD (EtOH, Ac) samples had the largest SSA (386 $m^2 g^{-1}$), equivalent pore size (14.3 μm) and pore volume (1.4 $cm^3 g^{-1}$). The equivalent pore size was similar to the rest of the samples (around 11 μm) but the pore volume was significantly lower for cryofixed samples than for CPD samples. Less than 2% of all pores in all samples were of micro scale, and the rest of the pores were mesopores or larger (Table 1 and Fig. 7). This could mean that even though the volume of the pores in cryofixed samples was lower than in CPD samples, the pore structure was similar. According to the results, CPD drying was able to prevent the coalescence of the fibril structure better than cryofixing; however, most of the micropores in the structure were not preserved or could not be detected. As high SSA values as 500–600 $m^2 g^{-1}$ have been reported for TEMPO-oxidized liquid crystalline CNF-aerogels dried by using CPD and EtOH–solvent exchange.[34] The liquid crystalline arrangement achieved by acid-treatment could have promoted the structure stability, which was also observed as high toughness of the dried material. CPD has been reported to be a promising drying method also for TCNF-nanopapers, yielding SSA values of 480 $m^2 g^{-1}$ measured by N_2-sorption[40] and TCNFs dehydrated with EtOH and AE before CPD showed higher nitrogen adsorption and SSA than samples fixed with GA and OsO_4 before dehydration in EtOH. The last AE step could be more beneficial for CPD as the CO_2-gas is more miscible with AE than with EtOH.[62] In electron microscopy, GA in combination with OsO_4 is a commonly used protein fixative of both plant and animal samples.[53,63] On the other hand, it has been observed to be more efficient in preservation of internal plant structures than surfaces,[63] and did not provide any significant support for cellulose-fibril structures against the ion beam damage in the current study.

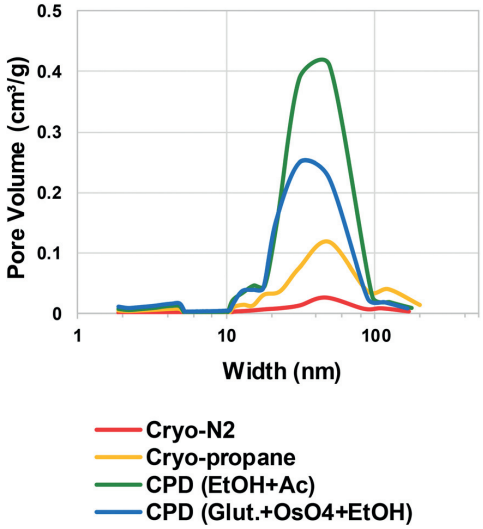

Fig. 7 Estimated pore size distribution obtained using BET method of the TCNFs dried with different gentle drying methods. Average pore width (nm) on the *x*-axis at logarithmic scale and pore volume ($cm^3 g^{-1}$) on the *y*-axis.

Again, cryo-LPGS samples showed higher nitrogen adsorption and SSA (172 $m^2 g^{-1}$) than cryo-LN_2 samples (SSA 42 $m^2 g^{-1}$). LN_2 is known to suffer from the Leidenfrost-effect, and the low SSA was probably a result of the coalescence of fibrils by the ice crystal formation. The corresponding results of drying efficiency of cellulose microfibrils (CMF) with CPD, LN_2 and LPGS have been previously reported.[15] Sehaqui *et al.* (2011)[11] reported a SSA of 150–280 $m^2 g^{-1}$ for TCNFs dried from water using solvent exchange to EtOH and *tert*-butanol and cryofixing with LN_2. Exchanging the water inside the material to a solvent with low surface tension has been shown to increase the SSA also for regenerated cellulose (160–190 $m^2 g^{-1}$).[10] Thus, it could be possible to increase the SSA of cryo-LPGS samples by first conducting a solvent-exchange of the samples, like it is done with samples prepared for CPD. On the other hand, if the target is to image TCNFs as they appear in water, where certain charges and interactions between fibrils occur, the solvent-exchange from water to a non-polar solvent could also change these interactions and the surface structure. Thus, it is not obvious that the higher SSA value of the solvent-exchanged samples really describes the sample structure in aqueous conditions.

The calculated equivalent fibril diameters of TCNFs were approximately 7 nm, 15 nm and 60 nm for CPD, cryo-LPGS and cryo-LN_2 dried samples, respectively. Large fibril diameters of

Table 1 Mean values of the SSA, equivalent pore size and pore volume of TCNFs dried with different gentle drying methods

	BET surface area	Pore size[b]	Fibril diameter	Pore volume[a]	Micropore volume <2 nm
	$m^2\ g^{-1}$	nm	nm	$cm^3\ g^{-1}$	$cm^3\ g^{-1}$
Cryo-N_2	41.8	10.7	59.8	0.11	0.0012
Cryo-LPGS	171.8	11.6	14.6	0.50	0.0036
CPD (EtOH, Ac)	385.7	14.3	6.5	1.38	0.0193
CPD (GA, OsO_4, EtOH)	375.0	11.2	6.7	1.05	0.0176

[a] Single point desorption total pore volume of pores less than 193.5 nm width at $p/p_o = 0.990$. [b] Desorption average pore diameter ($4V/A$ by BET).

cryofixed TCNFs can be explained by the fibril agglomeration during drying. Multilayer adsorption of nitrogen can increase the detected surface area, which decreases the calculated fibril diameters, and the actual diameters were most likely larger. The BET results (Table 1) supported the observations from the HIM images of TCNFs (Fig. 2). CPD resulted more homogeneous and finer fibril structure, with less intensive film formation compared to cryofixing. As mentioned before, the smallest fibrils observed from the HIM images were approximately 20 nm in width (Fig. 2c, f, i and l), which was significantly larger than the width estimates from the BET-analysis. This could be due to beam damage during the imaging, making the smallest fibrils disappear or due to the multilayer adsorption of nitrogen in the BET-analysis that affected the SSA calculations. In addition, the HIM-images show only the surfaces of the samples and do not represent the whole structure.

Quantitative differences between different drying methods was not obtained by microscopy, and for that N_2-sorption and BET-analysis were needed. Based on these results (Fig. 2 and Table 1), the solvent exchange in EtOH/AE combined with CPD drying is the most preferred method, and also involves less hazardous chemicals and liquid exchange steps than treatment with GA/OsO_4/EtOH. Solvent exchange with AE combined with CPD is found to result in a high SSA also with the fibres;[64] however, is worth to keep in mind that solvent exchange could modify the interactions between the fibrils that occur in water. TCNFs have added carboxyl groups on the cellulose chain, which increases their hydrogen bonding ability in water. When water is exchanged to the less polar media the hydrogen bonding is hindered and can be responsible for more open fibril structure in the dried material. Cryofixing in LPGS surpasses LN_2 in SSA values, but cryofixing in LN_2 is more simple and faster than cryofixing in LPGS. In order to select a suitable drying method for TCNFs one needs to consider if a highly preserved structure is necessary, and how much time and effort is practical to use.

4 Conclusions

The suitability of HIM for imaging the porous TCNF-aerogels with high resolution was evaluated and different aerogel preparation methods using gentle drying were compared. High-resolution HIM-imaging of TCNFs was compromised by the dose-related damage as not described before with ion beams. Further research is needed about ion beam induced damage on the organic materials to have reliable imaging methods in the future. Comparison of the different gentle drying methods showed that all methods preserved the wet structure of TCNFs at some degree. CPD was considered to be the best method for drying delicate samples with SSA of 386 $m^2\ g^{-1}$. Cryo-LPGS provided moderate result with SSA of 172 $m^2\ g^{-1}$, but SSA for cryo-LN_2 was only 42 $m^2\ g^{-1}$, and should be carefully considered if detailed surface structures of wet cellulose fibril materials are studied. Sample handing procedure in the preparation phase seemed also to affect the large-scale structures of the sample, but clear systematic differences between the samples was seen only in nanoscale.

Conflicts of interest

There are no conflicts to declare.

Acknowledgements

This research was part of the Academy of Finland funded project ExtBioNet (Tailored fibre–fibre interactions for boosted extensibility of bio-based fibre networks, decision No. 285627). The authors thank Mr Panu Lahtinen (Biomass processing, VTT, Espoo) for providing the fibrillated cellulose materials and Ms Mirja Muhola (Thermochemical conversions, VTT, Espoo) for the BET-analysis of the CNF samples.

References

1 N. Lavoine, I. Desloges, A. Dufresne and J. Bras, *Carbohydr. Polym.*, 2012, **90**, 735–764.
2 T. Saito and A. Isogai, *Biomacromolecules*, 2004, **5**, 1983–1989.
3 S. Ahola, M. Österberg and J. Laine, *Cellulose*, 2008, **15**, 303–314.
4 K. Torvinen, F. Pettersson, P. Lahtinen, K. Arstila, K. Vinay, R. Österbacka, M. Toivakka and J. J. Saarinen, *Flexible Printed Electron.*, 2007, **2**, 024004.
5 F. W. Brodin, Ø. W. Gregersen and K. Syverud, *Nord. Pulp Pap. Res. J.*, 2014, **29**, 156–166.

6 H. Orelma, I. Filpponen, L.-S. Johansson, M. Österberg, O. J. Rojas and J. Laine, *Biointerphases*, 2012, **7**, 61.
7 M. Hubbe, O. J. Rojas, M. A. Hubbe, A. Ferrer, P. Tyagi, Y. Yin and C. Salas, *Bioresources*, 2017, **12**, 2143–2233.
8 M. A. Hubbe, P. Tayeb, M. Joyce, P. Tyagi, M. Kehoe, K. Dimic-Misic and L. Pal, *Bioresources*, 2017, **12**, 9556–9661.
9 H. Kangas, P. Lahtinen, A. Sneck, A.-M. Saariaho, O. Laitinen and E. Hellén, *Nord. Pulp Pap. Res. J.*, 2014, **29**, 129–143.
10 H. Jin, Y. Nishiyama, M. Wada and S. Kuga, *Colloids Surf., A*, 2004, **240**, 63–67.
11 H. Sehaqui, Q. Zhou and L. A. Berglund, *Compos. Sci. Technol.*, 2011, **71**, 1593–1599.
12 N. T. Cervin, C. Aulin, P. T. Larsson and L. Wågberg, *Cellulose*, 2012, **19**, 401–410.
13 M. Henriksson, L. A. Berglund, P. Isaksson, T. Lindström and T. Nishino, *Biomacromolecules*, 2008, **9**, 1579–1585.
14 A. Isogai, T. Saito and H. Fukuzumi, *Nanoscale*, 2011, **3**, 71–85.
15 J. T. Korhonen, P. Hiekkataipale, J. Malm, M. Karppinen, O. Ikkala and R. H. A. Ras, *ACS Nano*, 2011, **5**, 1967–1974.
16 M. Kettunen, R. J. Silvennoinen, N. Houbenov, A. Nykänen, J. Ruokolainen, J. Sainio, V. Pore, M. Kemell, M. Ankerfors, T. Lindström, M. Ritala, R. H. A. Ras and O. Ikkala, *Adv. Funct. Mater.*, 2011, **21**, 510–517.
17 M. Pääkko, M. Ankerfors, H. Kosonen, A. Nykänen, S. Ahola, M. Österberg, J. Ruokolainen, J. Laine, P. T. Larsson, O. Ikkala and T. Lindström, *Biomacromolecules*, 2007, **8**, 1934–1941.
18 B. W. Ward, J. A. Notte and N. P. Economou, *J. Vac. Sci. Technol., B: Microelectron. Nanometer Struct.–Process., Meas., Phenom.*, 2006, **24**, 2871.
19 L. Scipioni, L. Stern and J. Notte, *Microsc. Today*, 2007, **15**, 12–15.
20 M. T. Postek, A. E. Vladar, J. Kramar, L. A. Stern, J. Notte and S. McVey, *AIP Conf. Proc.*, 2007, **931**, 161–167.
21 M. T. Postek, A. Vladár, J. Dagata, N. Farkas, B. Ming, R. Wagner, A. Raman, R. J. Moon, R. Sabo, T. H. Wegner and J. Beecher, *Meas. Sci. Technol.*, 2011, **22**, 24005.
22 M. Leppänen, L.-R. Sundberg, E. Laanto, G. M. de Freitas Almeida, P. Papponen and I. J. Maasilta, *Adv. Biosyst.*, 2017, **1700070**, 1–8.
23 D. Emmrich, A. Beyer, A. Nadzeyka, S. Bauerdick, J. C. Meyer, J. Kotakoski and A. Gölzhäuser, *Appl. Phys. Lett.*, 2016, **108**, 163103.
24 M. E. Schmidt, T. Iwasaki, M. Muruganathan, M. Haque, H. Van Ngoc, S. Ogawa and H. Mizuta, *ACS Appl. Mater. Interfaces*, 2018, **10**, 10362–10368.
25 D. C. Bell, *Microsc. Microanal.*, 2009, **15**, 147–153.
26 M. S. Joens, C. Huynh, J. M. Kasuboski, D. Ferranti, Y. J. Sigal, F. Zeitvogel, M. Obst, C. J. Burkhardt, K. P. Curran, S. H. Chalasani, L. A. Stern, B. Goetze and J. A. J. Fitzpatrick, *Sci. Rep.*, 2013, **3**, 1–7.
27 Z. Li, J. Liu, K. Jiang and T. Thundat, *Nano Energy*, 2016, **25**, 161–169.
28 J. Virtanen, M. Janka and S. Tuukkanen, in *EMBEC & NBC 2017, IFMBE Proceedings 65*, ed. H. Eskola et al., Springer, Singapore, 2018, pp. 1029–1032.
29 G. Daniel and I. Duchesne, in *Proceedings of 7th Int. Conf. Biotechnol. in the Pulp and Paper Industry*, Vancouver, Canada, 1998, pp. B81–B84.
30 A. C. Pierre and G. M. Pajonk, *Chem. Rev.*, 2002, **102**, 4243–4265.
31 J. T. Korhonen, M. Kettunen, R. H. A. Ras and O. Ikkala, *ACS Appl. Mater. Interfaces*, 2011, **3**, 1813–1816.
32 C. Jiménez-Saelices, B. Seantier, B. Cathala and Y. Grohens, *Carbohydr. Polym.*, 2017, **157**, 105–113.
33 M. Pääkkö, J. Vapaavuori, R. Silvennoinen, H. Kosonen, M. Ankerfors, T. Lindström, L. A. Berglund and O. Ikkala, *Soft Matter*, 2008, **4**, 2492–2499.
34 Y. Kobayashi, T. Saito and A. Isogai, *Angew. Chem.*, 2014, **126**, 10562–10565.
35 R. T. Olsson, M. A. S. Azizi Samir, G. Salazar-Alvarez, L. Belova, V. Ström, L. A. Berglund, O. Ikkala, J. Nogués and U. W. Gedde, *Nat. Nanotechnol.*, 2010, **5**, 584–588.
36 Y. Peng, D. J. Gardner and Y. Han, *Cellulose*, 2012, **19**, 91–102.
37 Y. Peng, D. J. Gardner, Y. Han, Z. Cai and M. A. Tshabalala, *J. Colloid Interface Sci.*, 2013, **405**, 85–95.
38 Y. Peng, D. J. Gardner, Y. Han, A. Kiziltas, Z. Cai and M. A. Tshabalala, *Cellulose*, 2013, **20**, 2379–2392.
39 S. Brunauer, P. H. Emmett and E. Teller, *J. Am. Chem. Soc.*, 1938, **60**, 309–319.
40 H. Sehaqui, Q. Zhou, O. Ikkala and L. A. Berglund, *Biomacromolecules*, 2011, **12**, 3638–3644.
41 S. Josset, L. Hansen, P. Orsolini, M. Griffa, O. Kuzior, B. Weisse, T. Zimmermann and T. Geiger, *Cellulose*, 2017, **24**, 3825–3842.
42 A. E. Ketola, A. Strand, A. Sundberg, J. Kouko, A. Oksanen, K. Salminen, S. Fu and E. Retulainen, *BioResources*, 2018, **13**, 5319–5342.
43 E. P. Barrett, L. G. Joyner and P. P. Halenda, *J. Am. Chem. Soc.*, 1951, **73**, 373–380.
44 A. J. Stamm and L. A. Hansen, *J. Phys. Chem.*, 1937, **41**, 1007–1016.
45 J. Sugiyama, R. Vuong and H. Chanzy, *Macromolecules*, 1991, **24**, 4168–4175.
46 M. Rubin and C. Lampert, *Sol. Energy Mater.*, 1982, LBL-14462.
47 F. Jiang and Y.-L. Hsieh, *J. Mater. Chem. A*, 2014, **2**, 350–359.
48 D. Fox, Y. B. Zhou, A. O'Neill, S. Kumar, J. J. Wang, J. N. Coleman, G. S. Duesberg, J. F. Donegan and H. Z. Zhang, *Nanotechnology*, 2013, **24**, 335702.
49 R. Livengood, S. Tan, Y. Greenzweig, J. Notte and S. McVey, *J. Vac. Sci. Technol., B: Microelectron. Nanometer Struct.–Process., Meas., Phenom.*, 2009, **27**, 3244.
50 R. M. Brown, *J. Polym. Sci., Part A: Polym. Chem.*, 2004, **42**, 487–495.
51 M. R. Brown and I. M. Saxena, *Plant Physiol. Biochem.*, 2015, **38**, 41–53.
52 Y. Ogawa, H. Chanzy and J.-L. Putaux, *Cellulose*, 2019, **26**(1), 17–34.
53 G. R. Bullock, *J. Microsc.*, 1984, **133**, 1–15.
54 M. J. Talbot and R. G. White, *Plant Methods*, 2013, **9**, 1.

55 H. Fukuzumi, T. Saito, T. Wata, Y. Kumamoto and A. Isogai, *Biomacromolecules*, 2009, **10**, 162–165.
56 T. Okamoto and G. Meshitsuka, *Cellulose*, 2010, **17**, 1171–1182.
57 K. S. W. Sing, D. H. Everett, R. A. Haul, L. Moscou, R. Pierotti, J. Rouquerol and T. Siemieniewska, *Pure Appl. Chem.*, 1985, **57**, 603–619.
58 K. S. W. Sing and R. T. Williams, *Adsorpt. Sci. Technol.*, 2004, **22**, 773–782.
59 F. Rouquerol, J. Rouquerol, K. S. W. Sing, G. Maurin and P. Llewellyn, *Adsorption by Powders and Porous Solids: Principles, Methodology and Applications*, Elsevier Science & Technology, 2nd edn, 2014.
60 S. Liu, Q. Yan, D. Tao, T. Yu and X. Liu, *Carbohydr. Polym.*, 2012, **89**, 551–557.
61 L.-S. Johansson, T. Tammelin, J. M. Campbell, H. Setälä and M. Österberg, *Soft Matter*, 2011, **7**, 10917.
62 C. J. Chang, C.-Y. Day, C.-M. Ko and K.-L. Chiu, *Fluid Phase Equilib.*, 1997, **131**, 243–258.
63 A. K. Pathan, J. Bond and R. E. Gaskin, *Micron*, 2008, **39**, 1049–1061.
64 V. A. Lovikka, P. Khanjani, S. Väisänen, T. Vuorinen and T. C. Maloney, *Microporous Mesoporous Mater.*, 2016, **234**, 326–335.

IV

MICROENCAPSULATION OF SALMONELLA-SPECIFIC BACTERIOPHAGE FELIX O1 USING SPRAY-DRYING IN A PH-RESPONSIVE FORMULATION AND DIRECT COMPRESSION TABLET-ING OF POWDERS INTO A SOLID ORAL DOSAGE FORM

by

Vinner, G. K., Rezaie-Yazdi, Z., Leppanen, M., Stapley, A. G. F., Leaper, M. C. & Malik, D. J. 2019.

Pharmaceuticals 12 (1), 43.

pharmaceuticals

MDPI

Article

Microencapsulation of *Salmonella*-Specific Bacteriophage Felix O1 Using Spray-Drying in a pH-Responsive Formulation and Direct Compression Tableting of Powders into a Solid Oral Dosage Form

Gurinder K. Vinner [1], Zahra Rezaie-Yazdi [1], Miika Leppanen [2], Andrew G.F. Stapley [1], Mark C. Leaper [1] and Danish J. Malik [1,*]

[1] Department of Chemical Engineering, Loughborough University, Loughborough LE11 3TU, UK; G.Vinner@lboro.ac.uk (G.K.V.); Z.Rezaie-Yazdi@lboro.ac.uk (Z.R.-Y.); a.g.f.stapley@lboro.ac.uk (A.G.F.S.); M.C.Leaper@lboro.ac.uk (M.C.L.)

[2] Department of Physics, Department of Biological and Environmental Science, Nanoscience Center, University of Jyväskylä, 40014 Jyväskylä, Finland; miika.j.leppanen@jyu.fi

* Correspondence: d.j.malik@lboro.ac.uk; Tel.: +44-(0)1509-222507

Received: 6 February 2019; Accepted: 18 March 2019; Published: 22 March 2019

Abstract: The treatment of enteric bacterial infections using oral bacteriophage therapy can be challenging since the harsh acidic stomach environment renders phages inactive during transit through the gastrointestinal tract. Solid oral dosage forms allowing site-specific gastrointestinal delivery of high doses of phages, e.g., using a pH or enzymatic trigger, would be a game changer for the nascent industry trying to demonstrate the efficacy of phages, including engineered phages for gut microbiome modulation in expensive clinical trials. Spray-drying is a scalable, low-cost process for producing pharmaceutical agents in dry powder form. Encapsulation of a model *Salmonella*-specific phage (*Myoviridae* phage Felix O1) was carried out using the process of spray-drying, employing a commercially available Eudragit S100® pH-responsive anionic copolymer composed of methyl methacrylate-*co*-methacrylic acid formulated with trehalose. Formulation and processing conditions were optimised to improve the survival of phages during spray-drying, and their subsequent protection upon exposure to simulated gastric acidity was demonstrated. Addition of trehalose to the formulation was shown to protect phages from elevated temperatures and desiccation encountered during spray-drying. Direct compression of spray-dried encapsulated phages into tablets was shown to significantly improve phage protection upon exposure to simulated gastric fluid. The results reported here demonstrate the significant potential of spray-dried pH-responsive formulations for oral delivery of bacteriophages targeting gastrointestinal applications.

Keywords: antibiotic resistance; bacteriophages; direct compression; microparticles; pH-responsive; spray drying; *salmonella*; tablets

1. Introduction

The emergence of antibiotic resistance in pathogenic bacteria is a serious global health threat. Common enteric bacterial pathogens are becoming progressively resistant to frontline antibiotics. The pipeline for the development of new classes of broad-spectrum antibiotics is not looking promising [1]. In addition to treating gastrointestinal infections in humans, a safe and low-cost strategy to reduce pathogen carriage in livestock and poultry is also needed. National health agencies are increasingly banning general antibiotic use in animals grown for human consumption, e.g., see the European Union (EU) directive on additives for use in animal nutrition [2]. There is an increasing

awareness of the need to move away from broad-spectrum antibiotics and use more specific treatments which do not cause dysbiosis of the microbiome [3].

Lytic bacteriophages (phages) are viruses that infect and kill bacteria including antibiotic-resistant ones in a highly species-specific manner. Commonly occurring gastrointestinal infections are caused by several types of bacteria including *Clostridium difficile*, *Escherichia coli*, *Salmonella* spp., and *Vibrio cholera* [4]. It is estimated that *Salmonella* alone accounts for 1.2 million foodborne illnesses in the United States, with 23,000 hospitalisations and 450 deaths costing an estimated 365 million dollars in medical costs each year [5]. Increasing centralisation and industrialisation of food supply increases the risk of distribution of these hardy organisms. Antimicrobial resistance to "first-line" drugs is increasingly common among *Salmonella* worldwide [6–9]. In animals, decolonisation of the gastrointestinal tract from *Salmonella* may be beneficial for biocontrol to reduce dissemination of harmful bacteria through the food chain, e.g., lairage-associated *Salmonella* transmission in pigs [10]. Phages incorporated in solid oral dosage forms may be mixed in with animal feed for prophylactic or therapeutic applications.

The use of phage therapy is a particularly promising alternative to using broad-spectrum antibiotics for acute enteric infections, because typically in such cases intestinal concentration of the infecting bacteria is high and the causative agent and strain may be suitably diagnosed using rapid diagnostic tools. Solid oral dosage forms that are capable of reliably delivering a therapeutically high phage dose to the site of infection is a major barrier for the treatment of gastrointestinal infections [11–14]. Phages are biological entities requiring protection from stresses typically encountered during manufacturing and storage [15]. The harsh conditions encountered in the human stomach (pH ~1), as well as exposure to bile and digestive enzymes in the gastrointestinal tract, render phages inactive [12,13,16–20]. Previous studies on phage encapsulation focused on extrusion methods, e.g., to produce hydrogel microparticles with variable levels of acid protection [16,17,21]. Recently, more sophisticated microfluidic methods were used, giving precise control over the fabrication of microcapsules. Such methods, however, are difficult to scale-up, costly, and better suited for high-value products [12,13]. There is a need for scalable low-cost methods for producing stable oral dosage forms for delivering bacteriophages to the gastrointestinal tract.

Spray-drying is an industrially acceptable process used to manufacture dry powder forms carrying bioactive agents such as proteins, peptides, attenuated antibodies, and phages [22]. Spray-drying was previously used for producing phage-containing powders in sugar formulations suitable for pulmonary delivery [23–25]. Published studies employing spray-drying to produce phage-containing powders with pH-responsive characteristics are relatively rare; however, a previous study employing spray-dried *E. coli* phages using pure Eudragit S100® showed a ~1 log loss in phage titre in the final spray-dried powder [26]. The *E. coli* phage titre was shown to fall significantly (between 2–3 log reduction) during storage over a period of one year at 20 °C for different phages evaluated in the study [26]. However, the focus of previous research was not on optimising the spray-drying conditions, and evaluation of the effects of excipients on phage viability and storage stability were not adequately addressed. Research is, therefore, needed to evaluate suitable formulations and optimum spray-drying conditions to produce acid stable solid dosage forms for enteric delivery, and these are addressed in this study. Dry powder forms are favoured due to their ease of handling and long-term storage stability, e.g., at ambient temperatures, thereby avoiding the need for a cold supply chain for storage. Encapsulating phages in a stable dry powder form opens possibilities for their use in oral solid dosage forms, e.g., using direct compression to produce tablets for enteric delivery [27].

Commercial spray-dryers typically operate at high temperatures with powders exposed to temperatures around or exceeding 100 °C [28]. This ensures low residual moisture content in the dried product which impacts positively on powder handling and storage stability. Exposing phages to elevated temperatures can be detrimental to phage viability, resulting in the loss of phage titre in the final dried powder. Phages were previously spray-dried at low outlet temperatures using small laboratory-scale spray-dryers with outlet temperatures typically between 40 and 60 °C and using excipients such as trehalose to provide protection from thermal stresses [23,25]. Good excipients

such as trehalose prevent or minimise the effect of thermal stress on the active agents and act as water-replacing agents. Phage proteins may undergo irreversible damage due to the removal of water, which is essential for the maintenance of the hydrogen bonds necessary to stabilise their secondary structure [24]. Trehalose replaces these hydrogen bonds and vitrifies the phages, yielding dry powders with high glass transition temperatures [29].

The aim of the present study was to investigate the effect of spray-drying temperatures and formulation parameters, varying the amount of trehalose and the pH-responsive polymer Eudragit S100® to produce stable dry powders having a high amount of encapsulated phage and good storage stability. The spray-dried powders were tableted using a direct compression process. Powders and tablets containing phages were exposed to simulated gastric fluid to evaluate acid protection. The work reported here allows evaluation of the suitability of these low-cost scalable methods for phage encapsulation in oral solid dosage forms. This study addresses the urgent unmet need for the development of scalable delivery methods to facilitate translation of phages from bench-to-bedside in order to demonstrate the effectiveness of phage therapy in both humans and animals.

2. Materials and Methods

2.1. Model Bacterium and Phage

Salmonella and phage Felix O1 were used as the model bacterium and phage for this study. *Salmonella enterica* ATCC19585 was purchased from LGC standards, EU. Phage Felix O1 was kindly donated by Dr Cath Rees, University of Nottingham, UK [30]. An *S. enterica* strain was used to propagate and enumerate Felix O1.

Bacterial growth and phage propagation were carried out using previously published methods [13]. Briefly, a log-phase culture of *Salmonella* at an optical density (OD) of 0.2 (this typically equates to a viable cell count of ~10^8 colony-forming units (CFU)/mL) was inoculated with Felix O1 at a multiplicity of infection (MOI) of 0.01. The lysate was centrifuged at 2000× *g* and filtered using a 0.2-µm pore size in-line syringe filter (Millipore, Watford, UK) and stored at 4 °C until further use. Plaque assays were used to enumerate phage concentration employing the double overlay agar method; serial dilutions of phages were spotted on a bacterial lawn overlay. All measurements were performed in triplicate. The plaque-forming units (PFU) were counted after incubation for 24 h at 37° C.

2.2. Spray-Drying Conditions and Formulations

Eudragit S100 was kindly supplied by Evonik Germany. D-(+)-Trehalose dihydrate was purchased from Fisher Scientific (Loughborough, UK). Solutions containing different excipient (Eudragit S100 or trehalose) amounts were dissolved in 500 mL of deionised distilled water (dH_2O). For ease of presentation, the following nomenclature is used in the manuscript: the amount of polymer (Eudragit, denoted as "P") to sugar (trehalose, denoted as "S") corresponds to the dissolved percentage (*w*/*v*) of polymer and sugar in the solutions used for spray-drying, e.g., PS21 refers to 2% (*w*/*v*) polymer and 1% (*w*/*v*) sugar in the solution. The following formulations with different proportions of trehalose and polymer were evaluated in the study: PS04 (4% *w*/*v* trehalose), PS30 (3% *w*/*v* polymer), PS32 (3% *w*/*v* polymer, 2% *w*/*v* trehalose), PS21 (2% *w*/*v* polymer, 1% *w*/*v* trehalose), and PS24 (2% *w*/*v* polymer, 4% *w*/*v* trehalose).

In order to dissolve Eudragit, the pH of the water was changed to alkaline (pH 12) via addition of 4 M NaOH (Fisher Scientific, UK) to allow polymer dissolution, followed by pH adjustment to pH 7 using 0.1 M HCl prior to addition of trehalose powder, its dissolution, and then addition of bacteriophages to the solution. For each formulation, typically 1% (*v*/*v*) high-titre phage Felix O1 (~10^{11} PFU/mL) was added to the solution, yielding phage titres of ~10^9 PFU/mL in the final formulations. The phage-containing solutions were spray-dried using a commercially available Labplant spray-dryer SD-06 (Labplant, UK Limited), which is a co-current dryer with a pneumatic

atomiser and a cylindrical drying chamber of dimensions 215 mm outer diameter and 420 mm height. The air exit stream was passed through a high-efficiency particulate air (HEPA) filter prior to discharge. The diameter of the atomization nozzle used throughout the work was 0.5 mm with the measured feed liquid flow rate at 280 mL·h^{-1} and a drying gas air flow rate of ~20 L·s^{-1}. The air inlet temperatures were set at 100 °C, 120 °C, 150 °C, and 180 °C resulting in corresponding air outlet temperatures of 56 ± 2 °C, 66 ± 2 °C, 82 ± 2 °C, and 96 ± 2 °C, respectively. The outlet temperature is only indicative of the highest temperature the phages could be exposed to as dry powders in the collection bottle; temperature in the collection bottle varied between 40 and 60 °C.

2.3. Powder Storage

Following collection, the phage-containing spray-dried powders were stored in sealed screw top bottles. These were stored at either 4 °C or 23 °C for a period of up to three months. At specific time intervals, 0.1 g of powder was removed and dissolved in simulated intestinal fluid (SIF) (10 mg/mL of pancreatin in 0.5 mM KH_2PO_4, pH 7) and the phage titre was enumerated using a plaque assay (described above). Similarly, experiments involving powder or tablet exposure to simulated gastric fluid (SGF) (composition 3.2 mg/mL of pepsin in 0.2 M NaCl, pH adjusted to pH 2 using 5 M HCl) involved weighing a known amount of powder or tablet (typically 0.3 g) and these were subsequently exposed to 10 mL of SGF for 2 h at 37 °C. Following SGF exposure, the powder or tablet samples were centrifuged at 2000× *g* to pellet the suspended solids. Supernatant SGF was removed using a pipette. Then, 10 mL of SIF was added to the pelleted solid material, which was gently vortexed to resuspend the solids, before being left in an orbital incubator shaker (Certomat, Sartorius, UK) at 37 °C and 120 rpm. Complete dissolution of the powders (SIF exposure for 3 h at 37 °C) and tablets (SIF exposure for 5 h at 37 °C) was achieved. Thereafter, 10 µL of the supernatant was removed using a micropipette; then, the sample was serially diluted and plaque assays were performed to measure phage release.

2.4. Direct Compression Tableting of Spray-Dried Powders

Spray-dried powders at an inlet temperature of 150 °C were used for tableting using a Riva Minipress MII (UK) tabletting machine. Approximately 0.3 g of powder was loaded into the punch hole and compressed at a force of 5 kN. The produced tablets were weighed before being stored at 4 °C in sealed tubes for further analysis.

2.5. Ion Microscopy

To analyse the morphology of spray-dried powders, a representative sample from formulation PS21 spray-dried at an inlet temperature 150 °C was examined with ion microscopy. Dried powder was applied on carbon tape attached to a sample stub, and any excess was blown away. A Zeiss Orion NanoFab (University of Jyväskylä) with Ne^+ beam and acceleration voltage of 10 kV was used to cut the microparticle in half. Milling was done using a 45° tilted angle by setting the reduced raster scan rectangle over the area to be removed and scanned until the material disappeared. Ion current values used were typically ~20 pA, resulting in a total processing time of about 1 h. Following sample cutting by milling, the sample stage was rotated through 180° and the cross-section was imaged with He^+. An acceleration voltage of 33 kV, a current of 0.20 pA, 32 line averages, and 1 µs of dwell time were used for He^+ imaging. Flood-gun charge compensation was used during both milling and imaging.

2.6. Moisture Content

The average moisture content (wet basis) of the spray-dried powder was measured gravimetrically. A known mass of sample (approximately 0.5 g) was placed in a dry ceramic crucible and dried in a vacuum oven at 120 °C for a period of 24 h. Measurements were done in triplicate. The sample was then removed, cooled over silica gel in a sealed desiccator, and immediately weighed to limit water

absorption from the atmosphere. The initial and final masses were then used to calculate the wet basis moisture content.

2.7. Particle Size Distribution

A Coulter LS 130 Particle Size Analyzer (Beckman Coulter Inc., High Wycombe, UK) was used to determine the particle size distribution of the spray-dried powders. The device is laser-modulated and uses the optical model Fraunhofer to detect laser diffraction caused by particles. A representative sample from formulation PS21 was taken, loaded into a glass sample containing *n*-hexane (Sigma Aldrich, Gillingham, U.K.) as a suspending medium. The cell was equipped with a stirrer to keep the particles suspended in the solvent. The volume size and cumulative distribution were measured.

2.8. Differential Scanning Calorimetry (DSC) Analysis of Spray-Dried Trehalose Powders

Typically, ~15 mg of the spray-dried powder PS04 (stored upon collection in a dry atmosphere over silica gel in a sealed desiccator) was placed in a pre-weighed DSC aluminium pan. The pan was then hermetically sealed and weighed to 0.1-mg accuracy. The sample was placed in a Q10 DSC (TA Instruments, Crawley, Sussex, UK) and scanned from 25 to 120 °C at a programmed heating rate of 10 °C/min. An empty pan was used as a reference. All DSC measurements were carried out in duplicate. The DSC instrument was calibrated for enthalpy and temperature using an indium standard at the same scan rate. The glass transition temperature was computed from each thermal curve.

2.9. Statistical Analysis

Statistical analysis was carried out using Minitab version 18 (USA). Two-sample *t*-tests were performed ($n = 3$) with reporting of $p < 0.05$ as statistically significant. Where multiple tests were done, the value of alpha was adjusted using the Bonferroni correction. Error bars represent a single standard deviation for the mean values of the replicates.

3. Results

3.1. Optimisation of Spray-Drying Formulation of Felix O1 Phage

Felix O1 at a phage titre of 5×10^9 PFU/mL was spray-dried individually in trehalose (PS04) and Eudragit alone (PS30). The moisture content of PS04 spray-dried powders was typically in the range of ~2–10% (*w*/*w*) and less than 5% (*w*/*w*) for inlet drying temperatures 150 °C and above (Figure S1, Supplementary Materials). The moisture content of PS30 spray-dried powders was considerably higher in the range of ~15–25% (*w*/*w*). The effect of inlet air temperature on phage survival following the spray-drying process was evaluated. The spray-dried phage-containing powders were exposed to SIF for a period of 3 h or until complete dissolution of powder, and the resulting phage concentration was measured (Figure 1). Trehalose was found to be an excellent excipient for the protection of Felix O1 phages exposed to outlet temperatures which were varied between 56 and 96 °C. Phage titre of the feed solution used for spray-drying was 5×10^9 PFU/mL, equating to a theoretical phage concentration of ~1.7×10^9 PFU/g using the assumption that all the phage virions present in the original solution remained viable in the final collected powder, accounting for the amount of dissolved solids in the feed solution. There was no measurable loss in phage titre in the PS04 powders for the entire range of drying temperatures evaluated ($p > 0.05$), and the mean phage titre in the powders was the same as the theoretical yield of ~1×10^9 PFU/g. Felix O1 phages spray-dried in pure Eudragit S100 (PS30) resulted in a significant loss in phage titre; typically, a ~4 log reduction in phage titres was observed at all temperatures post spray-drying in PS30. A two-sample *t*-test of means indicated that the phage titre in the powders at 180 °C was lower in comparison with the phage yield in PS30 powders spray-dried at lower temperatures. For example, at 100 °C, the 95% confidence interval for the mean was between 1.8×10^5 and 3.6×10^5 PFU/g, compared with between 4.6×10^4 and 2.6×10^5 PFU/g at 180 °C

($p < 0.05$). There was no difference in phage titres for PS30 powders spray-dried at 120 °C and 150 °C compared with 100 °C ($p > 0.05$).

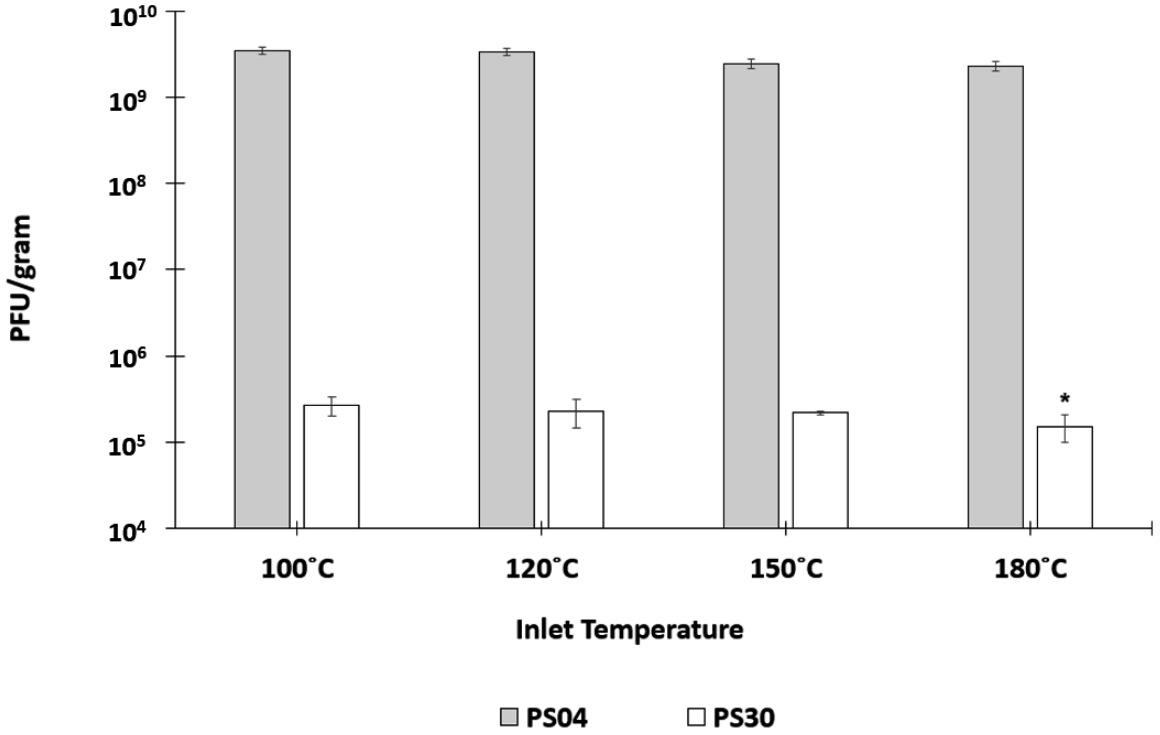

Figure 1. Phage Felix O1 spray-dried at varying inlet air drying temperatures in formulations PS04 and PS30 (see text for description) followed by complete release of phages in simulated intestinal fluid (SIF) (titre measured after 3 h of exposure to SIF). The phage titre of feed solution used for spray-drying was 5×10^9 PFU/mL, equating to a theoretical final phage concentration of ~1.7×10^9 PFU/g. * Indicates significant difference in means for samples at a given temperature compared with the spray-dried sample at 100 °C for the same formulation ($p < 0.05$) using a two-sample *t*-test. Error bars represent one standard deviation; all measurements were done in triplicate ($n = 3$).

The effect of combining trehalose (thermal protection and desiccation resistance) and Eudragit S100® (pH resistance and pH trigger for release) on phage survival following spray-drying at 150 °C was examined using formulations with varying proportions of trehalose (Figure 2). In comparison with phage survival in formulation PS04 (100% trehalose, 2.4×10^9 PFU/g), phage titres remained high at 2.5×10^9 PFU/g (PS24, 67% trehalose), 1.8×10^9 PFU/g (PS32, 40% trehalose), and 1.1×10^9 PFU/g (PS21, 33% trehalose). A two-sample t-test comparing the means for samples PS24 and PS32 with sample PS04 showed no statistical difference in means. However, there was a difference for PS21 (95% confidence interval for difference in means was 5×10^8–2.2×10^9 PFU/g higher for PS04 compared with PS21), i.e., similar in magnitude to the titre of PS21. This suggests that the proportion of trehalose in the polymer formulations does affect phage survival during spray-drying with higher trehalose proportions in the powders PS24 and PS32 yielding higher phage titres.

Spray-dried formulations PS24, PS32, and PS21 were all exposed to SGF for 2 h followed by quantification of the remaining viable phage after dissolution of the polymer in SIF. Felix O1 phages encapsulated in formulations PS24 and PS32 were not sufficiently protected from acid exposure at pH 2. Phage titre in the powders fell by ~2 log from ~10^9 PFU/g to ~10^7 PFU/g for PS24 and PS32. The sample with a higher proportion of polymer content (PS21) showed a considerably smaller reduction in phage titre upon acid exposure from 1.1×10^9 PFU/g to 2.2×10^8 PFU/g, i.e., around a 1 log reduction. The higher loss of phage viability in sample PS24 and PS32 compared with PS21 may be attributed to the higher proportion of trehalose (67% trehalose in PS24 and 40% trehalose in PS32

compared with 33% in PS21) dispersed in the microparticle shell material; sugar may readily dissolve upon exposure to SGF, exposing phages to the acid environment.

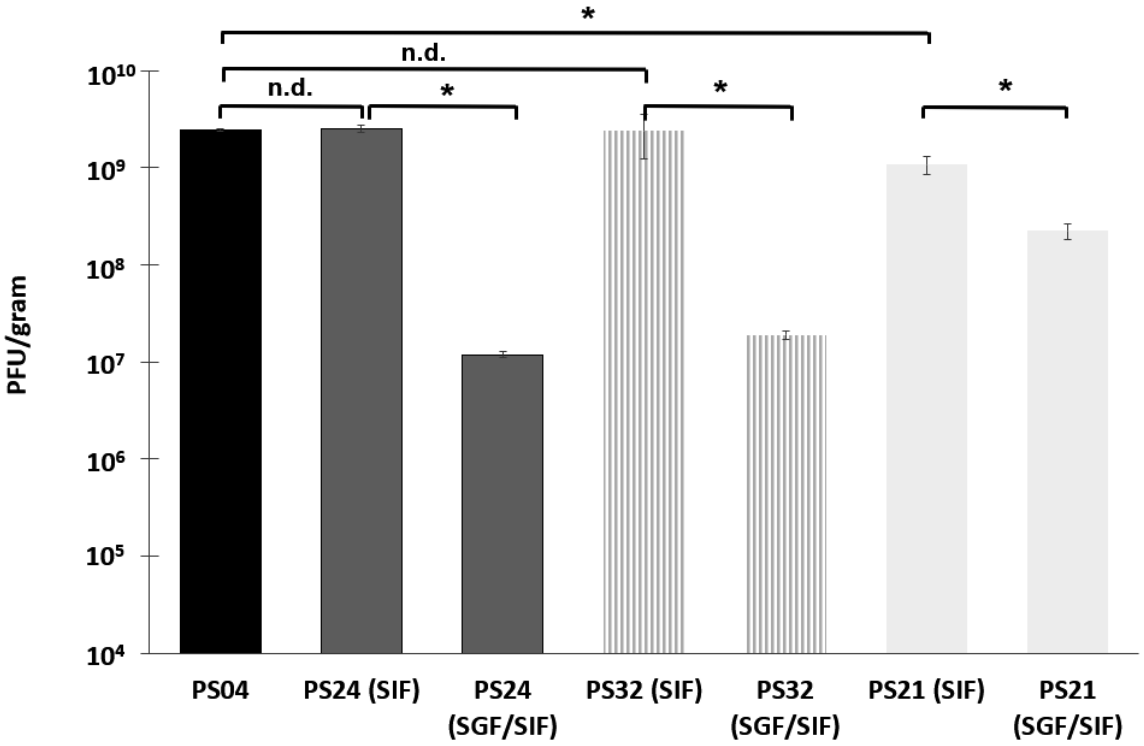

Figure 2. Concentration of encapsulated phage Felix O1 released from spray-dried powders after complete dissolution in SIF (~3 h). Samples labelled SIF were exposed to SIF only without acid exposure, whereas samples labelled simulated gastric fluid (SGF)/SIF were first exposed to simulated gastric fluid (pH 2) for 2 h, subsequently centrifuged to remove the acid supernatant, and then SIF (pH 7) was added to the sample to dissolve the polymer. All formulations were spray-dried at 150 °C inlet temperature corresponding to 82 °C outlet temperature. * Indicates significant difference in means ($p < 0.05$) using a two-sample *t*-test; n.d. means no difference ($p > 0.05$). Error bars represent one standard deviation; all measurements were done in triplicate ($n = 3$).

3.2. Powder Characterisation

Helium ion microscopy (HIM) imaging of the spray-dried powders (PS21) revealed the morphology of the microparticles (Figure 3). Spray-dried microparticles were also examined for their size distribution (see Figure S2, Supplementary Materials). The sizes of the PS21 microparticles spray-dried at an inlet temperature of 150 °C were in the range of 1–10 μm with a d_{50} value of 6 μm and a d_{90} value of 11 μm from the cumulative particle size distribution (Figure S2, Supplementary Materials). The results were consistent with sizes of particles observed using HIM. The microparticles were spheres or flattened spheres with a smooth, defect-free, non-porous surface (Figure 3b). After the milling process, the core of the microparticles was found to be hollow, indicating that the phages were encapsulated in the thin shell structure (Figure 3c). The red circle highlights the capsid heads of two phage virions protruding out of the shell matrix. Small "bumps" (indicated by the red arrow) on the surface of the shell may potentially be phage virions entrapped inside the shell structure (Figure 3d). These bumps were not visible in control particles not containing phages (Figure 3e). The thickness of the microparticle shell was estimated to be between 200 and 300 nm, which is similar in magnitude to phage dimensions (length ~200 nm). The images showed no merging of microparticles or any surface perforations (absence of blow holes).

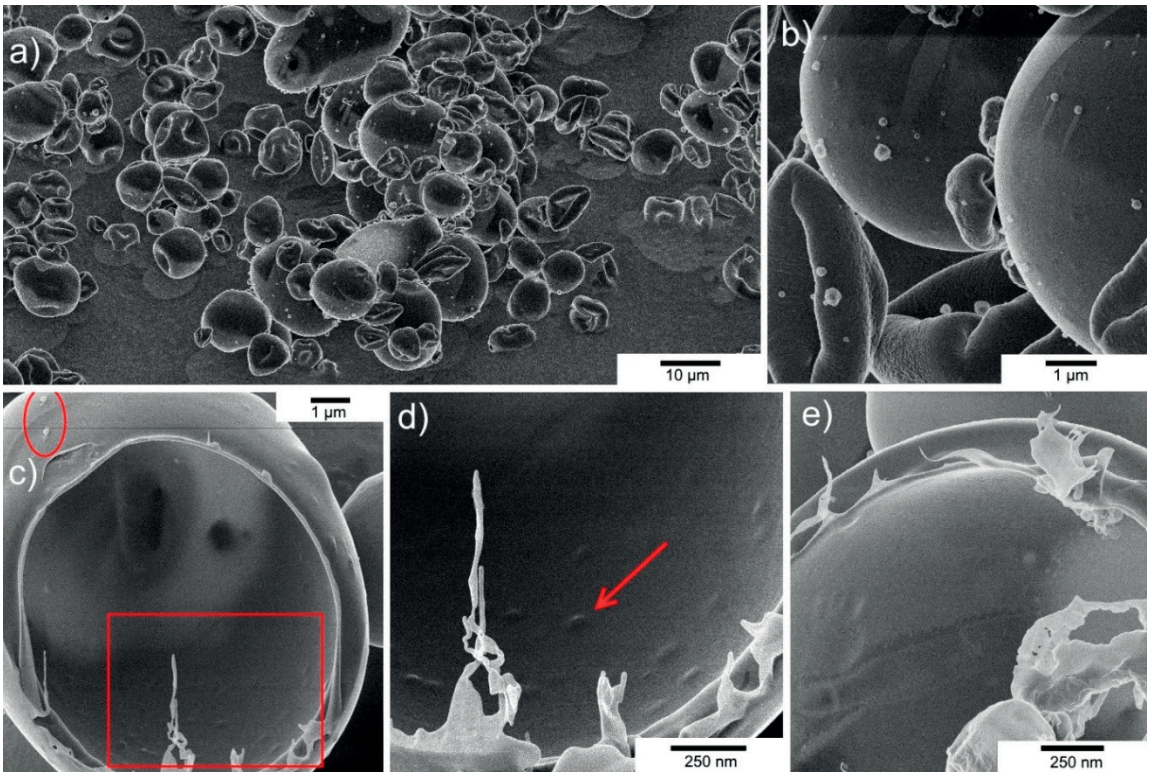

Figure 3. Helium ion microscopy (HIM) images of spray-dried PS21 microparticles (inlet drying temperature 150 °C). (**a**) Spray-dried microparticles were typically <10 µm in size and did not display surface defects such as blow holes. (**b**) Some particles were spherical, whereas others were flattened spheres, and some had a lens-shaped appearance. (**c**) A spherical particle about 10 µm in size was cut in half using a neon ion beam and, after 180° rotation, was imaged with a helium ion beam. Two phage virion particles can be seen in the top left-hand corner (red circle). (**d**) Expanded view of red box area shown in frame (**c**). Bumps in the inside wall of the sphere were found in microparticles containing phages imaged using a higher magnification (red arrow). (**e**) Inside wall of a control microparticle not containing phages.

3.3. Direct Compression Tableting of Spray-Dried Phage

Spray-dried microparticles were tableted using the process of direct compression. The spray-dried powder had suitable processing characteristics, i.e., flowability and hardness to undergo direct compression to produce tablets. The tablets had the following dimensions: diameter of 1 cm, thickness of 0.4 cm, and average weight of 0.3 g (Figure S3, Supplementary Materials). The tablets used in the study were all visually identical (any deformed or chipped tablets were discarded).

Powders containing different proportions of trehalose were evaluated in terms of acid stability following formation of tablets. The results showed there to be a significant difference between the three formulations (Figure 4). Post-spray-drying release in SIF showed titres of more than 1×10^9 PFU/g in the spray-dried powders for all three formulations, which was similar in magnitude to the maximum theoretical phage titre yield (~1.7×10^9 PFU/g) based on the phages present in the original spray-drying solution surviving the spray-drying process. The phage dose loaded in each tablet was approximately 6×10^8 PFU per tablet, and no adverse effect of the compression force on subsequent phage viability was observed (Figure 4). A significant loss of phage titre was observed for all formulations in powder form after exposure to SGF (pH 2) for 2 h. For PS21, phage titre fell from 1.7×10^9 PFU/g to 1.6×10^8 PFU/g, i.e., ~1 log, whereas, for PS24 and PS32, the phage titre fell from ~10^9 PFU/g to ~10^7 PFU/g, i.e., ~2 log. The effect of tableting on acid protection resulted in marked improvement in acid stability for all three formulations. PS21 showed no observable loss in phage titre following 2 h of exposure to SGF (Figure 4). PS24 and PS32 showed only a ~1 log reduction compared

with samples not exposed to SGF, along with a viable phage concentration in the tablets of 1×10^8 PFU/g; this was ~1 log greater than that compared with PS24 and PS32 powders following exposure to SGF (~10^7 PFU/g).

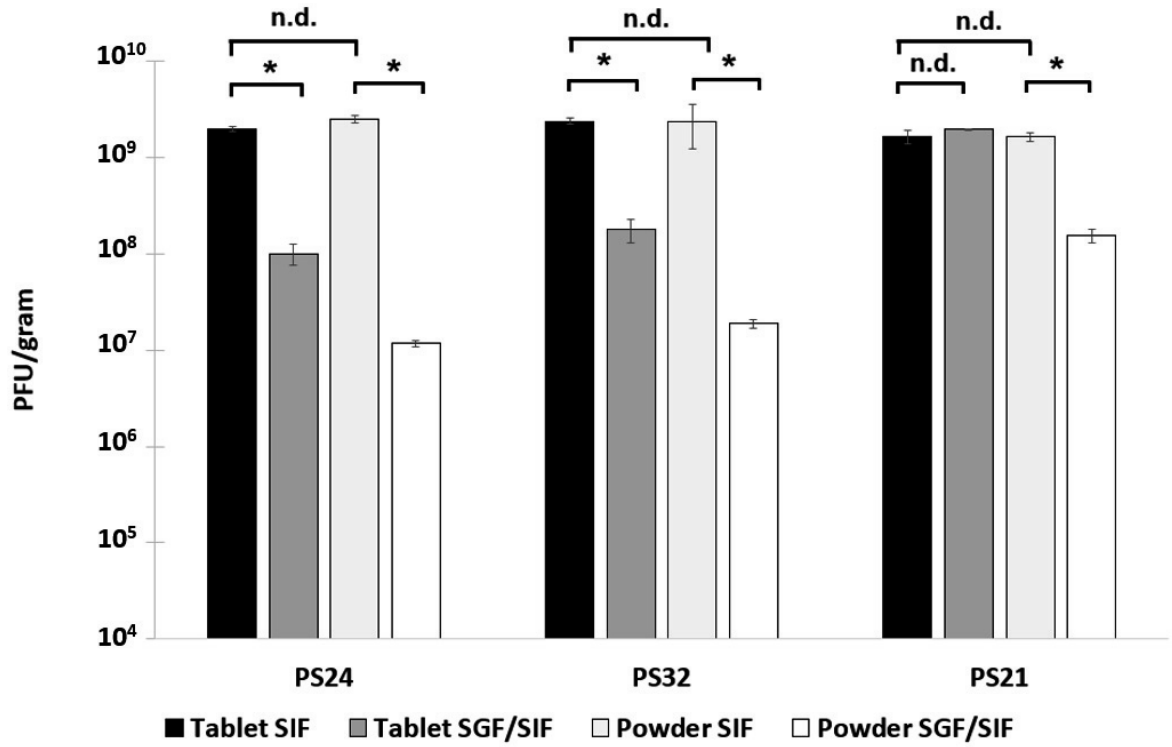

Figure 4. Encapsulated Felix O1 phages released in SIF from spray-dried powders and corresponding tablets using three different formulations. Samples labelled SIF were exposed to SIF only without acid exposure, whereas samples labelled SGF/SIF were exposed first to simulated gastric fluid (pH 2) for 2 h and were then centrifuged, before the supernatant was withdrawn and SIF was added to the sample. Phage titres were measured after 3 h of exposure to SIF for powders and 5 h of exposure to SIF for tablets to ensure complete dissolution of tablets. * Indicates significant difference in means ($p < 0.05$) using a two-sample *t*-test; n.d. means no difference ($p > 0.05$). Error bars represent one standard deviation; all measurements were done in triplicate ($n = 3$).

3.4. Storage Stability of Spray-Dried Phages in Powders

The most promising formulation in terms of acid stability (PS21) was compared with PS04 in terms of storage stability. Spray-dried powders had different initial moisture contents with PS04 3% (*w*/*w*) and PS21 9% (*w*/*w*) (Figure S1, Supplementary Materials). The powders were stored at two different temperatures (4 °C and 23 °C) for a period of three months. A significant loss in phage titre was observed after three months of storage for both PS04 (titre falling from 2.4×10^9 PFU/g to 1.8×10^8 PFU/g) and PS21 (titre falling from 2.7×10^9 PFU/g to 2.4×10^8 PFU/g) at 23 °C in comparison with the phage titre immediately after spray-drying (Figure 5). There was no statistical difference in phage titres for samples stored for one month at 23 °C for both PS04 and PS21 compared with titres immediately after production (0 months). There was no statistical difference in sample means for Felix O1 formulated in PS04 and stored at 4 °C for a period of three months (starting titre 2.4×10^9 PFU/g, and 1.9×10^9 PFU/g after three months). A slight decrease in phage titre was recorded after three months of storage at 4 °C for PS21 (titre falling from 2.7×10^9 PFU/g to 1.1×10^9 PFU/g).

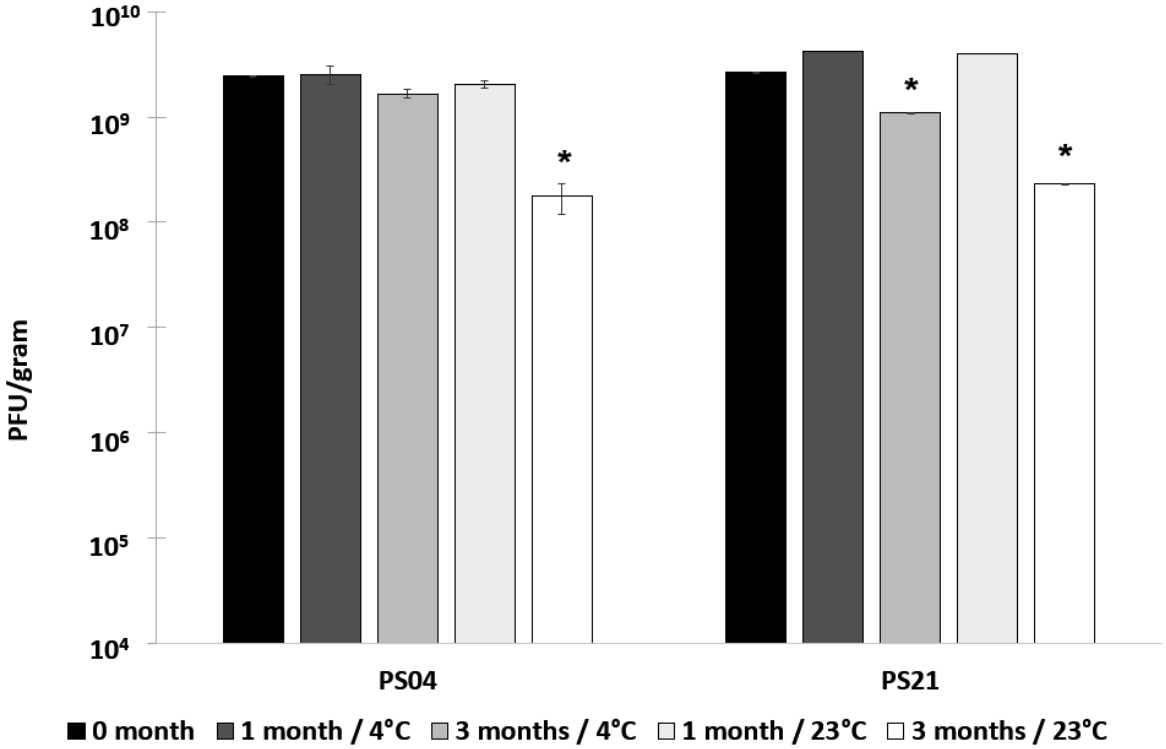

Figure 5. Storage results for formulations PS04 and PS21 used to spray-dry phage Felix O1. Phage titre was measured after one month and three months of storage at 4 °C and 23 °C. * Indicates a significant difference in means in comparison with the mean value immediately after spray-drying (0 months) using a two-sample *t*-test, ($p < 0.05$). Error bars represent one standard deviation; all measurements were done in triplicate ($n = 3$).

4. Discussion

Trehalose was previously shown to protect phages during the spray-drying process [24]. The role of trehalose is both in stabilising phage protein conformation through hydrogen bonding and vitrification due to a high glass transition temperature of the spray-dried powder [29]. High residual moisture in samples spray-dried using relatively low drying temperatures results in lower glass transition temperatures and recrystallisation of the trehalose, which negatively affects phage stability [24]. Spray-drying Felix O1 phage formulated in pure trehalose resulted in no significant loss in phage titre at all spray-drying temperatures tested in the present study. The glass transition temperature of trehalose powders was previously correlated with residual moisture in the sample and amorphous trehalose samples, with moisture content typically below 5% (w/w) having T_g values greater than 50 °C [31]. The glass transition temperatures for PS04 samples were typically above 60 °C immediately following drying, due to low residual moisture content and the amorphous nature of spray-dried trehalose (Figure S4, Supplementary Materials). Phages encapsulated in a glassy matrix in samples having a low moisture content may result in better storage stability at low and ambient storage temperatures (Figure 5). It was not possible to reliably measure the glass transition temperatures of the composite trehalose–polymer PS21 microparticles. However, the moisture content of the samples was found to be dependent on the spray drying temperatures (Figure S1, Supplementary Materials). Spray-drying at a drying temperature of 150 °C resulted in PS21 powder having moisture content less than 10% (w/w) and high titres of viable phages in the dry powders. During the early stages of drying where the droplet surface remains saturated with moisture (100% relative humidity, RH), the droplet surface temperature is maintained at the wet bulb temperature, which is significantly lower than the hot air temperature. As drying progresses, the droplet temperature begins to increase as water diffusion to the droplet surface is not able to maintain 100% RH. As the air flow was co-current, the air

temperature dropped due to evaporative cooling. Once the moisture content of the particles drops, the temperature of the particles begins to increase. However, the exposure period to high temperatures is fairly short due to the short residence times of the particles in the dryer. Felix O1 phages spray-dried in formulations containing ES100 and trehalose, e.g., PS21, remained viable at outlet drying temperatures as high as 82 °C. These results are particularly encouraging since industrial spray-dryers operate at similar temperatures (80–100 °C), which are markedly higher than those previously employed in published studies using small laboratory-scale dryers [25,32]. However, individual phages may show considerable differences in thermal stability and, therefore, spray-drying conditions may need to be optimised appropriately [32].

Spray-drying Felix O1 in a formulation containing only Eudragit S100® (PS30) resulted in a significant loss in phage activity in the final dried powders (Figure 1) compared with spray-drying under identical conditions using pure trehalose (PS04). High residual moisture content in the polymer only powders coupled with the thermal stress may play an important role with respect to phage viability during spray-drying. In the present study, encapsulation of Felix O1 phage in a composite matrix containing different proportions of trehalose and Eudragit S100® resulted in pH-responsive microparticles with good retention of high titres of viable phages (~10^9 PFU/g) in the spray-dried powders. Addition of trehalose in the polymer formulation afforded phages significant protection from the thermal and desiccation stresses encountered during spray-drying compared with phages formulated in the polymer without any trehalose present. PS21 powders had lower moisture content compared with PS30 (Figure S1, Supplementary Materials). A higher proportion of trehalose in the formulation resulted in higher phage titres, e.g., PS32 (40% (*w*/*w*) trehalose) was higher than PS21 (33% (*w*/*w*) trehalose). The particle morphology of PS21 powders was spherical and defect-free (Figure 3). The particles were hollow internally and had an outer skin with phages presumably encapsulated within the shell (Figure 3). The absence of blow holes suggested that the drying temperature and rate of drying were not excessive and, consequently, did not result in an increase in the internal water pressure to burst the microparticles. Formulations resulting in a high proportion of trehalose in the structure of the composite microparticles (PS32 and PS24) showed poor acid stability (Figure 2). However, increasing the proportion of polymer in the microparticle shell (PS21) enhanced acid protection for the phages exposed to SGF at pH 2 for 3 h (Figures 2 and 4). Acid stability of the spray-dried phage powders was improved considerably by forming tablets using a direct compression tabletting process routinely used in the pharmaceutical industry (Figure 4). The physical properties such as bulk density, brittle fracture, and plastic behaviour of the spray-dried microparticles were suitable for the formation of robust tablets (Figure S3, Supplementary Materials). The process of direct compression did not adversely affect the phage titre (Figure 4). The proportion of trehalose in the formulation affected phage acid stability in the tablets with the high polymer-containing formulation (PS21) showing complete acid protection (Figure 4). Felix O1 phages were stable in formulation PS21 stored at 4 °C over a period of three months. The moisture content of the PS21 powders was higher ~9% (*w*/*w*) compared with trehalose-only powders (PS04) under similar drying conditions, which may have adversely impacted on storage stability (Figure S1, Supplementary Materials). Future work will evaluate phage stability in PS21 powders dried at 180 °C which had low moisture content similar in magnitude to PS04 (Figure S1, Supplementary Materials). Optimisation of the proportion of trehalose and Eudragit S100® was needed to ensure good thermal protection for the phages, attributed to trehalose during the spray-drying process, whilst ensuring acid protection due to the presence of high amounts of polymer in the microparticle shell encapsulating the phage. Formulation PS21 was found to be superior to PS24 and PS32 in terms of protecting phages from acid exposure after forming tablets using direct compression. Formulation PS21 afforded phage protection during thermal spray-drying, resulting in dry powders with high viable phage titres showing good storage stability. PS21, therefore, fulfils the criteria of a suitable formulation for production of acid stable oral solid dosage forms using spray-drying.

Spray-drying is a highly scalable industrial process which is suitable for manufacturing encapsulated phages in aqueous polymer formulations, such as the one evaluated in the present

study. The spray-dried powders were spherical with good mechanical and flowability properties and could be reliably tabletted into oral solid dosage forms suitable for enteric delivery. One limitation of the present study is the short residence times and small particle sizes achieved using small laboratory-scale spray-dryers. Bench-top spray-dryers are only capable of producing small particles, typically <10 μm, similar to those produced in this study, which require drying times of only a few seconds. Industrial-scale dryers produce larger particles ~50 μm and, therefore, have considerably longer residence times [28]. Future work needs to evaluate the stability of the phages produced using a pilot-scale spray-dyer resulting in larger particles.

The tableted phages would allow ease of use (good for patient compliance) and reliable delivery of high titres of viable phages at the site of infection in the gastrointestinal tract. These are important advantages and can be achieved using the relatively simple, highly scalable, and low-cost process evaluated in the present study. Phage-containing tablets in standard blister packs would need to be stored under refrigerated conditions, which is not ideal; therefore, further work is needed to improve the formulation such that the tablets can be stored without the need for a cold supply chain. Future work is also needed to evaluate the in vivo release characteristics of the phage-containing tablets and the targeted delivery of phages at specific locations in the gastrointestinal tract.

Supplementary Materials: The following are available at http://www.mdpi.com/1424-8247/12/1/43/s1.

Author Contributions: G.K.V. and D.J.M. conceived and designed the experiments; G.K.V., Z.R.-Y., M.L. and D.J.M. performed the experiments; D.J.M. and G.K.V. analyzed the data; D.J.M., M.C.L., M.L. and A.G.F.S. contributed reagents/materials/analysis tools; G.K.V. and D.J.M. wrote the paper.

Funding: This research was funded by the UK Engineering and Physical Sciences Research Council (EPSRC), grant number EP/M027341/1 and the APC was funded by EPSRC.

Conflicts of Interest: The authors declare no conflict of interest.

References

1. Freire-Moran, L.; Aronsson, B.; Manz, C.; Gyssens, I.C.; So, A.D.; Monnet, D.L.; Cars, O.; ECDC-EMA Working Group. Critical shortage of new antibiotics in development against multidrug-resistant bacteria—Time to react is now. *Drug Resist. Updat.* **2011**, *14*, 118–124. [CrossRef] [PubMed]
2. The European Parliament and the Council of The European Union. *Regulation (EC) No 1831/2003 of the European Parliament and of the Council of 22 September 2003 on Additives for Use in Animal Nutrition*; European Union: Brussels, Belgium, 2003.
3. Sheth, R.U.; Cabral, V.; Chen, S.P.; Wang, H.H. Manipulating Bacterial Communities by in situ Microbiome Engineering. *Trends Genet.* **2016**, *32*, 189–200. [CrossRef] [PubMed]
4. Wikswo, M.E.; Kambhampati, A.; Shioda, K.; Walsh, K.A.; Bowen, A.; Hall, A.J. Outbreaks of Acute Gastroenteritis Transmitted by Person-to-Person Contact, Environmental Contamination, and Unknown Modes of Transmission—United States, 2009–2013. *MMWR Surveill. Summ.* **2015**, *64*, 1–16. [CrossRef] [PubMed]
5. Scallan, E.; Hoekstra, R.M.; Angulo, F.J.; Tauxe, R.V.; Widdowson, M.A.; Roy, S.L.; Jones, J.L.; Griffin, P.M. Foodborne Illness Acquired in the United States—Major Pathogens. *Emerg. Infect. Dis.* **2011**, *17*, 7–15. [CrossRef] [PubMed]
6. Hohmann, E.L. Nontyphoidal Salmonellosis. *Clin. Infect. Dis.* **2001**, *32*, 263–269. [PubMed]
7. Hyeon, J.Y.; Chon, J.W.; Hwang, I.G.; Kwak, H.S.; Kim, M.S.; Kim, S.K.; Choi, I.S.; Song, C.S.; Park, C.; Seo, K.H. Prevalence, Antibiotic Resistance, and Molecular Characterization of *Salmonella* Serovars in Retail Meat Products. *J. Food Prot.* **2011**, *74*, 161–166. [CrossRef] [PubMed]
8. Liu, W.-B.; Chen, J.; Huang, Y.-Y.; Liu, B.; Shi, X.-M. Serotype, Genotype, and Antimicrobial Susceptibility Profiles of *Salmonella* from Chicken Farms in Shanghai. *J. Food Prot.* **2010**, *73*, 562–567. [CrossRef]
9. Klemm, E.J.; Wong, V.K.; Dougan, G. Emergence of dominant multidrug-resistant bacterial clades: Lessons from history and whole-genome sequencing. *Proc. Natl. Acad. Sci. USA* **2018**, *115*, 12872–12877. [CrossRef]
10. Wall, S.K.; Zhang, J.; Rostagno, M.H.; Ebner, P.D. Phage therapy to reduce preprocessing *Salmonella* infections in market-weight swine. *Appl. Environ. Microbiol.* **2010**, *76*, 48–53. [CrossRef]

11. Malik, D.J.; Sokolov, I.J.; Vinner, G.K.; Mancuso, F.; Cinquerrui, S.; Vladisavljevic, G.T.; Clokie, M.R.J.; Garton, N.J.; Stapley, A.G.F.; Kirpichnikova, A. Formulation, stabilisation and encapsulation of bacteriophage for phage therapy. *Adv. Colloid Interface Sci.* **2017**, *249*, 100–133. [CrossRef]
12. Vinner, G.K.; Vladisavljevic, G.T.; Clokie, M.R.J.; Malik, D.J. Microencapsulation of *Clostridium difficile* specific bacteriophages using microfluidic glass capillary devices for colon delivery using pH triggered release. *PLoS ONE* **2017**, *12*, e0186239. [CrossRef] [PubMed]
13. Vinner, G.K.; Malik, D.J. High precision microfluidic microencapsulation of bacteriophages for enteric delivery. *Res. Microbiol.* **2018**, *169*, 522–530. [CrossRef] [PubMed]
14. Andreatti Filho, R.L.; Higgins, J.P.; Higgins, S.E.; Gaona, G.; Wolfenden, A.D.; Tellez, G.; Hargis, B.M. Ability of bacteriophages isolated from different sources to reduce *Salmonella enterica* serovar enteritidis in vitro and in vivo. *Poult. Sci.* **2007**, *86*, 1904–1909. [CrossRef] [PubMed]
15. Jończyk, E.; Kłak, M.; Międzybrodzki, R.; Górski, A. The influence of external factors on bacteriophages—Review. *Folia Microbiol. (Praha)* **2011**, *56*, 191–200. [CrossRef] [PubMed]
16. Ma, Y.; Pacan, J.C.; Wang, Q.; Xu, Y.; Huang, X.; Korenevsky, A.; Sabour, P.M. Microencapsulation of Bacteriophage Felix O1 into Chitosan-Alginate Microspheres for Oral Delivery. *Appl. Environ. Microbiol.* **2008**, *74*, 4799–4805. [CrossRef] [PubMed]
17. Ma, Y.; Pacan, J.C.; Wang, Q.; Sabour, P.M.; Huang, X.; Xu, Y. Enhanced alginate microspheres as means of oral delivery of bacteriophage for reducing *Staphylococcus aureus* intestinal carriage. *Food Hydrocoll.* **2012**, *26*, 434–440. [CrossRef]
18. Dini, C.; Islan, G.A.; de Urraza, P.J.; Castro, G.R. Novel Biopolymer Matrices for Microencapsulation of Phages: Enhanced Protection Against Acidity and Protease Activity. *Macromol. Biosci.* **2012**, *12*, 1200–1208. [CrossRef] [PubMed]
19. Tang, Z.; Huang, X.; Baxi, S.; Chambers, J.R.; Sabour, P.M.; Wang, Q. Whey protein improves survival and release characteristics of bacteriophage Felix O1 encapsulated in alginate microspheres. *Food Res. Int.* **2013**, *52*, 460–466. [CrossRef]
20. Colom, J.; Cano-Sarabia, M.; Otero, J.; Aríñez-Soriano, J.; Cortés, P.; Maspoch, D.; Llagostera, M. Microencapsulation with alginate/$CaCO_3$: A strategy for improved phage therapy. *Sci. Rep.* **2017**, *7*. [CrossRef]
21. Tang, Z.; Huang, X.; Sabour, P.M.; Chambers, J.R.; Wang, Q. Preparation and characterization of dry powder bacteriophage K for intestinal delivery through oral administration. *LWT Food Sci. Technol.* **2015**, *60*, 263–270. [CrossRef]
22. Wanning, S.; Suverkrup, R.; Lamprecht, A. Pharmaceutical spray freeze drying. *Int. J. Pharm.* **2015**, *488*, 136–153. [CrossRef] [PubMed]
23. Matinkhoo, S.; Lynch, K.H.; Dennis, J.J.; Finlay, W.H.; Vehring, R. Spray-Dried Respirable Powders Containing Bacteriophages for the Treatment of Pulmonary Infections. *J. Pharm. Sci.* **2011**, *100*, 5197–5205. [CrossRef]
24. Vandenheuvel, D.; Meeus, J.; Lavigne, R.; Van Den Mooter, G. Instability of bacteriophages in spray-dried trehalose powders is caused by crystallization of the matrix. *Int. J. Pharm.* **2014**, *472*, 202–205. [CrossRef]
25. Leung, S.S.Y.; Parumasivam, T.; Nguyen, A.; Gengenbach, T.; Carter, E.A.; Carrigy, N.B.; Wang, H.; Vehring, R.; Finlay, W.H.; Morales, S.; et al. Effects of storage conditions on the stability of spray dried, inhalable bacteriophage powders. *Int. J. Pharm.* **2017**. [CrossRef]
26. Stanford, K.; McAllister, T.A.; Mazzocco, A.; Waddell, T.E.; Johnson, R.P. Oral delivery systems for encapsulated bacteriophages targeted at *Escherichia coli* O157: H7 in feedlot cattle. *J. Food Prot.* **2010**, *73*, 1304–1312. [CrossRef] [PubMed]
27. Jivraj, M.; Martini, L.G.; Thomson, C.M. An overview of the different excipients useful for the direct compression of tablets. *Pharm. Sci. Technol. Today* **2000**, *3*, 58–63. [CrossRef]
28. Ameri, M.; Maa, Y.F. Spray drying of biopharmaceuticals: Stability and process considerations. *Dry Technol.* **2006**, *24*, 763–768. [CrossRef]
29. Grasmeijer, N.; Stankovic, M.; De Waard, H.; Frijlink, H.W.; Hinrichs, W.L.J. Unraveling protein stabilization mechanisms: Vitrification and water replacement in a glass transition temperature controlled system. *Biochim. Biophys. Acta Proteins Proteom.* **2013**, *1834*, 763–769. [CrossRef] [PubMed]
30. De Siqueira, R.S.; Dodd, C.E.R.; Rees, C.E.D. Evaluation of the natural virucidal activity of teas for use in the phage amplification assay. *Int. J. Food Microbiol.* **2006**, *111*, 259–262. [CrossRef]

31. Chen, T.; Fowler, A.; Toner, M. Literature review: Supplemented phase diagram of the trehalose-water binary mixture. *Cryobiology* **2000**, *40*, 277–282. [CrossRef] [PubMed]
32. Vandenheuvel, D.; Singh, A.; Vandersteegen, K.; Klumpp, J.; Lavigne, R.; Van Den Mooter, G. Feasibility of spray drying bacteriophages into respirable powders to combat pulmonary bacterial infections. *Eur. J. Pharm. Biopharm.* **2013**, *84*, 578–582. [CrossRef] [PubMed]

V

MICROENCAPSULATION OF ENTERIC BACTERIOPHAGES IN A PH RESPONSIVE SOLID ORAL DOSAGE FORMULATION USING A SCALABLE MEMBRANE EMULSIFICATION PROCESS

by

Vinner, G. K., Richards, K., Leppanen, M., Sagona, A. P., & Malik D. J. 2019.

Pharmaceutics, 11(9), 475

pharmaceutics

MDPI

Article

Microencapsulation of Enteric Bacteriophages in a pH-Responsive Solid Oral Dosage Formulation Using a Scalable Membrane Emulsification Process

Gurinder K. Vinner [1], Kerry Richards [1], Miika Leppanen [2], Antonia P. Sagona [3,*] and Danish J. Malik [1,*]

[1] Chemical Engineering Department, Loughborough University, Loughborough, LE11 3TU, UK; G.Vinner@lboro.ac.uk (G.K.V.); K.Richards@lboro.ac.uk (K.R.)

[2] Department of Physics, Department of Biological and Environmental Science, Nanoscience Center, University of Jyväskylä, Jyväskylä, FI-40014, Finland; miika.j.leppanen@jyu.fi

[3] School of Life Sciences and Warwick Integrative Synthetic Biology Centre, University of Warwick, Coventry, CV4 7AL, UK

* Correspondence: d.j.malik@lboro.ac.uk (D.J.M.); a.sagona@warwick.ac.uk (A.P.S.)

Received: 16 July 2019; Accepted: 10 September 2019; Published: 14 September 2019

Abstract: A scalable low-shear membrane emulsification process was used to produce microencapsulated *Escherichia coli*-phages in a solid oral dosage form. Uniform pH-responsive composite microparticles (mean size ~100 μm) composed of Eudragit® S100 and alginate were produced. The internal microstructure of the gelled microcapsules was studied using ion-milling and imaging, which showed that the microparticles had a solid internal core. The microencapsulation process significantly protected phages upon prolonged exposure to a simulated gastric acidic environment. Encapsulated phages that had been pre-exposed to simulated gastric acid were added to actively growing bacterial cells using in vitro cell cultures and were found to be effective in killing *E. coli*. Encapsulated phages were also shown to be effective in killing actively growing *E. coli* in the presence of human epithelial cells. Confocal microscopy images showed that the morphology of encapsulated phage-treated epithelial cells was considerably better than controls without phage treatment. The encapsulated phages were stable during refrigerated storage over a four-week period. The process of membrane emulsification is highly scalable and is a promising route to produce industrial quantities of pH-responsive oral solid dosage forms suitable for delivering high titres of viable phages to the gastrointestinal tract.

Keywords: microencapsulation; bacteriophage therapy; controlled release; enteric infections; pH-triggered release; *E. coli*; Eudragit S100

1. Introduction

The emergence of antibiotic resistance in bacteria is a serious global threat to human health. Common enteric bacterial pathogens have become progressively more resistant to conventional frontline antibiotics [1,2]. Treatment of antibiotic resistant bacterial infections is an urgent priority. National State Health Departments around the world are banning general antibiotic use in animal husbandry; alternative, safe, and low-cost biocontrol strategies to reduce pathogen carriage in livestock and poultry are urgently needed. Development of new classes of novel antibiotics are not keeping pace with the rate of antibiotic resistance [3]. Exploration of alternative treatment options are urgently needed [4]. Truly virulent bacteriophages (phages) are viruses that infect and kill bacteria in a highly specific manner. They represent a promising approach to targeting bacterial infections in

a treatment known as phage therapy [5–8]. The specific interaction between bacteriophages and their bacterial hosts makes them an attractive alternative to employing broad spectrum antibiotics in modulating and maintaining a healthy gut microbiome [4,9]. In instances of enteric bacterial infections where the causative agent and strain may be suitably diagnosed, treatment with a sufficiently high initial phage dose could promote rapid in situ phage multiplication and killing of the targeted bacteria [10–12]. Enteric infections worldwide are typically caused by pathogens such as *Escherichia coli*, *Salmonella spp*, *Vibrio cholerae*, and *Clostridium difficile* [13]. Enteric pathogens could be promising candidates for the development of phage therapy; however, there are significant barriers to be overcome in terms of the logistics of delivering a stable, defined phage dose to the infection site [14].

There is likely to be a significant loss in the titre of orally administered phages by the time they reach the intended infection site [15]. Liquid phage formulations taken orally exposes phages to stomach acidity and digestive tract contents (enzymes such as pepsin and pancreatin), increasing the risk of phage viability loss [16]. A recent in vivo study in chickens showed a significant reduction (3 log reductions compared to the dose given) in viable phages reaching the gastrointestinal tract due to stomach acid exposure [17]. Mice receiving an oral dose (T4 coliphages in drinking water) of 10^9 PFU/g gut contents had a thousand-fold lower phage titer, indicating a sizable loss in phage activity [16]. Phage inactivation attributed to stomach acidity may in part have been responsible for failure of a recent clinical trial in children using phage therapy to treat acute bacterial diarrhoea symptoms [14]. Acidity in the stomach as well as bile and digestive enzymes and other proteases in the intestinal tract and stomach are important environmental stresses for phage inactivation [18–20]. Oral application of phages in Georgia and Poland are typically preceded by gastric neutralization [21]. There is a clear need to protect phages against adverse gastrointestinal environmental conditions and to control their targeted release at the site of infection such as in the lower gastrointestinal tract (GIT) compartments of the cecum and colon for *E. coli* infections; this is achievable through encapsulation [19,20,22]. Microencapsulated phages may also result in longer transit times through the GIT in comparison with application of free phages due to mucoadhesive interactions with the gastrointestinal mucus [23] or in animals such as chickens, where retention of microparticles in the crop may result in slowing their transit through the GIT [17]. The purpose of encapsulation is to protect phages from harsh environmental stresses found in the gastrointestinal tract as well as to protect the phages during processing and storage prior to use [24], whilst yielding a product that is easy to handle and apply, e.g., with animal feed [17].

We report here for the first time the use of a scalable membrane emulsification platform technology to encapsulate phages suitable for targeted delivery to the gastrointestinal tract. Small microparticles with encapsulated *E. coli*-phage K1F in a composite ES100® and alginate matrix were produced using microsieve membranes, which are arrays of uniform micropores. A novel aspect of the research presented here is demonstration of the suitability of microencapsulation of phages using a low-shear membrane emulsification process that allows the manufacture of uniform micron-sized, pH-responsive solid oral dosage forms using acidified oil for the precipitation of Eudragit® S100 (ES100) and calcium ions to induce alginate gelation in solution. The technique affords control over the choice of formulation as well as morphology of the microparticles, including their size and size distribution; these influence phage release kinetics, phage loading, and encapsulation efficiency. The resulting pH-sensitive microcapsules were designed to survive the transition of phages delivered orally via the mouth and through the stomach, followed by phage release in the intestine. The small size of the microcapsules is particularly useful for efficacy testing of encapsulated phages via oral delivery using small-bore gavage tubes for testing in animal models such as in mice and rats.

2. Materials and Methods

2.1. Chemical Reagents

A methyl methacrylate co-methacrylic acid copolymer Eudragit® S100 was bought from Evonik, Germany. Alginate (medium viscosity) was bought from Sigma Aldrich, Gillingham, UK. Miglyol

840 (propylene glycol diester of caprylic/capric acid) was bought from Safic-Alcan UK Ltd., Warrington, UK. Food grade Castor oil was purchased from Elf Foods, Loughborough, UK. Polyglycerol polyricinoleate (PGPR), which is an oil-soluble surfactant, was bought from Aston Chemicals Ltd., Aylesbury, UK. Calcium chloride, *p*-toluenesulfonic acid, Tween 20, and sodium chloride were bought from Fisher Scientific, Loughborough, UK. Sorensen's buffer (0.2 M) was used to dissolve the microparticles. It was prepared by mixing different proportions of potassium phosphate monobasic (KH_2PO_4) with sodium phosphate dibasic (Na_2HPO_4) (for pH 7, 50 mL of KH_2PO_4, and 50 mL of Na_2HPO_4) (Fisher Scientific, Loughborough, UK). Pancreatin and pepsin were bought from Sigma Aldrich, UK for addition to the simulated intestinal fluid and simulated gastric fluid, respectively.

2.2. Model Bacterium and Bacteriophage

E. coli strain EV36, which is a K12/K1 hybrid developed by conjugation of Hfr kps + strain [25], was kindly provided by Dr. Eric R. Vimr. This strain is susceptible to K1-specific phages, including K1F and K1-5 [26]. Phage K1F was kindly provided by Dr. Dean Scholl (to Dr. Sagona) and is a T7-like phage first isolated from sewage in 1984 [27]. *E. coli* strain EV36 cells were made electrocompetent and were transformed with an RFP plasmid according to a published protocol [28].

E. coli strain EV36-RFP cells were cultured in a Luria–Bertani (LB) medium (Oxoid, Ltd., Basingstoke, UK) with the addition of 0.5 mM IPTG and 10 mg/mL Ampicillin sodium salt (Sigma Aldrich, Gillingham, UK).

Phage K1F was propagated on *E. coli* strain EV36-RFP. Phage stocks were propagated by growing a fresh culture of *E. coli* strain EV36-RFP in an incubator shaker at 37 °C until the OD_{550} reached 0.2. Subsequently, phage K1F was added at a Multiplicity of Infection (MOI) of 0.01. Following complete lysis of the bacteria, the culture was centrifuged for 15 min at 2000× g and the supernatant was filtered through a 0.2-μm filter (Millipore, Watford, UK). The phage stock was stored at 4 °C until further use.

The double-layer agar method was used for plaque assays, as described by Mahony et al. [29] and Goh at al. [30]. Briefly, 10 μl of overnight culture of *E. coli* strain EV36-RFP was added to a 50:50 mixture of LB soft agar 0.9% (*w/v)* and salt mixture (0.4 M $MgCl_2$ and 0.1 M $CaCl_2$; Oxoid Ltd. Basingstoke, UK). This was poured onto LB agar plates and set under a laminar flow hood. Ten μL of phage solution was serially diluted ten-fold in LB over an 8-log dilution range 10^{-1} through 10^{-8}. Each dilution was spotted in triplicate and incubated at 37 °C overnight. The next day, the number of phage plaques in each spot were enumerated. In a similar manner, for bacterial growth, serial dilutions of bacterial cultures were spotted on LB agar and incubated overnight at 37 °C. Bacteria concentration was determined by counting colonies and expressed as a colony forming unit (CFU/mL).

2.3. Free Phage Sensitivity at Different pH Values

Simulated gastric fluid (SGF) was used to test phage sensitivity to different pH values. SGF formulation contained 0.2 M NaCl with pepsin at 3.2 mg/mL. Solution pH 2, 2.5, and 3 were adjusted using 0.1 M HCl. For simulated intestinal fluid (SIF) at pH 4 to 7, 0.2 M Sorensen's buffer was used with the addition of 10 mg/mL pancreatin. Time points were taken at 0 min, 30 min, 1 h, 3 h, 5 h, and 24 h. For phages exposed to pH 2 and 2.5, exposure time points were also taken every minute for the first 10 min. A 10-μL sample was removed at each time point and serially diluted 10-fold in LB to 10^{-8} as described above. LB broth was used as a positive control.

2.4. Preparation of Bacteriophage-Containing Water-in-Oil (W/O) Emulsion

The dispersed phase (aqueous phase containing the bacteriophages mixed in a pH-responsive polymer formulation) was prepared by dissolving Eudragit® S100 powder (final working concentration of 10% (*w/v*) in ultrapure water. Typically, 4 mL of 4 M NaOH solution was added to 36 mL of deionised water and 4 g of S100 powder was added to this solution in 100-mL Duran bottles

equipped with a magnetic stirrer bar to aid stirring. The solution was left stirring overnight at 60 °C or until the solution was clear, with complete dissolution of the S100 powder. The resulting solution pH was typically between pH 6.5–7. To this solution, 0.4 g of sodium alginate powder was dissolved by stirring overnight at 60 °C. Ten mL of phage stock with titre ~10^9 PFU/mL in an SM buffer (Trizma base (50 mM, Sigma Aldrich, Gillingham, UK), NaCl (100 mM, Fisher Scientific, Loughborough, UK), $MgSO_4 \cdot 7H_2O$ (8 mM, Fisher Scientific, Loughborough, UK), and 5 M HCl (~10 mL added per litre to adjust to pH 7.5)) was concentrated ten-fold using 100 kDa Amicon Ultrafiltration centrifuge tubes (Millipore, Watford, UK). One mL of concentrated phage stock was added to the cooled S100/alginate solution, resulting in a final phage titre of ~10^9 PFU/mL in the final formulation used to make the microparticles. The continuous (oil) phase for the water-in-oil (W/O) emulsion was prepared by dissolving 5% (*w*/*w*) of PGPR in a mixture of Miglyol 840 and castor oil (9:1 by volume).

Phage-containing S100/alginate droplets were prepared as a W/O emulsion using a batch membrane emulsification dispersion cell (Micropore Technologies Ltd., Redcar, UK). The dispersed phase was introduced into the bottom of the cylindrical glass emulsion chamber (working volume ~100 mL) using a syringe pump (Harvard Apparatus, Cambourne, UK). The base of the cell was equipped with a flat stainless-steel membrane having circular (3.3 cm diameter), 40-µm micropore arrays (Figure 1). The flow rate of the aqueous phase was controlled at 25 mL/h, equating to a flux of 29 l/m^2 h. The glass cell carried the continuous oil phase above the membrane surface. Controlled shear was provided at the membrane surface using a paddle-blade stirrer operated by a 12-V DC motor with the rotation rate set at 250 rpm. Shear at the membrane surface is necessary for droplet detachment from the membrane pore resulting in a W/O emulsion. The dispersed phase was injected through uniformly spaced membrane pores, which were dispersed uniformly over the membrane surface. The stainless-steel membranes were purchased from Micropore Technologies Ltd. (Teesside, UK). They were pretreated with a hydrophobic silane coating by immersing the membrane for 10 min in 1H, 1H, 2H, 2H-Perfluorodecyltriethoxysilane (Sigma Aldrich, Gillingham, UK) prior to use. The stainless-steel membrane with pore size 40 µm had an effective surface area of 8.54 cm^2, with pores spaced at a distance of 200 µm. The continuous phase volume used was 50 mL for every 5 mL of dispersed phase introduced into the glass cell.

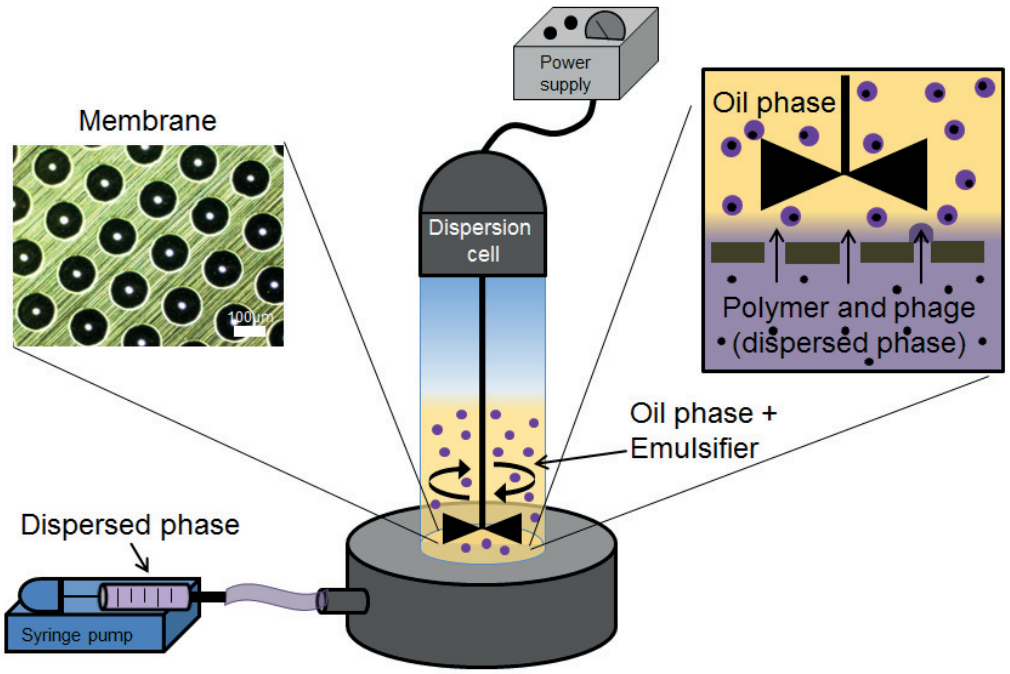

Figure 1. Schematic representation of the membrane emulsification system used for microencapsulation of bacteriophages.

2.5. Preparation and Characterisation of S100/Alginate Microparticles

Fifty-five mL of the W/O emulsion was transferred into 60 mL of the acidified-oil phase in a 150-mL glass vessel. The vessel was equipped with an overhead-stirrer with a three-bladed marine impeller (to provide good axial mixing), which was operated at a low agitation rate ~150 rpm (to avoid droplet breakup and settling). The acidified oil consisted of a 9:1 mixture of miglyol to castor oil with 5% (*v*/*v*) PGPR and 0.05 M toluenesulfonic acid (TSA). The droplets were left to crosslink for 1 h and then allowed to settle (overhead stirrer was turned off). The supernatant was discarded, and any residual miglyol was washed out using 99.9% analytical grade hexane (Sigma Aldrich, Gillingham, UK). The TSA-crosslinked microparticles were resuspended in 0.1 M calcium chloride ($CaCl_2$) with 2% (*v*/*v*) Tween 20, and the solution was pre-acidified at pH 3 (using 0.1 M HCl). Microparticles were left in suspension to crosslink the alginate for 2 h. The crosslinked particles were subsequently allowed to settle, the $CaCl_2$ solution was removed, and the microparticles were washed with 2% (*v*/*v*) Tween 20 acidified at pH 3. The gelled microparticles were stored at 4 °C in sealed, 15-mL falcon tubes.

Photographs of the droplets and particles were taken with an optical microscope (Nikon Eclipse E200, Kingston-Upon-Thames, UK) using a ×4 magnification objective lens. The particle sizes for the W/O emulsion and the gelled microparticles were measured using a Coulter LS series 130 (Beckman Coulter Inc., High Wycombe, USA) instrument employing a Fraunhofer optical model for data regression.

2.6. Sample Preparation for the Ion Microscopy

Critical point drying (CPD) and freeze-drying methods were used to prepare the hydrogel samples for ion microscopy. In the CPD-method, the silicon substrate (Tedpella, Redding, CA, USA) was incubated for 5 min in poly-l-lysine (150–300 kMW, Sigma-Aldrich, Hamburg, Germany), washed three times with ion-exchanged water, and allowed to dry under ambient conditions (room temperature and atmospheric pressure). Using a spatula, hydrogel microparticles were added to 500 µl acetate buffer (50 mM, pH 5, 20 mM $CaCl_2$) and vortexed. The solution was pipetted over the lysine coated substrate, and the microparticles were allowed to adhere for about 1 h at 4 °C and, after that, were fixed overnight with 2.5% glutaraldehyde in 0.1 M acetate buffer (pH 5) at 4 °C. After fixing, the sample was washed two times with 0.1 M acetate buffer (pH 5), stained with 1% OsO_4 for 30 min, and then washed three times with the buffer. Samples were dehydrated in ethanol (EtOH) using a series of steps with increasing EtOH concentration: 50, 70, 90, 95, and 2 × 99.5%, 15 min each. Dehydrated samples were dried to ambient conditions with CPD (Leica CPD 300) using 16 exchange cycles. The dried sample was attached to the metal stub with carbon tape prior to microscopy. In the freeze-drying method, gelled microparticles were frozen on filter paper (0.2-µm pore size, Millipore Ltd., Watford, UK) at −20 °C overnight. The particles were freeze dried (VirTis Wizard 2.0, SP Scientific, New York, NY, USA) for 24 h at 50 Pa pressure and −20 °C. Dried powder was applied directly on the carbon tape, which was attached to the sample stub.

2.7. Ion Microscopy

To analyse the morphology of the hydrogel particles, both freeze-dried and critical-point-dried hydrogels were examined with ion microscopy. Zeiss Orion NanoFab (University of Jyväskylä) with He^+ beam and acceleration voltage 35 kV, 0.20 pA current, 32 line averages, and 1 µs dwell time was used for He^+ imaging. For cutting, an about 20-pA Ne^+ beam with 10 kV acceleration voltage was used. Milling was carried out using a 45 degrees tilted angle by setting the reduced raster scan rectangle over the area to be removed and scanning until the material disappeared. After cutting, the sample stage was rotated 180° and the cross section was imaged with a He^+ beam. Flood gun charge compensation was used during both milling and imaging.

2.8. Encapsulated Phage Release from Microparticles in SIF Following Exposure to SGF

Typically, 1 g of hydrogel microparticles was added to prewarmed 10 mL SIF and shaken in a temperature-controlled incubator shaker (Certomat, Sartorius, UK) at 120 rpm and 37 °C. For SGF exposure, the microparticles were first added to 10 mL SGF and left shaking for an exposure period of 2 h at 37 °C. Particles were centrifuged at 2000× g for 10 min and resuspended in 10 mL SIF (pH adjusted to 5, 6, or 7) until dissolution of the particles was complete. Spot assays were used for enumeration of the released phage by removing 10 μL of the sample at hourly intervals, by serially diluting in LB broth, and by spotting on a host bacterial lawn.

2.9. Storage Stability of Bacteriophages Encapsulated in the Microparticles

Microparticles were stored in screw-top bottles under controlled refrigerated conditions (4 °C) for a period of 4 weeks. At specific time intervals, 0.1 g of microparticles was weighed and dissolved in SIF (as per the protocol outlined above). Phage release was enumerated using plaque assays.

2.10. In Vitro Assay to Measure Phage Release and E. coli Killing Dynamics

The effect of encapsulated phage (EK1F) and free phages in killing bacterial was investigated. Bacteria were grown from a single colony until log phase was reached at 0.2 (O.D. 550) (approximately 10^8 CFU/mL). *E. coli* strain EV36 bacteria were grown either in LB or cell culture media (Leibovitz), as described previously [28]. Two mL of bacteria (at 0.2 OD) were added to 24-well tissue-culture plates. Twenty μL of free phage (non-encapsulated) was added at different concentrations (resulting in working concentrations of 10^2, 10^4, 10^6, and 10^8 PFU/mL). Twenty μL of encapsulated phages (EK1F) were also added to separate wells containing 2 mL of bacterial culture. Encapsulated phages were tested either without acid exposure or after exposure to SGF (pH 2) for 2 h. Negative controls contained 20 μL of EK1F in LB media or cell culture media without bacteria. Positive controls contained bacteria only. After phage/EK1F addition, the samples were withdrawn at hourly intervals up to 5 h post phage/EK1F addition. At each time point, 1 mL of sample was removed to record the O.D. One mL of the sample was centrifuged at 2000× g to remove infected cells and to measure phage titre using plaque assay.

2.11. E. coli Killing Using Encapsulated Phages in an Epithelial Cell Culture Assay

The human urinary bladder epithelial cell line (ATCC® HTB-4™) was acquired from LGC Standards (UK). T24 cells were cultured in uncoated T75 flasks containing McCoy's 5A (Modified) medium (Gibco, MA, USA) supplemented with 10% *v/v* Foetal Bovine Serum (FBS) (Labtech International, UK) and 1% *v/v* Penicillin-Streptomycin and were maintained in 5% CO_2 under a humidified atmosphere, as described previously [28]. For the live microscopy experiments, the T24 cells were seeded onto uncoated 35-mm glass-bottom microscope dishes (ThermoFisher Scientific, UK) at a density of approximately 4×10^4 cells/cm^2 in McCoy's 5A (Modified) medium (supplemented with 10% *v/v* FBS only) and were allowed to settle for 24 h. The culture media were aspirated and replaced with Leibovitz medium (Lonza, Switzerland) that sustains cell viability in the absence of CO_2 equilibrium. While maintaining the confluent cultures at 37 °C, the cultures were incubated with *E. coli* strain EV36-RFP at OD 600 nm of approximately 0.4 to 0.6 (~10^8 CFU/mL), which was added to 1 mL of Leibovitz media for 2 h. Controls included bacteria left to grow with the addition of LB (20 μL) without phages. Free phages at different titres (10^2, 10^4, 10^6, and 10^8 PFU/mL) (volume 20 μL) were added to wells as positive controls. Microparticles with phage K1F (EK1F) were exposed to pH 2 for 2 h before they (20 μL, ~10 mg) were added to infected epithelial cells. In the last 20 min of infection, NucBlue® Live (ThermoFisher Scientific, UK) was added as a stain for the nucleus. The samples were then visualized under an Andor/Nikon Spinning Disk Confocal Laser Microscope. Imaging was taken at hourly intervals (each sample was staggered accordingly). During imaging, the temperature was maintained at 37 °C.

For the experiments with fixed cells on the confocal microscope, T24 cells were seeded onto uncoated 22 × 22 mm coverslips in 6-well plates at a density of 4×10^4 cells/cm^2 and were allowed to settle for 24 h. The cultures were fixed in 4% paraformaldehyde (PFA) (ThermoFisher Scientific, UK),

permeabilised in ice-cold PEM (PIPES, EGTA, Magnesium) buffer with 0.05% Saponin, and quenched with 50 mM NH_4Cl in PBS (Phosphate-Buffered Saline). A wash step with PBS was performed between each step, as described previously [28]. In order to visualize the periphery of the cells, an actin filament stain, Phalloidin CF680R Conjugate (Biotium, CA, USA), was used at a concentration of 5 ug/mL. Finally, the stained cells were mounted on microscope slides using Flouroshield Mounting Medium (Abcam, UK) containing DAPI nuclear stain. All fixed cells were imaged using the Zeiss LSM 880 confocal microscope with Airyscan.

2.12. Statistical Analysis of Results

Minitab version 18 (Minitab UK Ltd, Coventry, UK) was used for carrying out statistical analysis of the data. Sample means were compared using two-sample t-tests ($n = 3$) with reporting of $p < 0.05$ as statistically significant. For multiple tests, the alpha value was adjusted using Bonferroni correction.

3. Results

3.1. Production of Microencapsulated Phages Using Membrane Emulsification

Membrane emulsification was used to prepare phages encapsulated in a W/O emulsion with the volume mean droplet size d50 of ~200 μm (Figure 2). The size distribution of the W/O emulsion indicated the presence of smaller droplets that contributed around 20% of the total volume fraction (Figure 2c). The mean droplet size could easily be varied by changing the shear rate (by varying the rotation speed of the impeller), the membrane pore size, and the viscosity of the continuous phase (data not shown). Conditions were selected to yield droplets in the 100–300 μm range. Gelation of the drops by crosslinking with TSA and calcium chloride resulted in distinct gelled solid microspheres. A slight reduction in the final particle size was noted compared with the primary W/O emulsion, d50 reducing to just over 100 μm (Figure 2b). The hydrogel microparticles easily passed through a 15 G oral gavage needle, indicating they were suitable for oral administration in mice or rats.

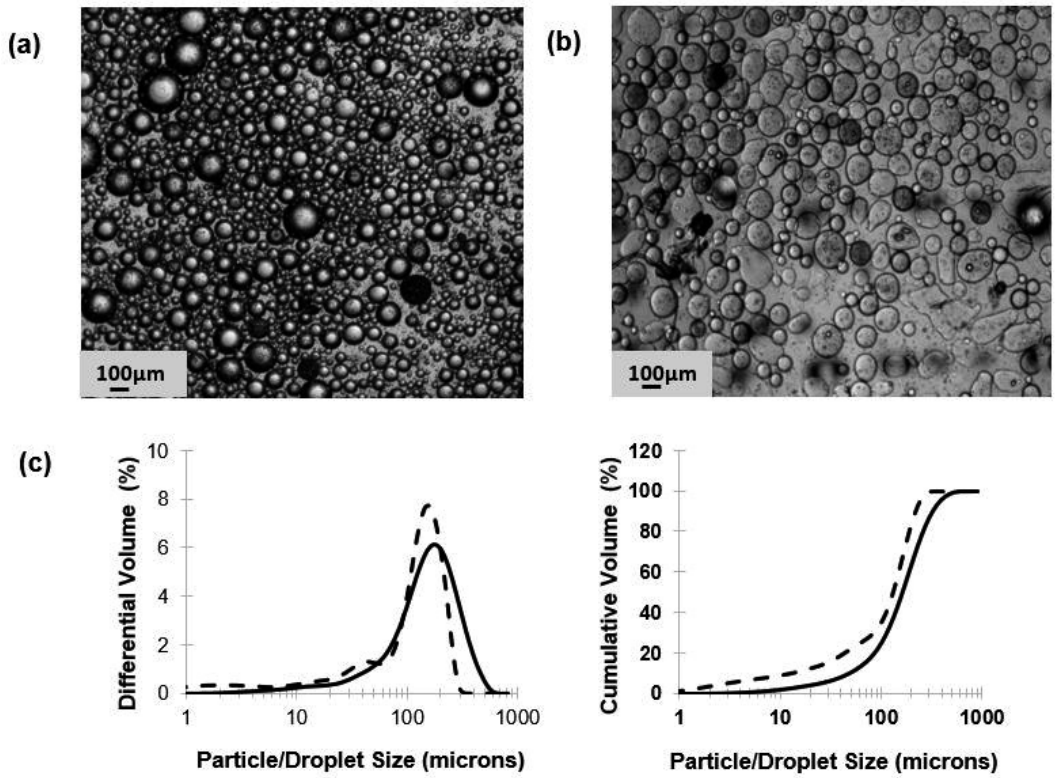

Figure 2. Optical images of water-in-oil (W/O) emulsion droplets, crosslinked microparticles, and size distribution of phage-containing emulsion droplets and microparticles: (**a**) water-in-oil emulsion, (**b**)

microparticles produced from W/O emulsions following toluenesulfonic acid (TSA) and $CaCl_2$ crosslinking, and (**c**) droplet and particle size distributions (solid lines—droplets; dashed lines—particles).

3.2. Microstructure of pH-Responsive Hydrogel Microparticles

The morphology of the microparticles was found to depend upon the sample preparation method (Figure 3). Freeze-dried microparticles appeared as spheres with a smooth and uniform surface (Figure 3a,b). Cutting with Ne^+ allowed visualization of the internal structure of the freeze-dried microparticles, which were found to be porous (Figure 3c). CPD-dried microparticles displayed a sponge-like surface (Figure 3d). The internal structure was found to be porous with an interconnected network of much smaller pores compared to the freeze-dried sample (Figure 3e,f).

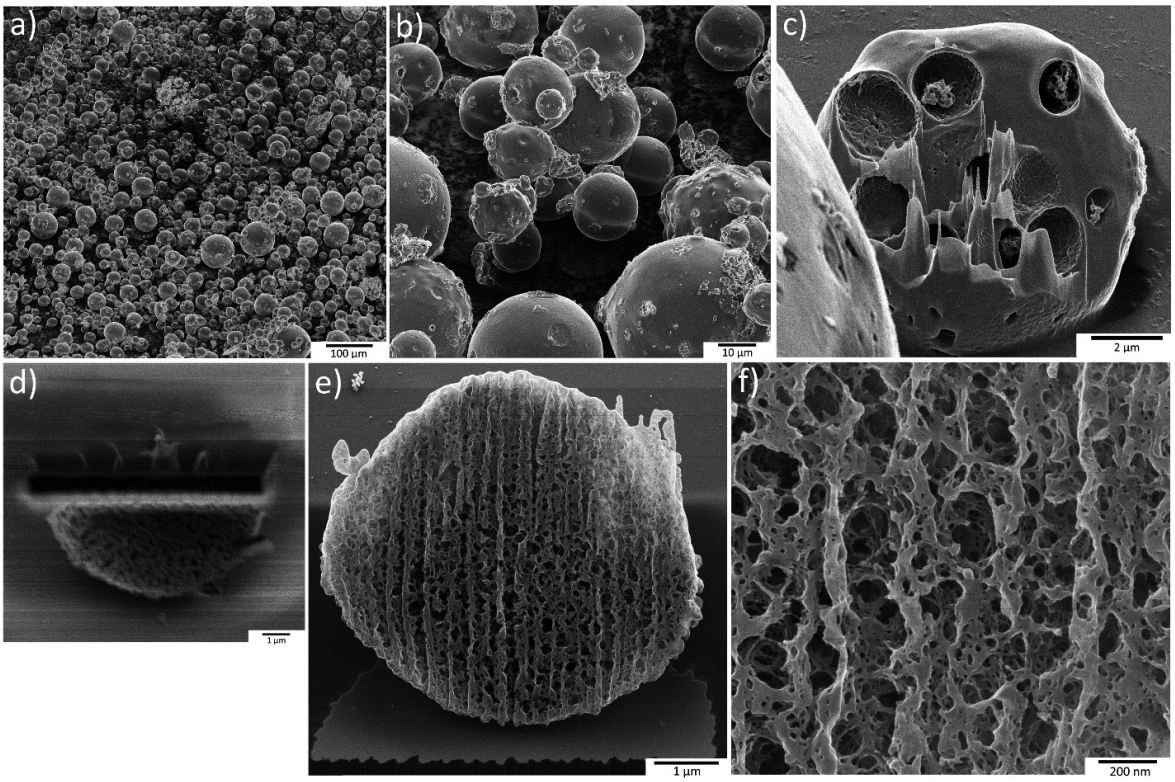

Figure 3. HIM images of freeze-dried and CPD-dried microcapsules: (**a**) Freeze-dried sample with a 1-mm field of view and (**b**) with higher magnification, and (**c**) a microcapsule having a particle size of about 10 µm was cut in half using a Ne^+ beam and, after a 180° rotation, was imaged with He^+. (**d**) A CPD-dried microparticle was also milled with the Ne^+ beam. (**e**) After 180° rotation, the cut surface was imaged with He^+. (**f**) A higher magnification image of the cross section shows the internal porous matrix of the polymer.

3.3. Effect of Acid Exposure on Free Phage and Encapsulated Phage Viability

E. coli-phage K1F lost nearly all activity within 30 min of exposure to pH 2.5 with a modest reduction in phage titre upon exposure to pH 3 (Figure 4). Unencapsulated phages were stable upon exposure to solutions with pH adjusted to pH 4 and above over a 24 h exposure period.

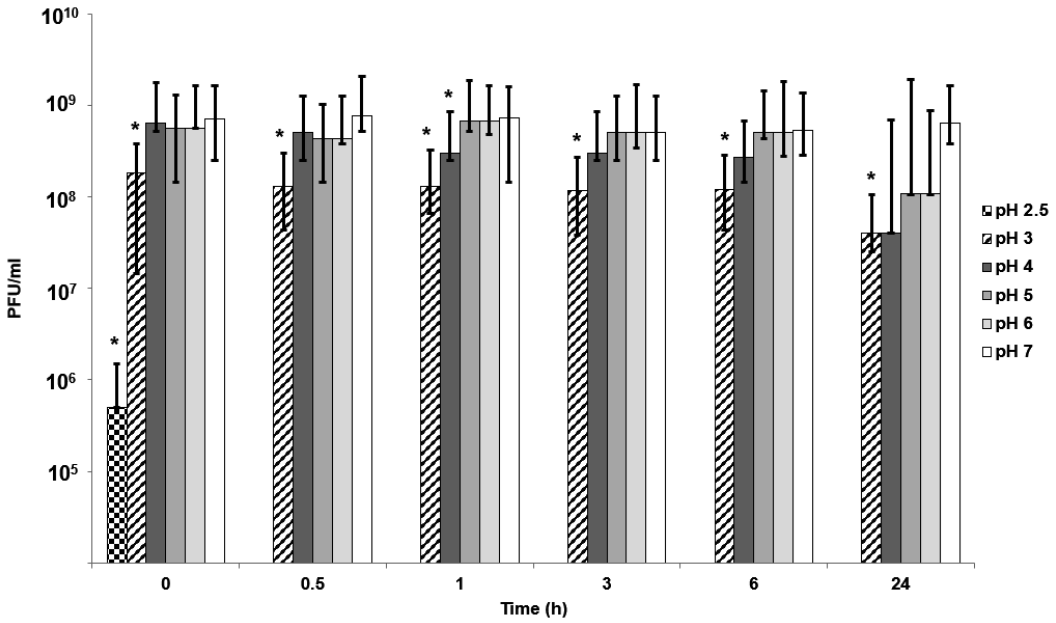

Figure 4. Effect of pH on free phage viability in 0.2 M NaCl solution. *Significantly different phage titres using a 2-sample *t*-test at each condition compared with phages exposed to pH 7 at the corresponding time point. Time point 0 h denotes the time between 0–10 min for phages exposed to all pH values except pH 2.5, where the phage titre reduced rapidly, and data is plotted 10 s post exposure.

Acid stability of encapsulated K1F phages was assessed by exposing the encapsulated phages to SGF with pH adjusted to pH 2 and pH 2.5 (exposure period 6 h). Thereafter, the microparticles were exposed to SIF (pH 7). There was no statistically significant difference in the amount of phages recovered post exposure to pH 2 and pH 2.5 compared with virgin microparticles exposed only to SIF (Figure 5a). Thus, the microparticles afforded complete protection to the encapsulated phages from SGF and released the phages upon subsequent exposure to SIF at pH 7 (Figure 5b). Measurement of the phage release kinetics indicated that most of the encapsulated bacteriophages were released within a 2 h period post SIF exposure for the virgin microparticles; however, the acid exposed microparticles showed around 50% of the encapsulated phages were released after 2 h (Figure 5a). Almost full phage release took ~5 h for the acid exposed microparticles with the amount of viable phages no different to those released from the virgin microparticles (not exposed to SGF).

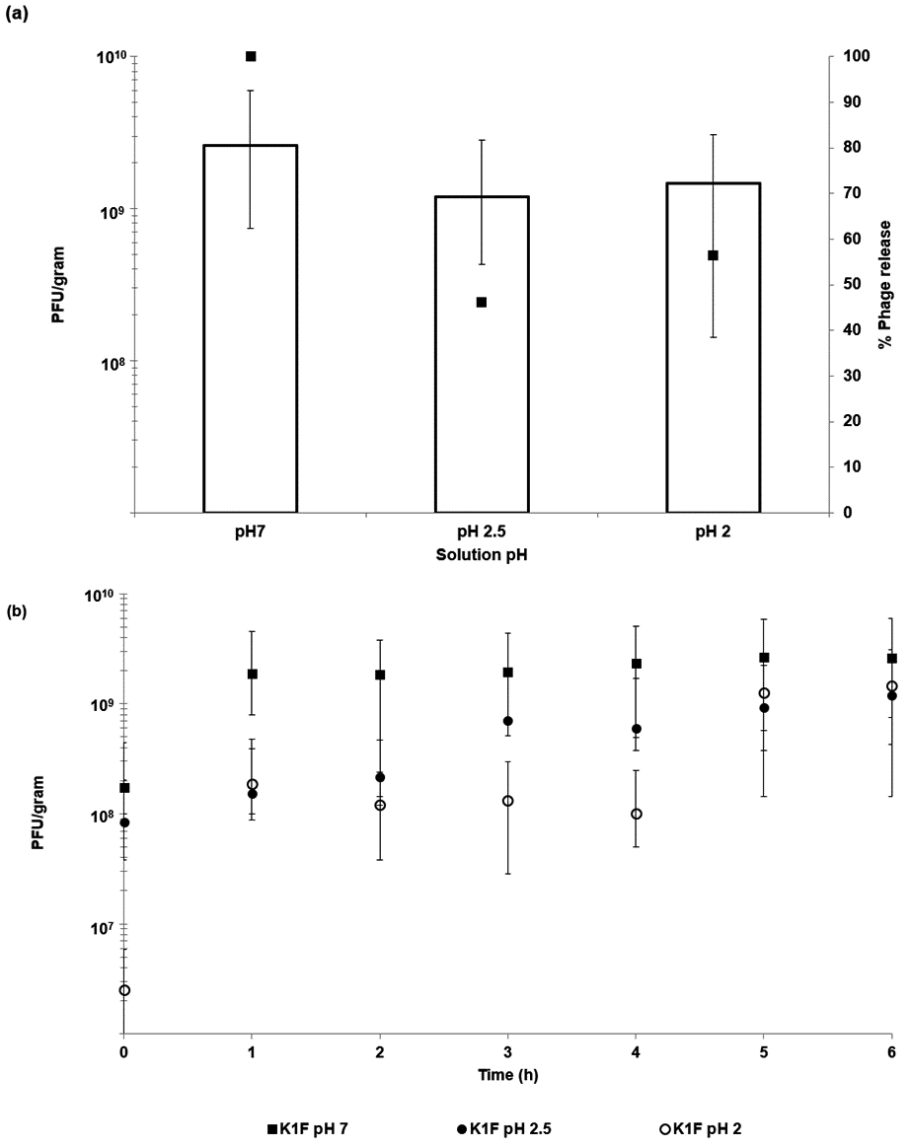

Figure 5. Release of encapsulated bacteriophages from ES100/Alg (EK1F) microparticles: (**a**) Total phage release from EK1F microparticles after 6 h exposure to Simulated Intestinal Fluid (SIF) at pH 7 with and without exposure to Simulated Gastric Fluid (SGF) at pH 2 and pH 2.5 (exposure to SGF for 2 h). The black squares represent the % phage release compared to microparticles not exposed to SGF (pH 7). (**b**) Phage release kinetics from EK1F microparticles over a 6 h exposure period to SIF at pH 7 without and with exposure to SGF at pH 2 and pH 2.5.

Phage-encapsulated microparticles that were previously exposed to SGF (exposure for 2 h, at pH 2) were subsequently tested for phage release at different pH (pH 5, 6, and 7). Less than 10% of the total encapsulated phage dose was released from the microparticles at pH 5 after 2 h (Figure 6). This increased to around 40% at pH 6 and complete release at pH 7 indicating encapsulated phages would be released in areas of the gastrointestinal tract where the pH was 6 or higher.

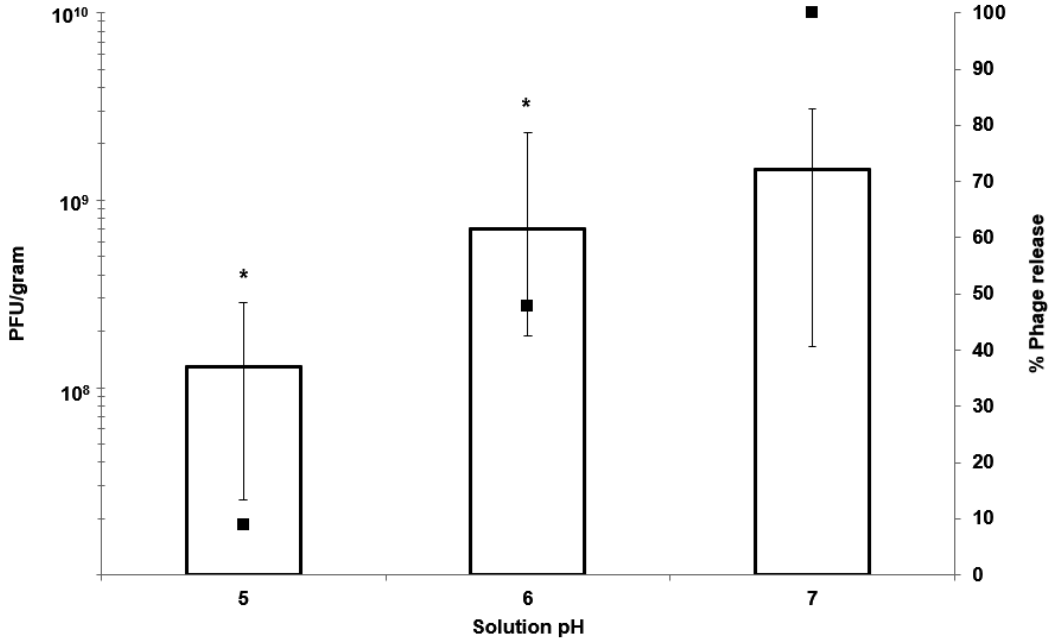

Figure 6. Release of encapsulated bacteriophages from EK1F microparticles: Phage release (PFU g^{-1}) after 5 h from EK1F microparticles in Simulated Intestinal Fluid (SIF) at different pH values following prior exposure of microparticles to Simulated Gastric Fluid (SGF) at pH 2 (2 h exposure to SGF). The black squares represent the % phage release. *Significantly different phage titres ($p < 0.05$) for a 2-sample *t*-test with each sample compared with phage release from EK1F exposed to pH 7.

3.4. Dynamics of Bacteria Killing by Free Phage and Encapsulated Phage Using an In Vitro Assay

The optical density of bacterial cultures was rapidly reduced (within 1 h) following the addition of free phages (not encapsulated) at doses of 10^6 and 10^8 PFU/mL (Figure 7a) as compared with negative controls (no added phage). Addition of free phages at lower doses of 10^2 and 10^4 PFU/mL resulted in continued increase in the optical density of the cultures for the first hour, followed by a decline thereafter; the sample dosed with 10^2 PFU/mL of free phages took 3 h for the OD value to fall below 0.1. The OD profile for the SGF-exposed microencapsulated phages (EK1F) mimicked that of the 10^4 PFU/mL dose. Phage amplification in cultures with low phage dose addition at 10^2 and 10^4 PFU/mL lagged those where doses of 10^6 and 10^8 PFU/mL had been added (Figure 7b). Addition of SGF-exposed EK1F microparticles resulted in in situ phage amplification mimicking the profiles for the low free phage dosed cultures. Phage amplification from virgin and SGF-exposed microparticles in the bacterial cultures showed no significant difference in the time it took for the released phages to amplify (Figure 7c). Negative controls (absence of bacteria) showed release of a dose of 10^6 PFU of phages from the virgin microparticles after 1 h of exposure to the culture media.

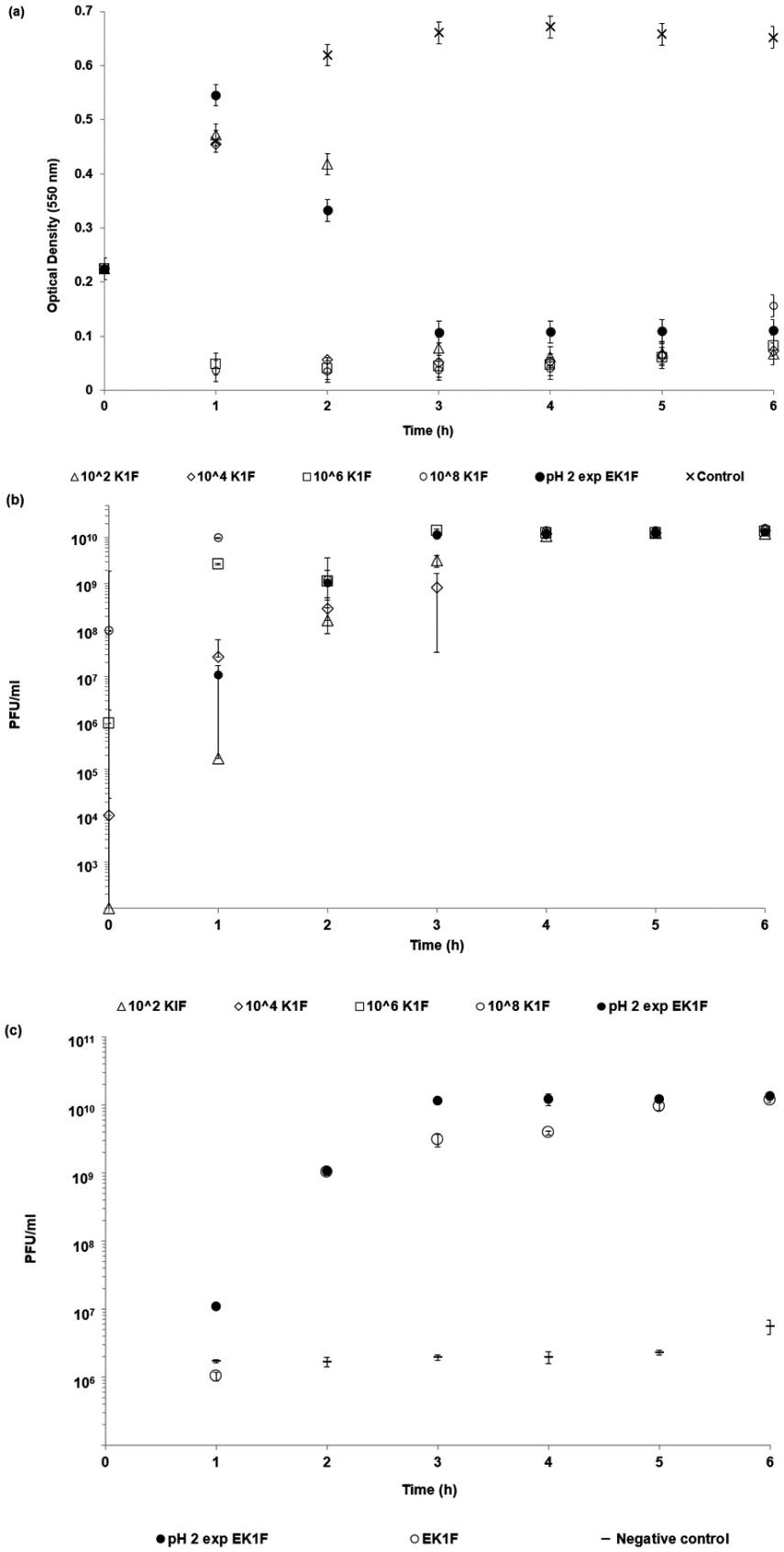

Figure 7. Dynamics of phage killing of *E. coli* strain EV36 bacteria with K1F bacteriophages: (**a**) Optical density curves showing bacteria killing in the presence of different concentrations of added phage, (**b**) phage amplification in the presence of *E. coli* strain EV36, and (**c**) comparison of the phage amplification of EK1F phages encapsulated in microparticles with and without exposure to SGF (2 h). Error bars represent one standard deviation.

3.5. Dynamics of Bacteria Killing by Encapsulated Phage Using an In Vitro Epithelial Cell Assay Observed Using Live and Confocal Microscopy

Actively growing *E. coli* strain EV36 bacterial cells could be visualised using live and confocal microscopy in the presence of epithelial cells (Figure 8, highlighted by the pink/red fluorescent rods). Epithelial cells growing in the presence of actively replicating bacteria showed signs of stress, including shrinking cell nucleus morphology and cell death (Figure 8a i–iii) and visible damage to the actin cytoskeleton (Figure 8c ii). Actin provides support for the cell shape, cell division, and other cellular processes. Epithelial cells treated with SGF-exposed encapsulated phages (phage dose 10^8 PFU/mL) showed clear differences compared with untreated controls (where no phage had been added but bacteria were actively replicating). Phage amplification in the presence of epithelial cells was similar to free phages added at an equivalent dose (Figure 8b i). The concentration of bacterial cells was significantly reduced by the addition of encapsulated phages (Figure 8b ii,iii). The morphology of the epithelial cell nucleus was considerably better, and taut microtubules could be seen (Figure 8c iii) compared with collapsed ones for the untreated controls (Figure 8c ii). Under these conditions, the human cells were considerably healthier and homogeneous compared to control, uninfected cells. The nucleus of healthy cells (Figure 8c i,iii) had a clear round or oval shape and were large. The nuclei of infected cells not treated with phages lost their round shape and appeared considerably smaller. The perimeter of 3 nuclei per image were selected (Figure S1), and corresponding areas for the nuclei were calculated. The area of the nucleus of infected cells was around 50% smaller compared with healthy controls (Table S2).

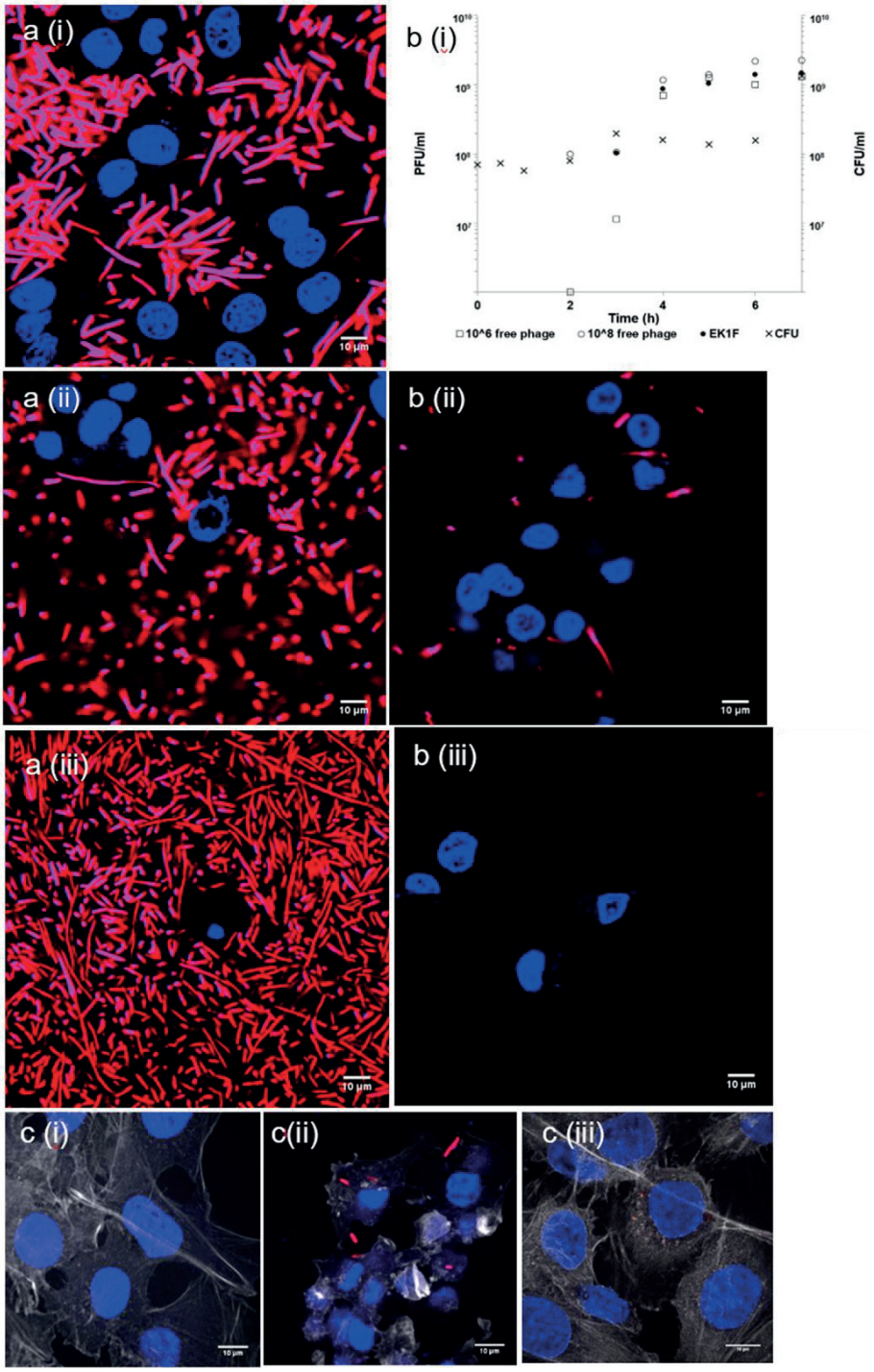

Figure 8. Live and confocal microscopy images of *E.coli* strain EV36-RFP cells (red) treated with microencapsulated EK1F in the presence of epithelial cells (blue): (**a**) Controls without phages (i) 2 h, (ii) 3 h, and (iii) 5 h following incubation of epithelial cells with *E. coli* strain EV36; (**b**) (i) phage amplification of free phages and EK1F in the presence of *E.coli* strain EV36, and live microscopy images of EK1F treated samples at (ii) 3 h and (iii) 5 h following incubation of epithelial cells with *E.coli* strain EV36; (**c**) (i) control epithelial cells not exposed to *E.coli* strain EV36, (ii) damaged actin visible for epithelial cells exposed to EV36 with no phage treatment, and (iii) the condition of actin of epithelial cells exposed to *E.coli* strain EV36 and treated with EK1F.

3.6. Storage Stability of Encapsulated Phage

EK1F microparticles were stored over a course of 4 weeks under refrigerated conditions (at 4 °C). There was no statistical change in the K1F phage titre, which remained constant at ~10^8 PFU g^{-1} over the storage period ($p < 0.05$) (Figure 9 and Table S1).

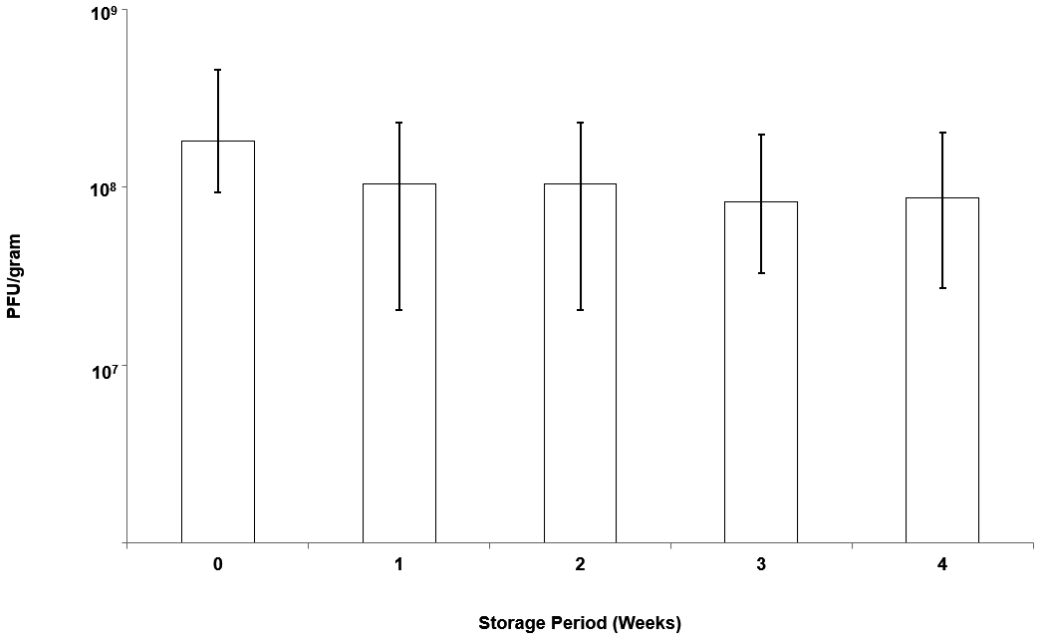

Figure 9. Storage stability of K1F phages in EK1F microparticles refrigerated at 4 °C: Phage titre was evaluated by exposing microparticles to SIF.

4. Discussion

The motivation behind the microencapsulation of phages in solid oral dosage forms stems from the need to protect bacteriophages from gastric acidity and to ensure delivery of high phage doses to specific intestinal compartments at the site of infection, such as the ileum or colon. Targeted delivery of viable phages avoids issues such as a reduction in phage titres due to dilution effects *en route* to the infection site in the lower gastrointestinal tract. Small microparticles (size less than 0.5 mm) are particularly useful for phage delivery via oral gavage for routine preclinical in vivo testing in small animals such as mice and rats. Previous published studies suggest that particles around 100 μm are well suited in terms of protecting bacteriophages from gastric acidity typically encountered in the stomach environment [23,31]. We have previously demonstrated the potential of microfluidic fabrication processes for phage microencapsulation in uniform small pH-responsive microparticles (mean size ~100 μm) containing an encapsulated *Salmonella Myoviridae* Felix O1 phage [31]. Microfluidic single droplet generation units suffer from low throughputs with typical production rates of less than 1 mL/h. Here, we have demonstrated the scalability afforded by the process of membrane emulsification whereby phages may be encapsulated under low shear rate conditions resulting in near 100% phage encapsulation efficiency and preparation of large industrial quantities of uniform small microcapsules (Figure 2). The process can be scaled-up based on the membrane area, e.g., a typical tubular membrane module (50-cm tube length and 1-cm diameter) would produce 0.5 L/h of microparticles operating under the conditions used in the present study. Tube bundles in a shell-and-tube arrangement would allow considerably higher production rates. The membrane emulsification process itself is generic in terms of production of W/O emulsions containing different enteric phages. The process is highly flexible such that different formulations can be used and microparticles with phage-release properties can be tailored for specific applications using different stimuli-responsive polymers. Phages are known to be sensitive to chemical and physical stresses; these include pH [32], temperature [33], exposure to organic solvents [34,35], shear [33,36], and ionic strength [37]. A number of studies have previously shown that particle size is an important factor affecting phage protection from SGF for acid permeable beads [31,38]. We have shown that Eudragit

ES100 co-formulated with medium viscosity alginate in 100-μm microcapsules protected the phages exposed to SGF at pH 2 for an exposure period of 2 h (Figure 5). We have also shown that, when using an in vitro bacterial growth assay, phage-mediated rapid killing of actively growing bacteria requires high titres of viable phages to arrest bacterial growth in a timely fashion (Figure 7). Furthermore, we have demonstrated the suitability of using membrane emulsification to prepare *E. coli*-specific K1F phages encapsulated in pH-responsive microcapsules suitable for gastrointestinal applications (Figure 5). The internal microstructure of the hydrogel beads was shown to consist of a matrix-like polymer network. In all likelihood, the polymer microstructure is swollen in a hydrated state yielding solid core microparticles, which afforded the phages protection from the external gastric acid environment (Figure 3). It was not possible to image encapsulated bacteriophage particles within the internal structure, suggesting that most probably these were buried within the hydrogel matrix. Preparation methods clearly affected visualization of the inner structure of the microparticles. CPD-dried samples most probably represent the wet hydrogel microstructure more accurately because CPD-drying avoids all phase boundaries during the drying process. Previously, it has been shown that freeze-drying modifies the gel matrix structure towards bigger pores [39].

In vitro phage stability experiments where phages (encapsulated and free phages) are exposed to different acidic pH encountered in vivo may be a useful predictor of in vivo phage survival and a prerequisite during formulation development prior to testing in animal models. Unencapsulated bacteriophages were highly sensitive to acidic pH exposure with complete loss of viable phages within 10 min at pH 2.5 (Figure 4). The loss of unencapsulated phage activity upon exposure to an acidic environment highlights the need for encapsulation in order to deliver controlled high doses of viable phages to the infected gut using oral dosage forms. Phage encapsulation in the ES100/alginate microparticles protected them from acid damage at pH 2 (Figure 5). The combination of small particle size (Figure 2) and pH-responsive character of the ES100/alginate microcapsules resulted in release of encapsulated K1F phages within the first hour upon exposure to pH 7 (Figure 5b). Ten percent of the encapsulated phage dose was released at pH 5, whereas 50% of it was released at pH 6 after 2 h of exposure to SIF. Complete phage release and complete dissolution of microparticles occurred within 1 h upon exposure to pH 7 (Figure 5b). It took 1 h longer for SGF-exposed EK1F phages to amplify to levels reached in bacterial cultures compared with a free phage dose of 10^6 PFU/mL (Figure 7b). This delay may be attributed to slower release kinetics of SGF-exposed EK1F phages (Figure 5b). The encapsulated phages were not released immediately upon addition of the microparticles to the bacterial cultures; therefore, it took extra time for the phage titre to reach levels similar to an equivalent free phage dose. Previous published research on phage encapsulation employing large microparticles (~1mm) reported slower sustained-release kinetics for phages encapsulated in alginate microcapsules [19,22]. Colom et al. [23] reported faster release from small alginate microparticles containing $CaCO_3$ as antacid (mean size ~100 μm). However, in that particular study, exposure to simulated gastric fluid (pH 2.8 for 60 min) resulted in between 2 and 3 log reduction in *Salmonella* phage titre, suggesting that even with the addition of $CaCO_3$, phages were highly susceptible to SGF [23]. The ES100/alginate formulation used in the present study for similarly sized small microparticles showed considerably better acid protection and released phages in response to a pH-trigger.

A number of in vivo animal studies have demonstrated dose-dependent phage therapy outcomes for the treatment of bacterial infections, with high doses resulting in better clinical results [40–43]. Controlling the phage dose delivered at the site of infection and controlling the timing of the delivery are important considerations [14]. Careful formulation and encapsulation of phages in uniform-sized microcapsules may facilitate better control over the phage release dynamics. This would allow control over the accurate delivery of high concentrations of phages and effective killing of actively growing *E. coli* strain EV36 cells as shown using an in vitro assay (Figure 7). Even after exposure of encapsulated K1F phages in the microparticles to simulated gastric fluid at pH 2 for 2 h, the released phage dose was unchanged: ~10^9 PFU g^{-1} of microparticles (Figure 5). In humans the mean residence time for gastric emptying is typically less than 3 h for both pre-fed and fasted states [44]. In the absence of phage encapsulation, a loss in phage titre due to stomach acidity exposure would result in a low dose of phages reaching the site of infection. This may potentially result in a

lack of in situ phage amplification in the presence of low concentrations of bacteria during infection [14].

Phage delivery systems and their formulation will impact phage bioavailability at the site of infection. Constituents of the formulation should not be toxic to the host (human) cells. Bacterial killing by K1F phages released from the microcapsules in the presence of epithelial cells suggested that the phages retained potency at levels similar to free phages at the same dose levels (Figure 8). Confocal and live microscopy images provided visual confirmation that phages released from microcapsules arrested bacterial damage to the epithelial cell actin cytoskeleton and significantly decreased the number of bacteria in the human cell environment compared with controls containing bacteria but not treated with phages (Figure 8). Furthermore, the release of encapsulated phages was not hindered by the microparticles interacting with epithelial cells. These in vitro results are encouraging in the development of phage oral dosage formulations as a precursor to future evaluation in animal systems such as mice or rats.

5. Conclusions

We have demonstrated the suitability of using membrane emulsification for phage microencapsulation to produce stimuli-responsive controlled release microparticles. The process is scalable and compatible with cGMP manufacturing and could have significant impact in the field of phage therapy. The controlled release formulations developed in the present study would allow precise delivery of high doses of enteric phages at the site of infection in the GIT with phage release triggered by a change in environmental pH. Other triggers such as the presence of certain enzymes or virulence factors should be explored in future studies.

Supplementary Materials: The following are available online at www.mdpi.com/1999-4923/11/9/475/s1, Figure S1: Measurement of cell nucleus perimeter using Fiji image processing software and calculation of nucleus area for each of the cells shown in Figure 8c. Table S1: Summary of microencapsulated EKF1 storage results. Table S2: Summary of calculated areas of each cell nucleus.

Author Contributions: conceptualization, D.J.M and A.P.S.; methodology, D.J.M and A.P.S.; Helium Ion Microscopy, M.L.; validation, D.J.M. and A.P.S.; formal analysis, G.K.V.; investigation, G.K.V., M.L. and K.R.; resources, D.J.M and A.P.S.; writing—original draft preparation, G.K.V., D.J.M and A.P.S.; writing—review and editing, D.J.M and A.P.S .; supervision, D.J.M.; project administration, D.J.M.; funding acquisition, D.J.M and A.P.S.

Funding: D.J.M. acknowledges the EPSRC Grant no. EP/M027341/1, Tackling Antimicrobial Resistance: An Interdisciplinary Approach. A.P.S. acknowledges the BBSRC Future Leader Fellowship (Grant no. BB/N011872/1) for supporting this work.

Acknowledgments: APS would also like to acknowledge Dr. Dean Scholl, AvidBiotics Corporation, for providing phage K1F and Dr. Eric R. Vimr and Dr. Susan M. Steenbergen for providing the *E. coli* EV36 strain. She would also like to acknowledge WISB (Warwick Integrative Synthetic Biology Centre) for letting her use their microscopy equipment.

Conflicts of Interest: The authors declare no conflict of interest.

References

1. Huttner, A.; Harbarth, S.; Carlet, J.; Cosgrove, S.; Goossens, H.; Holmes, A. Antimicrobial resistance: a global view from the 2013 World Healthcare-Associated Infections Forum. *Antimicrob. Resist. Infect. Control* **2013**, *2*, 31.
2. Merril, C.R.; Scholl, D.; Adhya, S.L. The prospect for phage therapy in western medicine. *Nat. Rev. Drug Discov.* **2003**, *2*, 489–497.
3. Freire-Moran, L.; Aronsson, B.; Manz, C.; Gyssens, I.C.; So, A.D.; Monnet, D.L.; Cars, O. Critical shortage of new antibiotics in development against multidrug-resistant bacteria—Time to react is now. *Drug Resist. Updat.* **2011**, *14*, 118–124. doi:10.1016/j.drup.2011.02.003.
4. Czaplewski, L.; Bax, R.; Clokie, M.; Dawson, M.; Fairhead, H.; A Fischetti, V.; Foster, S.; Gilmore, B.F.; Hancock, R.E.W.; Harper, D.; et al. Alternatives to antibiotics—A pipeline portfolio review. *Lancet Infect. Dis.* **2016**, *16*, 239–251. doi:10.1016/S1473-3099(15)00466-1.

5. Alisky, J.; Iczkowski, K.; Rapoport, A.; Troitsky, N. Bacteriophages show promise as antimicrobial agents. *J. Infect.* **1998**, *36*, 5–15. doi:10.1016/S0163-4453(98)92874-2.
6. Abedon, S.T.; Kuhl, S.J.; Blasdel, B.G.; Kutter, E.M. Phage treatment of human infections. *Bacteriophage* **2011**, *1*, 66–85. doi:10.4161/bact.1.2.15845.
7. Allen, H.K.; Trachsel, J.; Looft, T.; Casey, T.A. Finding alternatives to antibiotics. *Ann. N. Y. Acad. Sci.* **2014**, *1323*, 91–100. doi:10.1111/nyas.12468.
8. Abedon, S.T. Kinetics of phage-mediated biocontrol of bacteria. *Foodborne Pathog. Dis.* **2009**, *6*, 807–815.
9. Bikard, D.; Euler, C.; Jiang, W.; Nussenzweig, P.M.; Gregory, W.; Duportet, X.; Fischetti, V.A.; Marraffini, L.A. Development of sequence-specific antimicrobials based on programmable CRISPR-Cas nucleases. *Nat. Biotechnol.* **2015**, *32*, 1146–1150. doi:10.1038/nbt.3043.Development.
10. Barrow, P.A.; Soothill, J.S. Bacteriophage therapy and prophylaxis: rediscovery and renewed assessment of potential. *Trends Microbiol.* **1997**, *5*, 268–271.
11. Galtier, M.; De Sordi, L.; Maura, D.; Arachchi, H.; Volant, S.; Dillies, M.-A.; Debarbieux, L. Bacteriophages to reduce gut carriage of antibiotic resistant uropathogens with low impact on microbiota composition. *Environ. Microbiol.* **2016**, *18*, 2237–2245. doi:10.1111/1462-2920.13284.
12. Levin, B.R.; Bull, J.J. Population and evolutionary dynamics of phage therapy. *Nat. Rev. Microbiol.* **2004**, *2*, 166–173. doi:10.1038/nrmicro822.
13. Viswanathan, V.K.; Hodges, K.; Hecht, G. Enteric infection meets intestinal function: how bacterial pathogens cause diarrhoea. *Nat. Rev. Microbiol.* **2009**, *7*, 110–119. doi:10.1038/nrmicro2053.
14. Alam Sarker, S.; Sultana, S.; Reuteler, G.; Moine, D.; Descombes, P.; Charton, F.; Bourdin, G.; McCallin, S.; Ngom-Bru, C.; Neville, T.; et al. Oral Phage Therapy of Acute Bacterial Diarrhea With Two Coliphage Preparations: A Randomized Trial in Children From Bangladesh. *EBioMedicine* **2016**, *4*, 124–137. doi:10.1016/j.ebiom.2015.12.023.
15. Young, R.; Gill, J.J. Phage therapy redux—What is to be done? *Science (80-)* **2015**, *350*, 1163–1164. doi:10.1126/science.aad8222.
16. Denou, E.; Bruttin, A.; Barretto, C.; Ngom-Bru, C.; Brüssow, H.; Zuber, S. T4 phages against *Escherichia coli* diarrhea: Potential and problems. *Virology* **2009**, *388*, 21–30. doi:10.1016/j.virol.2009.03.009.
17. Ma, Y.-H.; Islam, G.S.; Wu, Y.; Sabour, P.M.; Chambers, J.R.; Wang, Q.; Wu, S.X.Y.; Griffiths, M.W. Temporal distribution of encapsulated bacteriophages during passage through the chick gastrointestinal tract. *Poult. Sci.* **2016**, *95*, 2911–2920.
18. Choinska-Pulit, A.; Mitula, P.; Sliwka, P.; Choi, A.; Wojciech, Ł.; Skaradzinska, A. Bacteriophage encapsulation: Trends and potential applications a. *Trends Food Sci. Technol.* **2015**, *45*, 212–221. doi:10.1016/j.tifs.2015.07.001.
19. Ma, Y.; Pacan, J.C.; Wang, Q.; Xu, Y.; Huang, X.; Korenevsky, A.; Sabour, P.M. Microencapsulation of Bacteriophage Felix O1 into Chitosan-Alginate Microspheres for Oral Delivery. *Appl. Environ. Microbiol.* **2008**, *74*, 4799–4805. doi:10.1128/AEM.00246-08.
20. Tang, Z.; Huang, X.; Baxi, S.; Chambers, J.R.; Sabour, P.M.; Wang, Q. Whey protein improves survival and release characteristics of bacteriophage Felix O1 encapsulated in alginate microspheres. *Food Res. Int.* **2013**, *52*, 460–466. doi:10.1016/j.foodres.2012.12.037.
21. Slopek, S.; Durlakova, I.; Weber-Dąbrowska, B.; Kucharewicz-Krukowska, A.; Dabrowski, M.; Bisikewicz, R. Results of bacteriophage treatment of suppurative bacterial infections. I. General evaluation of results. *Arch. Immunol. Ther. Exp. (Warsz)* **1983**, *31*, 267–291.
22. Kim, S.; Jo, A.; Ahn, J. Application of chitosan-alginate microspheres for the sustained release of bacteriophage in simulated gastrointestinal conditions. *Int. J. Food Sci. Technol.* **2015**, *50*, 913–918. doi:10.1111/ijfs.12736.
23. Colom, J.; Cano-Sarabia, M.; Otero, J.; Aríñez-Soriano, J.; Cortés, P.; Maspoch, D.; Llagostera, M. Microencapsulation with alginate/CaCO3: A strategy for improved phage therapy. *Sci. Rep.* **2017**, *7*, 41441. doi:10.1038/srep41441.
24. Merabishvili, M.; Vervaet, C.; Pirnay, J.-P.; De Vos, D.; Verbeken, G.; Mast, J.; Chanishvili, N.; Vaneechoutte, M. Stability of Staphylococcus aureus Phage ISP after Freeze-Drying (Lyophilization). *PLoS ONE* **2013**, *8*, 1–7. doi:10.1371/journal.pone.0068797.
25. Vimr, E.R.; Troy, F.A. Regulation of Sialic Acid Metabolism in *Escherichia coli*: Role of N-acylneuraminate pyruvate-lyase. *J. Bacteriol.* **1985**, *164*, 854–860.
26. Scholl, D.; Adhya, S.; Merril, C. Escherichia *coli* K1's Capsule Is a Barrier to Bacteriophage T7. *Appl. Environ.*

Microbiol. **2005**, *71*, 4872–4874. doi:10.1128/AEM.71.8.4872.
27. Scholl, D.; Merril, C. The genome of bacteriophage K1F, a T7-like phage that has acquired the ability to replicate on K1 strains of *Escherichia coli*. *J. Bacteriol.* **2005**, *187*, 8499–8503. doi:10.1128/JB.187.24.8499-8503.2005.
28. Møller-Olsen, C.; Ho, S.F.S.; Shukla, R.D.; Feher, T.; Sagona, A.P. Engineered K1F bacteriophages kill intracellular *Escherichia coli* K1 in human epithelial cells. *Sci. Rep.* **2018**, *8*, 1–18. doi:10.1038/s41598-018-35859-6.
29. Mahony, D.E.; Bell, P.D.; Easterbrook, K.B. Two Bacteriophages of Clostridium difficile. *J. Clin. Microbiol.* **1985**, *21*, 251–254. doi:10.1016/j.disamonth.2009.04.010.
30. Goh, S.; Chang, B.J.; Riley, T.V. Effect of phage infection on toxin production by Clostridium difficile. *J. Med. Microbiol.* **2005**, *54*, 129–135. doi:10.1099/jmm.0.45821-0.
31. Vinner, G.K.; Malik, D.J. High precision microfluidic microencapsulation of bacteriophages for enteric delivery. *Res. Microbiol.* **2018**, *169*, 522–530. doi:10.1016/j.resmic.2018.05.011.
32. Briers, Y.; Miroshnikov, K.; Chertkov, O.; Nekrasov, A.; Mesyanzhinov, V.; Volckaert, G.; Lavigne, R. The structural peptidoglycan hydrolase gp181 of bacteriophage phiKZ. *Biochem. Biophys. Res. Commun.* **2008**, *374*, 747–751. doi:10.1016/j.bbrc.2008.07.102.
33. Vandenheuvel, D.; Singh, A.; Vandersteegen, K.; Klumpp, J.; Lavigne, R.; Van Den Mooter, G. Feasibility of spray drying bacteriophages into respirable powders to combat pulmonary bacterial infections. *Eur. J. Pharm. Biopharm.* **2013**, *84*, 578–582. doi:10.1016/j.ejpb.2012.12.022.
34. Lee, S.W.; Belcher, A.M. Virus-based fabrication of micro- and nanofibers using electrospinning. *Nano Lett.* **2004**, *4*, 387–390. doi:10.1021/nl034911t.
35. Puapermpoonsiri, U.; Spencer, J.; Van Der Walle, C.F. A freeze-dried formulation of bacteriophage encapsulated in biodegradable microspheres. *Eur. J. Pharm. Biopharm.* **2009**, *72*, 26–33. doi:10.1016/j.ejpb.2008.12.001.
36. Leung, S.S.Y.; Parumasivam, T.; Gao, F.G.; Carrigy, N.B.; Vehring, R.; Finlay, W.H.; Morales, S.; Britton, W.J.; Kutter, E.; Chan, H.-K. Production of Inhalation Phage Powders Using Spray Freeze Drying and Spray Drying Techniques for Treatment of Respiratory Infections. *Pharm. Res.* **2016**, *33*, 1486–1496. doi:10.1007/s11095-016-1892-6.
37. Knezevic, P.; Obreht, D.; Curcin, S.; Petrusic, M.; Aleksic, V.; Kostanjšek, R.; Petrović, O. Phages of Pseudomonas aeruginosa: Response to environmental factors and in vitro ability to inhibit bacterial growth and biofilm formation. *J. Appl. Microbiol.* **2011**, *111*, 245–254. doi:10.1111/j.1365-2672.2011.05043.x.
38. Tang, Z.; Huang, X.; Sabour, P.M.; Chambers, J.R.; Wang, Q. Preparation and characterization of dry powder bacteriophage K for intestinal delivery through oral administration. *LWT - Food Sci. Technol.* **2015**, *60*, 263–270. doi:10.1016/j.lwt.2014.08.012.
39. Ketola, A.E.; Leppänen, M.; Turpeinen, T.; Papponen, P.; Strand, A.; Sundberg, A.; Arstila, K.; Retulainen, E. Cellulose nanofibrils prepared by gentle drying methods reveal the limits of helium ion microscopy imaging. *RSC Adv.* **2019**, *9*, 15668–15677. doi:10.1039/c9ra01447k.
40. Smith, W.; Huggins, M.B.; Shaw, K.M. The Control of Experimental *Escherichia coli* Diarrhoea in Calves by Means of Bacteriophages. *J. Gen. Microbiol.* **1987**, *133*, 1111–1126.
41. Wills, Q.F.; Kerrigan, C.; Soothill, J.S. Experimental Bacteriophage Protection against Staphylococcus aureus Abscesses in a Rabbit Model Experimental Bacteriophage Protection against Staphylococcus aureus Abscesses in a Rabbit Model. *Antimicrob. Agents Chemother.* **2005**, *49*, 1220–1221. doi:10.1128/AAC.49.3.1220.
42. Biswas, B.; Adhya, S.; Washart, P.; Paul, B.; Trostel, A.N.; Powell, B.; Carlton, R.; Merril, C.R. Bacteriophage Therapy Rescues Mice Bacteremic from a Clinical Isolate of Vancomycin-Resistant Enterococcus faecium. *Infect. Immun.* **2002**, *70*, 204–210. doi:10.1128/IAI.70.1.204.
43. Cerveny, K.E.; DePaola, A.; Duckworth, D.H.; Gulig, P.A. Phage Therapy of Local and Systemic Disease Caused by Vibrio vulnificus in Iron-Dextran-Treated Mice. *Infect. Immun.* **2002**, *70*, 6251–6262. doi:10.1128/IAI.70.11.6251.
44. Ibekwe, V.C.; Fadda, H.M.; McConnell, E.L.; Khela, M.K.; Evans, D.F.; Basit, A.W. Interplay between intestinal pH, transit time and feed status on the in vivo performance of pH responsive ileo-colonic release systems. *Pharm. Res.* **2008**, *25*, 1828–1835. doi:10.1007/s11095-008-9580-9.

VI

RESOLVING BIO-NANO INTERACTIONS OF E.COLI BACTERIA-DRAGONFLY WING INTERFACE WITH HELIUM ION AND 3D-STRUCTURED ILLUMINATION MICROSCOPY TO UNDERSTAND BACTERIAL DEATH ON NANOTOPOGRAPHY

by

Bandara, C., Ballerin, G., Leppänen, M., Tesfamichael, T., Ostrikov K., Whitchurch, C. 2020.

ACS Biomater. Sci. Eng (forthcoming)
DOI: 10.1021/ acsbiomaterials.9b01973

Resolving Bio-Nano Interactions of E.coli Bacteria-Dragonfly Wing Interface with Helium Ion and 3D-Structured Illumination Microscopy

Chaturanga D. Bandara[†‡], Giulia Ballerin[†], Miika Leppänen[§], Tuquabo Tesfamichael[‡], Kostya (Ken) Ostrikov[‡], and Cynthia B. Whitchurch[†]*

[†]The ithree institute, University of Technology Sydney, Ultimo, NSW 2007, Australia

[‡]School of Chemistry, Physics and Mechanical Engineering, Science and Engineering Faculty, Queensland University of Technology (QUT), Brisbane, Queensland 4001, Australia

[§]Nanoscience Center, Department of Physics, Department of Biological and Environmental Science, University of Jyvaskyla, FI-40014 Jyvaskyla, Finland

Corresponding Author: chaturangab@yahoo.com

ABSTRACT

Obtaining a comprehensive understanding of the bactericidal mechanisms of natural nanotextured surfaces is crucial for the development of fabricated nanotextured surfaces with efficient bactericidal activity. However, the scale, nature, and speed of bacteria-nanotextured surface interactions make the characterization of the interaction a challenging task. There are currently several different opinions regarding the possible mechanisms by which bacterial membrane damage occurs upon interacting with nanotextured surfaces. Advanced imaging methods could clarify this by enabling visualization of the interaction. Charged particle microscopes can achieve the required nanoscale resolution but are limited to dry samples. In contrast, light-based methods enable the characterization of living (hydrated) samples but are limited by the resolution achievable. Here we utilized both helium ion microscopy (HIM) and 3D structured illumination microscopy (3D-SIM) techniques to understand the interaction of Gram-negative bacterial membranes with nanopillars such as those found on dragonfly wings. Helium ion microscopy enables cutting and imaging at nanoscale resolution while 3D-SIM is a super-resolution optical microscopy technique that allows visualization of live, unfixed bacteria at ~100 nm resolution. Upon bacteria-nanopillar interaction, the energy stored due to the bending of natural nanopillars was estimated and compared with fabricated vertically aligned carbon nano tubes. With the same deflection, shorter dragonfly wing nanopillars store slightly higher energy compared to carbon nanotubes. This indicates that fabricated surfaces may achieve similar bactericidal efficiency as dragonfly wings. This study reports *in situ* characterization of bacteria-nanopillar interactions in real-time close to its natural state. These microscopic approaches will help further understanding of bacterial membrane interactions with nanotextured surfaces and the bactericidal mechanisms of nanotopographies so that more efficient bactericidal nanotextured surfaces can be designed, fabricated and their bacteria-nanotopography interactions can be assessed *in situ*.

KEYWORDS: bactericidal topography, bio-nano interactions, 3D SIM, dragonfly wing, helium ion microscopy, ion beam milling

INTRODUCTION

The ability of bacteria to adhere, survive and subsequently form biofilms on abiotic surfaces is the leading cause for infection of prostheses after surgery, resulting in implant failure and revision surgery.[1-2] In recent years, there have been significant efforts to reduce infection by developing various nanotextured surfaces on implantable medical devices.[3-4] These nanotextured surfaces are often inspired by nature and the fabricated topographies are expected to reduce initial bacterial adhesion or kill any bacteria attempting to attach to the surface. The investigation of bacteria-nanotopography interactions has, therefore, become a significant research interest for the efficient and effective development of advanced fabricated bactericidal nanotextured surfaces (NTS) for biomaterials application.[5-8] This is a growing field of research as nanotextured surfaces do not leach bactericidal chemicals, and therefore, the bactericidal property is conserved for longer periods compared to chemical approaches.[9-10] Furthermore, nanotextured surfaces are non-toxic and more effective at controlling bacterial strains that produce extracellular polymeric substance (EPS) secretions.[11-12]

The mechanical bactericidal efficacy of nanotextured surfaces is dependent on the nanotopography, architecture of the nanostructures, surface chemistry, and the type of bacteria.[5, 8, 13-16] However, the antibacterial mechanisms and effectiveness of surface parameters are not well understood due to the limited understanding of the bacteria-nanotopography interactions. Recently, various views and explanations have been proposed for understanding the mechanism of membrane damage.[5-8, 13, 17-21]

Cicada wing-like nanostructures are mainly bactericidal against Gram-negative bacteria.[7, 22-23] The initial report of bacterial membrane damage upon interaction with cicada wing nanostructures used a differential DNA staining method with confocal microscopy to

predict the membrane integrity.[6, 24] This approach is an indirect measurement of the membrane condition, where two separate fluorescent markers are used to stain the nuclear material. As this approach only stains the DNA, it cannot be used to directly visualize the bacterial membrane. Furthermore, due to the limitations in spatial resolution, confocal microscopy can only resolve the color variation of the bacterium and cannot provide detailed information on its membrane integrity. Therefore, to obtain a comprehensive understanding of the effects on the bacterial membrane during the interaction with nanostructures it would be better to directly visualize the bacterial membrane using super-resolution microscopy techniques such as 3D structured illumination microscopy (3D-SIM) which utilizes spatially patterned fluorescence excitation beams to achieve a resolution of ~100 nm.[25-26]

Recently, the interfaces where bacteria and natural nanotopographies interact have been observed at nanoscale resolution through the use of some of the most advanced microscopic techniques available to-date including helium ion microscopy (HIM), transmission electron microscopy (TEM), focused ion beam (FIB) techniques and faster atomic force microscopy (AFM).[13-14, 17, 27-33] These approaches have furthered our understanding of bacteria-nanotopography interactions of natural surfaces. High-resolution TEM images of cross-sectioned interfaces revealed that the natural nanopillars under the bacteria are bent during the interaction and that dead bacteria appeared to have produced EPS.[13]

A recent study on the interactions of bacteria with Vertically Aligned Carbon Nano Tubes (VACNT) reported the bending of these nanostructures during bacteria-VACNT interactions.[19] This is in line with the previously reported bactericidal effects of natural nanopillar topography of dragonfly wing with *E.coli.*[13] In this study of bacteria-VACNT interactions, the energy stored during bending of multiple lengths of VACNT were quantified and it was determined that shorter VACNT had more efficient bactericidal activity.[19] The bactericidal mechanisms of VACNT and black silicon (bSi) have been described in terms of purely physical mechano-

bactericidal basis and significant differences in the two different surfaces were observed. In bSi, no significant difference in bactericidal activity was reported with changing nanopillar height or its surface chemistry. bSi nanostructure was identified as rigid structures that do not bend when interacting with bacteria.[24] A separate study suggested that adhesion is important but that the membrane is not necessarily pierced by the bSi nanostructures to achieve bactericidal activity.[14] For VACNT, it was reported that the shorter nanopillars are more efficient and that VACNT bend during interaction with bacteria and in some cases, the bottom surface of bacteria is wrapped by VACNT.[19] Furthermore, when the surface chemistry of VACNT was changed using O_2 or CF_4 plasma, significant changes to bacterial adhesion on the surface and bactericidal activity of *Pseudomonas aeruginosa* were identified.

One plausible mechanism to explain bacterial membrane damage upon interaction with nanopillars is that the bacterial cell first attaches onto the nanopillars, and then while attempting to move parallel to the surface, the nanopillars are bent and membrane damage occurs through shearing.[13] Another study has suggested that attempted bacterial cell division on the titanium nanotopography causes bacterial membrane damage.[34] When the membrane damage occurs, characteristic EPS production, bending of nanopillars and leaking of cytoplasm are observed. These post-membrane damage characteristics have recently been observed in HIM, TEM, SEM and confocal studies.[13-14, 17, 19, 28-32, 35] However, as these events occur rapidly, and only at the cell surface, the images obtained using these techniques commonly show the bacteria flattened on the nanopillars, apparently due to membrane damage. It should be noted that the interaction between bacterial membranes and nanostructures can't be resolved with these microscopic tools due to the limitation in the time-scale or spatial resolution. For instance, extensive sample preparation steps are required prior to imaging the bacteria-nanotopography interaction by TEM, and for FIB, metal deposition is required to reduce charge accumulation for successful

cross-sectioning.[13, 35] As these steps are time-consuming, they prevent capturing the initial stages of the bacterial membrane damage process.

The different observations and interpretations in reports of the mechanobactericidal action of different nanotextured surfaces provides the rationality for further investigations. It remains of urgent and significant importance to evaluate the mechanism of bactericidal activity and bio-nanotopography interactions for both fabricated and natural nanotopographies towards gaining a deeper understanding of the bactericidal mechanism for the efficient design of bactericidal biomaterials.

A combination of approaches could be used to overcome the technical limitations encountered to-date in order to more clearly understand the membrane damage process. One approach would be to freeze the initial stages of bacteria-nanosurface interactions and utilize an imaging technique such as HIM which has nanoscale resolving power with a larger depth of focus and microscale field of view to image the entire interaction. A second, complementary approach could be to utilize a super-resolution optical imaging technique such as 3D-SIM to image bacteria-nanotopography interactions *in situ* under physiological conditions in real-time. The aim of this work, therefore, was to explore the possibilities of utilizing both HIM and 3D-SIM to provide further insights into *E.coli* bacteria-nanotopography interactions in real-time and thereby further our understanding of the mechanobactericidal activity of the natural nanotopography of dragonfly wings to Gram-negative bacteria. This work supplements previous studies carried out with Gram-negative *Escherichia coli* and dragonfly wings using HIM, AFM, FIB and TEM.[13, 35] In previous studies, we have used TEM and FIB to expose the interface. Here, we use the Ne^+ beam to cross-section and He^+ to image exposed interface using HIM, thereby we avoid excessive sample preparation steps associated with TEM and FIB. Special attention is given to the characteristics of the bacteria-nanopillar interface.

RESULTS AND DISCUSSION

Interfacial characteristics of dragonfly wing nanopillars-*Escherichia coli* bacterium by Helium Ion Microscopy (HIM). We used helium ion microscopy (HIM), to examine the bacteria-nanotopography interface of *E. coli* on dragonfly wings. Thin planes of bacteria attached to dragonfly wings were precisely milled using a Ne^+ beam, and the exposed interface imaged using a He^+ beam.[36] This cross-sectioning was carried out without any conductive metal coating, as is required for focused ion beam (FIB) or scanning electron microscopy (SEM).[13, 17] Hence, the bacteria-nanotopography interface images acquired by HIM are not obscured and remain close to their natural state, limiting possible artifacts that might occur during the metal coating processes involved in FIB/SEM. Compared to TEM, this method is flexible for performing cross-sections at various positions, lengths and directions whereas TEM is limited to tiny sections of lamellas and positions of cross-sections cannot be controlled.

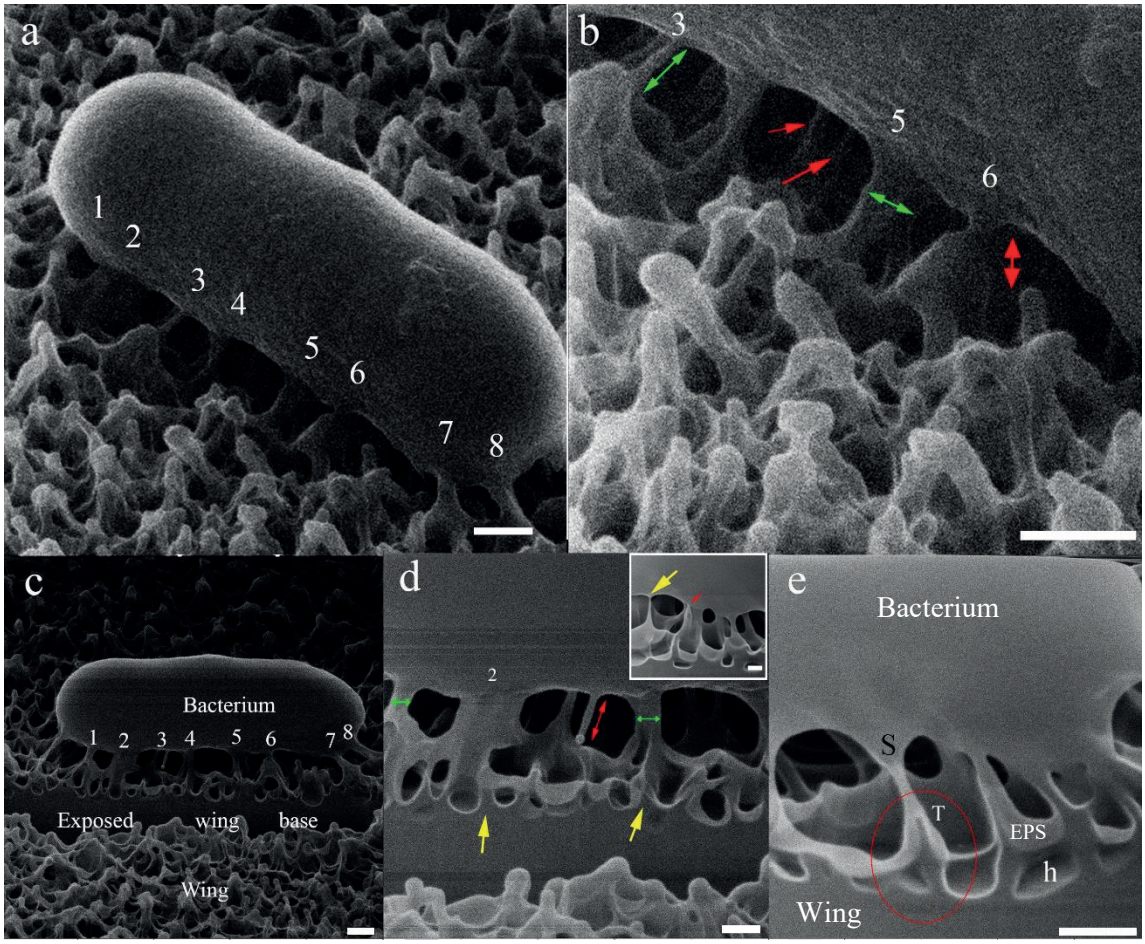

Figure 1: Helium ion beam micrographs showing initial attachment of bacteria to the nanopillars of dragonfly wings. Panel (a) shows an attached bacterium on to dragonfly wing. Visible connections between the protrusions arising from the bacterium and the nanopillars are numbered for further reference in other panels. b) Magnified region of the bacterium shown in panel (a). The double-headed green arrow represents protrusions that arise from bacterium connecting to the nanopillar on the wing. Red arrows show more connections under the bacterium. The red double-headed arrow shows the gap between a nanopillar and the bacterial membrane. c-e) Interface of *E.coli* bacteria-nanotextured dragonfly wing interface exposed by progressive longitudinal Ne milling. c) Cross-section of the wing and bacteria to expose the interface after approx. 1/3 of the bacterium is removed. Finger-like extensions that connect the bacterium with wing nanopillars are visible. d) Magnified area of (c) and both '2's are the same location. Visible connection marked 2 is an area where bacterial components heavily flood the underlying nanopillars. Yellow arrows mark the base of nanopillars where the top is flooded by bacterial components. Green double headed arrows are protrusions connecting bacteria and nanopillars. The red

double-headed arrow shows finger-like extension from bacteria attaching to nanopillars. Inset shows a magnified area of the interface. A string-like connection is marked by the yellow arrowhead, while a red arrow shows bacterial components flooding e) The circled area shows a bent nanopillar flooded by a possible EPS secretion, or cytoplasmic conent from the bacterium and a partly stretched and deformed membrane marked as 'S'. The tip of the nanopillar is marked T. Holes on the wing are marked h. All scale bars represent 200 nm.

Here, we present the Gram-negative bacteria-natural nanopillar interactions imaged under HIM (Figure 1). *Escherichia coli* cells were incubated for 15 minutes at room temperature on a dragonfly wing and then fixed with 2% glutaraldehyde and subjected to ethanol dehydration before Ne milling and He imaging. This made it possible to image the bacteria-nanotexture interactions before the bacteria are flattened and disintegrate on the nanopillars. The attached bacterium shows multiple connections with the wing via protrusions, some of which are thin and long, while some connections are comparatively thick.

Subsurface details exposed after Ne^+ beam milling of samples are shown in Figure 1c-e. Figure 1c reveals the interface after a longitudinal cross-section was performed at approximately 1/3 of the way across the bacterium and the wing. Here, different connections between the bacterium and the nanostructures are identified and are numbered from 1 to 8 (Figure 1c). These finger-like protrusions connecting the bacterium and the nanotexture are about 100 nm in length and 10-50 nm in diameter. The presence of secreted EPS, cytoplasm, or deformed membrane, finger-like extensions (red double-headed arrow) are visible on the tips of nanopillars (Figure 1d). A red double-headed arrow marks a thin and long extension of material from the bacteria. This suggests that membrane deformations take place at the interface between the bacterial membrane and the nanopillars. The connection numbered 2 in Figure 1d is thicker than the majority of connections identified, which are typically about 100 nm in length and more than 100 nm in thickness. These thick connections could be a

consequence of flooding of the nanopillars by a bacterially-derived substance (Figure 1d) which could be EPS secretions from the bacteria produced upon attachment, leaked cytoplasmic content and/or deformed membrane, indicating membrane damage. The inset (Figure 1d) magnifies a string-like stretch (labeled by a yellow arrow) which starts from the bacterial membrane and floods the top of the adjacent nanopillars. The latter has a thick blanket-like cover that can be identified as a light colored layer on the wing. Collectively, these visible connections and finger-like protrusions between the bacterium and nanopillars appear to be consistent with the extracellular polymeric substances (EPS) identified in the previous TEM and SEM/FIB reports.[13] However, at this stage, the composition of this material is not clear and more studies are needed to determine their composition.

The space between the bacterial membrane and nanopillar tips is barely filled by visible connections or finger-like extensions of the bacteria. Most of the nanopillar tips are flooded by bacterial secretions and remain 100-200 nm below the level of the bacterial membrane. Therefore this space is obscured by bacterial secretions. Finger-like connections extending from the bacterial membrane and continuous with nanopillars filling the space, make it difficult to distinguish the bacterial membrane from the nanopillars. Though He ion microscopy is a better technique compared to electron microscopy in contrasting different compositions,[37-41] here, we emphasize that the similar composition of the different components of the sample, make it difficult to distinguish distinct borders of the different components. Nanopillars of the wing are composed of hydrophobic long-chain hydrocarbons[15, 42] and bacterial membranes are comprised of hydrophobic lipid bilayer and a hydrophilic peptidoglycan layer.[43-44] Therefore, in a favourable chemical environment, interactions between these components may be possible and a partial or even full encasing of the nanopillars with bacterial membranes could account for the adhesion between Gram-negative bacteria and the nanopillars. Though we have used a

strain without flagella in this study, a one contains flagella would show much favourable interactions with superhydrophobic surfaces.[45]

The circled area of Figure 1e highlights a nanopillar flooded by membrane deformations, EPS or cytoplasm. The bacterial membrane appears to be extended and stretched towards the nanopillar to form the connection while the nanopillar is slightly tilted or bent to the left from its vertical position. This bending and stretching could be a result of strong adhesion of bacteria and its attempts to move away from the surface.

The above observations and analysis suggest that a series of complex interactions could take place between *E.coli* and natural nanopillar topography before the bacterial membrane is damaged. Therefore, the biological effects of such interactions should also be considered when developing reliable models of the bactericidal effects of anti-bacterial surfaces.

Further chemical composition studies are required to determine the composition of the finger-like connections we observed between bacteria and nanopillars by HIM. Although we were unable to characterise the nature of the extracellular bacterial-derived substances in this study, at this stage, our approach contributes toward a greater understandingof the mechanism of action and will reduce future experimental bias towards just one single bactericidal mechanism.

Interfacial characteristics of dragonfly wing nanopillars-*Escherichia coli* interactions by 3D-SIM. *E. coli* cells were introduced to the wing surface and immediately imaged using 3D-SIM. Cell membranes were pre-stained with the fluorescent lipophilic stain FM1-43 (green) and imaged in the presence of the cell impermeant Ethidium homodimer-III (EthD-III, red) that binds only to the DNA of cells with a compromised membrane. With live 3D-SIM imaging, the dragonfly wing showed faint green autofluorecence whereas the FM1-43-stained bacterial cell membranes show much brighter green fluorescence intensity (Figure 2). Figure 2A shows bacterial cells (arrows) attached to the wing. Membrane damaged bacteria (white arrows) have

green membranes and red nuclear DNA (Figure 2A). Figure 2B shows the cross-section of the bacteria-wing interface, where unevenness of the wing is evident. The wing is indicated by a green arrow and a membrane damaged bacterium by a white arrow. Interestingly, the bacterial cell membrane appears to be missing at the side of the bacterial cell that is in contact with the dragonfly wing (Figure 2A, C). The section views (Figure 2C) clearly shows that the bacterial membrane is discontinuous when in contact with the wing surface, thereby allowing the DNA stain EthD-III to enter the cell. Interestingly, we observed that cells that had taken up the dead cell stain (EthD-III) presented different red fluorescence intensities (white arrows, Figure 2A) which suggests that membrane damage may have occurred at different times and/or that different levels of membrane damage has occurred. 3D-SIM utilizes spatially patterned excitation beams to achieve the resolution below the diffraction limit, thereby surpassing the classical spatial resolution limit of conventional microscopy. The 3D-SIM platform used in this study provides a lateral and axial resolution of 110 nm and 280 nm, respectively.[25] By using stains specific for membranes and DNA of membrane-compromised cells, we were able to explore membrane damage in live bacterial cells interacting with dragonfly wings while maintaining physiological conditions. This is the first report of such live *in-situ* imaging of *E.coli* interacting with dragonfly wings with a higher contrast between the membrane and nuclear material.

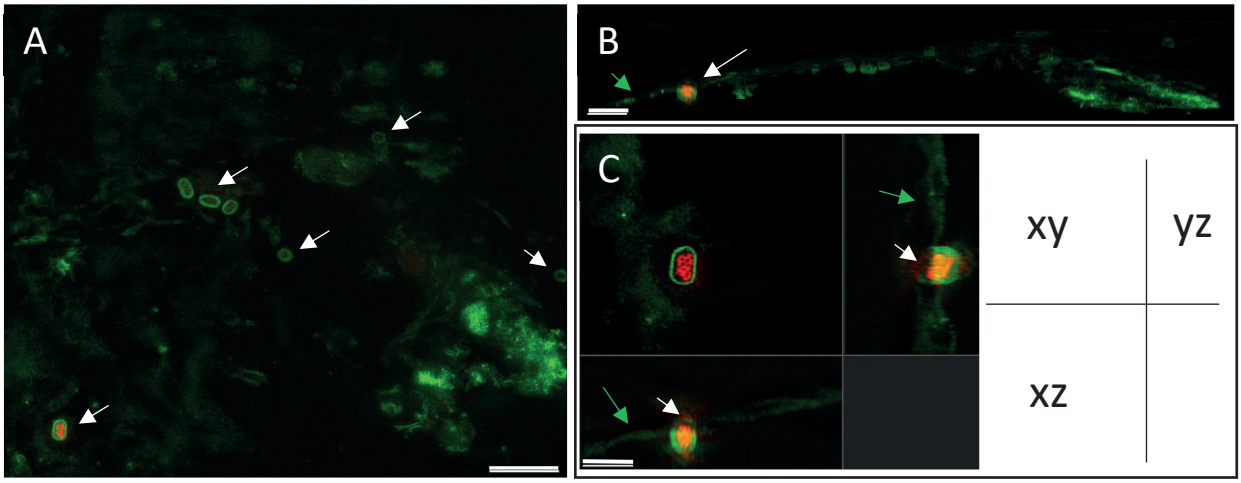

Figure 2: Reconstructed 3D-SIM micrographs showing *E. coli* on dragonfly wings a.) Maximum intensity projection showing bacterial cells (white arrows) attached to the wing (green autofluorescence). Scale bar = 5 µm. B.) 3D side view of image A, showing membrane-damaged bacteria (white arrow). The membrane is stained in green and nuclear material stained in red. The green arrow points to the wing. Scale bar = 3 µm. C) Section view of the cell highlighted by the white arrow in image B clearly showing damage (white arrows) at the side of the cell in contact with the dragonfly wing. Scale bar = 2 µm. The graphic shows xy, xz and yz axes for image C.

Elastic energy estimate of bent nanopillars. While our microscopic approach confirms the bending of nanopillars, bacterial membrane stretching, deformation, and damage, microscopy alone does not provide the mechanism that leads to these consequences. The lack of a comprehensive understanding of the bactericidal mechanism ultimately limits the translational potential towards real-world applications of nanotopography. Achieving such knowledge will ultimately lead to the efficient and effective development of real-world applications. A number of recent publications have indicated that the arrangement of nanopillars is not sufficient to achieve bactericidal activity, but that external factors including the movement of bacteria, and bending of nanopillars also contribute to the bactericidal activity of dragonfly nanopillars.[21, 46]

To assess the contribution of bending of dragonfly nanopillars on the underlying mechanism of bactericidal activity, we estimated the amounts of the stored elastic energies of natural

nanotopography of dragonfly wings during interactions with bacteria. This data could then be used to design artificial bactericidal surfaces, and compare them with fabricated nanopillars. As we have identified that bending of dragonfly wing nanopillars occurs when the bacterial membrane is being damaged,[13] we assessed the storage of energy in the bending of dragonfly nanopillars. According to the model suggested by Linklater *et al.*[19] for a surface with VACNT, using Bernoulli's beam theory, a force, P (load) acting on the tip of a nanopillar parallel to the substratum when a bacterium attempts to move predicts a deflection of the tip, δ as;

$$\delta = \frac{PL^3}{3\,EI} \qquad (1)$$

where L is the length of the nanopillar, E is the material's Young modulus, and I the area moment.

According to Eq. (1), the deflection is much bigger in a longer nanopillar. On the other hand, the elastic energy stored, $U = \frac{3EI\delta^2}{2L^3}$, can be balanced by the external energy, $W = \frac{P\delta}{2}$. Thus for a constant deflection (δ) of the nanopillar, the elastic energy (U) is proportional to the Young's modulus (E) and inversely related to L^3. That means, for a given deflection, longer nanopillars stores smaller energy.

According to these storage energy calculations, both dragonfly wing nanopillars and 1 μm CNT store similar energies upon the same tip deflection (Figure 3). With the same tip displacement, short nanopillars of the dragonfly wing exert stronger forces than tall nanopillars, while 1 μm VACNT energy storage values are in between short and tall nanopillars. Consequently, the natural nanotopography of dragonfly wings may induce more damage to the bacterial cell membrane than CNT.

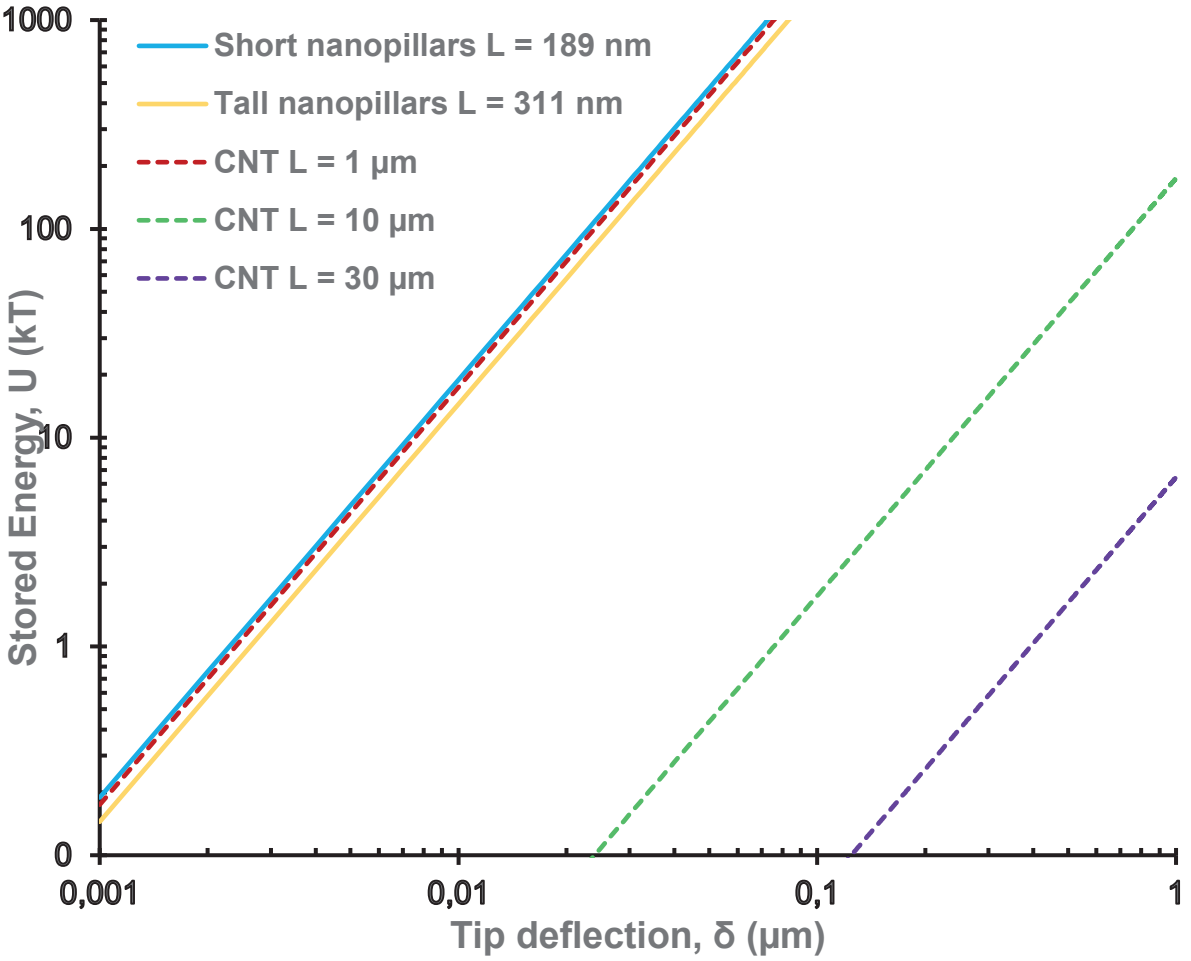

Figure 3: Stored energy comparison in CNT and dragonfly nanopillars against tip deflection. Shorter and taller dragonfly wing nanopillars store energies similar to those stored in 1 µm CNT. Dragonfly wing data are plotted as solid lines and CNT data are plotted as dotted lines. 1 kT at 298 K corresponds to 4.11 x 10^{-21} J. *Data reproduced with permission from "Linklater et al, ACS Nano 2018, 12, 7, 6657-6667, DOI: 10.1021/acsnano.8b01665 copyright © 2018, American Chemical Society.*

We observed with HIM that the interacting nanopillars with bacteria are bent, maybe when bacterium attempts to move. The stored energy due to bending of the nanopillars may release, leading to further stretching of the bacterial membrane causing physical damage to the membrane.

CONCLUSIONS

To address the challenges of characterizing the interface of bacterial cells and biological nanotopographies and interpreting the mechanical basis of bactericidal activities we have designed an approach to examine the nano-biointerface close to its natural state. This unique approach has highlighted several key characteristics that have important implications for the design of efficient and effective nanotextured surfaces for biomedical applications.

This study has utilized sophisticated imaging techniques with minimal sample processing that has important implications for the comprehensive understanding of the biointerface. By using Ne^+ beam and flood gun we eliminated the use of a conductive metal coating that is used in SEM and avoids the application of metal layer onto the sample prior to cross-sectioning as reported previously in FIB/SEM and TEM studies.[13, 17, 19, 27] Elimination of both metal coating and Pt deposition allowed us to image the bacteria-nanopillar interaction close to its natural state. Ne^+ beam cross-sectioning has allowed us to cross-section small amounts of the sample at specific positions, where TEM cross-sections are random. This has allowed us to observe the interfacial features, at precise locations with more clarity and without disturbance at nanoscale resolution. In *E.coli*, it was found that bacteria and nanopillars make contacts at specific anchor locations. Finger-like protrusions, possible secreted EPS, cytoplasmic material and membrane deformations were also visible, however, they were not able to be distinguished using ion beam microscopy. Further, it was confirmed that the membrane is not pierced by the nanopillars, but is more likely stretched and deformed during the interaction.

With live 3D-SIM, bacterial membranes and the nuclear material of membrane-compromised cells were resolved. However, the nanopillars or finger-like protrusions that we observed with HIM could not be visualized with 3D-SIM due to the resolution limit of this technique. We were, however, able to observe that membrane damage occurred at the surface of the bacterial

cell that was in contact with the dragonfly wing. Although neither of the imaging methods alone could fully resolve the interactions between the nanopillar and the bacteria, this study provides useful insight into the limits and possibilities of the imaging methods. It is evident from this study that multiple experimental approaches that involve minimal sample processing are necessary to comprehensively asses the bactericidal activity of nanotextured surfaces.

Further mechanical insights were obtained by estimating the bending energy storage of short and tall nanopillars of dragonfly wings. These elastic energy storage estimations indicated that short nanopillars are slightly higher in energy storage compared to tall nanopillars of dragonfly wing. It was also found that 1 μm VACNT energy storage is between that of the tall and short nanopillars of dragonfly wings. This indicates that both natural bactericidal nanotopography and VACNT are likely to mechanically behave quite similarly in achieving bactericidal activity. This suggests that soft materials are capable of achieving bactericidal effects and that antibacterial surfaces do not necessarily need to be designed using hard solid materials.

The microscopy techniques that we utilized in this study distinguished the features of the interface between a Gram negative bacterium and the dragonfly wing. Given that Gram-negative and Gram-positive bacteria have significant differences in their cell wall and membrane structures, in future studies bacterial surface/nanotopography interfaces should be examined with techniques capable of nano-scale and molecular resolution with minimal processing. Our approach could be applied to examine interactions of Gram-positive and Gram-negative bacteria and eukaryotic cells with various nanotopographies to guide the design of efficient nanofabrication.

EXPERIMENTAL SECTION

Dragonfly wing collection and sample preparation. The dragonfly specimens were collected in Brisbane, Australia and wings were aseptically removed from the body, washed with flowing deionized water and stored in the dark at 4°C in sterile containers.

Bacterial growth conditions and sample preparation for HIM. The *Escherichia coli* (NCTC 10418) strain was used for HIM study. Bacterial cultures were grown overnight at 37 ºC in 5 mL of nutrient broth. The culture was collected at the logarithmic stage of growth and the bacteria suspension was washed twice with 0.01 M PBS (pH=7.4) and adjusted to OD_{600}=0.3. A 200 µL aliquot of of bacterial suspension was placed on a 5 mm x 5 mm size wing and allowed to incubate at room temperature (22ºC) in a Petri dish.[13, 27] Wings were then gently washed with sterile MiliQ water to remove non-attached cells.

Ne^+ milling and He^+ imaging of interface with Helium Ion Microscope. For Ne^+ milling, *E.coli* cells incubated for 15 minutes on dragonfly wing was used. Samples were fixed with 2% glutaraldehyde and subjected to membrane staining and ethanol dehydration.[13, 27] Dehydrated and dried wings were mounted using double-sided carbon tape onto an aluminium stab for imaging. Zeiss Orion NanoFab equipped with Ne^+ and He^+ beam was used for cross-sectioning of bacterial cells attached to the dragonfly wing. Samples were not coated and no other depositions were performed before imaging/milling. Bacteria were cross-sectioned in longitudinal direction progressively and micrographed after each cross-section so that interactions can be studied. Milling was performed with and Ne^+ at an acceleration voltage of 15 kV. Ion current varied between 4-10 pA during the milling and pixel dwell time was set to 2-5 µs. Milling was done from the 50 degrees tilted angle by drawing the reduced raster scan rectangle over the area to be removed and waiting until the material disappeared. The sample was then rotated and imaged with He^+. When imaging, 30 kV acceleration voltage and 0.2-0.4 pA ion current were used with line averages of 16 or 32 and dwell time 0.5 or 1 µs. During

both milling and imaging, flood gun charge compensation was used. For a single dragonfly wing sample, 3-5 wing cells were analysed. A cell of a dragonfly wing is the membranous areas that are enclosed by the veins. We have analysed at least 3 bacterial cells within a single cell of a wing, which makes about 10 cells per sample. We have carried out experiments in duplicate.

Bacterial growth conditions and sample preparation for 3D-SIM microscopy. *E. coli* MG1655 was cultured in LB media at 37 ºC overnight with vigorous shaking. 500 µL of the overnight culture was harvested by centrifugation at 9000 rpm for 1.5 min and re-suspended in 500 µL of PBS. The bacterial suspension was stained with FM1-43FX (Life Technologies) at 4 µg/mL for 15 minutes. The bacterial suspension was then washed twice in PBS and re-suspended in 500 µL of PBS. A small piece of dragonfly wing (5 x 5 mm) was immersed in the membrane-stained bacterial suspension for about 30 min to allow bacteria attachment on the wing. The wing was then carefully removed from the solution and washed in 500 µL of PBS to remove non-adherent bacterial cells. The wing was then immersed in 500 µL of PBS containing Ethidium homodimer-III (Biotium) at 1 µM and stained for 15 min. The wing was then immersed in 500 µL of fresh PBS to wash dye excess. An adhesive frame (Gene Frame®, Thermo Fisher Scientific) was placed on a microscope slide to create a chamber, the wing was attached inside the chamber using a UV glue (Dymax) and PBS was used as mounting media for imaging. A #1.5, 22x22 mm glass coverslip was ethanol sterilized and placed on top.

3D-Structured Illumination Microscopy (3D-SIM). Samples were immediately imaged using the DeltaVision OMX-SR (GE Healthcare) platform at 37 ºC with a 60x oil objective. 3D images were acquired with a z-step size of 0.125 µm for 3 µm total thickness. Raw images were processed with SoftWoRx (GE Healthcare) for image reconstruction and channel alignment and then prepared with IMARIS (v 9.1.2, Bitplane).

AUTHOR INFORMATION

Corresponding Author

chaturangab@yahoo.com

ORCID

Chaturanga D. Bandara 0000-0002-0688-4260

Giulia Ballerin 0000-0001-9551-7405

Miika Leppänen 0000-0002-1855-8390

Tuquabo Tesfamichael 0000-0001-7012-4904

Kostya (Ken) Ostrikov 0000-0001-8672-9297

Cynthia Whitchurch 0000-0003-2296-3791

Author contributions

C.D.B. initiated the project, prepared the samples, performed cell viability tests, HIM imaging and wrote the manuscript. M.L. performed HIM milling and imaging of bacteria. G.B. performed 3D-SIM imaging. All authors contributed to the data analysis, results interpretation, manuscript preparation, and approved the final version.

Notes

The authors declare no competing financial interest.

ACKNOWLEDGEMENTS

Work of Miika Leppänen was supported by the Jane and Aatos Erkko Foundation. Work of Chaturanga Bandara was partly supported by SEF Write-up scholarship. Authors

acknowledge Facilities of Central Analytical Research Facility (CARF, IFE) at Queensland University of Technology and ithree Institute at University of Technology Sydney.

REFERENCES

1. Berne, C.; Ducret, A.; Hardy, G. G.; Brun, Y. V., Adhesins involved in attachment to abiotic surfaces by Gram-negative bacteria. *Microbiology spectrum* **2015,** *3* (4), 10.1128/microbiolspec.MB-0018-2015. DOI: 10.1128/microbiolspec.MB-0018-2015.
2. Petrova, O. E.; Sauer, K., Sticky Situations: Key Components That Control Bacterial Surface Attachment. *J. Bacteriol.* **2012,** *194* (10), 2413-2425. DOI: 10.1128/jb.00003-12.
3. Nejadnik, M. R.; van der Mei, H. C.; Norde, W.; Busscher, H. J., Bacterial adhesion and growth on a polymer brush-coating. *Biomaterials* **2008,** *29* (30), 4117-4121. DOI: 10.1016/j.biomaterials.2008.07.014.
4. Harris, L.; Meredith, D. O.; Eschbach, L.; Richards, R. G., Staphylococcus aureus adhesion to standard micro-rough and electropolished implant materials. *J. Mater. Sci. Mater. Med.* **2007,** *18* (6), 1151-1156. DOI: 10.1007/s10856-007-0143-0.
5. Watson, G. S.; Green, D. W.; Watson, J. A.; Zhou, Z.; Li, X.; Cheung, G. S. P.; Gellender, M., A Simple Model for Binding and Rupture of Bacterial Cells on Nanopillar Surfaces. *Advanced Materials Interfaces* **2019**, 1801646. DOI: 10.1002/admi.201801646.
6. Pogodin, S.; Hasan, J.; Baulin, V. A.; Webb, H. K.; Truong, V. K.; Phong Nguyen, T. H.; Boshkovikj, V.; Fluke, C. J.; Watson, G. S.; Watson, J. A.; Crawford, R. J.; Ivanova, E. P., Biophysical model of bacterial cell interactions with nanopatterned cicada wing surfaces. *Biophys. J.* **2013,** *104* (4), 835-840.
7. Ivanova, E. P.; Hasan, J.; Webb, H. K.; Truong, V. K.; Watson, G. S.; Watson, J. A.; Baulin, V. A.; Pogodin, S.; Wang, J. Y.; Tobin, M. J.; Löbbe, C.; Crawford, R. J., Natural bactericidal surfaces: Mechanical rupture of pseudomonas aeruginosa cells by cicada wings. *Small* **2012,** *8* (16), 2489-2494.
8. Liu, T.; Cui, Q.; Wu, Q.; Li, X.; Song, K.; Ge, D.; Guan, S., Mechanism Study of Bacteria Killed on Nanostructures. *J. Phys. Chem. B* **2019,** *123* (41), 8686-8696. DOI: 10.1021/acs.jpcb.9b07732.
9. AshaRani, P. V.; Low Kah Mun, G.; Hande, M. P.; Valiyaveettil, S., Cytotoxicity and Genotoxicity of Silver Nanoparticles in Human Cells. *ACS Nano* **2009,** *3* (2), 279 - 290. DOI: 10.1021/nn800596w.
10. Gatti, A. M.; Montanari, S.; Gambarelli, A.; Capitani, F.; Salvatori, R., In-vivo short- and long-term evaluation of the interaction material-blood. *J. Mater. Sci. Mater. Med.* **2005,** *16* (12), 1213-9. DOI: 10.1007/s10856-005-4731-6.
11. Das, B.; Khan, M. I.; Jayabalan, R.; Behera, S. K.; Yun, S. I.; Tripathy, S. K.; Mishra, A., Understanding the Antifungal Mechanism of Ag@ZnO Core-shell Nanocomposites against Candida krusei. *Sci. Rep.* **2016,** *6*, 36403. DOI: 10.1038/srep36403.
12. Kruszewski, K. M.; Nistico, L.; Longwell, M. J.; Hynes, M. J.; Maurer, J. A.; Hall-Stoodley, L.; Gawalt, E. S., Reducing Staphylococcus aureus biofilm formation on stainless steel 316L using functionalized self-assembled monolayers. *Materials Science and Engineering: C* **2013,** *33* (4), 2059-2069. DOI: http://dx.doi.org/10.1016/j.msec.2013.01.023.
13. Bandara, C. D.; Singh, S.; Afara, I. O.; Tesfamichael, T.; Wolff, A.; Ostrikov, K.; Oloyede, A., Bactericidal Effects of Natural Nanotopography of Dragonfly Wing on Escherichia coli. *ACS Applied Materials & Interfaces* **2017,** *9* (8), 6746-6760. DOI: 10.1021/acsami.6b13666.
14. Michalska, M.; Gambacorta, F.; Divan, R.; Aranson, I. S.; Sokolov, A.; Noirot, P.; Laible, P. D., Tuning antimicrobial properties of biomimetic nanopatterned surfaces. *Nanoscale* **2018,** *10* (14), 6639-6650. DOI: 10.1039/C8NR00439K.
15. Román-Kustas, J.; Hoffman, J. B.; Reed, J. H.; Gonsalves, A. E.; Oh, J.; Li, L.; Hong, S.; Jo, K. D.; Dana, C. E.; Miljkovic, N.; Cropek, D. M.; Alleyne, M., Molecular and Topographical Organization:

Influence on Cicada Wing Wettability and Bactericidal Properties. *Advanced Materials Interfaces* **2020**, 2000112. DOI: 10.1002/admi.202000112.
16. Ziegler, N.; Sengstock, C.; Mai, V.; Schildhauer, T. A.; Koller, M.; Ludwig, A., Glancing-Angle Deposition of Nanostructures on an Implant Material Surface. *Nanomaterials (Basel)* **2019,** *9* (1). DOI: 10.3390/nano9010060.
17. Linklater, D. P.; Juodkazis, S.; Rubanov, S.; Ivanova, E. P., Comment on "Bactericidal Effects of Natural Nanotopography of Dragonfly Wing on Escherichia coli". *ACS Applied Materials & Interfaces* **2017,** *9* (35), 29387-29393. DOI: 10.1021/acsami.7b05707.
18. Xue, F.; Liu, J.; Guo, L.; Zhang, L.; Li, Q., Theoretical study on the bactericidal nature of nanopatterned surfaces. *J. Theor. Biol.* **2015,** *385*, 1-7. DOI: 10.1016/j.jtbi.2015.08.011.
19. Linklater, D. P.; De Volder, M.; Baulin, V. A.; Werner, M.; Jessl, S.; Golozar, M.; Maggini, L.; Rubanov, S.; Hanssen, E.; Juodkazis, S.; Ivanova, E. P., High Aspect Ratio Nanostructures Kill Bacteria via Storage and Release of Mechanical Energy. *ACS Nano* **2018,** *12* (7), 6657-6667. DOI: 10.1021/acsnano.8b01665.
20. Jenkins, J.; Mantell, J.; Neal, C.; Gholinia, A.; Verkade, P.; Nobbs, A. H.; Su, B., Antibacterial effects of nanopillar surfaces are mediated by cell impedance, penetration and induction of oxidative stress. *Nature Communications* **2020,** *11* (1), 1626. DOI: 10.1038/s41467-020-15471-x.
21. Valiei, A.; Lin, N.; Bryche, J.-F.; McKay, G.; Canva, M.; Charette, P. G.; Nguyen, D.; Moraes, C.; Tufenkji, N., Mechano-bactericidal nanopillars require external forces to effectively kill bacteria. *bioRxiv* **2020**, 2020.03.27.012153. DOI: 10.1101/2020.03.27.012153.
22. Hasan, J.; Crawford, R. J.; Ivanova, E. P., Antibacterial surfaces: the quest for a new generation of biomaterials. *Trends Biotechnol.* **2013,** *31* (5), 295-304. DOI: 10.1016/j.tibtech.2013.01.017.
23. Hasan, J.; Webb, H. K.; Truong, V. K.; Pogodin, S.; Baulin, V. A.; Watson, G. S.; Watson, J. A.; Crawford, R. J.; Ivanova, E. P., Selective bactericidal activity of nanopatterned superhydrophobic cicada Psaltoda claripennis wing surfaces. *Appl. Microbiol. Biotechnol.* **2012,** *97* (20), 1-6. DOI: 10.1007/s00253-012-4628-5.
24. Ivanova, E. P.; Hasan, J.; Webb, H. K.; Gervinskas, G.; Juodkazis, S.; Truong, V. K.; Wu, A. H.; Lamb, R. N.; Baulin, V. A.; Watson, G. S.; Watson, J. A.; Mainwaring, D. E.; Crawford, R. J., Bactericidal activity of black silicon. *Nat Commun* **2013,** *4*, 2838. DOI: http://dx.doi.org/10.1038/ncomms3838.
25. Huang, B.; Bates, M.; Zhuang, X., Super-Resolution Fluorescence Microscopy. *Annu. Rev. Biochem.* **2009,** *78* (1), 993-1016. DOI: 10.1146/annurev.biochem.77.061906.092014.
26. Turnbull, L.; Toyofuku, M.; Hynen, A. L.; Kurosawa, M.; Pessi, G.; Petty, N. K.; Osvath, S. R.; Cárcamo-Oyarce, G.; Gloag, E. S.; Shimoni, R.; Omasits, U.; Ito, S.; Yap, X.; Monahan, L. G.; Cavaliere, R.; Ahrens, C. H.; Charles, I. G.; Nomura, N.; Eberl, L.; Whitchurch, C. B., Explosive cell lysis as a mechanism for the biogenesis of bacterial membrane vesicles and biofilms. *Nature communications* **2016,** *7*, 11220-11220. DOI: 10.1038/ncomms11220.
27. Imihami Mudiyanselage, C. C. D. B. Characterisation of the bactericidal efficacy of natural nano-topography using dragonfly wing as a model. Ph.D. Dissertation, Queensland University of Technology, Brisbane, QLD, 2017. DOI: 10.5204/thesis.eprints.106746.
28. Oh, Y. J.; Khan, E. S.; Campo, A. d.; Hinterdorfer, P.; Li, B., Nanoscale Characteristics and Antimicrobial Properties of (SI-ATRP)-Seeded Polymer Brush Surfaces. *ACS Applied Materials & Interfaces* **2019,** *11* (32), 29312-29319. DOI: 10.1021/acsami.9b09885.
29. Reed, J. H.; Gonsalves, A. E.; Román, J. K.; Oh, J.; Cha, H.; Dana, C. E.; Toc, M.; Hong, S.; Hoffman, J. B.; Andrade, J. E.; Jo, K. D.; Alleyne, M.; Miljkovic, N.; Cropek, D. M., Ultrascalable Multifunctional Nanoengineered Copper and Aluminum for Antiadhesion and Bactericidal Applications. *ACS Applied Bio Materials* **2019,** *2* (7), 2726-2737. DOI: 10.1021/acsabm.8b00765.
30. Nakade, K.; Jindai, K.; Sagawa, T.; Kojima, H.; Shimizu, T.; Shingubara, S.; Ito, T., Adhesion and Bactericidal Properties of a Wettability-Controlled Artificial Nanostructure. *ACS Applied Nano Materials* **2018,** *1* (10), 5736-5741. DOI: 10.1021/acsanm.8b01340.

31. Boinovich, L. B.; Modin, E. B.; Aleshkin, A. V.; Emelyanenko, K. A.; Zulkarneev, E. R.; Kiseleva, I. A.; Vasiliev, A. L.; Emelyanenko, A. M., Effective Antibacterial Nanotextured Surfaces Based on Extreme Wettability and Bacteriophage Seeding. *ACS Applied Nano Materials* **2018,** *1* (3), 1348-1359. DOI: 10.1021/acsanm.8b00090.
32. Ito, T.; Nakade, K.; Jindai, K.; Sagawa, T.; Kojima, H.; Shimizu, T.; Shingubara, S., *Time-lapse imaging of bactericidal effect on nanostructural surface*. SPIE: 2019; Vol. 10965.
33. Banner, D. J.; Firlar, E.; Jakubonis, J.; Baggia, Y.; Osborn, J. K.; Shahbazian-Yassar, R.; Megaridis, C. M.; Shokuhfar, T., Correlative ex situ and Liquid-Cell TEM Observation of Bacterial Cell Membrane Damage Induced by Rough Surface Topology. *Int J Nanomedicine* **2020,** *15* (15), 1929-1938. DOI: 10.2147/IJN.S232230.
34. Köller, M.; Ziegler, N.; Sengstock, C.; Schildhauer, T. A.; Ludwig, A., Bacterial cell division is involved in the damage of gram-negative bacteria on a nano-pillar titanium surface. *Biomedical Physics & Engineering Express* **2018,** *4* (5), 055002. DOI: 10.1088/2057-1976/aad2c1.
35. Imihami Mudiyanselage, C. C. D. B. Characterisation of the bactericidal efficacy of natural nano-topography using dragonfly wing as a model. PhD, 2017. DOI: 10.5204/thesis.eprints.106746.
36. Leppänen, M., Imaging Bacterial Colonies and Phage-bacterium Interaction at Sub-nanometer Resolution Using Helium Ion Microscopy. 2017.
37. Bell, D., Contrast Performance: Low Voltage Electrons vs. Helium Ions. *Microsc. Microanal.* **2011,** *17* (SupplementS2), 660-661. DOI: doi:10.1017/S143192761100417X.
38. Joy, D. C., Helium Ion Microscopy : Principles and Applications. 1 ed.; Springer: Dordrecht, 2013. http://QUT.eblib.com.au/patron/FullRecord.aspx?p=1466751.
39. Boseman, A.; Nowlin, K.; Ashraf, S.; Yang, J.; LaJeunesse, D., Ultrastructural analysis of wild type and mutant Drosophila melanogaster using helium ion microscopy. *Micron* **2013,** *51*, 26-35. DOI: http://dx.doi.org/10.1016/j.micron.2013.06.005.
40. Joens, M. S.; Huynh, C.; Kasuboski, J. M.; Ferranti, D.; Sigal, Y. J.; Zeitvogel, F.; Obst, M.; Burkhardt, C. J.; Curran, K. P.; Chalasani, S. H.; Stern, L. A.; Goetze, B.; Fitzpatrick, J. A. J., Helium Ion Microscopy (HIM) for the imaging of biological samples at sub-nanometer resolution. *Sci. Rep.* **2013,** *3*, 3514. DOI: 10.1038/srep03514.
41. Ki Woo, K., Biological Applications of Helium Ion Microscopy. *Applied Microscopy* **2013,** *43* (1), 9-13.
42. Ivanova, E. P.; Nguyen, S. H.; Webb, H. K.; Hasan, J.; Truong, V. K.; Lamb, R. N.; Duan, X.; Tobin, M. J.; Mahon, P. J.; Crawford, R. J., Molecular Organization of the Nanoscale Surface Structures of the Dragonfly *Hemianax papuensis* Wing Epicuticle. *PLoS One* **2013,** *8* (7), e67893. DOI: 10.1371/journal.pone.0067893.
43. Tortora, G. J.; Funke, B. R.; Case, C. L., *Microbiology an introduction*. 10 ed.; Pearson Education Inc.: San Francisco, CA 94111, 2010.
44. Vollmer, W.; Seligman, S. J., Architecture of peptidoglycan: more data and more models. *Trends Microbiol.* **2010,** *18* (2), 59-66. DOI: http://dx.doi.org/10.1016/j.tim.2009.12.004.
45. Friedlander, R. S.; Vogel, N.; Aizenberg, J., Role of Flagella in Adhesion of Escherichia coli to Abiotic Surfaces. *Langmuir* **2015,** *31* (22), 6137-6144. DOI: 10.1021/acs.langmuir.5b00815.
46. Jindai, K.; Nakade, K.; Masuda, K.; Sagawa, T.; Kojima, H.; Shimizu, T.; Shingubara, S.; Ito, T., Adhesion and bactericidal properties of nanostructured surfaces dependent on bacterial motility. *RSC Advances* **2020,** *10* (10), 5673-5680. DOI: 10.1039/C9RA08282D.

Resolving Bio-Nano Interactions of E.coli Bacteria-Dragonfly Wing Interface with Helium Ion and 3D-Structured Illumination Microscopy

Chaturanga D. Bandara[†‡], Giulia Ballerin[†], Miika Leppänen[§], Tuquabo Tesfamichael[‡], Kostya (Ken) Ostrikov[‡], and Cynthia B. Whitchurch[†]*

[†]The ithree institute, University of Technology Sydney, Ultimo, NSW 2007, Australia

[‡]School of Chemistry, Physics and Mechanical Engineering, Science and Engineering Faculty, Queensland University of Technology (QUT), Brisbane, Queensland 4001, Australia

[§]Nanoscience Center, Department of Physics, Department of Biological and Environmental Science, University of Jyvaskyla, FI-40014 Jyvaskyla, Finland

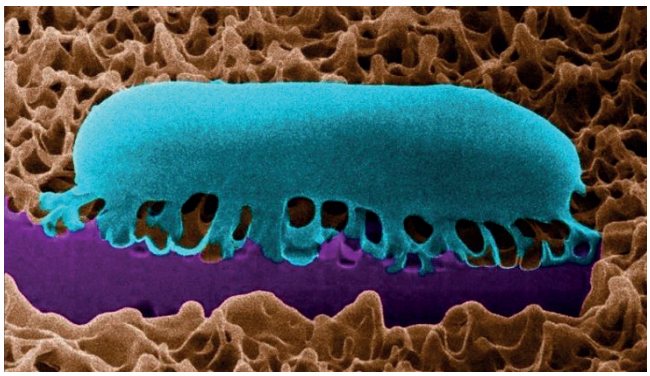

TOC Figure

VII

BACTERIOPHAGE IMAGING: PAST, PRESENT AND FUTURE

by

Almeida, G. M., Leppanen, M., Maasilta, I. J. & Sundberg, L. R. 2018.

Research in microbiology 169 (9), 488-494

Research in Microbiology xxx (2018) 1–7

Contents lists available at ScienceDirect

Research in Microbiology

journal homepage: www.elsevier.com/locate/resmic

Bacteriophage imaging: past, present and future

Gabriel MF. Almeida [a, *], Miika Leppänen [a, b], Ilari J. Maasilta [b], Lotta-Riina Sundberg [a]

[a] Centre of Excellence in Biological Interactions, Department of Biological and Environmental Science, Nanoscience Center, University of Jyväskylä, Survontie 9C, FI-40014, Jyväskylä, Finland
[b] Department of Physics, Nanoscience Center, University of Jyväskylä, Survontie 9C, FI-40014, Jyväskylä, Finland

ARTICLE INFO

Article history:
Received 31 January 2018
Accepted 22 May 2018
Available online xxx

Keywords:
Bacteriophage
Phage
Virus
Imaging
Structure
Microscopy

ABSTRACT

The visualization of viral particles only became possible after the advent of the electron microscope. The first bacteriophage images were published in 1940 and were soon followed by many other publications that helped to elucidate the structure of the particles and their interaction with the bacterial hosts. As sample preparation improved and new technologies were developed, phage imaging became important approach to morphologically classify these viruses and helped to understand its importance in the biosphere. In this review we discuss the main milestones in phage imaging, how it affected our knowledge on these viruses and recent developments in the field.

1. Earlier years (1940–1948)

Although the existence of viruses was known since the end of the 19th century, the true nature of the so called "*contagium vivum fluidum*", and whether it was liquid or particulated, remained unknown for many years [1]. Direct imaging of viral particles only became possible after the advent of the transmission electron microscope, allowing the determination of viral morphological characteristics. These machines were developed in the late 1930s by two different groups: one working at the Siemens & Halske laboratory company in Germany and another working at the University of Toronto in Canada. Ernst Ruska led the German team while James Hillier led the Canadian team, in development processes based on a concept that was already old by 1930, as mentioned by Hillier several years later. While Ernst Ruska developed a model for Siemens in Europe, Hillier and Prebus got a model working in America, and by the end of the thirties both teams had fully functional machines [2,3]. Helmut Ruska, Ernst's brother, was part of the team that used the German "hypermicroscope" to image a virus for the first time in 1938. The virus in question was ectromelia, a large DNA virus from the *Poxviridae* family, capable of infecting mice [4].

The first bacteriophage micrographs appeared on the literature in 1940, in two papers published at the same issue of the Naturwissenschaften journal. In one paper Helmut Ruska imaged infected bacterial cells and was able to show virus adsorption, cell lysis and resistant bacterial cells (Fig. 1a). Phages were described as small round particles, and crystalloid structures were seen and hypothesized to be centers for genesis of viral proteins [5]. In the other paper Pfankuch and Kausche, also working at the Siemens & Halske laboratory, analyzed purified phage suspensions and described the viruses as small rounded corpuscles that aggregate in higher concentrations [6]. Both papers mention particle destruction by electron irradiation. It is now believed that the phages seen at the time were T7 coliphages. Translated reprints of both articles were published in 2011 [7]. Following these publications, phage images spread in Europe causing excitement, reaching even Felix d'Herelle, one of the discoverers of these viruses. Helmut Ruska continued to be an important influence on phage imaging. In the early forties he described some phage particles obtained from bacterial lysates as being club-like, possessing distinct heads and tails (probably these were T4-like phages); reported at least four phage morphotypes; proposed a morphological classification for viruses and even introduced the term "phage" as an abbreviation to the term bacteriophage [7–10].

Meanwhile Luria and Anderson used the commercial version of Hillier's microscope to analyze unstained *Escherichia coli* and *Staphylococcus* phages in New York. In their first paper on the subject it is mentioned that phage imaging can "*offer favorable*

* Corresponding author.
E-mail addresses: gabriel.m.almeida@jyu.fi (G.MF. Almeida), miika.j.leppanen@jyu.fi (M. Leppänen), ilari.j.maasilta@jyu.fi (I.J. Maasilta), lotta-riina.sundberg@jyu.fi (L.-R. Sundberg).

https://doi.org/10.1016/j.resmic.2018.05.006
0923-2508/

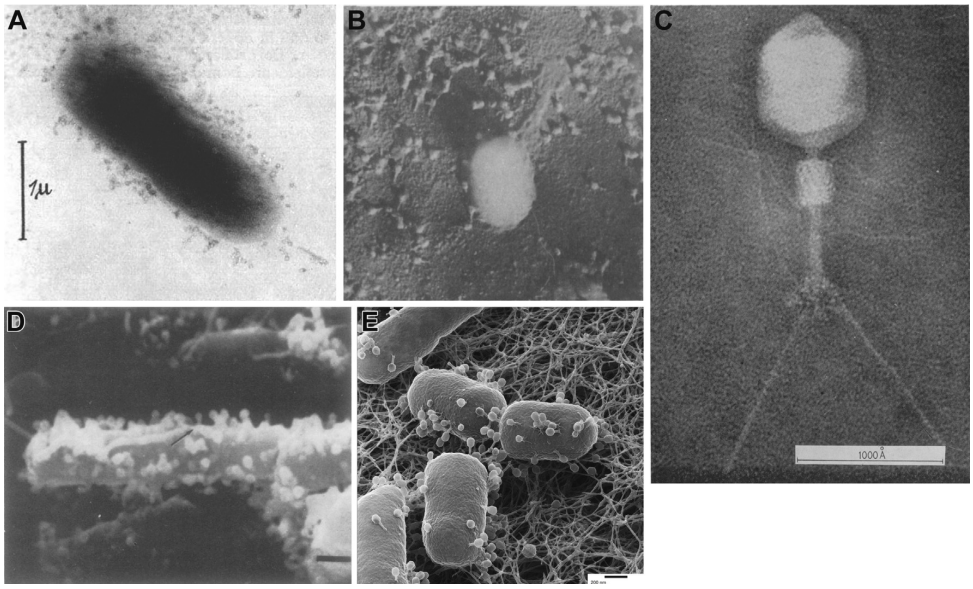

Fig. 1. Comparison between selected milestones in phage imaging. a) First phage electron micrograph published (1940). b) First phage electron micrograph published in which contrast was used in sample preparation (1948). c) One of the first negative stained phage electron micrographs published (1959). d) One of the first scanning electron microscope phage electron micrographs published (1975). e) First scanning helium ion microscope phage image published (2017).
Reprint Permissions: All images reproduced with permission from the original publishers. The original source details are: a) Ruska H. Die Sichtbarmachung der bakteriophagen Lyse im Übermikroskop. Naturwissenschaften 1940; 28:45–6. Permission obtained from Springer Nature, license number 4343490675464. b) Wyckoff R. The electron microscopy of developing bacteriophage. I. Plaques on solid media. Biochim Biophys Acta 1948; 2:27–37. DOI: 10.1016/0006-3002(48)90005-5. Permission obtained from Elsevier, license number 4325171419142.c) Brenner S, Streisinger G, Horne RW, Champe SP, Barnett L, Benzer S et al. Structural components of bacteriophage. J Mol Biol 1959; 1:IN9-IN21. DOI: 10.1016/S0022-2836(59)80035-8. Permission obtained from Elsevier, license number 4325180199035. d) Wendelschafer-Crabb G, Erlandsen SL, Walker DH. Conditions critical for optimal visualization of bacteriophage adsorbed to bacterial surfaces by scanning electron microscopy. J Virol 1975; 15:1498–503. Permission obtained from the American Society for Microbiology, license number 4325191273206. e) Leppänen M, Sundberg L-R, Laanto E, de Freitas Almeida GM, Papponen P, Maasilta IJ. Imaging Bacterial Colonies and Phage–Bacterium Interaction at Sub-Nanometer Resolution Using Helium-Ion Microscopy. Adv Biosyst 2017:1700070. Permission obtained from John Wiley and Sons, license number 4325200163356.

possibilities for the identification of the virus particles through a study of the reaction between the individual particles and the bacterial cell under the microscope" [11]. Interestingly, the imaging papers published by German authors including Ruska were mentioned, showing that despite the Second World War scientific information was still flowing from Europe to America. Luria and Anderson described coliphages as extremely constant particles composed of a round head and a much thinner tail, with the heads not being homogeneous in their composition but consisting of a pattern of granules. Adsorption and cell lysis were visually described, but due to the lack of knowledge on virus biology and genetics at the time, some of the speculations on their mechanisms have later proven to be wrong (such as mentioning that adsorption could happen by either head or tail, and that phage reproduction might take place at the cell wall). Imaging of Staphylococcal phages was mentioned to be harder, but particles containing heads and tails, able to adsorb to the host cells, were also detected. In their conclusions Luria and Anderson highlighted the interest of finding constant and relatively elaborate structural differentiation of macromolecular entities, and mentioned that the correspondence between particle size determined from microscopy to that obtained from indirect methods of measurement was remarkable. They also hypothesized that electron microscopy could also have an impact for genetics, since genes are also macromolecular entities and had been indirectly measured before [11]. The phages described in this study were later classified as T2 (T-even type) [7,12].

One year later Luria, Delbrück and Anderson published another paper on phage imaging [13], mentioning in the introduction the revival of interest in phages and the advantage of using these organisms as models. Images were taken from crude or partially purified viral suspensions, and also from dried drops of bacterial and phage mixtures for studying interaction between both. Besides typical tailed phage visualizations, a rounded phage without tail was described. It was mentioned that differential centrifugation mechanically inactivated one of the tailed phages (as noted by broken tails in the micrographs). Different multiplicities of infection were tested, which showed an agreement between the numbers of visible adsorbed particles to infective titers obtained by titrations. Micrographs also confirmed the eclipse period, allowed the observation of several steps of the phage infection cycle, and showed long *E. coli* cells (mentioned as "*not unusual*" in young broth cultures of the strain used). It was seen that new viruses were liberated from the interior of the bacterial cell, but it was not possible to determine where inside the bacteria the viruses are produced (deep interior or inner surfaces). The absence of bacterial components of size comparable to viruses released by lysed cells was used to explain why crude suspensions, differential centrifugation and filtrations can be used successfully for phage work. It was also noted, unexpectedly at the time as pointed out by the authors, that adsorbed particles remained at the cell surface. This was considered to be the finding of greatest consequence, and the most plausible theory chosen to explain was that only one particle enters the cell and then makes the bacteria impermeable to other viruses (an analogy to monospermic eggs fecundation was made, with the caution to mention that there was no conclusive data to fully support it). This imaging paper also helped to test and

Please cite this article in press as: G.M. Almeida, et al., Bacteriophage imaging: past, present and future, Research in Microbiology (2018), https://doi.org/10.1016/j.resmic.2018.05.006

eliminate three theories concerning phages that existed at the time: 1) no phage aggregates were seen, contradicting an idea that some phages would normally bind to larger unspecific carriers (such as bacterial debris); 2) the homogeneity of particle size disproved that there was a reversible equilibrium between small and large viral particles; 3) and the consistency in progeny morphology when the same host was infected with different phages debunked a proposition that bacterial cells could contain a precursor of the phage particle, which upon infection would be converted to viruses. These three theories were based on indirect measurements made by diffusion on differential filtration, by sedimentation rate in ultracentrifugation, or as an analogy to proteolytic enzymes and its precursors, and were all disproved by direct imaging on the electron microscope. There was also a discussion on the common practice at the time of considering viruses to be molecules, warning that "*such a terminology should not prejudice our views regarding the biological status of the viruses, which has yet to be elucidated*" [13].

2. Improvements on sample preparation (1948 onwards)

A next advance on phage imaging was the introduction of contrast to the samples. By using chromium vapor to cover the preparations, Wyckoff was able to obtain more information on height and shape of the particles. In 1948 he used the technique to study T coliphages, chosen for their distinct shapes and for the ease of working with their hosts when compared to opaque staphylococci or mucoid and capsular streptococci. Two papers were published. The first was based on imaging phage plaques on samples obtained from solid media, using the embedded replica technique [14] (Fig. 1b). Elongated *E. coli* were seen on young cultures and plaque characteristics were described and shown to differ between phages. The second paper focused on micrographs prepared from liquid samples [15]. Purified T4 preparations were used to describe phage morphology, and infected liquid cultures used for showing cells undergoing lysis with phages within and around their limits. Variation on the structure of phage heads and their contents was mentioned, and a correlation between grainy content inside the head and stages of maturation was made. Bacterial contents release by lysis were described, and their "conversion" to phages in favorable instances was noted as the most impressive result of the paper, hinted to be crucial in understanding how phages multiply.

Focusing on phage tails and the controversy concerning their role in the life cycle of phages at the time, Fraser and Williams used the freeze-drying technique to prepare T3 and T7 phages (believed to be tailless until then) for microscopy [16]. The technique was used for its minimal preparative distortion, and purified phages were freeze-dried for comparative analysis to air dried samples. Freeze-drying made clearer that phages are not spherical but geometrical, and short appendages ("*stubby tails*") were detected on the phages that were thought to be tailless at the time. The first result was taken as support of the affirmation that phages were much more complex than previously thought, while the second gave strength to the idea that tails serve an important purpose to the phage life cycle. The same technique was used shortly after to reexamine T-phages, in a larger effort to compare all these phages in similar conditions. Preservation of tails during freeze drying, possibility of artifacts generated by air drying, true three dimensional forms, the number of facets of phage heads, and particle dimensions were all discussed. The particle dimensions obtained by air drying were considered to be unreliable when compared to freeze drying [17].

By the end of the fifties the introduction of negative staining to viral electron microscope samples greatly improved the quality and clarity of the preparations [18]. It was quickly applied to phage samples and helped to describe the phage structural components such as head, tail sheath and tail fibers in details [19] (Fig. 1c). These samples were prepared by negative staining using the phosphotungstate method, and the microscopy results combined with biochemical analysis helped to better understand the phage particles. In the following year, negative staining was used to study 22 different phages in details, leading to morphological grouping and description of a subunit structure for heads and tails [20]. Besides coliphages, viruses that infect other bacterial genera such as *Staphylococcus*, *Streptococcus*, *Pseudomonas* and *Brucella* were visualized. Contrast differences were noted in phage heads and attributed to the presence or absence of DNA. Morphology was suggested to be an aid to the already confusing phage taxonomy, and one truly tailless phage was mentioned. After these studies negative staining of phage preparations and their analysis by transmission electron microscopy (TEM) became the most common practice to determine the phage structure and particle size in the following decades. A phage survey made in 2007 revealed that at least 5568 phages had been examined by negative stained TEM samples from 1959 to 2007 [21].

3. Complementary imaging approaches

Besides negatively stained TEM samples, other techniques were developed and used to image phages over the years. Direct observation of particles by TEM does not provide much insight on the phage life cycle or interaction with the host. For those purposes, pelleting of infected bacteria from liquid cultures and their subsequent fixation and drying was used, with the possibility of embedding the samples in polymers for ultrathin sectioning [22]. Based on worries about studying virology without the access to an electron microscope, a technique to visualize phages in a bright field light microscope was developed [23]. It was made possible by staining phages with flagella stain, a procedure that increases the particle size and make phage heads increase to the limits of detection of light microscopy. Obviously, the particles became deformed and no fine details could be seen, making the use of the technique limited. Nevertheless, it allowed crude phage imaging. The use of scanning electron microscope (SEM) has also been applied to phage imaging. Phage P1, capable of infecting *Shigella*, was used as model to test parameters related to sample preparation and visualization by SEM (Fig. 1d). The paper describes the best conditions for SEM sample preparation, and suggests a correlation of SEM and TEM images to study virus life cycles [24,25].

In the early nineties the scanning tunneling microscopy (STM) and atomic force microscopy (AFM) approaches were also applied for phage imaging. In 1990 coliphages T7 and fd were visualized by STM after coating with a thin metal layer and deposition on a flat non-conductive substrate, allowing imaging with some cost to resolution [26]. Two years later, in 1992, a paper was published describing T4 phage imaging by AFM, taking advantage of the fact that the technique allows imaging of non-conductive samples. Images shown intact viral particles, either isolated or on aggregates, and damaged particles with DNA streaming out from the viral heads [27]. More recently a force distance based AFM approach was used to image single phages extruding from living cells. Biochemically sensitive tips were used to image *E. coli* infected with filamentous phages, providing direct visualization of phage assembly and localization on host cells [28].

4. Techniques for three-dimensional structural determination

Although some viruses have been crystallized and studied by X-ray diffraction techniques, phage particles are often complex in structure and for that reason do not form ordered crystals that

Please cite this article in press as: G.M. Almeida, et al., Bacteriophage imaging: past, present and future, Research in Microbiology (2018), https://doi.org/10.1016/j.resmic.2018.05.006

could be used for whole virion structural determination. Besides, most phage particles are near the size limit of biological structures that can be determined by this approach. Nevertheless, X-ray crystallography techniques have also been used for phage structural analysis. Phage HK97 was the first tailed phage to have its capsid structure determined by crystallography. Empty heads of the phage were produced by expressing capsid proteins in *E. coli*, and after purification they were successfully crystallized and measured by X-ray diffraction [29]. In 2004 the structure of the membrane-containing phage PRD1 was determined by X-ray crystallography [30]. As with other types of proteins, crystallization and X-ray diffraction have been used to study several individual phage particle components, such as the gene V from phage f1, fibers from phage Pf1 and the major capsid proteins of phage P23-77 [31–33]. In 2017 soft X-ray diffraction, an X-ray tomography approach that can be applied to samples without prior crystallization, has been used to image coliphage PR772, opening new possibilities for studying phage structures [34].

Cryo-electron microscopy (cryo-EM) is a technique that does not need fixing and staining during sample preparation, and structures can be determined without the need to form crystals, making it an interesting alternative to X-ray crystallography. Recent advances in the cryo-EM field increased the resolution of the technique to near atomic levels. In 2010 the structure of human adenovirus was solved by X-ray and by cryo-EM at similar resolutions [35,36], making it relevant for viral studies. Three dimensional determination of structures is possible by algorithmic means, resulting in cryo-EM tomography and single particle cryo-EM. For example, the asymmetric structure of the phage MS2 attached to its receptor has been determined by cryo-EM tomography [37]. The capsid structure of the *Salmonella* phage epsilon 15 was analyzed by single particle cryo-EM at a level of detail close to X-ray crystallography, in near-native solution conditions [38]. Cryo-EM was also used to solve the structure of the T4 baseplate-tail tube complex, in pre and post host attachment states, helping to understand sheath contraction in atomic details [39]. The structure of the FLiP (Flavobacterium-infecting, lipid-containing phage) virion, a boreal lake ssDNA phage with limited sequence similarity to other known viruses, was also solved by cryo-EM technique [40]. The determination of particle structure helped to understand its evolutionary relationship to other viruses by complementing sequence based approaches. The capsid structure of the phage Sf6 has also been determined by cryo-EM [41].

Combining cryo-EM with other techniques has provided detailed insight on phages and their interactions with the host. An *E. coli* filamentous phage (f1.K) was imaged by the combination of cryo-microscopy with the concept of in line electron holography, resulting in the first electron hologram of an individual phage particle [42]. By using the combination of immuno-labeling, negative staining, cryo-EM and cryo-electron tomography (cryo-ET), it was possible to understand how PRD1, a lipid containing tailless phage, delivers its genome to the bacterial host across the cell envelope [43]. Furthermore, fluorescence microscopy has been combined with cryo-EM to study the replication of the phage 201f2-1 on *Pseudomonas chlororaphis*. The assembly of a nucleus-like structure that separates viral DNA from the cell cytoplasm was described, showing that at least this phage is able to use compartmentalization inside the host cell for virus replication [44].

5. Significance of microscopy in phage ecology and environmental studies

Imaging has also been applied to research phage “behavior”, using the lytic/lysogenic outcome of phage lambda infections as a model. Single cell fluorescence microscopy has been used to study infection results, showing that the fate of infected cells correlates with variations in cell size. Larger cells had increased frequency of lysogenic outcome [45]. Using a more detailed, single virus approach, it was demonstrated that the cell fate after infection can be explained by the combination of individual viral “decisions” that occur at the subcellular level [46]. More recently, a four-color fluorescence system has been designed to study single cells, single phages and single viral DNA at the same time. When combined with computational models, it has helped to observe subcellular behaviors like phage cooperation for lysogenization, competition during lysis, and even confusion between both pathways [47]. Fluorescence microscopy has also been used to show DNA translocation from phages to hosts in a single molecule resolution [48], and a fluorescence in situ hybridization protocol has been adapted for studying phage infections on a single cell level [49].

Besides phage morphology and host interaction, electron microscopy has also been used to study phage diversity in environmental samples. Seawater samples were prepared and fixed for direct observation on an electron microscope, without the use of an enrichment process for phage isolation. Even without taking extra steps to grow the phages before analysis, various phage particles with distinct morphologies were found, as well as phage particles bound to bacterial cells [50]. An estimative of 10^3 to 10^4 viruses per milliliter of sea water was made, but it was noted by the authors that it is probably lower than the real number due to phage loss during sample preparation. The presence of so many phages led to the speculation of their importance in microbial ecology. Phages of marine origin previously obtained by isolation in bacterial hosts were analyzed by TEM of negatively stained samples. Seventy five phages were imaged and divided into twelve different groups based on morphological similarities, showing new structures and high structural diversity [51]. The ecological importance of phages got even more evident after environmental aquatic samples were analyzed again by TEM. Water samples from different locations were analyzed directly, without an enrichment step, and this time the sample preparation process minimized phage loss. Different phages, either as free particles or attached to bacterial cells, were visualized. Phage counts varied between 10^4 to 10^8 particles per milliliter of water, depending on sampling location and time of the year, revealing that phage abundance in the environment was higher than previously thought. The impressive number of phages in unpolluted water samples led to speculations about the so far overlooked importance of phages for keeping bacterial populations in balance on the environment, and also of the impact of these viruses in genetic transfers in natural prokaryote populations [52]. An alternative imaging technique was developed for counting environmental viruses, based on staining the samples with a fluorochrome specific for nucleic acids and directly counting the particles on an epifluorescence microscope. Although this technique does not provide any structural details, its simplicity in sample preparation and equipment requirements made it the most common technique for enumerating viruses from the environment [53,54]. This method revealed that TEM analysis is not only more time consuming for this purpose but also tends to underestimate viral abundance. A variation of the technique, consisting of stained particles treated with Dnase I, has been applied for indirect evaluation of phage capsid structural deformity [55].

6. Moving away from electrons: helium ion microscopy

The scanning helium ion microscope (HIM) is a recent advance in imaging. Instead of using electrons, imaging is based on the use of a positively charged helium ion beam [56]. Helium beam allows higher image resolution (close to 0.5 nm), larger depth of focus and dispenses conductive coating of biological samples, this last

Please cite this article in press as: G.M. Almeida, et al., Bacteriophage imaging: past, present and future, Research in Microbiology (2018), https://doi.org/10.1016/j.resmic.2018.05.006

advantage being important for imaging of fragile sub-nanometer structures and for avoiding artifacts or masking generated by coating. Biological samples, including a bacterium, were imaged by HIM for the first time in 2013 [57]. In 2017 the nanoscale imaging capacity of the HIM was used to investigate plaques formed by T4 infection on *E. coli* bacterial lawns in order to test the applicability of helium ion microscopy to phage–host interaction studies [58] (Fig. 1e). The samples were directly prepared from pieces of double layered agar containing the bacteria lawn with phage plaques, so the imaging could be made on viral plaques as they naturally occurs. Various stages of T4 infection could be seen by imaging different spots within and around a plaque, since the infection spreads radially from the ground zero, with no cells in the center and newly infected cells on the edges. It was possible to obtain high resolution images of burst cells, cells with multiple phages attached, phages with normal morphology and phages with already contracted tails. Icosahedral head shape, widening in the tail end due to the baseplate structure, and tail fibers attached to the bacterial cell wall were also visualized in detail. A large number of elongated *E. coli* cells, also mentioned in older phage imaging papers [13,14], were also seen, hinting that these mutants may be more common than previously thought. Another characteristic of the HIM was also tested in the samples mentioned above. By increasing the ion current, it is possible to mill (cut) the material at specific locations. Cross sections of bacterial cells, of phage particles and removal of agar substrate pieces were all demonstrated by the milling process. Comparing to other imaging techniques, HIM imaging appears to be more straightforward to use and provides the opportunity to image whole colonies or plaques or other types of complex microbial samples directly on their substrate, with sub-nanometer resolution, with no need for metal coating [58].

We are continuing to apply helium ion microscopy to study phages and phage-bacteria interactions. We have developed protocols to avoid agar collapse during preparations, and gained experience with different types of organisms. In Fig. 2 we present a few images as examples of our latest phage-bacteria imaging. Sample preparation was made according to Leppänen et al., 2017 [58].

7. Conclusions and perspectives

From its origins almost eighty years ago to today, phage imaging has improved immensely (Fig. 1) and helped to understand much of these intriguing and important organisms. The earlier years of the electron microscope development resulted in James Hillier and Ernst Ruska sharing the 1960 Albert Lasker Award for Basic Medical Research for their contribution to the development of the first electron microscopes, and Ernst Ruska receiving a Nobel Prize in 1986 for his fundamental work in electron optics and for the design of the first electron microscope [2,3]. It is also possible to see in the first Luria, Delbruck and Anderson phage imaging papers [13] their interest in basic molecular biology that led to the shared Nobel

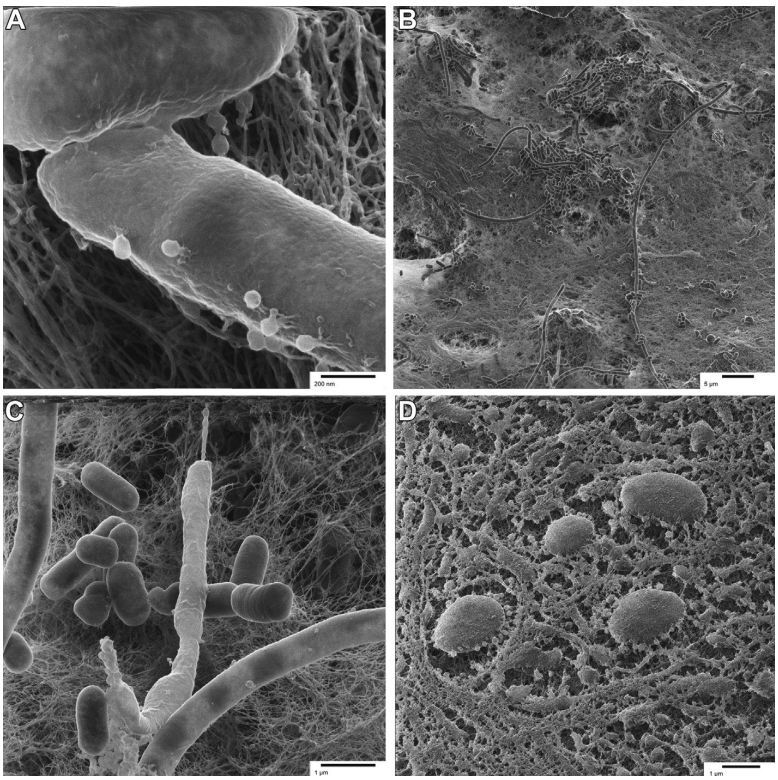

Fig. 2. Phage and bacteria interaction images obtained with helium ion microscopy. a) *E. coli* cells infected with T4 phage. b) *E. coli* cells on the edge of a T4 plaque, growing as cell islands with long cells apparently scanning the surface. c) Higher magnification of the previous picture showing a lysed long cell (in white) and another one with several white patches on its cell wall. White-grayish spots on the cell wall might indicate endolysin activity from within. d) Details of susceptible *Flavobacterium columnare* cells infected with the FCL-2 phage. Note the high number of dead cells on the field and four rounded cells, probably losing its characteristic morphology before bursting.

Please cite this article in press as: G.M. Almeida, et al., Bacteriophage imaging: past, present and future, Research in Microbiology (2018), https://doi.org/10.1016/j.resmic.2018.05.006

Prize in 1969 related to replication mechanisms and genetic structure of viruses. In 2017, Dubochet, Frank and Henderson were awarded a Nobel Prize in chemistry for developing cryo-EM, a method that has had a significant impact in high-resolution imaging and consequently in three-dimensional structure determination of biomolecules and viruses. Electron microscopy in all its variations and other imaging techniques were crucial for better understanding phages, from structural details to interaction with hosts and diversity. Imaging has contributed to the knowledge that phages are the most abundant organisms in the biosphere, are crucial in regulating global biochemical cycles, have had an important role as models for molecular biology studies and are a viable alternative to treat bacterial diseases by the use of phage therapy.

It is hard to imagine how imaging techniques will improve in the next decades, and what knowledge will be gained from their use. However, it can be expected that there will always be attempts to improve existing equipment and technologies, and to create new ones. From a technical point of view, advances in the ability to see in more detail at molecular or atomic resolution, at shorter time scales, and close to native conditions may be the main motivations [59]. From a biological point of view, there is a high interest in single-cell live imaging, which can also be applied in combination to single-virus and single-molecule imaging. It has been advancing in relation to time resolution (changes detected in milliseconds) and sensitivity (detection of few photons per pixel), but still requires the use of light microscopy and fluorescent labels [60]. Latest developments in AFM include the High-Speed AFM, which allow the following of single molecules dynamics in real time, with potential to be applied to viruses [61]. Mega-electron-volt (MeV) ion beams have been recently used for imaging cells, and the capacity of penetrating through several microns of biological tissue with little deflection (thus maintaining spatial resolution) can also be useful for viral infection studies [62]. Current advances in state of the art microscopy are based on the use of quantum mechanics for photoionization microscopy. A quantum magnetic resonance microscope approach was recently used to image copper complexes in solution, by a non-invasive and non-interfering process that could perhaps in time be applied to living cells [63]. A combination of adaptive optics to lattice light-sheet microscopy (AO-LLSM) was used to visualize cellular processes tri-dimensionally recently [64]. Its non-invasive imaging of events at different scales has potential to be adapted to the study of phage infected cells. As technology gets more advanced sample preparation steps and sample modifications prior to imaging may decrease, optimally leading to analysis of samples close to their native state by higher definition approaches.

Conflict of interests

There is no conflict of interests between the authors.

Acknowledgements

This work was supported by the Finnish Centre of Excellence Program of the Academy of Finland (CoE in Biological Interactions 2012–2017 #252411), by the Academy of Finland (grants #266879 and #304615), by the Jane and Aatos Erkko Foundation, and by the Academy of Finland FIRI2014 infrastructure programme.

References

[1] Lustig A, Levine A. One hundred years of virology. J Virol 1992;66:4629–31.
[2] Oransky I. James Hillier. Lancet 2007;369:1162.
[3] Kruger DH, Schneck P, Gelderblom HR. Helmut Ruska and the visualisation of viruses. Lancet 2000;355:1713–7.
[4] von Borries B, Ruska E, Ruska H. Bakterien und Virus in übermikroskopischer Aufnahme. Klin Wochenschr 1938;17:921–51938. 17:921–5.
[5] Ruska H. Über die Sichtbarmachung der bakteriophagen Lyse im Übermikroskop. Naturwissenschaften 1940;28:45–6.
[6] Peankuch E, Kausche GA. Isolierung und übermikroskopische Abbildung eines Bakteriophagen. Naturwissenschaften 1940;28:46.
[7] Ackermann H-W. The first phage electron micrographs. Bacteriophage 2011;1:225–7.
[8] Ruska H. Morphologische Befunde bei der bakteriophagen Lyse. Arch Gesamte Virusforsch 1942:345–87.
[9] Ruska H. Versuch zu einer Ordnung der Virusarten. Arch Gesamte Virusforsch 1943;2:480–98.
[10] Ruska H. Ergebnisse der Bakteriophagenforschung und ihre Deutung nach morphologischen Befunden. Ergeb Hyg Bakteriol Immunforsch Exp Ther 1943:437–98.
[11] Luria SE, Anderson TF. The identification and characterization of bacteriophages with the electron microscope. Proc Natl Acad Sci USA 1942;28:127–30.1.
[12] Sharma S, Chatterjee S, Datta S, Prasad R, Dubey D, Prasad RK, et al. Bacteriophages and its applications: an overview. Folia Microbiol (Praha) 2017;62:17–55.
[13] Luria SE, Delbrück M, Anderson TF. Electron microscope studies of bacterial viruses. J Bacteriol 1943;46:57–77.
[14] Wyckoff R. The electron microscopy of developing bacteriophage. I. Plaques on solid media. Biochim Biophys Acta 1948;2:27–37.
[15] Wyckoff R. The electron microscopy of developing bacteriophage. II. Growth of T4 in liquid culture. Biochim Biophys Acta 1948;2:246–53.
[16] Fraser D, Williams RC. Details of frozen-dried T3 and T7 bacteriophages as shown by electron microscopy. J Bacteriol 1953;65:167–70.
[17] Williams RC, Fraser D. Morphology of the seven T-bacteriophages. J Bacteriol 1953;66:458–64.
[18] Brenner S, Horne RW. A negative staining method for high resolution electron microscopy of viruses. Biochim Biophys Acta 1959;34:103–10.
[19] Brenner S, Streisinger G, Horne RW, Champe SP, Barnett L, Benzer S, et al. Structural components of bacteriophage. J Mol Biol 1959;1:IN9–21.
[20] Bradley DE, Kay D. The fine structure of bacteriophages. J Gen Microbiol 1960;23:553–63.
[21] Ackermann HW. 5500 Phages examined in the electron microscope. Arch Virol 2007;152:227–43.
[22] Bradley DE. Ultrastructure of bacteriophage and bacteriocins. Bacteriol Rev 1967;31:230–314.
[23] McCamish J, Mickelson JC. Staining of bacteriophages for light microscopy. Appl Microbiol 1971;21:149.
[24] Wendelschafer-Crabb G, Erlandsen SL, Walker DH. Conditions critical for optimal visualization of bacteriophage adsorbed to bacterial surfaces by scanning electron microscopy. J Virol 1975;15:1498–503.
[25] Broers AN, Panessa BJ, Gennaro JF. High-resolution scanning electron microscopy of bacteriophages 3C and T4. Science 1975;189:637–9.
[26] Keller RW, Dunlap DD, Bustamante C, Keller DJ. Scanning tunneling microscopy images of metal-coated bacteriophages and uncoated, double-stranded DNA. J Vac Sci Technol A Vac Surf Film 1990;8.
[27] Kolbe WF, Ogletree DF, Salmeron MB. Atomic force microscopy imaging of T4 bacteriophages on silicon substrates. Ultramicroscopy 1992;42–44:1113–7.
[28] Alsteens D, Trabelsi H, Soumillion P, Dufrêne YF. Multiparametric atomic force microscopy imaging of single bacteriophages extruding from living bacteria. Nat Commun 2013;4.
[29] Wikoff WR, Duda RL, Hendrix RW, Johnson JE. Crystallization and preliminary X-ray analysis of the dsDNA bacteriophage HK97 mature empty capsid. Virology 1998 Mar 30;243(1):113–8.
[30] Abrescia NGA, Cockburn JJB, Grimes JM, Sutton GC, Diprose JM, Butcher SJ, et al. Insights into assembly from structural analysis of bacteriophage PRD1. Nature 2004;432:68–74.
[31] Skinner MM, Zhang H, Leschnitzer DH, Guan Y, Bellamy H, Sweet RM, et al. Structure of the gene V protein of bacteriophage f1 determined by multiwavelength x-ray diffraction on the selenomethionyl protein. Proc Natl Acad Sci USA 1994;91(6):2071–5.
[32] Welsh LC, Marvin DA, Perham RN. Analysis of X-ray diffraction from fibres of Pf1 Inovirus (filamentous bacteriophage) shows that the DNA in the virion is not highly ordered. J Mol Biol 1998;284(5):1265–71.
[33] Rissanen I, Pawlowski A, Harlos K, Grimes JM, Stuart DI, Bamford JKH. Crystallization and preliminary crystallographic analysis of the major capsid proteins VP16 and VP17 of bacteriophage P23-77. Acta Crystallogr Sect F Struct Biol Cryst Commun 2012;68:580–3.
[34] Reddy HKN, Yoon CH, Aquila A, Awel S, Ayyer K, Barty A, et al. Coherent soft X-ray diffraction imaging of coliphage PR772 at the Linac coherent light source. Sci Data 2017;4.
[35] Reddy VS, Natchiar SK, Stewart PL, Nemerow GR. Crystal structure of human adenovirus at 3.5 a resolution. Science 2010;329(5995):1071–5.
[36] Liu H, Jin L, Koh SBS, Atanasov I, Schein S, Wu L, et al. Atomic structure of human adenovirus by Cryo-EM reveals interactions among protein networks. Science 2010;329(5995):1038–43.
[37] Dent KC, Thompson R, Barker AM, Hiscox JA, Barr JN, Stockley PG, et al. The asymmetric structure of an icosahedral virus bound to its receptor suggests a mechanism for genome release. Structure 2013;21:1225–34.

Please cite this article in press as: G.M. Almeida, et al., Bacteriophage imaging: past, present and future, Research in Microbiology (2018), https://doi.org/10.1016/j.resmic.2018.05.006

[38] Jiang W, Baker ML, Jakana J, Weigele PR, King J, Chiu W. Backbone structure of the infectious epsilon15 virus capsid revealed by electron cryomicroscopy. Nature 2008;451:1130–4.
[39] Taylor NMI, Prokhorov NS, Guerrero-Ferreira RC, Shneider MM, Browning C, Goldie KN, et al. Structure of the T4 baseplate and its function in triggering sheath contraction. Nature 2016;533:346–52.
[40] Laanto E, Mäntynen S, De Colibus L, Marjakangas J, Gillum A, Stuart DI, et al. Virus found in a boreal lake links ssDNA and dsDNA viruses. Proc Natl Acad Sci 2017;114(31):8378–83.
[41] Zhao H, Li K, Lynn AY, Aron KE, Yu G, Jiang W, et al. Structure of a headful DNA-packaging bacterial virus at 2.9 Å resolution by electron cryo-microscopy. Proc Natl Acad Sci 2017;114:3601–6.
[42] Stevens GB, Krüger M, Latychevskaia T, Lindner P, Plückthun A, Fink HW. Individual filamentous phage imaged by electron holography. Eur Biophys J 2011;40:1197–201.
[43] Peralta B, Gil-Carton D, Castaño-Díez D, Bertin A, Boulogne C, Oksanen HM, et al. Mechanism of membranous tunnelling nanotube formation in viral genome delivery. PLoS Biol 2013;11(9).
[44] Chaikeeratisak V, Nguyen K, Khanna K, Brilot AF, Erb ML, Coker JKC, et al. Assembly of a nucleus-like structure during viral replication in bacteria. Science 2017;355:194–7 (80).
[45] St-Pierre F, Endy D. Determination of cell fate selection during phage lambda infection. Proc Natl Acad Sci 2008;105:20705–10.
[46] Zeng L, Skinner SO, Zong C, Sippy J, Feiss M, Golding I. Decision making at a subcellular level determines the outcome of bacteriophage infection. Cell 2010;141:682–91.
[47] Trinh JT, Székely T, Shao Q, Balázsi G, Zeng L. Cell fate decisions emerge as phages cooperate or compete inside their host. Nat Commun 2017;8.
[48] Van Valen D, Wu D, Chen YJ, Tuson H, Wiggins P, Phillips R. A single-molecule Hershey-chase experiment. Curr Biol 2012;22:1339–43.
[49] Allers E, Moraru C, Duhaime MB, Beneze E, Solonenko N, Barrero-Canosa J, et al. Single-cell and population level viral infection dynamics revealed by phage FISH, a method to visualize intracellular and free viruses. Environ Microbiol 2013;15:2306–18.
[50] Torrella F, Morita RY. Evidence by electron micrographs for a high incidence of bacteriophage particles in the waters of Yaquina Bay, Oregon: ecological and taxonomical implications. Appl Environ Microbiol 1979;37:774–8.
[51] Frank H, Moebus K. An electron microscopic study of bacteriophages from marine waters. Helgoländer Meeresuntersuchungen 1987;41:385–414.
[52] Bergh Ø, BØrsheim KY, Bratbak G, Heldal M. High abundance of viruses found in aquatic environments. Nature 1989;340:467–8.
[53] Hara S, Terauchi K, Koike I. Abundance of viruses in marine waters: assessment by epifluorescence and transmission electron microscopy. Appl Environ Microbiol 1991;57:2731–4.
[54] Hermes KP, Suttle CA. Direct counts of viruses in natural waters and laboratory cultures by epifluorescence microscopy. Limnol Oceanogr 1995;40:1050–5.
[55] Naicker K, Durbach SI. Epifluorescent microscopy to evaluate bacteriophage capsid integrity. Biotechniques 2007;43:473–6.
[56] Ward BW, Notte JA, Economou NP. Helium ion microscope: a new tool for nanoscale microscopy and metrology. J Vac Sci Technol B Microelectron Nanom Struct 2006;24:2871.
[57] Joens MS, Huynh C, Kasuboski JM, Ferranti D, Sigal YJ, Zeitvogel F, et al. Helium Ion Microscopy (HIM) for the imaging of biological samples at sub-nanometer resolution. Sci Rep 2013;3.
[58] Leppänen M, Sundberg L-R, Laanto E, de Freitas Almeida GM, Papponen P, Maasilta IJ. Imaging bacterial colonies and phage-bacterium interaction at sub-nanometer resolution using helium-ion microscopy. Adv Biosyst 2017;1.1700070.
[59] Zhu Y, Dürr H. The future of electron microscopy. Phys Today 2015;68:32–8.
[60] Schneider JP, Basler M. Shedding light on biology of bacterial cells. Philos Trans R Soc B Biol Sci 2016;371:20150499.
[61] Takayuki U, Scheuring S. Applications of high-speed atomic force microscopy to real-time visualization of dynamic biomolecular processes. Biochim Biophys Acta 2018;1862:229–40.
[62] Bettiol AA, Mi Z, Watt F. High-resolution fast ion microscopy of single whole biological cells. Appl Phys Rev 2016;3.
[63] Simpson DA, Ryan RG, Hall LT, Panchenko E, Drew SC, Petrou S, et al. Electron paramagnetic resonance microscopy using spins in diamond under ambient conditions. Nat Commun 2017;8.
[64] Liu TL, Upadhyayula S, Milkie DE, Singh V, Wang K, Swinburne IA, et al. Observing the cell in its native state: imaging subcellular dynamics in multicellular organisms. Science 2018;360. eaaq1392.

Please cite this article in press as: G.M. Almeida, et al., Bacteriophage imaging: past, present and future, Research in Microbiology (2018), https://doi.org/10.1016/j.resmic.2018.05.006